

# Local structure and symmetry of paramagnetic ions in ferroelectric ceramics

Vom Fachbereich Chemie  
der Technischen Universität Darmstadt

zur Erlangung des akademischen Grades eines

Doctor rerum naturalium (Dr. rer. nat.)

genehmigte

Dissertation

vorgelegt von

Dipl.-Phys. Hrvoje Meštrić

aus Varaždin in Kroatien

Berichterstatter: Prof. Dr. Klaus-Peter Dinse

Mitberichterstatter: Prof. Dr. Rolf Schäfer

Tag der Einreichung: 24.01.2006

Tag der mündlichen Prüfung: 22.05.2006

Darmstadt 2006

D 17



This study is a result of the work carried out from October 2002 to January 2006 at the Eduard-Zintl-Institute for Inorganic and Physical Chemistry, Darmstadt University of Technology, under the supervision of Prof. Dr. Klaus-Peter Dinse. It was conducted and financed as a part of the Joint Research Project 595 *Electric Fatigue in Functional Materials* of the German Science Foundation.



# Acknowledgements

I wish to thank to all the people who supported me throughout this work and contributed to this study. Especially I would like to thank to ...

... my supervisor Prof. Dr. Klaus-Peter Dinse;  
... my project leader Dr. Rüdiger-Albert Eichel;  
... Prof. Dr. Michael Böhm for proofreading;  
... Prof. Dr. Rolf Schäfer for agreeing to be coreferent of the thesis;  
... and the other members of our research group: Dipl. Ing. Björn Corzilius, Dr. Ing. Armin Gembus, Dipl. Geol. Ulla Henkes, Dr. Ing. Peter Jakes, Dr. Ing. Elvir Ramić, Dr. Norbert Weiden und Viktor Tissen for their generous help and permanent support;  
... Dipl. Ing. Thomas Kloss, Dipl. Ing. Christopher Neumann and Dipl. Ing. Christian Quick for their contributions as undergraduate students.

The present study would not be possible without help and interdisciplinary cooperation with many research groups. I would like to express my acknowledgements to...

...Dr. Hans Kungl and Prof. Dr. Michael J. Hoffman at the Institute of Ceramics in Mechanical Engineering, University of Karlsruhe for providing the samples;  
...Dipl. Ing. Kristin Schönau, Dr. Martin Knapp, Dr. Helmut Ehrenberg and Prof. Dr. Hartmut Fuess at the Materials Science Department, Darmstadt University of Technology for high resolution diffraction measurements;  
...Dipl. Ing. Sonja Laubach, Dipl. Ing. Stefan Laubach and Prof. Dr. Peter C. Schmidt at the Eduard-Zintl-Institute on the Darmstadt University of Technology for performing *ab initio* calculations;  
...Dr. Andrew Ozarowski, Dr. Johan van Tol and Dr. Louis Claude Brunel at the Center for Interdisciplinary Magnetic Resonance, National High Magnetic Field Laboratory on the Florida State University for high-field EPR measurements;  
...Dipl. Phys. Emre Erdem, Dipl. Phys. Joachim Hoentsch and Prof. Dr. Rolf Böttcher from the Institute of Experimental Physics, University of Leipzig for high-temperature and Q-band EPR measurements;  
...Dipl. Ing. Nina Balke, Dr. Doru Lupascu, Dr. Rhuzong Zuo and all other members of SFB 595 Joint Research Project.

I would particularly like to thank to my wife Klara and to my whole family.



# CONTENTS

1. INTRODUCTION . . . . .	11
<i>Part I Theory</i>	15
2. FERROELECTRIC MATERIALS . . . . .	17
2.1 Electric properties of crystals . . . . .	17
2.2 Ferroelectric behaviour . . . . .	19
2.2.1 Ferroelectric crystals . . . . .	19
2.2.2 Microscopic description of ferroelectrics . . . . .	19
2.2.3 Ferroelectric domains and poling . . . . .	20
2.2.4 Polarisation hysteresis loop . . . . .	22
2.2.5 Antiferroelectricity . . . . .	23
2.2.6 Fatigue and ageing . . . . .	23
2.3 Role of defects in ferroelectrics . . . . .	24
2.3.1 Point defects . . . . .	25
2.3.2 Defect chemistry in perovskite compositions . . . . .	25
2.3.3 Impact of defects on ferroelectric properties . . . . .	27
3. PARAMAGNETIC IONS IN CRYSTAL FIELD . . . . .	29
3.1 Free ion . . . . .	29
3.1.1 One-electron atom . . . . .	29
3.1.2 Many-electron atoms . . . . .	31
3.1.3 Paramagnetic ions . . . . .	33
3.1.4 Effective spin Hamiltonian . . . . .	33
3.2 Ions in a crystal field . . . . .	36
3.2.1 Crystal field . . . . .	36
3.2.2 Crystal field potential . . . . .	38
3.3 S-state ions . . . . .	39
3.3.1 Energy levels for S-state ions . . . . .	39
3.3.2 Spin Hamiltonian for S-state ions in a crystal field . . . . .	40
3.4 Overview of the Newman superposition model . . . . .	43
3.4.1 Role of the Newman superposition model . . . . .	43
3.4.2 Assumptions of the Newman superposition model . . . . .	44
3.4.3 The Newman superposition model for the spin Hamiltonian . . . . .	45

---

4. ELECTRON PARAMAGNETIC RESONANCE . . . . .	49
4.1 Physical backgrounds of electron paramagnetic resonance . . . . .	49
4.1.1 The resonance phenomenon . . . . .	49
4.1.2 Thermal equilibrium . . . . .	50
4.1.3 Transition probabilities . . . . .	51
4.1.4 Line widths . . . . .	51
4.2 Perturbative solutions for the spin Hamiltonian . . . . .	53
4.2.1 High-field approximation . . . . .	53
4.2.2 Low-field approximation . . . . .	56
4.3 EPR spectra of polycrystalline samples . . . . .	60
4.4 Numerical simulations of EPR spectra . . . . .	62
 <i>Part II Experiments and results</i>	 65
5. OVERVIEW OF EXPERIMENTS . . . . .	67
5.1 X-band EPR . . . . .	67
5.1.1 Microwave source . . . . .	68
5.1.2 Resonant cavities . . . . .	69
5.1.3 Signal detection . . . . .	70
5.1.4 Magnet unit . . . . .	70
5.2 W-band EPR . . . . .	71
5.2.1 Microwave source . . . . .	71
5.2.2 Resonant cavities . . . . .	71
5.2.3 Magnet unit . . . . .	71
5.3 High-frequency EPR . . . . .	73
5.3.1 Microwave sources . . . . .	73
5.3.2 Sample holder . . . . .	73
5.3.3 Signal detection . . . . .	74
5.3.4 Magnet system . . . . .	74
6. STRUCTURAL CALCULATIONS . . . . .	75
6.1 Newman superposition model – previous studies . . . . .	75
6.1.1 NSM parameters for $3d^5$ ions . . . . .	75
6.1.2 Application of the NSM for perovskite structures . . . . .	76
6.2 Newman superposition model – calculation procedure . . . . .	78
6.2.1 Computational algorithm . . . . .	78
6.2.2 Limitations of the NSM . . . . .	81
7. LEAD TITANATE: EXPERIMENTS . . . . .	83
7.1 Introduction to $\text{PbTiO}_3$ . . . . .	83
7.1.1 Preparation of $\text{PbTiO}_3$ . . . . .	84
7.1.2 Determination of the crystal structure of $\text{PbTiO}_3$ . . . . .	84



---

7.2	Previous EPR measurements . . . . .	87
7.3	EPR measurements of $\text{Fe}^{3+}$ centre in $\text{PbTiO}_3$ . . . . .	88
7.3.1	Low frequency measurements of $\text{Fe}^{3+}:\text{PbTiO}_3$ . . . . .	88
7.3.2	W-band measurements of $\text{Fe}^{3+}:\text{PbTiO}_3$ . . . . .	90
7.3.3	High frequency measurements of $\text{Fe}^{3+}:\text{PbTiO}_3$ . . . . .	93
7.4	Determination of the spin Hamiltonian parameters of $\text{Fe}^{3+}:\text{PbTiO}_3$ . . . . .	95
7.4.1	Perturbational analysis of the $\text{Fe}^{3+}:\text{PbTiO}_3$ spectra . . . . .	95
7.4.2	Numerical simulations of the $\text{Fe}^{3+}:\text{PbTiO}_3$ spectra . . . . .	97
8.	LEAD TITANATE: STRUCTURAL CALCULATIONS . . . . .	99
8.1	The NSM analysis of $\text{Fe}^{3+}$ in $\text{PbTiO}_3$ . . . . .	99
8.2	DFT analysis of $\text{Fe}^{3+}:\text{PbTiO}_3$ . . . . .	103
8.2.1	DFT analysis of undoped $\text{PbTiO}_3$ . . . . .	103
8.2.2	DFT analysis of $\text{Fe}^{3+}$ -doped $\text{PbTiO}_3$ . . . . .	105
8.3	Discussion of the structure of $\text{Fe}^{3+}:\text{PbTiO}_3$ . . . . .	106
9.	LEAD ZIRCONATE: EXPERIMENTS . . . . .	111
9.1	Introduction to lead zirconate . . . . .	111
9.1.1	Preparation of $\text{PbZrO}_3$ . . . . .	111
9.1.2	Determination of the crystal structure of $\text{PbZrO}_3$ . . . . .	112
9.2	EPR measurements of the $\text{Fe}^{3+}$ centre in $\text{PbZrO}_3$ . . . . .	115
9.2.1	Low frequency measurements $\text{Fe}^{3+}:\text{PbZrO}_3$ . . . . .	115
9.2.2	W-band measurements $\text{Fe}^{3+}:\text{PbZrO}_3$ . . . . .	117
9.2.3	High frequency measurements $\text{Fe}^{3+}:\text{PbZrO}_3$ . . . . .	118
9.3	Determination of the spin Hamiltonian parameters of $\text{Fe}^{3+}:\text{PbZrO}_3$ . . . . .	120
9.3.1	Perturbational analysis of the $\text{Fe}^{3+}:\text{PbZrO}_3$ spectra . . . . .	120
9.3.2	Numerical simulations of $\text{Fe}^{3+}:\text{PbZrO}_3$ spectra . . . . .	121
10.	LEAD ZIRCONATE: STRUCTURAL CALCULATIONS . . . . .	127
10.1	The NSM Analysis of $\text{Fe}^{3+}$ in $\text{PbZrO}_3$ . . . . .	127
10.2	Discussion of the structure of $\text{Fe}^{3+}:\text{PbZrO}_3$ . . . . .	132
11.	CONCLUSIONS AND OUTLOOK . . . . .	137
12.	ZUSAMMENFASSUNG . . . . .	141



# 1. INTRODUCTION

Mechanical, chemical and electrical properties of materials are determined by their structure in nanoscale. Atoms in crystals are positioned in regular, periodical patterns which obey various degrees of symmetry. The perfection and symmetry of real crystal lattices is often interrupted by alien atoms. These impurities or defects occur rarely - one in a million of regular atoms, or even less. They nevertheless can have a large influence on the properties of crystals. For instance, defects cause electric conductivity in non-metal crystals. In piezoelectric crystals, defects strongly influence the electromechanical properties. A complete understanding of the influence of defects on macroscopic properties still remains a scientific challenge.

The magnetic properties of open-shell defects in crystals can be studied by *electron paramagnetic resonance* (EPR) spectroscopy. EPR spectroscopy measures transitions between the energy levels of atomic magnetic moments. These levels are additionally influenced by an external magnetic field. Moreover, the magnetic properties of atoms are largely changed when they are incorporated as defect centres in a crystal. The investigation of the paramagnetic atoms provides many information on the nature of the impurities on the particular crystal host. This information can be used to explain the macroscopic properties of the crystal.

Many solid materials have a so-called *polycrystalline* structure. These materials are formed by grains of crystalline solids. The grains are randomly oriented relative to each other. They are usually very small, but still large enough to encompass thousands of atoms with periodical arrangement. Polycrystalline materials have only a short range order. One important class of polycrystalline materials is ceramic.

The investigation of defects via EPR in polycrystalline structures is more complex than in monocrystals. Symmetry is preserved only in small, statistically distributed grains. A higher amount of disorder and statistical fluctuations is to be expected. However, modern high-field EPR techniques are able to extract useful information on the magnetic interactions of defects in ceramics.

In this work the paramagnetic trivalent iron ion ( $\text{Fe}^{3+}$ ) is investigated. The  $\text{Fe}^{3+}$  ion with half-filled *d*-shell occurs as natural impurity in many oxide crystals. Its magnetic energy levels are split considerably when it is placed in a crystal lattice. Therefore the  $\text{Fe}^{3+}$  behaviour as impurity serves as a local probe for the description of the nanoscale structure of a host crystal.

Two oxide host crystals for the  $\text{Fe}^{3+}$  defect are investigated in this study: *lead titanate* ( $\text{PbTiO}_3$ ) and *lead zirconate* ( $\text{PbZrO}_3$ ). Both crystals possess a *perovskite* structure. The basic pattern of the perovskite structure consists of a central cation

(Ti or Zr) surrounded by an octahedron of the oxygen atoms. The oxygen octahedron is placed in the middle of a cube defined by the Pb atoms on the vertices. Although the basic structural pattern is similar, there are also important differences. In lead titanate the cube is elongated along one edge, resulting in a tetragonal crystal structure. The perovskite cube, however, still form the periodic unit cell. In lead zirconate, the cube is completely distorted. An array of eight cubes is needed to define the unit cell. Lead zirconate possesses an orthorhombic crystal structure.

Lead titanate and lead zirconate are used as components in solid solution *lead zirconate titanate* ( $\text{Pb}[\text{Zr}_x\text{Ti}_{1-x}]\text{O}_3$ , PZT). This ceramic material is, after quartz, the technologically most important ferroelectric material. It is a basis for many functional ceramics applications in modern electronics. PZT may be prepared by mixing of any ratio of lead titanate and lead zirconate. Its electrical and mechanical properties are important for applications in sensors, thin-film capacitors etc. They may be influenced by varying the ratio of the components. Thus, the characterisation of the pure compounds is a prerequisite to analyse the more complex PZT material.

In order to improve the properties of PZT, several transition metals or rare earths may be added intentionally as impurities. A variety of ferroelectric properties can be controlled in this way. For this reason it is important to understand the role of such extrinsic defects.

The addition of the  $\text{Fe}^{3+}$  ions to PZT material is technologically called ‘hard doping’. It has been noticed that this process increases the conductivity of PZT. As PZT is used as insulating material, this is an unwanted effect. Moreover, as more iron impurities are added, ferroelectric PZT material exhibits a resistance to ‘poling’ in an external electric field. This behaviour seriously affects its otherwise excellent features of retaining the electrical polarisation when the external field is removed. The influence of the  $\text{Fe}^{3+}$  impurities is still not completely understood. However, there is a clear connection between the  $\text{Fe}^{3+}$  defects and missing oxygen ions in the lattice of PZT. The so-called *oxygen vacancies* are the most important defects in ferroelectric. They serve as main ionic charge carriers in these materials. It is supposed that the  $\text{Fe}^{3+}$  atom and oxygen vacancies form strongly bonded defect associates which influence mobility of oxygen vacancies.

The purpose of this work is to investigate the local structure at the iron defect site in  $\text{PbTiO}_3$  and  $\text{PbZrO}_3$ . Important task is to analyse the atomic arrangement of the iron–oxygen vacancy association. The following question has to be answered: do the iron defects and the oxygen vacancies always form defect associates in  $\text{PbTiO}_3$  and  $\text{PbZrO}_3$ ? In these polycrystalline materials, it was only possible by high-field EPR.

Probes were synthesised with a well-defined iron content. The preparation of the samples was done by Hans Kungl and Michael J. Hoffman from the Institute of Ceramics in Mechanical Engineering at the University of Karlsruhe.

Many different EPR experiments were necessary to accomplish the analysis of the interplay between the  $\text{Fe}^{3+}$  ions and oxygen vacancies. They were mainly performed at the Eduard-Zintl-Institute at Darmstadt University of Technology. Additional EPR measurements were done with the help of Emre Erdem, Joachim Hoentsch and Rolf Böttcher from the Institute of Experimental Physics at the University of Leipzig. A special attention has been given to the so-called *high-field* techniques, where magnetic fields of more than 6 Tesla are used. The high-field EPR was performed by Andrew Ozarowski, Johan van Tol and Louis Claude Brunel at the Center for Interdisciplinary Magnetic Resonance of the National High Magnetic Field Laboratory at the Florida State University.

An important contribution to the investigation of this topic has been the exact determination of the crystal structure at low temperature. The high-resolution synchrotron diffraction measurements were accomplished by Kristin Schönau, Martin Knapp, Helmut Ehrenberg and Hartmut Fuess from the Materials Science Department at the Darmstadt University of Technology.

Another important part of this analysis were *ab initio* calculations of defect structures. They were carried out by Sonja Laubach, Stefan Laubach and Peter C. Schmidt from the Eduard-Zintl-Institute at the Darmstadt University of Technology.

This work is divided into two parts. The first part encompasses theoretical background and the second part presents experiments, calculations and results.

In Chapter 2 basic concepts of ferroelectricity are explained. Macroscopic electrical properties of these materials are considered from the view of crystal defects. The importance of crystal defects in ferroelectrics is elaborated.

In Chapter 3 the theoretical basis for the understanding of the paramagnetic atoms is summarised. First, free open-shell ions are considered. The spin Hamiltonian for free ions interacting with a magnetic field is presented. Second, a crystal field theory for paramagnetic ions in a crystal lattice is shortly explained. Special attention is focused on the so-called ‘S-state ions’ – i.e. ions with the outer shell exactly half-filled.  $\text{Fe}^{3+}$  belongs to this class of ions. The theoretical background of the semi-empirical *Newman superposition model* is also discussed in this Chapter. It relates geometrical and physical data of a paramagnetic ion in a crystal lattice.

In Chapter 4, the experimental techniques of electron paramagnetic resonance are reviewed. Various possibilities for the analysis of EPR experiments are discussed. Numerical simulations of EPR spectra of polycrystalline materials are described.

Chapter 5 reviews different experimental EPR setups used in this work. The continuous wave EPR in the X-band and W-band frequency ranges is described. The high-field EPR spectrometer used in this work is also shortly presented.

Calculations performed for the modelling of crystal defect structures via the Newman superposition model are elaborated in Chapter 6. A detailed description of the computational procedure is given. The limitations of this approach are also discussed.

Chapter 7 elaborates the crystal structure and the EPR measurements of  $\text{Fe}^{3+}$  in lead titanate. Various recorded spectra are shown and discussed.

Chapter 8 presents conclusions concerning the structure of the  $\text{Fe}^{3+}$  defect in lead titanate. These conclusions are derived from the EPR measurements, semi-empirical calculations and *ab initio* calculations. The results and possible impacts on the connection between  $\text{Fe}^{3+}$  defects and oxygen vacancies are discussed.

Chapter 9 deals with the crystal structure and the EPR measurements of  $\text{Fe}^{3+}$  in lead zirconate. A detailed interpretation of data is given.

In Chapter 10 the study of the local structure of  $\text{Fe}^{3+}$  in lead zirconate is elaborated. The results emerge only from EPR measurements and semi-empirical modelling. The possible influence of  $\text{Fe}^{3+}$  on the behaviour of oxygen vacancies in the  $\text{PbZrO}_3$  material is discussed.

Part I

THEORY





## 2. FERROELECTRIC MATERIALS

### 2.1 *Electric properties of crystals*

The regular spatial arrangement is what distinguishes crystals from liquids and gases. Crystals have periodical arrangements of structural elements and posses spatial symmetries. Only small movements around the equilibrium positions are allowed for ions in crystals.

The sources of electric fields inside ionic crystal are effective charges of the atoms. Electrical properties of a crystal are mainly determined by distribution of the effective charges.

The effective charges inside a crystal build electric moments. The potential of a neutral system of the effective charges has the same potential as a single electric dipole at large distances. Such an effective dipole moment for a system of charges is actually the product of all charges of the same sign with the distance between the 'centres of masses' of the positive and negative charges

$$\mathbf{p} = \mathbf{R}_{\pm} \sum_i q_i^+ \quad (2.1)$$

where

$$\mathbf{R}_{\pm} = \frac{\sum_i q_i^+ \mathbf{r}_i^+}{\sum_i q_i^+} - \frac{\sum_i q_i^- \mathbf{r}_i^-}{\sum_i q_i^-}$$

and  $q_i^{\pm}$  represent positive/negative effective charges and  $\mathbf{r}$  their position vectors. The above definition leads to the concept of *polar* and *nonpolar* crystals. A crystal is called *nonpolar* when its total dipole moment vanishes, i.e. when the 'centres of masses' for positive and negative charges are at the same point. The other crystals where 'centres of masses' for positive and negative charges do not coincide are called polar. Polar crystals do posses a total dipole moment.

The *macroscopic polarisation*  $\mathbf{P}$  is defined as the quantity of electric dipole moments per volume, averaged over the crystal lattice:

$$\mathbf{P} = \frac{\mathbf{p}}{V} \quad [\text{Cm}^{-2}] \quad (2.2)$$

Supposing that the crystal is build up only by point charges with preferably ionic bondings, it is possible in principle to calculate the magnitude and direction of the crystal electric dipole from its spatial arrangement.

Only a limited number of crystal classes can exhibit polar behaviour [74]. The symmetry elements of all macroscopic properties of crystal must include all symmetry elements of the crystal point group. Of the total 32 crystal symmetry classes, only 20 classes can be polarised. 10 of them can be polarised only due to external deforming force and only 10 of them can be spontaneously polarised. These 10 polar point groups are: 1, 2,  $m$ ,  $2mm$ , 4,  $4mm$ , 3,  $3m$ , 6, and  $6mm$  [101].

All charges in crystals produce a contribution to the *local field* - a field acting on a particular ion - which is the sum of the fields of atomic dipoles (2.1). This contribution is denoted as *macroscopic field*  $\mathbf{E}_m$ . Macroscopic field can be averaged over the crystal cell. The local field  $\mathbf{E}_{local}$  is generally different from the macroscopic field  $\mathbf{E}_m$ , since the latter is based on a continuum approximation for the dielectric medium [84].

In case of a linear dielectric with cubic symmetry *dielectric susceptibility*  $\chi$  can be defined. It is a proportionality factor which connects the macroscopic field  $\mathbf{E}_m$  and the polarisation  $\mathbf{P}$ :

$$\mathbf{P} = \epsilon_0 \chi \mathbf{E}_m \quad (2.3)$$

In crystals with cubic symmetry, the permittivity  $\epsilon$  can be defined as:

$$\epsilon = \frac{E + P/\epsilon_0}{E} = 1 + \chi \quad (2.4)$$

In analogy to cubic crystals, the dielectric behaviour in noncubic linear crystals can be described by the components of the susceptibility tensor  $\chi_{ij}$ . The tensor indices  $i, j$  are defined in the Cartesian coordinate system ( $i = 1 \rightarrow x$ ,  $i = 2 \rightarrow y$ ,  $i = 3 \rightarrow z$ ). The components of the dielectric displacement vector  $\mathbf{D}$  in this case are defined as (cf. [13]):

$$D_i = \sum_j \epsilon_{ij} E_j \quad (2.5)$$

From thermodynamic considerations it follows that the tensors  $\chi_{ij}$  and  $\epsilon_{ij}$  are symmetric.

Elastic properties of materials are described in terms of the 2<sup>nd</sup>-rank tensor parameters *strain*  $x_{ij}$  and *stress*  $X_{ij}$  which, in linear approximation, satisfy Hooke's law. The proportionality parameter between these parameters is called elastic compliance.

The ability of a polar crystal to reveal the polarisation when mechanical stress is exerted on it, is called the *piezoelectric effect*. The reverse effect, when applied electric field induces a strain in crystal, is called converse piezoelectric effect. This effect is described by a linear relation between applied stress  $X_{jk}$  and electric displacement  $D_i$ . Only a crystal with structure belonging to one of the 20 polar crystal classes can exhibit piezoelectric properties.

Polar crystals can exhibit a permanent electric moment. Thus they spontaneously polarise even without applying external electric field or mechanical stress. A change of the spontaneous polarisation  $P$  (2.2) as a function of temperature is experimentally observed. This behaviour is defined as the *pyroelectric effect*. Pyroelectric materials form a subset of piezoelectric materials.

## 2.2 Ferroelectric behaviour

### 2.2.1 Ferroelectric crystals

Only a certain number of pyroelectric crystals have the additional property that the direction of the spontaneous polarisation can be modified by applying an external electric field or mechanical stress. These materials are called *ferroelectric* materials. Ferroelectric materials (or *ferroelectrics*) are the polar materials that have at least two equilibrium orientations of the spontaneous polarisation which can be switched by an external electric field. Ferroelectric properties of some pyroelectric crystals cannot be derived or predicted from the crystal structure. It can be only discovered experimentally [37, 13].

For a given material, ferroelectric properties are generally limited to particular temperature range. The crystals undergo a *structural phase transition* from a high-temperature 'paraelectric' phase to a low-temperature ferroelectric phase.

Structural phase transition occur when the ionic forces which are dependent on temperature and pressure stabilise - at a certain temperature - another crystal structure. The phase transition temperature for ferroelectric materials occurs at the so-called *Curie point*  $T_C$ . At this temperature the value of the spontaneous polarisation falls to zero. The very high dielectric permittivity which is typical for ferroelectrics depends on temperature and the applied field. It reaches a maximum at the Curie point.

### 2.2.2 Microscopic description of ferroelectrics

A microscopic description of the ferroelectric behaviour requires the consideration of the lattice dynamics. This description is called *soft-mode theory* [53]. A typical perovskite-type ferroelectric crystal (for instance  $\text{PbTiO}_3$ ) consists of two sub-lattices: one is made of cations ( $\text{A}^+$ ) and the other of oxygen octahedra surrounding the second cation ( $\text{BO}_6^-$ ). Cations are located at the four-fold symmetry axis (tetragonal  $4mm$  symmetry). They are displaced from the centre of the anion-lattice. Therefore such a crystal possesses an inner electric field, a permanent electric moment and a spontaneous polarisation. In its paraelectric phase, the crystal has higher (cubic) symmetry and can be polarised along any of the 3 equivalent 4<sup>th</sup>-order axes. In the transition to the tetragonal symmetry, however, one direction has to be chosen by definition.

The transition order parameter - polarisation - is associated with a characteristic lattice vibrational mode (phonon), either acoustic or optical. In the former case all the ions move collectively with the same phase. In the latter case anions and cations move independently with the opposite phases. Both modes can be of longitudinal or transversal type. Their frequency depends on temperature. When a ferroelectric phase transition takes place, the transversal optical mode exhibits an instability and its frequency decreases towards zero (it 'softens'). At  $T_C$  the mode is 'frozen' and the

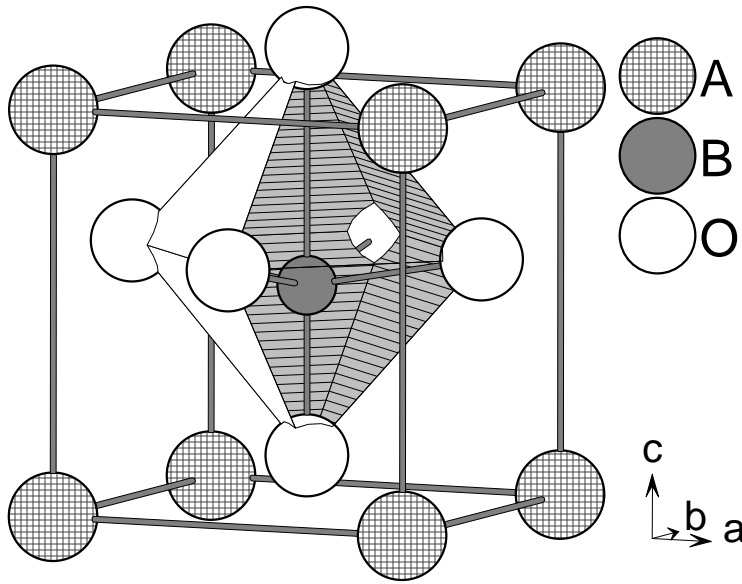


Fig. 2.1: Ideal perovskite crystal structure  $ABO_3$ . It consists of an octahedron of anions  $O^{2-}$  surrounded by a cube of cations A. The cation B sits in the middle of the octahedron.

mode frequency reaches zero. This enables a rise of a non-zero order parameter and lowers the crystal symmetry. Such a vibrational mode is called 'soft mode' [92].

### 2.2.3 Ferroelectric domains and poling

When a perovskite-type ferroelectric crystal undergoes a transition from its paraelectric cubic phase to the ferroelectric (e.g. tetragonal) phase, the orientation of the spontaneous polarisation has equal probability into any of the six equivalent directions of the cubic lattice. The actual direction of the polarisation thus depends on the mechanical and electric boundary conditions of the crystal. The consequence is the creation of differently polarised small regions within the crystal, so-called *domains* or *twins*. They are spontaneously formed in order to minimise the energy of the depolarisation field and the energy of strains [53]. Polarisation directions in two neighbouring domains are either oriented in opposite directions ( $180^\circ$ ) or they are mutually perpendicular ( $90^\circ$ ). As a matter of fact there exist two types of separation planes (*domain walls*) between domains which differ on the direction of the polarisation at their sides. The walls which separates oppositely oriented domains are called  $180^\circ$  domain walls. They minimise the depolarisation fields. The walls which split domains with mutually perpendicular polarisations are called  $90^\circ$  domain walls. They compensate for the internal mechanical stresses. Ferroelectric walls are very

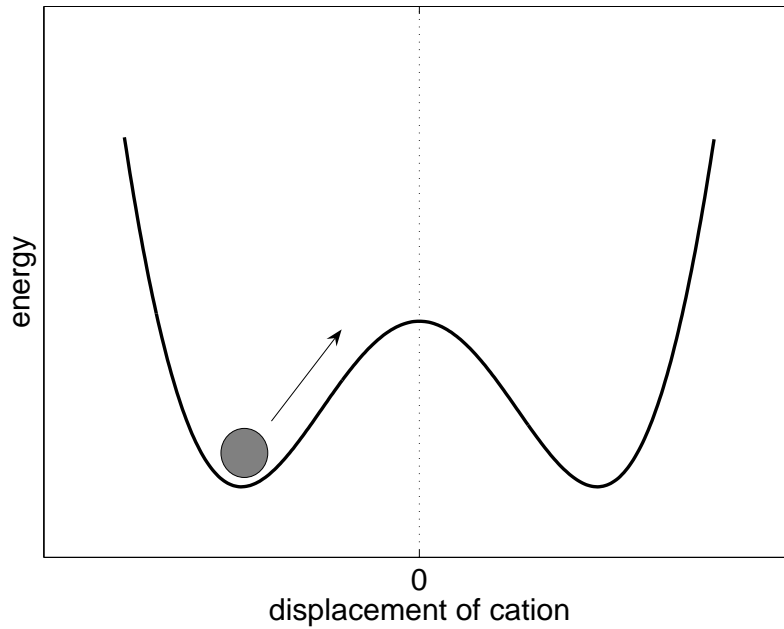


Fig. 2.2: The changeable spontaneous polarisation within a polar crystal is explained by a double potential well. The external field may switch the cation between two minimum positions.

narrow, usually 1-10 nm in ceramic materials [13]. In crystals with other symmetries there are more than two possible directions of polarisation. Then also other types of domain walls are permitted [23].

Because of the domains, grown ferroelectric crystals often have a reduced or even a zero net spontaneous polarisation. Their pyroelectric and piezoelectric effects are also reduced. In ferroelectric ceramics and thin films, the boundary conditions are more complicated and these materials are always divided into many domains. They cause a total zero polarisation and prohibit any pyroelectric or piezoelectric properties. However, by applying a strong electric field, of order of magnitude 10 kV/cm under proper temperature and time conditions, one can bring material in a polar state. The process, called *poling*, reorients ferroelectric domains within the materials along the direction of the applied field. It switches the spontaneous polarisation of a domain. Polarisation and field direction approach each other. The degree of coincidence is determined by the external boundary conditions. A single crystal can be brought by poling to a monodomain state - the state without any domains. In polycrystalline materials the poling process causes a reorientation of domains within the individual grains.

The poling process makes possible the piezoelectric and pyroelectric behaviour of the polycrystalline material [55]. The spontaneous polarisation which remains after the end of the poling process is denoted as *remnant polarisation*. The greater the

number of allowed orientations of polarisation within the crystal lattice, the more closely the polar axes can be brought to the direction of field. Therefore the maximal accessible remnant polarisation is dependent on the allowed domain states. For a polycrystalline ferroelectric with only  $180^\circ$  domain walls the maximum remnant polarisation  $P_R$  is equal to  $0.25P_S$ , where  $P_S$  is the single crystal spontaneous polarisation value. This ratio rises with the number of possible domain states [13].

#### 2.2.4 Polarisation hysteresis loop

The ferroelectric polarisation *hysteresis loop* is a specific, experimentally observable, dependence of the polarisation response to the applied electric field. The hysteresis loop can be explained microscopically by a potential of the central cation of the perovskite unit cell that has the form of a double well (cf. Fig. 2.2). An external field in a direction opposite to the polarisation direction moves the central cation from the potential minimum towards the octahedra-centre and thus reduces the polarisation. The polarisation is reversed after the field reaches its threshold value (*coercive field*,  $E_c$ ). When the field is removed, the cation stays in this well and the remnant polarisation  $P_r$  remains. In order to reverse polarisation, the field should be applied in the opposite direction and raised to the negative value of  $E_c$ . This polarisation-field dependence is described by an hysteresis curve [13].

Polarisation switching by an applied electric field causes a similar strain dependence which is called *butterfly loop*. Strain cannot have a negative value and therefore the butterfly hysteresis loop is symmetric [13].

On the macroscopic scale, the hysteresis loops have a different shape than predicted microscopically. This is caused by the role of domains in the switching process. In the unpoled ('fresh') material the domains have random orientations and the net polarisation of the material as a whole is zero. When an electric field is applied, those domains which have unfavourable orientation switch in the field direction. Once all domains are aligned, the polarisation and strain dependence becomes linear. After the removal of the field, some domains switch back, but the majority of them remain in their former orientation. This behaviour leads to remnant polarisation and remnant strain. They can be removed by applying the electric field in opposite direction until it reaches the coercive field. The polarisation and strain then pass through the zero point and domains switch into the other direction, up to the point where they reach the saturation.

In polycrystalline materials the hysteresis loop differs from the ideal symmetrical one where  $|E_c| = |-E_c|$  and  $|P_r| = |-P_r|$ . The coercive field, the remnant polarisation and the shape of the loop can be affected by many factors, e.g. grain size, mechanical stress, number of cycles through the loop and the presence of charged defects [96].

### 2.2.5 Antiferroelectricity

In dielectric crystals, besides the ferroelectric behaviour, also the other types of instability can develop when they go through a phase transition. These instabilities do not necessarily lead to a rise of the spontaneous polarisation. However, they are accompanied by strong changes in the dielectric constant. One of such a deformation process is called *antiferroelectricity*. In this process neighbouring ions are displaced in the opposite directions (cf. Fig. 2.3) [41]. Only the one-dimensional lines of ions in an antiferroelectric crystal are spontaneously polarised. The neighbouring lines are polarised in antiparallel direction, so that the net spontaneous polarisation of crystal as a whole is zero. Antiferroelectric materials do not exhibit a piezoelectric effect. One of the crystals with antiferroelectric behaviour is  $\text{PbZrO}_3$ . In this material a double-hysteresis polarisation loop is observed [101].

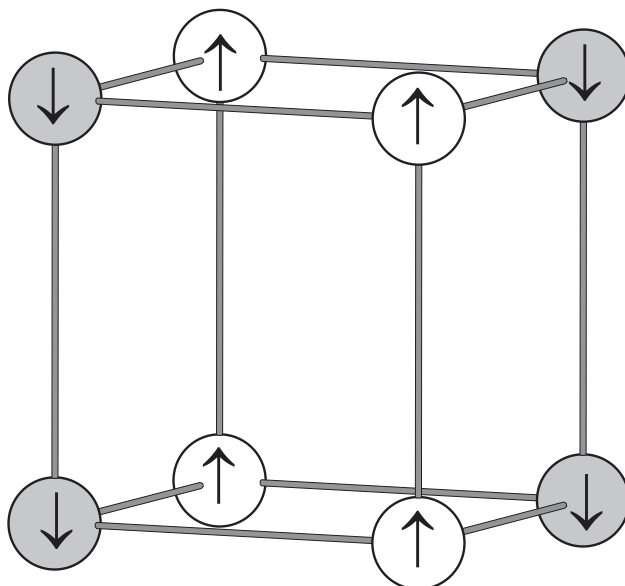


Fig. 2.3: Antiferroelectric displacements of atoms in a perovskite crystal.

### 2.2.6 Fatigue and ageing

Degradation of ferroelectric properties, e.g. loss of the remnant polarisation of ferroelectric materials as a function of a cyclic external (bipolar or unipolar) electric loading is called *ferroelectric fatigue*. The fatigue behaviour is described as the polarisation suppression and is usually represented as the remnant polarisation versus the number of switching cycles. After the period of ca.  $10^5$  cycles a logarithmic loss of polarisation and strain is observed, up to  $10^7$  cycles and after that a saturated stage

of weakened polarisation occurs. Besides the loss of polarisation, other effects are also observed in fatigued materials: a tilt of the polarisation hysteresis loop, changes in the coercive field, loss of strain and drop of piezoelectric coefficients [109]. Fatigue phenomena take place in both bulk ceramics and thin films. They considerably hinder further applications of the materials in electronic devices.

The physical mechanisms causing fatigue are still not well understood microscopically. However, phenomenologically the factors having influence on fatigue have been thoroughly investigated [55]. Among them the following phenomena are observed: the cycling field should be stronger than the  $E_c$ , temperature lowers the fatigue rate, dependence on the electroding method and material, surface treatment, porosity, grain size and doping with foreign atoms.

As origins of fatigue two main mechanisms are proposed: microcracking [36] and domain wall pinning [116]. *Microcracking* occurs mainly in structures with large tetragonal lattice distortion (e.g.  $\text{PbTiO}_3$ ) and near phase boundaries. It is always associated with deformations of ceramic grains. The fatigue due to microcracking is irreversible – the material cannot be rejuvenated. *Domain-wall pinning* is the process where the charged defects (cf. Sec. 2.3) hinder domain-wall movements. Some typical domain-wall pinning defects are oxygen vacancies and trapped electrons [13]. This type of fatigue is rather weak at higher temperatures. It appears to be reversible, i.e. the material can be nearly completely rejuvenated under certain conditions (electric field, high temperature and UV illumination).

Another degradation process in ferroelectric materials is *ageing*, i.e. suppression of certain properties as a function of time without any external electrical or mechanical load or temperature treatment. Subject to ageing are: dielectric permittivity, piezoelectric and piezoelectric coefficients. Usually they follow a logarithmic decrease in dependence of time [86]. Qualitative models for ageing explain its origin as gradual domain degradation. Domain walls can be stabilised with increasing of time. This can be either caused by the slow reorientation of defects along the spontaneous polarisation direction, or by their diffusion into domain walls. Both mechanisms stabilise domain-walls and hinder the switching of polarisation. Aged materials therefore possess internal bias fields which act as additional coercive fields reorienting aligned defects.

### 2.3 Role of defects in ferroelectrics

Non-stoichiometry – a deviation from ideal chemical atomic composition – in many ionic crystals and compounds was shown to be of importance for their electric properties. The introduction of foreign ions into ferroelectric materials has profound impact on properties like electrical conductivity, fatigue and ageing.



### 2.3.1 Point defects

Crystals can contain two types of defects: *point defects* and *dislocations*. The former occur when atoms are missing in the regular lattice array (vacancies) or when atoms are placed on the interstices between regular sites (interstitials). The latter are linear defects leading to the misalignment of atoms. They violate the periodicity of crystals. Although dislocations have also great influence on the properties of ferroelectric materials, our understanding of these defects is merely qualitative. Point defects are understood much better. First of all, they can be ‘visible’ in electron paramagnetic resonance experiments. Point defects are of two types: *Schottky defects* are unoccupied ion sites, *Frenkel defects* are interstitially displaced ions. Schottky defects of cations are always accompanied by the same concentration of anion defects and vice versa. Frenkel defects are accompanied by the same concentration of vacancies.

For describing defects in ionic crystals the *Kröger and Vink notation* is used, where symbols label the defects with the charge they have relative to the neutral lattice. A defect with a positive charge relative to the lattice is denoted with a dot (·) superscript and a defect with a negative charge relative to the lattice is denoted with a prime (′) superscript. Quite generally these effective charges differ from the real charges of ions. Subscripts denote the regular atom  $A$  which the defect is replacing. For the defect  $D$  replacing atom  $A$  that means:  $D_A$ . Interstitial sites are denoted with superscript  $I$ :  $D_I$ .

The effective charges carried by defects are always compensated by some other effective or real charges in order to conserve the overall charge neutrality of the lattice. For example, the double positive oxygen vacancy  $V_{\text{O}}^{\cdot\cdot}$  could be compensated by another cation vacancy which has double negative charge, or by two electrons.

Defect chemistry requires that a chemical equation has to satisfy the following conditions: (a) the total charge has to be zero, (b) the number of each chemical species (except vacancies) has to be equal on both sides, and (c) the available lattice sites have to be filled, even with vacancies. The equilibrium concentration of both types of defects can be calculated on the basis of statistical mechanics under consideration of the mass-action law.

### 2.3.2 Defect chemistry in perovskite compositions

In a perovskite structured crystal of general formula  $\text{ABO}_3$ , the  $A$  cation has an ionic radius exceeding the  $B$  cation radius. The perovskite lattice can be regarded as a simple cubic array of corner-sharing octahedra  $\text{BO}_6$  with their interstitial sites filled with  $A$  cations (cf. Fig. 2.1).

In perovskite crystals the important defects are vacancies at all three ion sites, electrons, holes and substitutional impurities. Frenkel defects play no important role [118]. All three types of vacancies are formed in a certain stoichiometric ratio:



where *nil* refers to the thermodynamic standard state - the defect-free crystal. The mass-action constant for this equation equals to:

$$K_S(T) = [V''_A][V'''_B][V_{\ddot{O}}]^{-3}$$

Under the assumption that the crystal has only the above mentioned defects, concentrations in thermodynamic equilibrium can be calculated. They are related as follows:

$$[V''_A] \approx [V'''_B] \approx \frac{1}{3} [V_{\ddot{O}}]$$

If the enthalpy change for the creation of a Schottky defect is  $\Delta H_S \approx 2$  eV, then  $[V''_A]/N \approx 10^{-6}$  at 1000 K [51], where  $N$  is the concentration of the A cations. This concentration of defects is observed also at room temperature, if the crystal is rapidly cooled down.

Point defects which play the most important role in the perovskite ferroelectrics are substitutional impurities. *Isovalent* substituents do not change the local charge, so they have no impact on the defect equilibrium. *Aliovalent* defects - substitutional ions with a charge that differs from the charge of the replaced ion - necessitate the creation of other compensating defects in order to maintain overall charge neutrality. An aliovalent substituent with a higher positive charge than that of the replaced ion is called *donor*, and an ion with a lower charge is called *acceptor*. For instance, in the case of  $\text{PbTiO}_3$ , the  $\text{La}^{3+}$  ion replacing  $\text{Pb}^{2+}$  is a donor, and  $\text{Fe}^{3+}$  replacing  $\text{Ti}^{4+}$  is an acceptor. Charge mismatch of  $\text{La}_{\text{Pb}}$  can be compensated by an electron, whereas two  $\text{Fe}'_{\text{Ti}}$  can be compensated by a  $V_{\ddot{O}}$  vacancy.

In nature, ions with low oxidation state are more abundant than ions with high oxidation state. Therefore the undoped perovskite ferroelectric crystals already contain a certain amount of naturally-occurring acceptor impurities. This natural concentration of defects is large enough to dominate the defect equilibrium.

Concerning the site preference for a specific substitutional defect, the ionic radius concept is widely used. With this concept one can estimate the preferred site position of an impurity atom. The *ionic radius* is determined from the distances between the centres of ions in different crystals. It is approximately the same for a given ion with the same coordination number in different compounds (cf. [66], pp. 10-11). Usually it is assumed that the ions with roughly the same ionic radii will replace each other. Large cations prefer to substitute the larger A cation, while small cations usually replace the smaller B cation. There is a general rule that defects with high charges are not probable when the lower-charged defect can be formed [118]. Therefore in  $\text{PbTiO}_3$ , for example,  $\text{Nb}^{+5}$  usually replaces  $\text{Ti}^{4+}$  forming the  $\text{Nb}_{\text{Ti}}$  donor, instead of forming the non-probable  $\text{Nb}_{\text{Pb}}$ . As a result of the exchange interaction between electrons, the ionic radii approach is of limited utility. Electron paramagnetic resonance measurements have become crucial in providing proofs for defects substitutions [59, 55].

### 2.3.3 Impact of defects on ferroelectric properties

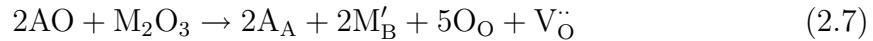
Ferroelectric materials which are used for applications - polycrystalline ceramics and thin films - always contain numerous defects, impurities and dislocations which interact in various ways with internal fields and domain walls. They are either intrinsic (unintentional) or extrinsic (intentional). They determine the ferroelectric and piezoelectric properties of material to large extend. The goal of intentional doping is to tailor the properties of material for specific application [118, 30]. Although a broad range of properties can be achieved by doping, most of the modified materials can be classified into acceptor- and donor-doped (cf. Table 2.1). When dealing with ceramics, the acceptor-doped materials are called ‘hard’, and the donor-doped materials – ‘soft’. This nomenclature origins from the empirical observation that acceptor-doping increases the coercive field. This causes more difficult poling and depoling of ‘hard’ ceramic. Lower coercive field is observed in donor-doped ‘soft’ materials which are therefore easier to pole and depole.

Tab. 2.1: Aliovalent impurities in  $\text{ABO}_3$  perovskites

A site donors	$\text{Bi}^{3+}$ , $\text{La}^{3+}$ , $\text{Nd}^{3+}$ , $\text{Gd}^{3+}$
B site donors	$\text{Nb}^{5+}$ , $\text{Sb}^{5+}$ , $\text{Ta}^{5+}$
A site acceptors	$\text{K}^+$ , $\text{Rb}^+$
B site acceptors	$\text{Sc}^{3+}$ , $\text{Cr}^{3+}$ , $\text{Mn}^{3+}$ , $\text{Mn}^{2+}$ , $\text{Fe}^{3+}$ , $\text{Co}^{3+}$ , $\text{Cu}^{3+}$ , $\text{Ga}^{3+}$ , $\text{Sr}^{2+}$

Acceptor dopants are compensated by oxygen vacancies and donor dopants by cation vacancies (or by electrons). Generally, a given dopant type suppresses a vacancy type that another dopant type promotes. The crucial difference between these two types of vacancies is their mobility. While oxygen vacancies move rather easily along continuous oxygen lattice structures, cation vacancies are separated by an energy barrier from other cations. Therefore they are rather immobile. Cations are surrounded by lattice of oxygen octahedra and they are separated from the neighbouring cations of the same kind by an entire unit cell (ca. 0.4 nm). Oxygen sites on the other hand are adjacent to each other at a shorter distance of ca. 0.28 nm. The oxygen vacancies can thus move more easily.

By *acceptor-doping* of ferroelectric perovskite materials, the ideal  $\text{ABO}_3$  composition is changed by replacing  $\text{BO}_2$  oxide content by e.g. trivalent acceptor oxide  $\text{M}_2\text{O}_3$  (M is symbol for acceptor atom). In this case the stoichiometric combination of the doped material can be written as  $\text{AB}_{1-x}\text{M}_x\text{O}_{3-x/2}$ . The formula suggests that the acceptor defects are electrically compensated by oxygen vacancies. Then the defect reaction reads:

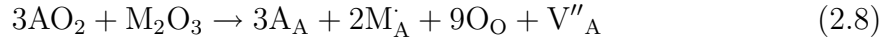


and charge neutrality is maintained by inducing defects which obey the following relation:  $[\text{M}'_\text{B}] \approx 2[\text{V}_\text{O}^\bullet]$ . From the considerations of defect chemistry the assumption

follows that the impurities, once in the lattice, are effectively frozen with slow diffusion rates. There is no association between oppositely charged defects [118].

It was suggested that the mobile defect dipoles ( $V_{\dot{O}} - M'_B$ ) tend to align themselves in the direction of the polarisation field within domains. Furthermore it is assumed that this alignment will stabilise the domain structure (cf. [115, 117]). A consequence of the stable domain-wall structure is a higher coercive field and more “hard” poling and depoling of ceramics. Acceptor doping also increases the conductivity of material. Because of reduced domain-wall motion, however, the dielectric loss is generally lower than in undoped ceramics. In thin films, doping with acceptor ( $Fe^{3+}$ ) has been found to positively affect the fatigue resistance [56]. All these effects are supposed to be connected with oxygen vacancies.

*Donor-doping* of perovskite  $ABO_3$  structure may be chemically written as follow. An amount of  $AO_2$  is replaced by  $M_2O_3$  where  $M^{3+}$  is now the donor atom. Donor doped materials has compositions where the cation  $A^{2+}$  has been replaced:  $A_{1-x/2}BM_xO_3$ . The defect equation can be represented as:



Here the overall charge neutrality is conserved while the concentrations of defects satisfy:  $2[M'_A] = [V''_A]$ . These additives and the cation vacancies enhance domain reorientation. Donor-doped materials are characterised by square hysteresis loops, low coercive fields, high remnant polarisation, high dielectric constants, maximum coupling factors, higher dielectric loss, high mechanical compliance, and reduced ageing. [30]. Simple arguments in connection with the mobility of vacancies may explain intuitively why  $V''_A$ - $M'_A$  pairs do not have a ‘hardening’ effect on ferroelectric materials. On the other side, there is no good explanation for the mechanisms responsible for the ‘softening’ effect of donors in the majority of ferroelectric materials [11].

### 3. PARAMAGNETIC IONS IN CRYSTAL FIELD

Paramagnetic ions have a permanent magnetic moment arising from their angular momentum and/or their electron spin. The theoretical understanding of the properties of paramagnetic ions in crystal lattices requires knowledge of their energy levels. The calculation of the energy levels can be divided into two parts: (i) the calculation of the energy levels of a free ion, (ii) their modifications, when the ion is placed at a crystal lattice site.

#### 3.1 Free ion

Different sets of approximations should be considered in order to achieve theoretical results which can be compared with experiments.

First the magnetic interactions of the Hamiltonian for one-electron atoms will be considered. These considerations are used as approximations for many-electron atoms which are of interest here.

##### 3.1.1 One-electron atom

Eigenfunctions of the Hamiltonian for the one-electron (hydrogen) atom – *orbitals* – can be decomposed into a radial and an angular part.

$$|nlm\rangle \equiv \psi(r, \theta, \phi) = \frac{R(r, n, l)}{r} Y_l^m(\theta, \phi) \quad (3.1)$$

where  $R(r, n, l)$  is the radial part and  $(r, \theta, \phi)$  are polar coordinates. It is dependent on the integer principal quantum numbers  $n$  ( $n = 1, 2, 3, \dots$ ). The spherical harmonics  $Y_l^m(\theta, \phi)$  represent the angular part. They are defined as in e.g. [119]. Spherical harmonics depend on the orbital quantum number  $l$  ( $l = 0, 1, 2, 3, \dots$ ) and the magnetic quantum number  $m$  ( $m = -l, l-1, \dots, l$ ). The orbital quantum numbers are denoted with the letters  $s, p, d, f, g, \dots$  for  $l = 0, 1, 2, 3, 4, \dots$ . The eigenvalues for the hydrogen atom depend only on the quantum number  $n$ , i.e. they are degenerate in  $l$  and  $m$ . That means that orthogonal eigenfunctions with different quantum numbers have the same energy. Degeneracy is always connected with certain symmetry properties of the Hamiltonian.

The one-electron Hamiltonian has to be corrected by the electron spin term. The result is a doubling of Hilbert space by introduction a spin component to the orbitals (3.1). The *spin orbitals* – apart from the radial quantum number  $n$  – can be written

as  $|lsm_l m_s\rangle$ .  $s$  is the spin quantum number of the electron ( $s = \frac{1}{2}$ ) and  $m_s$  is the spin projection quantum number. As long as the other terms in the one-electron Hamiltonian are not added, the introduction of the spin states only causes an additional twofold degeneracy.

The spin orbitals  $|lsjm\rangle$  are eigenfunctions of Hamiltonian  $\mathcal{H}$  and operators  $L^2$ ,  $S^2$ ,  $L_z$  and  $S_z$ . These operators are defined by angular momentum operator  $\mathbf{L}$  and spin operator  $\mathbf{S}$  (cf. [119]). The numbers  $j$  and  $m$  are the quantum numbers of the new angular momentum operator  $\mathbf{J} = \mathbf{S} + \mathbf{L}$ . The eigenfunctions in this representation are called *terms*. The orbital quantum numbers in the coupled representation are symbolised by capital letters: S, P, D, F... The spin multiplicity  $2s + 1$  is given as the left superscript, and  $j$  is given as the subscript. For example: term  ${}^2D_{3/2}$  means the eigenfunction  $|2\frac{1}{2}\frac{3}{2}m\rangle$ .

A direct consequence of introduction of spin in the quantum description of the hydrogen atom is the interaction of the spin with the orbital motion of electron. This is called the *spin-orbit coupling*. From the relativistic Hamiltonian of an electron in the Coulomb field the following term is derived:

$$\mathcal{H}_{SO} = -\frac{e^2\hbar^2}{2m^2c^2r^3} \mathbf{L} \cdot \mathbf{S} = \lambda \mathbf{L} \cdot \mathbf{S} \quad (3.2)$$

where  $\hbar$  is the Planck constant,  $c$  the speed of light  $e$  the electron charge and  $m$  the mass of electron. The  $\mathcal{H}_{SO}$  term is usually much smaller than the other terms in the Hamiltonian and therefore it is treated as a perturbation.

When the hydrogen atom interacts with an applied constant magnetic field  $\mathbf{B}$ , the Dirac relativistic electron Hamiltonian must be taken into account (cf. [60]). Considering only linear terms, the following form of the Hamiltonian interacting with magnetic field has been derived (cf. [119]):

$$\mathcal{H}_m = \frac{e\hbar}{2mc} \mathbf{B} \cdot (\mathbf{L} + 2\mathbf{S}) = \beta \mathbf{B} \cdot (\mathbf{L} + 2\mathbf{S}) \quad (3.3)$$

where the constant

$$\beta = 9.27 \cdot 10^{-24} \text{ [JT}^{-1}\text{]} \quad (3.4)$$

is the *Bohr magneton*. The former equation (3.3) can be compared with classical energy of magnetic dipoles  $\mu_L$  and  $\mu_S$  in magnetic field:

$$\mathcal{H}_m = -\mu_L \cdot \mathbf{B} - \mu_S \cdot \mathbf{B} \quad (3.5)$$

The parameters  $\mu_L \equiv -\beta \mathbf{L}$  and  $\mu_S \equiv -2\beta \mathbf{S}$  can be interpreted as the orbital and spin magnetic moments. However, the factor 2, which appears in the equation for the spin magnetic moment, has no classical counterpart. A more precise value of this factor can be derived from the Dirac equation in higher order corrections. It is usually denoted by  $g_e$  and it amounts to:

$$g_e = 2.0023 \quad (3.6)$$

and therefore the spin magnetic moment can be expressed as:

$$\mu_S = -g_e \beta \mathbf{S} \quad (3.7)$$

The Hamiltonian (3.3) is usually simplified by choosing a coordinate system where the  $z$ -axis coincides with the direction of the field:

$$\mathcal{H}_m = \beta B (L_z + 2S_z) \quad (3.8)$$

The behaviour of atom in a limit of a weak magnetic field is called *Zeeman effect*. The term of the spin-orbit coupling (3.2) is dominating over the magnetic term 3.3. The matrix elements  $\langle lsjm' | L_z + 2S_z | lsjm \rangle$  can be calculated by the means of the Landé formula (see e.g. [119], p. 162). The separation between the levels is determined by the so-called Landé  $g$ -factor. It can be expressed as follows:

$$g_j = 1 + \frac{j(j+1) + s(s+1) - l(l+1)}{2j(j+1)} \quad (3.9)$$

The Landé factor defines the separation between the hydrogen energy levels in the weak magnetic field. From the Eq. (3.8) the energy eigenvalues can be calculated:

$$E_m = \beta g_J B m \quad (3.10)$$

The Zeeman effect causes that the magnetic field lifts the degeneracy in the magnetic quantum numbers  $m$ . The splitting of the energy levels increases with an increasing of magnetic field.

### 3.1.2 Many-electron atoms

A suitable Hamiltonian for a many-electron ion contains the kinetic energy of the electrons, their Coulomb energy in the field of nuclei, the mutual Coulomb interaction among the electrons and the spin-orbit interaction:

$$\mathcal{H} = \sum_i^Z \frac{\mathbf{p}_i^2}{2m} + \sum_{i,k} \frac{-Ze^2}{|\mathbf{r}_i - \mathbf{R}_k|} + \frac{1}{2} \sum_{i \neq j} \frac{e^2}{r_{ij}} + \sum_{i=1}^N \lambda(r_i) \mathbf{l}_i \cdot \mathbf{s}_i \quad (3.11)$$

The indices  $i$  and  $j$  run over all electrons,  $k$  is a label for the nuclei,  $\mathbf{p}$  denotes the electron momentum operator,  $m$  is the electron mass,  $Z$  the number of protons of the  $k^{\text{th}}$  nucleus,  $e$  the electron charge and  $\mathbf{r}_i$ ,  $\mathbf{R}_j$  are the respective position vectors. The one-electron operators are then summed over all  $N$  electrons.

Since it is not necessary to take into account the operators involving more than two electrons, the many-electron Hamiltonian can be separated into a set of the simpler Hamiltonians.

For the low  $Z$  atoms, it can be shown that the kinetic and potential energy terms commute with the operators  $\mathbf{L}$  and  $\mathbf{S}$ . These are defined via the sums of the one-electron angular and spin momenta:

$$\mathbf{L} = \sum_i \mathbf{l}_i \quad \mathbf{S} = \sum_i \mathbf{s}_i \quad (3.12)$$

As a matter of fact, the mutual electronic interaction term must also commute with  $\mathbf{J} = \mathbf{L} + \mathbf{S}$ .

The eigenfunctions of the low- $Z$  Hamiltonian can be written with the help of kets  $|LSM_LM_S\rangle$ . This indicates that the eigenvalues of the operators  $L^2$ ,  $S^2$ ,  $L_z$  and  $S_z$  are  $L(L+1)$ ,  $S(S+1)$ ,  $M_L$  and  $M_S$ . The eigenfunctions of the high- $Z$  Hamiltonian, when  $\mathbf{L}$  and  $\mathbf{S}$  are coupled to  $\mathbf{J}$ , are represented as  $|LSJM\rangle$ .

The inter-electron repulsion cannot be taken as perturbation. In this case the so-called *central-field approximation* is used. It is supposed that an electron moves independently in the spherically symmetric Coulomb potential emerging from the nucleus and all other electrons.

In this approximation, the one-electron spin orbitals are uniquely characterised by four quantum numbers:  $n$ ,  $l$ ,  $m_l$  and  $m_s$ . The eigenvalues have to satisfy the *Pauli principle*: the wave function describing two electrons must reverse its sign (i.e. it has to be *antisymmetric*) when interchanging the electron coordinates (including both spatial and spin). A distribution of electrons determined only by quantum numbers  $n$  and  $l$  is called *configuration*. There are maximum  $2(2l+1)$  electrons in the configuration with the same  $n$  and  $l$ . The configuration with exactly  $2(2l+1)$  electrons is called *closed shell*. Electrons outside the closed shell are valence electrons.

When the non-spherical electronic repulsive perturbation is taken into account, electrons in a given configuration may have different energies. This interaction results in an energetic splitting of the configurations into *terms* with specific values of  $L$  and  $S$ . If, in addition, the spin-orbit interaction is considered, a further splitting of the terms into levels occurs. This splitting is usually denoted as *fine structure*. It builds up the *multiplet* of the given configuration.

In the LS-coupling scheme for many-electron atoms there are several different possible combinations, how to get the various total orbital and total spin quantum numbers  $L$  and  $S$ . This final antisymmetric wave function (term) is denoted by the ket  $|LSJM\rangle$ . The number  $2S+1$  is called *multiplicity* ( $S=0$  for a singlet,  $S=1$  for a triplet...). The term separations are of the order of  $10^4 \text{ cm}^{-1}$  (1.24 eV).

The *Hund rules* state that the term with the lowest energy is the one that: (a) has the highest multiplicity (highest  $S$ ), and (b) has the highest  $L$ . That means that for the two-electron system the triplet states lie lower than the singlet.

When the spin and orbital angular momenta are combined into the total angular momentum  $J$ , it can take values between  $(L-S)$  and  $(L+S)$ . If the shell is less than half occupied, the state of the lowest energy is determined by the minimum  $J$ . If the shell is more than half occupied, the lowest energy has the maximum  $J$ . These states in an external magnetic field have interaction similar to hydrogen (3.5):

$$\mathcal{H}_m = -\mu_J \cdot \mathbf{B} \quad (3.13)$$

where the magnetic moment  $\mu_J = -\beta g_J \mathbf{J}$  is defined with the help of the Landé  $g$ -factor. When the magnetic field is small compared to the spin-orbit interaction, the energy levels are linear in  $B$ . This is the Zeeman effect for many-electron atoms.

$$E_m = \langle JM | \mathcal{H}_m | J' M' \rangle = \beta g_J M B \delta_{JJ'} \delta_{MM'} \quad (3.14)$$



### 3.1.3 Paramagnetic ions

Ions that possess magnetic moments due to their orbital or spin angular momenta are called *paramagnetic ions*. They give rise to the phenomenon of atomic paramagnetism. In a closed shell system the orbital and the spin momenta are mutually cancelled. Closed shell arrangements are formed by the valence electrons in chemical bonding and no paramagnetism occurs.

Atomic paramagnetism, as an exception, occurs when bonds are broken. This process leaves unpaired electrons like in F-centres and free radicals. An *unpaired electron* is to be understood as a single electron in an orbital. In this case, the one-electron Zeeman effect occurs (cf. Eq. 3.10). The energy separations for an electron in the  $s$ -state under the applied magnetic field are:  $E_m = \pm\beta B$ . Experiments, where photons are used to excite transitions between the electron magnetic states, are known as *electron paramagnetic resonance* (cf. Chapter 4).

The atomic paramagnetism, which is considered in this work, occurs when the valence electron shells are not completely filled. Hence unpaired electrons are present. This is the case for transition metals: iron group ( $3d$  orbitals), palladium group ( $4d$ ), platinum group ( $5d$ ), rare earth group ( $4f$ ) and actinide group ( $5f$ ). The electron paramagnetic resonance experiment performed on a free paramagnetic ion measures transitions only between those levels that are split by the external magnetic field (Eq. 3.14). Their magnetic levels splitting is typically much smaller than others, and there are rarely more than eight levels. Energetic orders of magnitudes for the various interactions of a free ion are summarised in Table 3.1.

Tab. 3.1: Typical energies of the different contributions to the atomic Hamiltonian together with the associated photon frequencies.

Shell energy	$10^8 \text{ cm}^{-1}$	$10^{10} \text{ GHz}$	x-rays
Electron-electron	$10^4 - 10^5 \text{ cm}^{-1}$	$10^5 - 10^6 \text{ GHz}$	UV-visible
Spin-orbit	$10^2 - 10^3 \text{ cm}^{-1}$	$10^3 - 10^4 \text{ GHz}$	infra-red
Magnetic	$1 \text{ cm}^{-1}$	30 GHz	microwave

### 3.1.4 Effective spin Hamiltonian

The study of paramagnetic ions usually does not require the consideration of the complete atomic Hamiltonian (3.11). Only those states, which are populated through the Boltzmann distribution, are actually involved in electron paramagnetic resonance experiments (EPR). Their energies depend on the properties of the ion (spin-orbit coupling), nuclear interactions and on the applied magnetic field. Formally, it is possible to describe these levels as being an isolated subgroup orthogonal to the

others, although there is some influence from the higher levels. This method, leading to the called *spin Hamiltonian*, allows the description of the paramagnetic resonance experiment with a smaller number of parameters.

The spin Hamiltonian method uses the *effective spin* concept to describe the subset of the lowest-lying states. The effective spin  $S'$  is defined by equating the number of levels in the ground state with the effective spins multiplicity  $(2S' + 1)$ . Each level is described by the projection quantum number  $M_{S'}$  (similar as the total angular momentum quantum number  $M_J$  describes the ground state). Therefore, if the ground state is a doublet, then the effective spin is  $S' = \frac{1}{2}$ , if it is a triplet then  $S' = 1$  etc. **In the effective spin Hamiltonian the  $g$ -factor is no longer equated with the Landé splitting factor.** It is an experimental parameter, characteristic for the particular paramagnetic atom.

The eigenvalue equation for the spin Hamiltonian  $\mathcal{H}_S$  for such a fictitious spin  $S$  (the prime symbol is omitted from now on) reads:

$$\mathcal{H}_S|\psi_m\rangle = E_m|\psi_m\rangle; \quad m = 1, 2, \dots, (2S + 1) \quad (3.15)$$

where the eigenfunctions of  $\mathcal{H}_S$  are given by  $|\psi_m\rangle = \sum_n a_{mn}|M_m\rangle$ . Thus, the experimental task of the electron paramagnetic resonance is to obtain the precise form of  $\mathcal{H}_S$ . It yields the matrix elements  $a_{mn}$  and thus the energy eigenvalues  $E_m$  [82]. The original derivation is based on perturbation calculations applied to the lowest orbital singlet well separated from the next excited state within the ground state multiplet,  $(2S+1)L$ . Generally, the spin Hamiltonian contains several terms [90] arising from the effect of the magnetic field, spin-orbit coupling, nuclear interactions and particularly from the effect of crystal field (cf. Sec. 3.2). Each term requires the derivation of the various spin angular momentum operators acting on the states  $|M_m\rangle$ . In this work the effects of the nuclear interactions will be omitted.

The interaction in the spin Hamiltonian formalism between the magnetic field and the ion can be derived from the sum of the Hamiltonians (3.3) and (3.2). They describe the spin-orbit coupling and the Zeeman effect (cf. [119], p. 675):

$$\mathcal{H}_S = \lambda \mathbf{L} \cdot \mathbf{S} + \beta \mathbf{B} \cdot (\mathbf{L} + 2\mathbf{S}) \quad (3.16)$$

Then the first-order perturbation for the orbitally non-degenerate state  $\psi_0$  can be calculated:

$$E^{(1)} = \langle \psi_0 | \mathcal{H} | \psi_0 \rangle = \beta g_e \mathbf{B} \cdot \mathbf{S} \quad (3.17)$$

since  $\langle \psi_0 | \mathbf{L} | \psi_0 \rangle = 0$ .

The second order perturbation yields the following matrix elements:

$$\begin{aligned} E^{(2)} &= \sum_n \frac{\langle \psi_0 | \mathcal{H} | \psi_n \rangle \langle \psi_n | \mathcal{H} | \psi_0 \rangle}{E_0 - E_n} \\ &= \sum_n \frac{|\langle \psi_0 | \mathcal{H} | \psi_n \rangle|^2}{E_0 - E_n} \end{aligned}$$

In this equation the Hamiltonian (3.16) is inserted and  $|\langle\psi_0|\mathcal{H}|\psi_n\rangle|^2$  (the terms quadratic in magnetic field are neglected) is calculated. By definition:

$$\Lambda_{ij} = \sum_{n \neq 0} \frac{\langle\psi_0|L_i|\psi_n\rangle\langle\psi_n|L_j|\psi_0\rangle}{E_n - E_0} \quad (3.18)$$

one gets the second-order perturbation:

$$E^{(2)} = - \sum_{ij} \left( \lambda^2 \Lambda_{ij} S_i S_j + 2\beta \lambda \Lambda_{ij} S_i B_j \right) \quad (3.19)$$

With values  $\lambda$  and  $\Lambda_{ij}$  the symmetric  $3 \times 3$  matrices  $\mathbf{g}$  and  $\mathbf{D}$  are defined. Their components are:

$$g_{ij} \equiv g_e \delta_{ij} - 2\lambda \Lambda_{ij} \quad (3.20)$$

$$D_{ij} \equiv -\lambda^2 \Lambda_{ij} \quad (3.21)$$

They have to be symmetric because of the definition (3.18). With those matrices one yields the resulting perturbation Hamiltonian:

$$\mathcal{H}_S = E^{(1)} + E^{(2)} = \sum_{ij} \beta (g_e \delta_{ij} - 2\lambda \Lambda_{ij}) S_i B_j - \lambda^2 \Lambda_{ij} S_i S_j \quad (3.22)$$

$$= \sum_{ij} \beta g_{ij} S_i B_j + D_{ij} S_i S_j \quad (3.23)$$

$$= \beta \mathbf{B} \cdot \mathbf{g} \cdot \mathbf{S} + \mathbf{S} \cdot \mathbf{D} \cdot \mathbf{S} \quad (3.24)$$

In Hamiltonian (3.24) all operators act only on the spin states. Thus it is called the spin Hamiltonian. The eigenvalues of the spin Hamiltonian can be described as corrections to the energy of the original ground state. These corrections come from the combined effect of the applied magnetic field and the spin-orbit interaction.

By spatial transformations the symmetric real matrices  $\mathbf{g}$  and  $\mathbf{D}$  can always be transformed into diagonal forms. Then a coordinate system can be always found where the spin Hamiltonian can be written in terms of diagonal matrix elements  $g_x$ ,  $g_y$ ,  $g_z$  and  $D_x, D_y, D_z$ :

$$\mathcal{H}_S = \beta (g_x B_x S_x + g_y B_y S_y + g_z B_z S_z) + D_x S_x^2 + D_y S_y^2 + D_z S_z^2 \quad (3.25)$$

First term in the spin Hamiltonian (3.24) is called the effective Zeeman term. It yields a splitting under the influence of an external magnetic field which is directly proportional to the field strength. The second term is called *fine structure* or *zero-field splitting* because it splits the ionic energy levels without any external magnetic field.

Many different notations for the fine structure interaction exist in the literature [91]. A notation where the tensor  $\mathbf{D}$  is used, is called *conventional* or *spectroscopic*

notation. In the EPR spectroscopy also very common are the parameters  $D$  and  $E$ . They are defined as follows:

$$D \equiv \frac{3}{2}D_z; \quad E \equiv \frac{1}{2}(D_x - D_y) \quad (3.26)$$

By putting  $S^2 = S_x^2 + S_y^2 + S_z^2$  in (3.25) and equating the terms, the spin Hamiltonian can be written in the following form:

$$\mathcal{H}_S = \beta(g_x B_x S_x + g_y B_y S_y + g_z B_z S_z) + D[S_z^2 - \frac{1}{3}S(S+1)] + E(S_x^2 - S_y^2) \quad (3.27)$$

Here the constant energy of the unsplit level  $(D_{xx} + D_{yy} + D_{zz})S(S+1)/3$  has been put to zero because it shifts all levels equally. The factor  $DS(S+1)/3$  has been introduced for convenience. In a so-called 'proper coordinate system'  $x$ ,  $y$  and  $z$  axes have been chosen so that  $0 \leq E/D \leq 1/3$  [68].

If the symmetry of the ion is axial, then  $S_x^2 = S_y^2$  and the last term can be omitted:

$$\mathcal{H}_S = \beta g B S_z + D(S_z^2 - \frac{1}{3}S^2) \quad (3.28)$$

The  $g$ -tensor is taken to be isotropic and the magnetic field to be along the  $z$ -axis.

The above method can be used only for the special case that the lowest orbital singlet is well separated from the excited states within the ground state multiplet. It is valid only up to the second order in perturbation. In the case of an orbitally degenerate ground state the derivation of the spin Hamiltonian is more complex [54, 90]. Due to the Jahn-Teller theorem, this is a rare case for the paramagnetic ions. This theorem requires that a symmetric, degenerate ion or a molecule distorts spatially in such a way as to reduce the symmetry. This, in turn, lifts the degeneracy.

### 3.2 Ions in a crystal field

This work is not concerned with free paramagnetic ions. Therefore the ionic environment must be taken into account. In the following it will be assumed that paramagnetic ions under investigation are of low concentration and that these ions are situated close to crystal lattice site. The paramagnetic atoms are separated from each other with a distance long enough to make mutual magnetic interactions negligible. Therefore the small concentrations of paramagnetic ions present act as impurities in otherwise diamagnetic crystals. Such crystals are known as *magnetically dilute* materials. In particular, paramagnetic atoms considered in the present work are surrounded by an octahedron of six  $O^{2-}$  ions.

#### 3.2.1 Crystal field

The energy levels of a paramagnetic ion in a crystal lattice differ considerably from those of the free ion. The neighbouring atoms have a significant influence on the

energy levels. An electrostatic theory for this interaction is the so-called *crystal field model*. It was introduced in 1932 by Van Vleck [110]. The central atom is assumed to be surrounded by a distribution of charges that produce an electrostatic ('*crystal*') field over the ion. The crystal field model is purely electrostatic. **No sharing of the electronic charge between the paramagnetic ion and ligands is included.** This model requires a modification of the free ion Hamiltonian (3.11) by adding the term  $V(\mathbf{r})$  that is produced by the surrounding charge distribution (cf. [54, 75]). Hence the Hamiltonian of the ion in crystal field should be:

$$\mathcal{H} = \sum_i \left( \frac{p_i^2}{2m} - \frac{Ze^2}{r_i} \right) + \sum_{i < j} \frac{e^2}{r_{ij}} + \sum_i \lambda(r_i) \mathbf{s} \cdot \mathbf{l} + V(\mathbf{r}) \quad (3.29)$$

The order of magnitude of the crystal field energy  $V(\mathbf{r})$  may be roughly estimated by taking a free electron at a typical ligand distance of 0.2 nm from a neighbouring ion:  $V(r = 0.2 \text{ nm}) \approx 6 \cdot 10^4 \text{ cm}^{-1}$ . It is of the same order of magnitude as the electron-electron interaction (cf. Table 3.1). **Much smaller effects are expected if paramagnetism derives from inner shell electrons.** The crystal field interaction is less than  $100 \text{ cm}^{-1}$  – a number even smaller than the spin-orbit energy.

Low site symmetry has an additional effect to the crystal field. The potential  $V(\mathbf{r})$  in general is invariant to a smaller number of coordinate transformations than the free ion Hamiltonian. **This effect has the consequence that  $V(\mathbf{r})$  partially or completely lifts degeneracies of the ion states.**

In order to consider the crystal field as a perturbation, an assessment of the relative orders of magnitude should be done for the different terms of the Hamiltonian.

The weak crystal field correction is realised when the crystal field is weaker than both the spin-orbit coupling and the inter-electron Coulomb repulsion. This is found in rare earth ions and actinides with incomplete  $4f$  shells. The crystal field influence is shielded by the closed outer  $5f$  or  $4p$  shells. The crystal field term usually amounts only to  $0.1 - 1 \text{ cm}^{-1}$ . For the weak crystal field, the free ion calculation is valid up to the first approximation. However, it must be considered before considering magnetic field effects. **The crystal field partly raises the degeneracy of  $(2J + 1)$  levels into the doubly degenerate pairs  $M_J = \pm \frac{1}{2}, \pm \frac{3}{2}, \dots \pm J$  if the number of electrons is odd. If the number of electrons is even, the degeneracy is split into the levels  $M_J = 0, \pm 1, \pm 2, \dots \pm J$ .**

**The intermediate crystal field corresponds to the condition that the crystal field term is stronger than the spin-orbit coupling but weaker than the Coulomb repulsion.** This occurs frequently for elements with incomplete  $3d$  shell. Its typical energy splittings amount to  $10^2 - 10^3 \text{ cm}^{-1}$ . In this case the **orbital contribution is 'quenched' by the crystal field.** The **magnetic properties are then determined by the spin which is coupled weakly to the crystal field.** The effective  $g$ -factor is very close to the free electron value. The case of the intermediate crystal field is applicable to the  $\text{Fe}^{3+}$  ion.

The symmetry of the paramagnetic ions in crystals plays an important role in determining crystal field effects. Because of the regularity of the crystal lattice,

all paramagnetic ions – with a sufficient ion-ion separation – are surrounded by an identical array of atoms with the same point symmetry. However, there may be different sites which differ in symmetry. In practice, the symmetry of the ion is in practice only determined by the nearest neighbours.

In this work paramagnetic ions surrounded by six ligands are frequently considered. They are placed at the vertices of a regular octahedron. Another possibilities are: four-fold or *tetrahedral* coordination, twelve-fold or *cubeoctahedral* coordination... The ligand coordinations are described by the corresponding point symmetry groups. The Hamiltonian which describes the ion, should be invariant under this point groups. Therefore, an analysis of the symmetry of the site yields restrictions to the Hamiltonian, and *vice versa*.

### 3.2.2 Crystal field potential

In order to estimate the effect of the crystal field potential, the crystal field Hamiltonian has to be constructed. Generally, it is calculated with the help of the Coulomb potential:

$$V(\mathbf{r}) = -e\phi(\mathbf{r}) \quad (3.30)$$

The most general approach takes the real spatial distribution of the electron charge into account. A solution is obtained by solving the Laplace equation. It has the form of an expansion of spherical harmonics [119]:

$$\phi(\mathbf{r}) = \sum_{L=0} \sum_{M=-L \dots L} A_L^M r^L Y_{LM}(\theta, \phi) \quad (3.31)$$

Each term is used to derive an equivalent operator. The matrix elements of  $\phi(\mathbf{r})$  for the orbitals of the free atom has to be calculated. The  $A_L^M r^L$  factors are generally unknown. They are usually replaced by the experimental parameters  $B_L^M \equiv A_L^M r^L$ .

The matrix elements of this Hamiltonian can be represented by a linear combination of the following matrix elements  $\langle Y_{l'm'} | Y_{LM} | Y_{lm} \rangle$ . They vanish unless  $l' + L + l$  is even and  $-m' + M + m = 0$ . For *d* orbitals where  $l = 2$  and  $l' = 2$  this yields the only possible values in Eq. (3.31):  $L = 0, 2, 4$ . For *f* orbitals ( $l = l' = 3$ ) it follows:  $L = 0, 2, 4, 6$ , etc. The Hamiltonian terms have also the property that they are invariant under the symmetry transformations of the point symmetry group of the crystal site.

For convenience, the operator equivalents  $O_L^M$  have been introduced [20]. They are defined as the linear combinations of the spherical harmonics. The operator equivalent crystal field Hamiltonian acts upon the orbital states only. With the help of the operator equivalents, the crystal field Hamiltonian (3.30) can be written as:

$$V(\mathbf{r}) = \sum_{L=0} \sum_{M=-L \dots L} \langle r^M \rangle A_L^M O_L^M \quad (3.32)$$

The operators  $O_L^M$  are called *Stevens operators*. They have the algebraic form of polynomials in the components of the orbital angular momentum  $L$ . Table 3.3 con-

tains their explicit expressions, only the spin operator  $S$  should be interchanged by  $L$ .

Assuming that the crystal field is of intermediate strength, the electronic wave-functions can be described in terms of the quantum numbers  $L$  and  $S$ . This is possible because of the approximation that the crystal field potential is stronger than the spin-orbit coupling. The crystal field interacts only with the orbital momentum. Thus the problem is reduced to the calculation of the splitting of the  $2L + 1$  orbital levels after the ion is exposed to the crystal field.

### 3.3 *S-state ions*

This work deals with *S-state transition ions*. S-state ions are defined as ions with the half-filled  $d$ -shell. Therefore their angular momentum is zero in the ground state. The total angular momentum  $J = L + S$  is then equal to the spin  $S$ . That means in the case of the  $3d^5$  ions:  $J = 5/2$ , and in the case of the  $4f^7$  ions:  $J = 7/2$ . As  $J$  describes the multiplicity of the lowest group of levels, the multiplicity is  $(2J + 1) = 6$  and  $(2J + 1) = 8$  for the  $3d^5$  and  $4f^7$  ions respectively. Therefore the effective spin  $S$  used in the spin Hamiltonian is given by the total angular momentum.

Tab. 3.2: S-state ions

ion	configuration	ground state
Fe <sup>3+</sup>	$3d^5$	${}^6S_{\frac{5}{2}}$
Mn <sup>2+</sup>	$3d^5$	${}^6S_{\frac{5}{2}}$
Gd <sup>3+</sup>	$4f^7$	${}^8S_{\frac{7}{2}}$
Eu <sup>2+</sup>	$4f^7$	${}^8S_{\frac{7}{2}}$

#### 3.3.1 *Energy levels for S-state ions*

For S-state ions, as a result of the fact  $L = 0$ , the calculations of the spin Hamiltonian (cf. Sec. 3.1.4) can be obtained as a sole 1<sup>st</sup>-order effect (3.17). With an anisotropic  $g$ -tensor the spin Hamiltonian is written as:

$$\mathcal{H}_S = \beta \mathbf{B} \cdot \mathbf{g} \cdot \mathbf{S} \quad (3.33)$$

where  $\mathbf{S}$  is the total spin.

As the ground state of an S-state ion is nearly spherically symmetric, an anisotropy in the  $g$ -value is rarely detected [70]. The  $g$ -value of ions with an open  $3d$  shell (e.g. Fe<sup>3+</sup>) is very close to the free electron  $g$ -value of  $g_e = 2.0023$  obtained from quantum electrodynamics. A small deviation of  $g_e$  has been measured for Gd<sup>3+</sup> (open  $4f$  shell)

where  $g = 1.992 \pm 0.001$  [7]. This behaviour is caused by an admixture of excited  ${}^6L$  states into the ground state. The total angular momentum is then changed, i.e.  $\langle L \rangle \neq 0$  [123].

According to Kramers time reversal theorem (e.g. [119], p. 207), a many-electron Hamiltonian *without magnetic field* is invariant under time reversal. That means that for an odd number of electrons, the eigenvalues of the Hamiltonian may be degenerate with even parity. An electric field cannot raise degeneracies completely. On the other side, no additional degeneracies are required for an even number of electrons. Hamiltonians *with magnetic field*, as e.g. the spin Hamiltonian, are not invariant under time reversal. Hence their degeneracies can be totally removed for both an even and odd number of electrons.

The Kramers theorem has a great influence on the behaviour of S-state ions in a crystal field. The total spin is  $S = 5/2$  for the  $3d^5$  ions. As they have an odd number of electrons, an electric crystal field cannot remove the spin degeneracy of the orbital completely, at least two-fold degeneracy persists. So the spin states can have maximal multiplicity of  $(2S + 1)/2 = 3$  for  $3d^5$ . The remaining degenerate doublets characterised by  $M_S = \pm\frac{1}{2}, \pm\frac{3}{2}, \dots \pm S$  are usually called the *Kramers doublets* (cf. Figure 3.1).

For these systems the derivation of spin Hamiltonian must be carried out within the basis of states arising from the entire  $3d^5$  or  $4f^7$  configurations. In contrast to the simple form of the Hamiltonian (3.33), the calculation here should involve individual electronic spins  $s_i$ . It is not possible to derive directly an explicit form of the spin Hamiltonian in terms of the total electronic spin  $\Sigma s_i$  by the perturbation method. Therefore, to relate the parameters of the physical Hamiltonian to those of the effective one, indirect methods based on equivalence are used [90].

However, the concept of an effective spin Hamiltonian in S-state ions describes the experimentally observed fine structure within the ground orbital singlet by the means of the true spin  $S$ .

### 3.3.2 Spin Hamiltonian for S-state ions in a crystal field

The observed zero-field splitting for S-state ions is most successfully described with a spin Hamiltonian constructed from the sums of spin operators [1, 67, 73].

The first explanation of the splitting of  $\text{Fe}^{3+}$  was given by Bethe in 1929 by a group-theoretical method. There was shown that a crystal field of cubic symmetry can split a  ${}^6S_{5/2}$ -state up to a quartet and a doublet [4]. The secular equation for the energy levels with the magnetic field along the [100]-direction was given by Van Vleck and Penney [111]. The Zeeman energy was taken as a perturbation of the levels which are split already by a crystal field. Debye has calculated the splitting of six Kramers levels as the function of the magnetic field [15].

The spin Hamiltonian method in Sec. 3.1.4 after Pryce ([82]) is insufficient to describe the observed zero-field splitting of S-state ions in an axial crystal field. When the effective spin of the ion  $S \geq 1$ , an additional splitting of energy levels appears



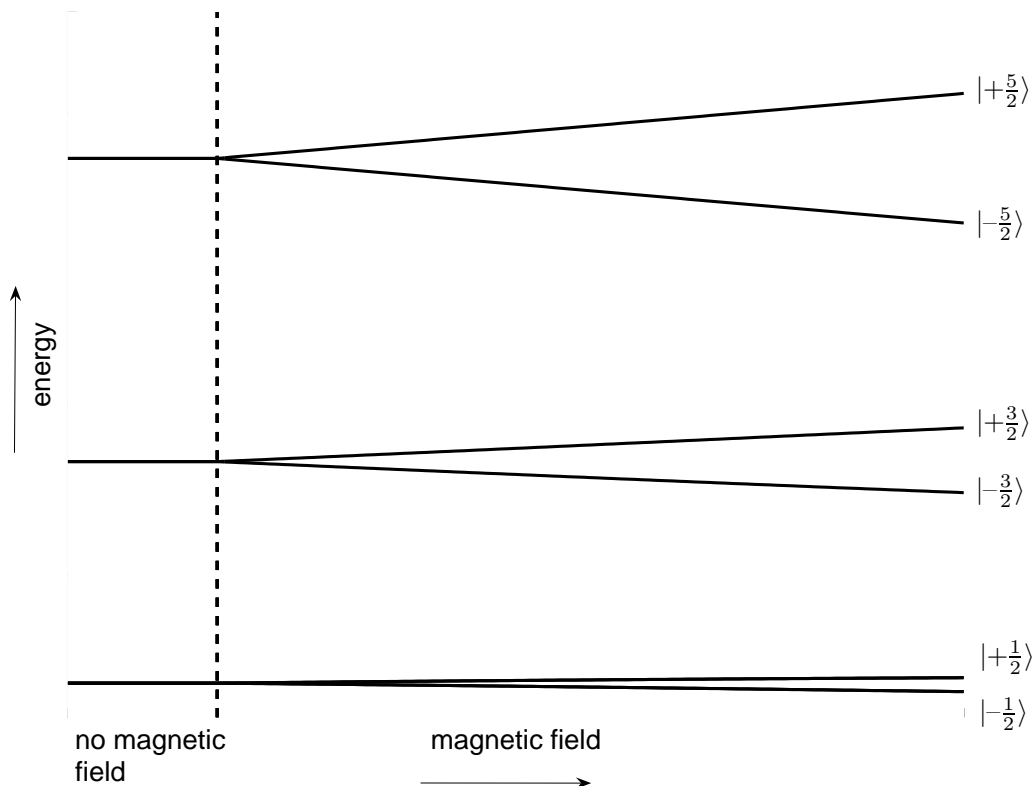


Fig. 3.1: Kramers doublets and their degeneracy removal in magnetic field for a  $3d^5$  ion

due to the crystal field. But the crystal field is not directly coupled to the spins. It is coupled only via small spin-orbit admixtures of the higher anisotropic  $L > 0$  states to the spherically symmetric  $L = 0$  ground state.

Therefore, the additional terms in the spin Hamiltonian (3.27) were added. For instance, the axial crystal field mixes the higher  $(3d^4)(4s)$  configuration into the  $(3d^5)$  ground configuration. A consequence is an ellipsoid spin distribution [2, 83] which is orientation-dependent. This argument explained the observation that the fine structure levels depend on the orientation. The spin-spin interaction couples the spin with the angular momentum in the same manner as the spin-orbit interaction. Therefore the same form of the spin Hamiltonian that should be employed for the states with  $L > 0$  (3.28) can explain the fine structure of the  $L = 0$  state.

The spin Hamiltonian that represents interactions of this type is obtained by adding *multipole terms* of higher power in  $S_z$ ,  $S_x$ ,  $S_y$ . [7, 88, 90]. They are grouped into combinations of spin operators which coincide with the parametrisation of the crystal field operators. Each group of operators is an operator equivalent of a combination of spherical harmonics (cf. Table 3.3). In contrast to the crystal field Hamiltonian (3.32), this parametrisation of the spin-Hamiltonian is not restricted to

one-electron, spin-independent interactions. The number of parameters needed for a full description is determined by: (i) the symmetry of the crystal field, (ii) the total spin of the state, and (iii) requirement of time reversal.

(i) The crystal site symmetry restricts the spin operators to a number that corresponds to the spherical harmonics of the particular symmetry. The total spin Hamiltonian has to be invariant under the same point symmetry group as the point symmetry of the paramagnetic ion. The symmetry properties of the spin Hamiltonian of the crystal field Hamiltonian coincide. A principal axis system may be chosen to make the number of terms as small as possible.

(ii) The maximum power of spin operators is determined by the total spin of the state. The operators of rank higher than  $2S$  have zero matrix elements. Thus, for  $S = \frac{5}{2}$  only operators up to the 4<sup>th</sup> rank are required. For  $S = \frac{7}{2}$  only operators up to the 6<sup>th</sup> rank are necessary, etc.

(iii) Further elimination of operators is possible because of the time reversal requirement. The Kramers' theorem states that the Hamiltonian with no external magnetic field has to be invariant under time reversal. Therefore, in the components  $S_i^a B_i^b$  of a Hamiltonian the sum of exponents  $a + b$  has to be even. Since the higher-rank terms include only the powers of spin  $S_i^a$ , only even-rank terms need to be included.

A general form of spin-Hamiltonian with multipole fine structure can be constructed as:

$$\mathcal{H} = \beta_e \mathbf{B} \cdot \mathbf{g} \cdot \mathbf{S} + \sum_{k \text{ even}, q < k} B_k^q O_k^q(S_x, S_y, S_z) \quad (3.34)$$

with operators  $O_k^q(S_x, S_y, S_z)$  as in Table 3.3.

Tab. 3.3: A list of the angular momentum operators  $O_k^q$  up to the 4<sup>th</sup> rank (for 6<sup>th</sup> cf. [73] or [1], p. 736). Operators with negative  $q$  are obtained by changing  $S_+^n + S_-^n$  to  $i(S_+^n - S_-^n)$

$O_2^0 = 3S_z^2 - S(S+1)$
$O_2^1 = \frac{1}{4}[S_z, S_+ + S_-]$
$O_2^2 = \frac{1}{2}(S_+^2 + S_-^2)$
$O_4^0 = 35S_z^4 - 30S(S+1)S_z^2 + 25S_z^2 - 6S(S+1) + 3S^2(S+1)^2$
$O_4^1 = \frac{1}{4}[7S_z^3 - 3S(S+1)S_z, S_+ + S_-]$
$O_4^2 = \frac{1}{4}[7S_z^2 - S(S+1) - 5, S_+ + S_-]$
$O_4^3 = \frac{1}{4}[S_z, S_+^3 + S_-^3]$
$O_4^4 = \frac{1}{2}(S_+^4 + S_-^4)$

It is convenient to use parameters  $b_k^q$  that scale the parameters  $B_k^q$ . They are

defined as:

$$b_k^q \equiv f_k^q B_k^q \quad (3.35)$$

with scaling factors  $f_2 = 3$ ,  $f_4 = 60$  and  $f_6 = 1260$ . This notation will be used from now on throughout this work. Conventional spin-Hamiltonian parameters, which are used in the literature to describe ions with  $3d^5$  configuration, are  $D$ ,  $E$ ,  $a$  and  $F$ . They are related to the scaled parameters as follows:

$$\begin{aligned} D &= b_2^0 \\ E &= b_2^2/3 \\ F &= 3(b_4^0 - b_4^4/5) \quad b_4^0 = F/3 + a/2 \\ a &= 2b_4^4/5 \quad b_4^4 = 5a/2 \end{aligned} \quad (3.36)$$

In the case of the cubic crystal symmetry (the point groups  $23$ ,  $m\bar{3}$ ,  $\bar{4}3m$ ,  $432$ ,  $m\bar{3}m$ ) the Cartesian coordinate axes coincide with the four-fold symmetry axes. Then the 2<sup>nd</sup>-rank terms vanish. From the 4<sup>th</sup>- and 6<sup>th</sup>-rank, only the terms  $b_4^4$ ,  $b_4^0$ ,  $b_6^4$ ,  $b_6^0$  are left. Additionally, there are mutual constraints among these parameters and the resulting spin Hamiltonian is given in the following form:

$$\mathcal{H} = \beta_e \mathbf{B}_0 \cdot \mathbf{g} \cdot \mathbf{S} + f_4 b_4^0 (O_4^0 + 5O_4^4) + f_6 b_6^0 (O_6^0 - 21O_6^4) \quad (3.37)$$

In the case of the tetragonal symmetry (the groups  $4$ ,  $\bar{4}$ ,  $4mm$ ,  $4/m$ ,  $\bar{4}2m$ ,  $422$ ,  $4/mmm$ ) the spin Hamiltonian reduces to the following terms:

$$\mathcal{H} = \beta_e \mathbf{B}_0 \cdot \mathbf{g} \cdot \mathbf{S} + f_2 b_2^0 O_2^0 + f_4 (b_4^0 O_4^0 + b_4^4 O_4^4) + f_6 (b_6^0 O_6^0 + b_6^4 O_6^4) \quad (3.38)$$

For the point group  $1$  ( $C_1$ ) the most general form of the Hamiltonian should be considered, at least in principle. However, many of the higher-rank parameters are too small to have any influence on the resulting spectrum. The spin Hamiltonian for other point groups can be found elsewhere (e.g. [102]).

### 3.4 Overview of the Newman superposition model

#### 3.4.1 Role of the Newman superposition model

The fine structure parameters for S-state ions have been determined for a large number of different crystals. However, there is no *ab initio* theoretical approach yet available for an explanation of the fine structure parameters on the basis of the crystal environment of the ion.

The Newman superposition model (NSM) was originally developed to separate geometrical and physical information in the crystal field parameters (3.32) of lanthanide ions [69]. The NSM was thereafter successfully applied to explain the crystal field of a number of the lanthanide, actinide and iron group ions [73, 71].

Later the NSM was extended to analyse the spin Hamiltonian parameters of  $\text{Gd}^{3+}$ ,  $\text{Eu}^{2+}$ ,  $\text{Fe}^{3+}$ ,  $\text{Mn}^{3+}$  and  $\text{Cr}^{3+}$  ions in oxides and fluorides. This was possible because the parameters of the fine-splitting parameters are mainly produced by interactions and processes that are linear in the crystal field [124, 113].

Application of the NSM to analyse available spin Hamiltonian data lead to different possible interpretations of experimental data: (i) prediction of various spin Hamiltonian parameters of the systems in new crystal environments, (ii) determination of sign of parameters which are not accessible by experiment, (iii) prediction of the effect of local arrangement of ligands on the fine structure parameters. In this work, mainly the fine structure parameters are calculated on the basis of the local arrangement of ligands, i.e. topic (iii) is studied.

### 3.4.2 Assumptions of the Newman superposition model

The NSM for the crystal-field parameters is based explicitly on the following assumptions:

- (a) The crystal field acting on the open-shell electrons of a paramagnetic ion is a linear sum of the contributions coming from other individual ions.
- (b) Only contributions from the neighbouring ions are taken into account.
- (c) A single ligand contribution is axially symmetric with the respect to the line joining the ligand and the paramagnetic ion.
- (d) Single ligand contributions depend only on the ligand type and on its distance from the paramagnetic ion. Other properties of the crystal have no influence.

The postulates (a)-(c) are explicitly built into the algebraic formulation of the NSM, whereas postulate (d) is used for interpretation. Nevertheless it may be possible that the postulate (d) does not hold. Then a modified form should be used with some additional parameters, such as e.g. polarisability [71].

The crystal field potential of the paramagnetic ion  $V_{CF}$  may be written according to the assumptions (a) and (b). It can be expressed as the sum over the energy contributions of  $N$  single ligands which are denoted by  $i = 1 \dots N$ :

$$V_{CF} = \sum_i V(r_i, \theta_i, \phi_i) \quad (3.39)$$

The particular ligand  $i$  is positioned at the coordinates  $(r_i, \theta_i, \phi_i)$ . The polar coordinate frame is defined with the origin at the paramagnetic ion and the  $z$ -axis along the principal axis of the crystal. According to the assumption (c), each  $V(r_i, \theta_i, \phi_i)$  is axially symmetric. Then a local coordinate frame can be defined so that the  $z$ -axis connects the centre of the ligand with the centre of the paramagnetic ion. In the local coordinate frame the ligand contribution can be written by the expression (3.32):

$$V(r_i, \theta_i, \phi_i) = \sum_{L=0} \bar{A}_L(r_i) O_L^0(i) \quad (3.40)$$

The operators  $O_L^0(i)$  are sums of Stevens operators over electron coordinates defined in the local coordinate frame.  $\bar{A}_L(r_i)$  are geometry independent coefficients. They

are called *intrinsic* crystal field parameters for ligand  $i$  at distance  $r_i$ . In order to get the crystal field parameters from (3.32), it is necessary to transform all single-ligand contributions (3.40) from the local ligand coordinate frame to the crystal coordinate frame:

$$V = \sum_i \sum_{L=0} \bar{A}_L(r_i) O_L^0 = \sum_i \sum_{L,M} \bar{A}_L(r_i) K_L^M(\theta_i, \phi_i) O_L^M \quad (3.41)$$

Here, *coordination factors*  $K_L^M(\theta_i, \phi_i)$  are introduced. They transform the operators  $O_L^0(i)$  between the coordinate systems and they are tabulated in Table 3.4. The crystal field parameters can be evaluated by a comparison of the equations (3.32) and (3.41). This condition gives the fundamental NSM relation:

$$\langle r^M \rangle A_L^M = \sum_i \bar{A}_L(r_i) K_L^M(\theta_i, \phi_i) \quad (3.42)$$

which allows the determination of the crystal field parameters. The intrinsic parameters  $\bar{A}_L(r_i)$  and the exact positions for every ligand are required as input. According to assumption (d) it is possible to calculate the  $\bar{A}_L(r_i)$  for different ligand distances  $r_i$ . Prerequisite is the knowledge of the experimentally obtained values of  $\langle r^M \rangle A_L^M$ . Additionally, the difference between the distances  $r_i$  has to be within a short range. Hence, a simplified dependence on distance of  $\bar{A}_L(r_i)$  is expected to hold in that range. It can be written in a form of a power law:

$$\bar{A}_L(r_i) = \bar{A}_L(r_0) \left( \frac{r_0}{r_i} \right)^{t_L} \quad (3.43)$$

The magnitude of the intrinsic parameters is reduced with the increasing ligand distance. Therefore the inequality  $t_L > 0$  holds for the power law exponents. Finally, it is possible to specify the distance-dependent  $\bar{A}_L(r)$  in terms of three parameters: the intrinsic value  $\bar{A}_L(r_0)$ , the fixed reference distance  $r_0$  and the exponent  $t_L$ .

### 3.4.3 The Newman superposition model for the spin Hamiltonian

The NSM has been established quite well for interpretation of the crystal field in rare earths and some iron group ions [71]. It was expected to work well also for the spin Hamiltonian parameters. It has been assumed that they have linear dependence on the crystal field. This was shown for the 2<sup>nd</sup>-rank spin Hamiltonian parameters of rare earths [124, 73]. While the crystal-field Hamiltonian acts on the states spanning a complete open-shell configuration, the spin Hamiltonian acts only on a few low-lying many-electron states of a single multiplet.

The NSM for the splitting parameters of the ground state can be formulated analogously to the NSM for the crystal field (3.42). For the spin Hamiltonian parameters it follows:

$$b_k^q = \sum_i \bar{b}_k(r_i) K_k^q(\theta_i, \phi_i) \quad (3.44)$$

Here, the index  $i$  denotes a single ligand, the intrinsic parameter  $\bar{b}_k(r_i)$  is the contribution from each single ligand,  $r_i$  is the distance between the  $i^{\text{th}}$  ligand and the

Tab. 3.4: Coordination factors  $K_k^q(\theta, \phi)$  in the Stevens normalisation. Negative  $q$  expressions are obtained by replacing  $\cos q\phi$  by  $\sin |q|\phi$

$K_2^0 = (3 \cos^2 \theta - 1)/2$
$K_2^1 = 3 \sin 2\theta \cos \phi$
$K_2^2 = (3 \sin^2 \theta \cos 2\phi)/2$
$K_4^0 = (35 \cos^4 \theta - 30 \cos^2 \theta + 3)/8$
$K_4^1 = 5(7 \cos^3 \theta - 3 \cos \theta) \sin \theta \cos \phi$
$K_4^2 = 5(7 \cos^2 \theta - 1) \sin^2 \theta \cos 2\phi/2$
$K_4^3 = 35 \cos \theta \sin^3 \theta \cos 3\phi$
$K_4^4 = 35 \sin \theta \cos 4\theta$

paramagnetic ion,  $\theta_i$  and  $\phi_i$  are the polar and axial angles between  $r_i$  and the symmetry axis of the paramagnetic centre. Coordination factors  $K_k^q(\theta_i, \phi_i)$  are functions of rank  $k$  of the polar angles. They coincide with the crystal field parameters tabulated in Table 3.4.

For a short-range dependence of the single-ligand contribution, the following empirical power law was established:

$$\bar{b}_k(r_i) = \bar{b}_k(r_0) \left( \frac{R_0}{r_i} \right)^{t_k} \quad (3.45)$$

The exponential parameter  $t_k$  is specific to a particular ion-ligand system. For a given ligand, the intrinsic parameters  $\bar{b}_k(r_i)$  are determined by the nature of the ligand and by the covalency of the bond. The covalency is assumed to depend exclusively on the bond length  $r_i$ . The intrinsic parameter  $\bar{b}_k(r_i)$  in this model depends only on the nature of the ligand and on its distance. Other properties of the host crystal are irrelevant in this model. With this assumption,  $\bar{b}_k(r_i)$  can be obtained from data of the same ion-ligand complex measured in other host crystals.

A full quantitative understanding of the ground multiplet splitting of S-state ions has not been obtained yet. The crystal field Hamiltonian, which gives good prediction for higher-lying orbital states, cannot be used for the calculation of the much smaller fine structure splittings. Even predictions of a sign of spin Hamiltonian parameters are not necessarily correct. For instance, in the [71], table 12, the measurements for the  $4f^7$  ions in different zircon structure crystals are shown. The spin Hamiltonian parameters  $b_2^0$  do not show any correlation to the corresponding crystal field parameters  $\langle r^M \rangle A_2^0$  in the same crystals.

At first, this failure has been attributed to quadratic contributions from higher configurations [44, 126, 89]. Another reason for this failure may be contributions

of the relativistic and many-body type of crystal field to the lowest multiplet [50]. Experimental support concerning the importance of these theories is missing. It is clear, however, that a successful application of the NSM for the spin Hamiltonian mainly depends on the neglecting the quadratic crystal field contributions.

This is the reason why the experimental validity of the NSM has to be tested for every particular ligand-ion system. Therefore the NSM is regarded as a semi-empirical model. The application of the NSM to particular case of the  $\text{Fe}^{3+}\text{-O}^{2-}$  system is explained in Chapter 6.





## 4. ELECTRON PARAMAGNETIC RESONANCE

### 4.1 Physical backgrounds of electron paramagnetic resonance

#### 4.1.1 The resonance phenomenon

Electron paramagnetic resonance (EPR) experiments are based: (a) on the quantum physical fact that the atomic energy has discrete, clearly separated levels; and (b) on Planck electromagnetic radiation law. The latter connects the energy of the radiation  $E$  with its frequency  $\nu = \omega/2\pi$ :

$$E = h\nu = \hbar\omega \quad (4.1)$$

where  $h = 2\pi\hbar = 6.6260 \cdot 10^{-34}$  [Js] is the Planck constant. A resonance phenomenon occurs under the condition that the energy difference between two discrete atomic levels coincides with the incident electromagnetic radiation. If these two levels are denoted by  $|a\rangle$  (higher level) and  $|b\rangle$  (lower level), the resonance condition can be written as:

$$E_a - E_b = h\nu \quad (4.2)$$

When the resonance condition is fulfilled, the electromagnetic radiation (a photon) is absorbed. It induces a transition between the atomic states, i.e. from the lower to higher energy. The reversed process, the spontaneous transition from the higher to the lower state is called *spontaneous emission*. Spontaneous emission results in the production of a photon. Alternatively, the atom in excited state may be perturbed by a photon with frequency  $\nu$ . In this case it releases a second photon of the same frequency. The atom will again decay into the ground state. This process is known as *stimulated emission*.

Specifically, the energy levels generated and shifted by external magnetic field are involved in EPR. The external magnetic field raises degeneracies in the magnetic orbital, spin, or total quantum numbers  $M_L$ ,  $M_S$  or  $M_J$ . In first order of perturbation these levels depend linearly on the strength of the magnetic field (3.14). Then the splitting of the one-electron magnetic levels splitting is represented with the help of the  $g$ -factor (3.24):

$$h\nu = E_a - E_b = g\beta B \quad (4.3)$$

Thus for an one-electron atom, the  $g$ -factor equals to  $g_e$  (3.6). For a free ion it is equal to the Landé splitting factor. For ions in a crystal field, the  $g$ -factor is an empirical constant to describe the splitting of the energy levels without frequency and field strength dependence.

After the inserting physical constants in Eq. (4.3), the resonance condition may be written as:

$$\frac{\nu [\text{GHz}]}{B [\text{mT}]} \approx g \cdot 0.014 [\text{GHz/mT}] \quad (4.4)$$

#### 4.1.2 Thermal equilibrium

In practice, the absorption and emission of electromagnetic radiation are not measured for a single atom. **An EPR experiment is performed on systems containing a large number of atomic magnetic dipoles.** Some of them are absorbing photons, and some of them are already in an excited state. In the case of resonance, the latter can emit photons. According to the Einstein radiation laws (cf. [119], p. 505), the probability for absorption coincides to that for the stimulated emission. Thus the fact that EPR measures a net absorption on a large number of paramagnetic atoms is due to a statistical distribution. Electrons are distributed so that one level is more populated than the other. The rate of the transition  $|a\rangle \rightarrow |b\rangle$  is proportional to the number of ions in the higher  $|a\rangle$  state ( $N_a$ ). The rate of  $|b\rangle \rightarrow |a\rangle$  is proportional to the number of ions  $N_b$  in the lower  $|b\rangle$  state. The net rate of absorption is then given by the difference between the rates of those two transitions.

The number of ions  $N_i$  in a specific state with energy  $E_i$  – i.e. its population in thermal equilibrium – is given by the Boltzmann distribution function:

$$N_i \propto e^{-\frac{E_i}{kT}} \quad (4.5)$$

where:  $k = 1.381 \cdot 10^{-23} [\text{JK}^{-1}]$  is the Boltzmann constant and  $T$  is the absolute temperature. Therefore the population ratio of two levels is:

$$\frac{N_b}{N_a} = e^{(E_a - E_b)/kT} = e^{h\nu/kT} \quad (4.6)$$

It follows that  $N_b > N_a$ . A consequence of this higher population of the lower state is that the incident electromagnetic radiation causes a net absorption. Of course, such a process will eventually destroy the population in thermal equilibrium. If the population of two levels will be equal ( $N_b = N_a$ ), the net absorption will fall to zero. The atomic system is said to become *saturated*.

Absorption process may become possible due to the coupling between the paramagnetic atoms and their environment, the crystal lattice. **The non-radiative process called *spin-lattice relaxation* returns the ions in their lower state.** If the spin-lattice coupling is high, the ion in the excited state loses its energy in higher amount than the electromagnetic radiation is able to supply. If the spin-lattice coupling is weak, already small radiation power will lead to saturation. The decay constant of the spin-lattice relaxation is denoted with  $T_1$ .

For ordinary temperatures, the exponent in Eq. (4.6) is very small and the exponential function can be expanded into:

$$\frac{N_b}{N_a} = 1 - \frac{h\nu}{kT} \quad (4.7)$$

Since the total population  $N \approx 2N_a \approx 2N_b$  and  $h\nu = g\beta B$ , the net absorption rate can be estimated as proportional to:

$$N_b - N_a = N \frac{g\beta B}{2kT} \quad (4.8)$$

This expression indicates that the sensitivity (net absorption) of EPR measurements increases with decreasing temperature and with increasing magnetic field strength. Since field strength is proportional to the microwave frequency, the sensitivity should be larger for operations at higher frequencies. However, at higher frequencies unwanted saturation effects may arise at low temperatures.

#### 4.1.3 Transition probabilities

In addition to the calculation of energy levels (cf. 4.2), the spin Hamiltonian is used to find the probability of induced transitions [75]. Many of the resonances, however, which might be expected are not realised experimentally. Appropriate selection rules can be derived only by the time-dependent perturbation theory.

The paramagnetic ion interacts not only with the crystal lattice and with the external magnetic field  $\mathbf{B}_0$ . It interacts also with a time-dependent magnetic field component  $\mathbf{B}_1$  of the incident radiation:

$$\mathbf{B}_1 = \mathbf{B}' \sin \omega t \quad (4.9)$$

$\omega$  is the frequency of the incoming microwave radiation and  $\mathbf{B}'$  is the amplitude. Therefore an oscillatory perturbation  $\mathcal{H}'$  is added to the spin Hamiltonian. By considering the time-dependent Schrödinger equation, the transition probability per unit time between states  $|a\rangle$  and  $|b\rangle$  is:

$$W_{ab} = \frac{\pi^2}{h^2} f(\nu) |\langle a | \mathcal{H}' | b \rangle|^2 = \frac{\pi^2}{h^2} \beta^2 f(\nu) |\langle a | g\mathbf{B}' \cdot \mathbf{S} | b \rangle|^2 \quad (4.10)$$

Here  $f(\nu)$  is a normalised line shape function. It describes the width of the transition (cf. Sec. 4.1.4). The rate of transitions between an occupied state  $|a\rangle$  and an unoccupied state  $|b\rangle$  is proportional to the square of the matrix element  $|\langle a | g\mathbf{B}' \cdot \mathbf{S} | b \rangle|^2$ . This matrix element is non-zero only for certain pairs of states. For a simple free spin, the selection rule requires that all non-zero matrix elements have  $m_S^a = m_S^b \pm 1$ . Departing from the free-spin case, one finds that the selection rules depend on the details of the ion and the symmetries of the environment. Except when the symmetry is rather high, the transition probability matrix elements must be evaluated individually.

#### 4.1.4 Line widths

In real physical systems the EPR absorption does not occur at a single frequency/field combination, but spans a finite interval of fields around the resonance field  $B_0$ . Resonance lines can be broadened by different mechanisms, homogeneous or inhomogeneous.

Homogeneous broadening, which occurs due to the Heisenberg uncertainty principle, is usually negligible in solid-state EPR. A finite lifetime of an excited state implies an uncertainty in the state energies of two levels involved. If the excited state has a decay constant  $T_1$ , the width of the associated resonance line is  $1/2\pi T_1$ .

Inhomogeneous broadening occurs because the total spins in a sample are not identical. A spin system might encounter slightly different crystal environments which induce distributions of the parameters of spin Hamiltonian. Additionally, hyperfine couplings in and around a single spin are usually too small to be resolvable. Therefore the spectral line shape is broadened [39, 80].

In the polycrystalline samples (cf. 4.3), the most important contribution to the linewidth comes from statistical distribution of orientations of paramagnetic centres. This effect usually overshadows former mechanisms of line broadening.

The line width is supposed to be of the Gaussian or Lorentzian shape [103]. They have functional dependence of the following forms:

$$\begin{aligned} f(\nu) &= \sqrt{\frac{2}{\pi}} \frac{1}{\sigma} e^{-2(\nu-\nu_0)^2/\sigma^2} && \text{Gaussian} \\ f(\nu) &= \frac{2}{\pi\sqrt{3}} \frac{1}{\sigma} \frac{1}{1+\frac{4}{3}\left(\frac{\nu-\nu_0}{\sigma}\right)^2} && \text{Lorentzian} \end{aligned} \quad (4.11)$$

The experimental linewidth parameter  $\sigma_{\text{FWHH}}$  describes full-width at maximum slope (half height) of the shape function. It is related to the Gaussian and Lorentzian shape constant  $\sigma$  as follows:

$$\begin{aligned} \sigma &= \sigma_{\text{FWHH}}/\sqrt{2 \ln 2} && \text{Gaussian} \\ \sigma &= \sigma_{\text{FWHH}}/\sqrt{3} && \text{Lorentzian} \end{aligned} \quad (4.12)$$

Departures of the single set of the spin Hamiltonian parameters are usually modelled as symmetric Gaussian distributions [22]. In this work distributions of the parameters of the fine structure spin Hamiltonian are considered. In the established model of Wenzel and Kim [120], the distribution of a parameter is assumed to be Gaussian and independent from other quantity. Small deviations of the parameters are treated as an additional *strain* energy term. This term can be interpreted as a first-order perturbation to the spin Hamiltonian. The resulting full width at maximum slope due to the strain term is given by

$$\sigma_{\text{strain}}^2 = \sigma_1^2 \left[ \langle a | S_z^2 | a \rangle - \langle b | S_z^2 | b \rangle \right]^2 + \sigma_2^2 \left[ \langle a | S_x^2 - S_y^2 | a \rangle - \langle b | S_x^2 - S_y^2 | b \rangle \right]^2 \quad (4.13)$$

where  $\sigma_1$  and  $\sigma_2$  are half-widths at maximum slope of the distributions of the parameters  $b_2^0$  and  $b_2^2$ , in energy units.  $|a\rangle$  and  $|b\rangle$  are the wavefunctions associated with the levels.

It can be assumed that different broadening mechanisms are mutually independent. Therefore their effects are added in a root-mean-square way. The width of a transition at half height will be then given by:

$$\sigma_{\text{FWHH}} = \left[ \sigma_{\text{lw}}^2 + \sigma_{\text{strain}}^2 \right]^{1/2} \quad (4.14)$$

## 4.2 Perturbative solutions for the spin Hamiltonian

The goal of EPR experiment is to obtain a complete set of parameters of the spin Hamiltonian specific to the system. The spin Hamiltonian is chosen in a way to describe all important physical processes in the paramagnetic system.

For S-state ions the spin Hamiltonian (3.34) is used (cf. Sec. 3.3.2). It is necessary to calculate its energy eigenvalues  $E_n$  in the space spanned by the effective spin states  $|SM_S\rangle$ . From these eigenvalues one should be able to predict the experimental field values rendering possible EPR transitions. The total spin multiplicity is  $2S + 1 = 6$  for  $\text{Fe}^{3+}$ . A secular equation of this dimension has to be solved, either by perturbation theory or exactly. The published formulae for the energy levels obtained from perturbation theory will be summarised in this work. The spin Hamiltonian (3.34) only up to 4<sup>th</sup> rank must be taken. However, the perturbation approach in many EPR experiments cannot be applied. In these cases numerical diagonalisation methods on a computer have to be employed.

### 4.2.1 High-field approximation

In the so-called *high-field approximation* the Zeeman term in the Hamiltonian (3.34) is taken as the most dominant term. The second term, fine structure, is taken as a perturbation:

$$\beta_e g \mathbf{B} \cdot \mathbf{S} \gg \sum_{k,q} f_k b_k^q O_k^q \quad (4.15)$$

**CUBIC SYMMETRY** A spin system with  $S = \frac{5}{2}$  in cubic symmetry is considered in the following discussion. Only the 4<sup>th</sup> rank cubic terms should be taken into account, as quoted in Hamiltonian (3.37). The secular determinant is of dimension  $6 \times 6$ . The matrix elements are denoted as  $\langle \pm\frac{1}{2}, \pm\frac{3}{2}, \pm\frac{5}{2} | \mathcal{H} | \pm\frac{5}{2}, \pm\frac{3}{2}, \pm\frac{1}{2} \rangle$ . If the magnetic field is applied along the cubic  $z$ -axis  $[001]$  ( $\mathbf{B} = B\hat{\mathbf{z}}$ ), the secular determinant will factorise, leading the following six eigenvalues [75]:

$$\begin{aligned} E_{1,2} &= \pm\frac{1}{2}G + \frac{2}{5}b_4^4 \\ E_{3,4} &= \frac{1}{2}(G - \frac{2}{5}b_4^4) \pm \frac{1}{2} \left[ 16G^2 + \frac{32}{5}Gb_4^4 + \frac{36}{25}(b_4^4)^2 \right]^{1/2} \\ E_{5,6} &= \frac{1}{2}(G - \frac{2}{5}b_4^4) \pm \frac{1}{2} \left[ 16G^2 + \frac{32}{5}Gb_4^4 + \frac{36}{25}(b_4^4)^2 \right]^{1/2} \end{aligned} \quad (4.16)$$

$$\text{with } G \equiv \beta_e g B$$

The  $g$ -value is taken as isotropic. In zero field ( $G = 0$ ), one gets a degenerate doublet at energy  $\frac{2}{5}b_4^4$  and a quartet at  $-\frac{1}{5}b_4^4$ . Except for  $\mathbf{B}$  applied along  $z$ , exact solutions are possible only when the  $\mathbf{B}$  is applied along cubic the  $[111]$  direction. For any other direction there is no analytical solution. However, the second order perturbation

calculation in the high-field approximation (4.15) can be applied for an arbitrary direction of the magnetic field. For the magnetic field defined as  $\mathbf{B} = B(l_x\hat{\mathbf{x}} + l_y\hat{\mathbf{y}} + l_z\hat{\mathbf{z}})$  relative to the cubic axes, the following formulae are calculated [14, 67]:

$$\begin{aligned} E_{1,2} &= \pm \frac{1}{2}G + \frac{2}{5}(1 - 5\phi)b_4^4 \mp \frac{8}{3}(7\phi - 25\phi^2)\frac{(b_4^4)^2}{5G} \\ E_{3,4} &= \pm \frac{3}{2}G - \frac{3}{5}(1 - 5\phi)b_4^4 \pm \frac{1}{20}(1 + 22\phi - 75\phi^2)\frac{(b_4^4)^2}{5G} \\ E_{5,6} &= \pm \frac{5}{2}G + (1 - 5\phi)b_4^4 \pm \frac{1}{60}(3 + 50\phi - 113\phi^2)\frac{(b_4^4)^2}{5G} \end{aligned} \quad (4.17)$$

with  $\phi \equiv l_x^2 l_y^2 + l_y^2 l_z^2 + l_z^2 l_x^2$  and  $G \equiv \beta g B$

From these formulae, the five resonance fields are calculated for a constant frequency  $\nu$ :

$$\begin{aligned} B_{1,2} \left( \pm \frac{5}{2} \leftrightarrow \pm \frac{3}{2} \right) &= B_0 \mp \frac{4}{5}(1 - 5\phi)b_4^4 + \frac{4}{15}\phi(1 - 7\phi)\frac{(b_4^4)^2}{(g\beta)^2 B_0} \\ B_{3,4} \left( \pm \frac{3}{2} \leftrightarrow \pm \frac{1}{2} \right) &= B_0 \pm (1 - 5\phi)b_4^4 - \frac{1}{60}\phi(3 + 178\phi - 625\phi^2)\frac{(b_4^4)^2}{(g\beta)^2 B_0} \\ B_5 \left( +\frac{1}{2} \leftrightarrow -\frac{1}{2} \right) &= B_0 + \frac{4}{3}\phi(7 - 25\phi)\frac{(b_4^4)^2}{(g\beta)^2 B_0} \end{aligned} \quad (4.18)$$

where  $B_0$  represents the resonant field at frequency  $\nu$ :  $B_0 = \frac{h\nu}{g\beta}$ .

These solutions are a function of the orientation angle of the magnetic field in the coordinate frame of the crystal.

**AXIAL SYMMETRY** For ions with  $S = \frac{5}{2}$  in a crystal field of axial (tetragonal) symmetry, the spin Hamiltonian (3.38) should be considered. Energy levels are expressed in the  $|SM_S\rangle$  basis. Solutions are expressed for the resonance fields determined for a constant frequency  $\nu$  (usual way to perform experiment). The parameters  $B_0 = h\nu/g\beta$  and  $\phi = l_x^2 l_y^2 + l_y^2 l_z^2 + l_z^2 l_x^2$  are defined identically as in cubic symmetry. The solutions are [5, 75]:

$$\begin{aligned} B_{1,2} \left( \pm \frac{5}{2} \leftrightarrow \pm \frac{3}{2} \right) &= B_0 \mp [2b_2^0(3\cos^2\theta - 1) + \\ &\quad + (b_4^0 - b_4^4/5)(35\cos^4\theta - 30\cos^2\theta + 3)/2 + 4(1 - 5\phi)b_4^4/5] \\ B_{3,4} \left( \pm \frac{3}{2} \leftrightarrow \pm \frac{1}{2} \right) &= B_0 \mp [b_2^0(3\cos^2\theta - 1) + \\ &\quad + 15(b_4^0 - b_4^4/5)(35\cos^4\theta - 30\cos^2\theta + 3)/24 + (1 - 5\phi)b_4^4] \\ B_5 \left( +\frac{1}{2} \leftrightarrow -\frac{1}{2} \right) &= B_0 \end{aligned} \quad (4.19)$$

Here  $\theta$  denotes the angle of the field with respect to the axial  $z$ -axis of the paramagnetic centre. When  $\theta = 0$  and 4<sup>th</sup> rank terms are neglected, a symmetric pattern of five transition arises. Central transition is located at  $B_0$  and side peaks are located at distances  $\pm 2b_0^2$  and  $\pm b_0^2$  (in field units). An example of the angular dependence of the solutions is shown in Fig. 4.1, lower diagram.

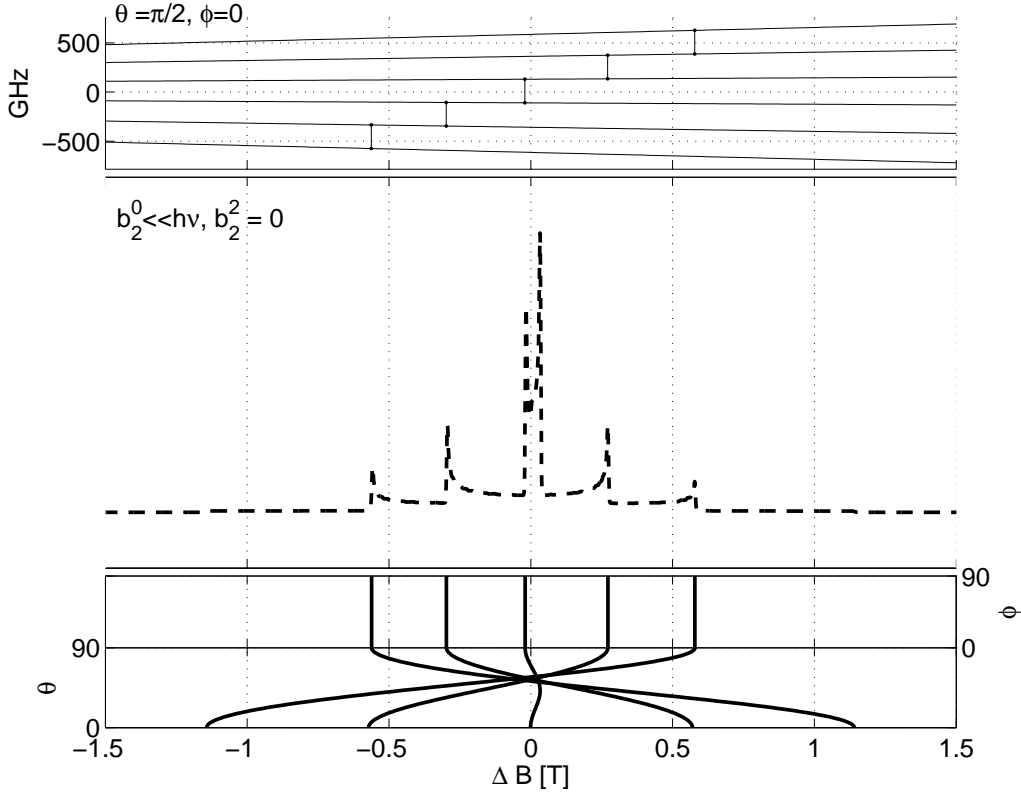


Fig. 4.1: Simulation of a  $S = \frac{5}{2}$  paramagnetic centre with axial symmetry near the high field limit ( $\nu = 240$  GHz): energy levels with transitions along the particular orientation as a function of the field (upper diagram), calculated EPR absorption of the powder sample (centre diagram), angular orientation of the transitions as a function of field (lower diagram)

**RHOMBIC SYMMETRY** If there is no symmetry of the crystal field, all terms in the spin Hamiltonian have to be considered. However, very often many of the high-order terms are very small and not accessible in an experiment. In order to perform a perturbation calculation, the following terms are taken into account: both 2<sup>nd</sup>-order terms and  $b_4^4 O_4^4$  and  $b_4^0 O_4^0$  from the 4<sup>th</sup>-order terms ('cubic' terms). The 2<sup>nd</sup>-order 'axial' term  $b_2^0 O_2^0$  together with the Zeeman term  $\beta_e \mathbf{B}_0 \cdot \mathbf{g} \cdot \mathbf{S}$  are taken as the zero-order interaction. The 2<sup>nd</sup>-order 'rhombic' term  $b_2^2 O_2^2$  together with the higher-order terms are taken as the perturbation. This calculation is valid only for the condition  $b_2^2/b_2^0 \ll 1$ . It is called the small 'rhombicity' condition. The magnetic field  $\mathbf{B}$  coincides with the  $z$ -axis. The formulae for the resonance fields read [9, 78]:

$$\begin{aligned}
 B_{1,2} \left( \pm \frac{5}{2} \leftrightarrow \pm \frac{3}{2} \right) &= B_0 \mp 4b_2^0 + \frac{(b_2^2)^2}{B_{1,2} \pm b_2^0} - \frac{5(b_2^2)^2}{9(B_{1,2} \pm 3b_2^0)} \mp 2b_4^0 \\
 B_{3,4} \left( \pm \frac{3}{2} \leftrightarrow \pm \frac{1}{2} \right) &= B_0 \mp 2b_2^0 \mp \frac{(b_2^2)^2}{B_{3,4} \pm b_2^0} \pm \frac{(b_2^2)^2}{(B_{3,4} - 3b_2^0)} - \frac{5(b_2^2)^2}{9(B_{3,4} \pm 3b_2^0)} \pm \frac{5}{2}b_4^0
 \end{aligned} \tag{4.20}$$

$$B_5 \left( +\frac{1}{2} \rightarrow -\frac{1}{2} \right) = B_0 - \frac{(b_2^2)^2}{B_5 - b_2^0} + \frac{5(b_2^2)^2}{9(B_5 + 3b_2^0)} - \frac{(b_2^2)^2}{B_5 + b_2^0} + \frac{5(b_2^2)^2}{9(B_5 - 3b_2^0)}$$

In combination with the calculated eigenvectors [78], the results show that the Zeeman quantisation number  $M_S$  remains a good quantum number along the principal axis of fine-structure Hamiltonian. The angular dependence of the transitions cannot be obtained analytically.

An example of the angular dependence of the general solutions of the rhombic crystal field is depicted in Fig. 4.2, lower picture. The solutions in a direction along the  $z$ -axis correspond to the resonances at  $(\theta = 0, \phi = 0)$ .

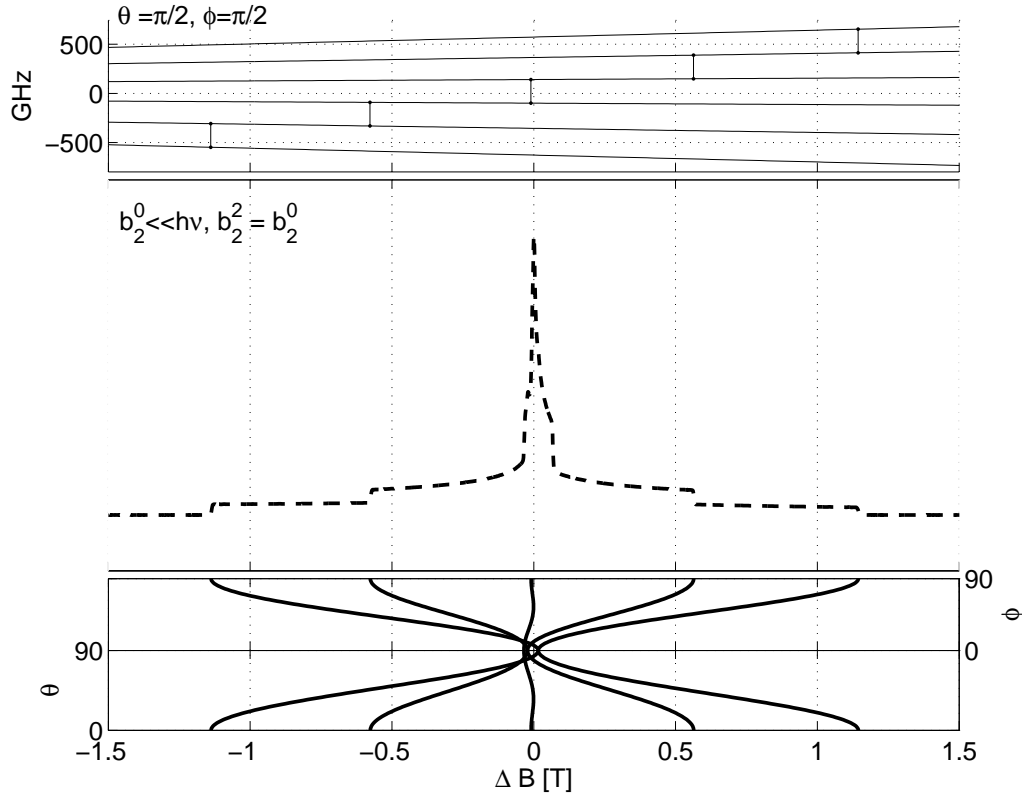


Fig. 4.2: Simulation of a  $S = \frac{5}{2}$  paramagnetic centre with maximal rhombic symmetry near the high field limit ( $\nu = 240$  GHz): energy levels with transitions as a function of the field (upper diagram), calculated EPR absorption of the powder sample (centre diagram), angular orientation of the transitions as a function of the field (lower diagram)

#### 4.2.2 Low-field approximation

The so-called low-field approximation takes a particular set of the fine structure terms in (3.34) as the dominant term. The Zeeman interaction is taken as a perturbation.



This approximation can be generally written as:

$$\beta_e g \mathbf{B} \cdot \mathbf{S} \ll \sum_{k,q} f_k b_k^q O_k^q \quad (4.21)$$

In this case the doublets are widely separated already without external field. As a matter of fact, EPR experiments performed at a constant frequency cannot induce transitions between the doublet levels. The transitions can be induced only within the Kramers doublets. A weak magnetic field removes the degeneracy of the doublets. The energy levels, however, are not shifted linearly with the field. Their positions critically depend on the orientation.

A pure phenomenological description of the spectra within the doublets is possible by writing an effective spin Hamiltonian for a particular doublet:

$$\mathcal{H}' = \beta \mathbf{B} \cdot \mathbf{g}' \cdot \mathbf{S}' \quad (4.22)$$

where  $\mathbf{g}'$  is the effective anisotropic  $\mathbf{g}$ -matrix and  $\mathbf{S}'$  the  $\frac{1}{2}$ -spin operator [77]. Effective  $\mathbf{g}$ -matrices of the Kramers doublets have a prominent angular anisotropy which reflects the angular dependence of the energy levels. Their strong field dependence can be described analytically by a perturbation up to 3<sup>rd</sup>-order [40].

**AXIAL SYMMETRY** In a crystal field of axial symmetry, the spin Hamiltonian has the form of (3.38). It is further assumed that the term  $b_2^0 O_2^0$  is the zero-order contribution and that  $\beta_e g \mathbf{B} \cdot \mathbf{S}$  is the perturbation. The formulae for the energy levels up to 3<sup>rd</sup>-order read [3]:

$$\begin{aligned} E_{\pm \frac{5}{2}} &= 10b_2^2/3 + b_4^0 \pm \frac{5}{2}G \cos \theta + \frac{5G^2 \sin^2 \theta}{16b_2^2} \mp \frac{5G^3 \cos \theta \sin^2 \theta}{(8b_2^2)^2} \\ E_{\pm \frac{3}{2}} &= -2b_2^2/3 - 3b_4^0 \pm \frac{3}{2}G \cos \theta + \frac{11G^2 \sin^2 \theta}{16b_2^2} \mp \frac{123G^3 \cos \theta \sin^2 \theta}{(8b_2^2)^2} \\ E_{\pm \frac{1}{2}} &= -8b_2^2/3 + 2b_4^0 \pm \frac{1}{2}G(1 + 8 \sin^2 \theta)^{\frac{1}{2}} - \frac{G^2}{b_2^2} \sin^2 \theta \pm \frac{G^3}{(2b_2^2)^2} \frac{2 - 11 \sin^2 \theta}{(1 + 8 \sin^2 \theta)^{\frac{1}{2}}} \end{aligned} \quad (4.23)$$

where  $G = \beta g B$ . In the absence of the magnetic field, the doublets are degenerate. They are split by  $2b_2^0$  and  $4b_2^0$ . If there is a contribution of higher order terms, the splittings become more complicated.

Using the effective  $\mathbf{g}$ -matrix, the spin Hamiltonian for the doublet  $|\frac{1}{2}\rangle \rightarrow |-\frac{1}{2}\rangle$  (4.22) may be written as:

$$\mathcal{H}' = \beta B g'_{\parallel} \cos \theta S_z + \beta B g'_{\perp} S_x \sin \theta \quad (4.24)$$

The general expression for the effective  $g'$ -value of the system with  $S = \frac{5}{2}$  may be written by solving the secular equation. By using 3<sup>rd</sup>-order perturbation theory [77],

the solutions can be written as:

$$g' = g \left[ 1 - \frac{1}{2} (1 - 3 \cos^2 \theta) \left( \frac{g\beta B \sin \theta}{b_2^0} \right)^2 \right] \quad (4.25)$$

From this formula it is possible to derive the angular dependence of the transition position in terms of the effective  $g'$ -value. The perpendicular and parallel values can be given by setting  $\theta = 90^\circ$  and  $\theta = 0^\circ$  and taking  $g = 2$ :

$$g'_{\parallel} \approx 2.0; \quad g'_{\perp} \approx 6.0$$

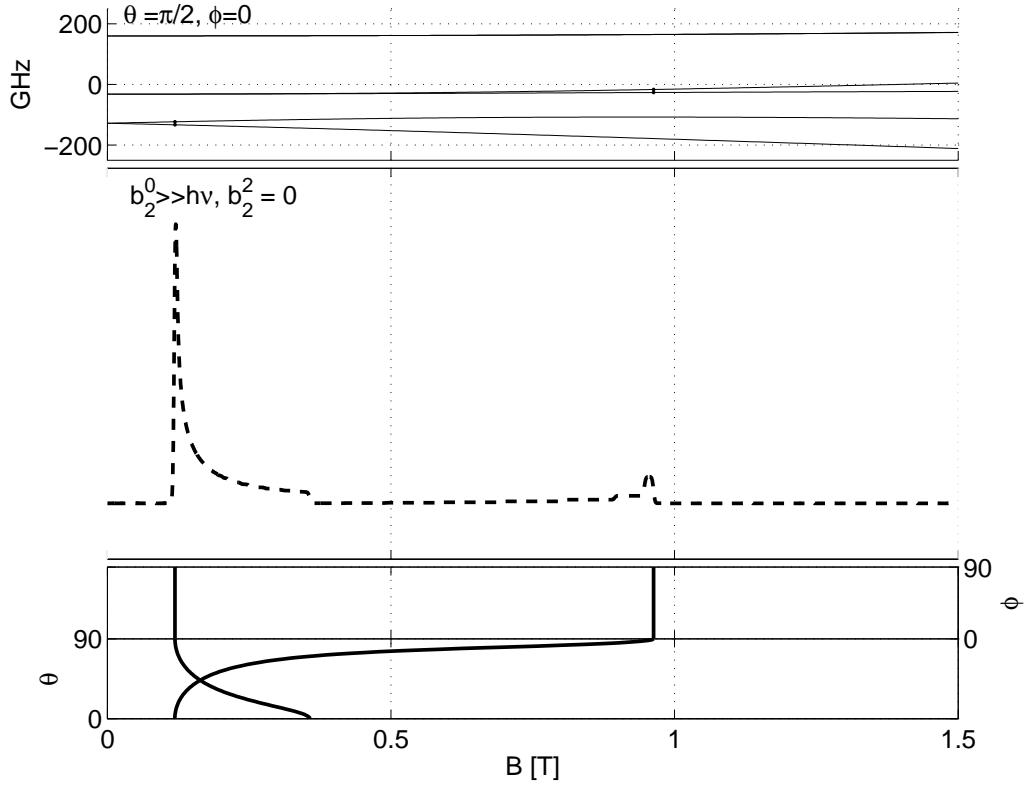


Fig. 4.3: Simulation of a  $S = \frac{5}{2}$  paramagnetic centre with axial symmetry near the low field limit ( $\nu = 10$  GHz): energy levels with the transitions as a function of the field (upper figure), calculated EPR absorption of the powder sample (middle figure), angular orientation of the transitions as a function of field (lower figure)

The fine structure parameter  $b_0^2$  can be obtained from Eq. (4.25) by precise measurements of  $g'_{\perp}$  at two different frequencies. If the measured values for the perpendicular transitions at two different frequencies  $\nu_1$  and  $\nu_3$  are  $g'_1$  and  $g'_2$ , the resonant fields are  $B_1$  and  $B_2$  [40]. Then the parameter  $b_0^2$  can be obtained by the

following formula:

$$b_2^0 = \frac{4}{3} \left( \frac{g'_1 B_2 - g'_2 B_1}{B_2 - B_1} \right) \left( \frac{g'_1 B_2^2 - g'_2 B_1^2}{g'_1 - g'_2} \right)^2 \quad (4.26)$$

The strong angular dependence of the transition field for the low-field limit shown in Fig. 4.3, lower diagram.

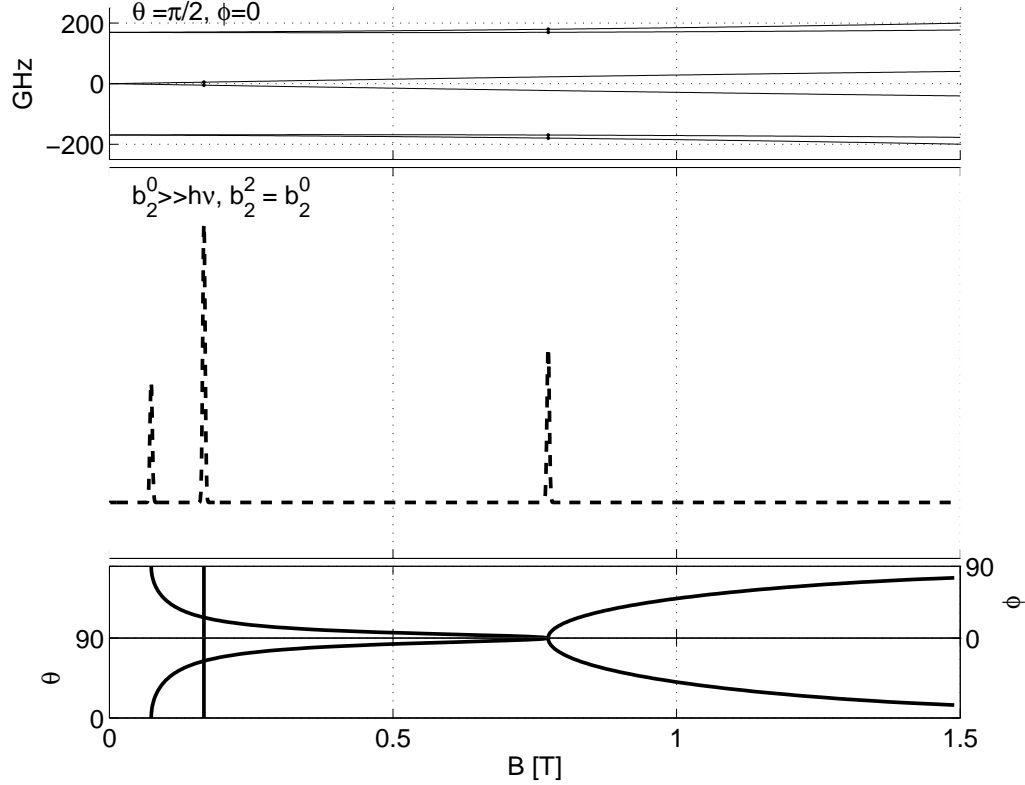


Fig. 4.4: Simulation of a  $S = \frac{5}{2}$  paramagnetic centre with maximal rhombic symmetry in the low field limit ( $\nu = 10$  GHz): energy levels with transitions as a function of the field (upper diagram), calculated EPR absorption of the powder sample (middle diagram), angular orientation of the transition as a function of the field (lower diagram)

**RHOMBIC SYMMETRY** In the crystal field of a symmetry lower than axial, both  $b_2^0$  and  $b_2^2$  from the 2<sup>nd</sup>-order parameters should be considered. Below we give an approximate estimate concerning their magnitude. One extreme case takes place when the  $b_2^2$  takes a maximum value of  $b_2^2/b_2^0 = 1$ . The spin Hamiltonian in the axis frame defined by  $b_2^0 \geq b_2^2$  is considered. This condition ('extreme rhombic') is equivalent to  $E/D = 1/3$  in conventional spectroscopic notation [114]. Under this

condition and for zero-field, the three degenerate doublets are split symmetrically around the energy zero. The following energy values have been calculated [8]:

$$\begin{aligned} E_{1,2} &= \frac{4\sqrt{7}}{3}b_2^0 \\ E_{3,4} &= 0 \\ E_{5,6} &= -\frac{4\sqrt{7}}{3}b_2^0 \end{aligned} \tag{4.27}$$

It can be calculated in the 1<sup>st</sup>-order perturbation that the central doublet splitting does not depend on the orientation. Therefore it causes a prominent isotropic effective  $g'$ -value. It amounts to  $g' \approx 30/7 = 4.3$ . This  $g$ -value is a typical fingerprint of a  $3d^5$ -ion in a highly distorted oxygen octahedron [122, 33]. An example is shown in Fig. 4.4, lower diagram, where the angular dependence on the transition field is calculated.

### 4.3 EPR spectra of polycrystalline samples

In this work only polycrystalline, ceramic and powder samples were investigated. In contrast to single crystals, these samples do not have a regular crystal structure. Single crystallites, ceramic corns or powder particles are randomly oriented relative to the external magnetic field. Each orientation has nearly the same probability. This situation can be interpreted as a statistical random distribution of all possible orientations of unit cells. As a result, the paramagnetic defects of a given sample show also random distribution.

Typical orientation-dependent EPR parameters are: the resonance field, the transition intensity and the line width. In order to explain powder EPR spectrum, an integral which contains the frequency (in practice: field) has to be evaluated over all possible orientations. The spectral signal in a powder sample can be written quantitatively as the following integral [78]:

$$S(B, \nu) = \sum_{i,j=i+1} \int_{\theta=0}^{\pi} \int_{\phi=0}^{\pi} W^2 f(\nu - \nu_0, \sigma) d(\cos \theta) d\phi \tag{4.28}$$

where  $S(B, \nu)$  denotes the EPR signal intensity,  $W$  the absolute value of the transition probability (4.10),  $\nu$  the microwave frequency,  $\nu_0$  the resonant frequency,  $\sigma$  the line width and  $f(\nu - \nu_0, \sigma)$  a spectral lineshape function (e.g. Gaussian form). The integrals are summed over all transitions ( $i, j$ ). The integration can be restricted to one hemisphere. Point symmetries of the paramagnetic centre further restrict the area necessary for integration.

In the bottom diagrams of Figs. 4.1, 4.1, 4.3 and 4.4 the orientational dependence of single-crystallite transitions is shown. Resonant fields are depicted as a function of the polar angles ( $\theta, \phi$ ) of magnetic field in the principal frame of the paramagnetic

centre. They are numerical eigenvalues of the general spin Hamiltonian (3.34). The resulting single orientation spectra has to be integrated as expressed in Eq. (4.28) in order to observe the powder spectra shown in the centre digrams. The geometrical weighting factors, the transition intensities and the line widths have also to be included in the calculations.

EPR spectra are normally recorded as the first derivative of the absorption vs. field. Dominant features in a powder spectrum will be observed at orientations characterised by large derivatives or by a sign change(cf. Fig. 4.5).

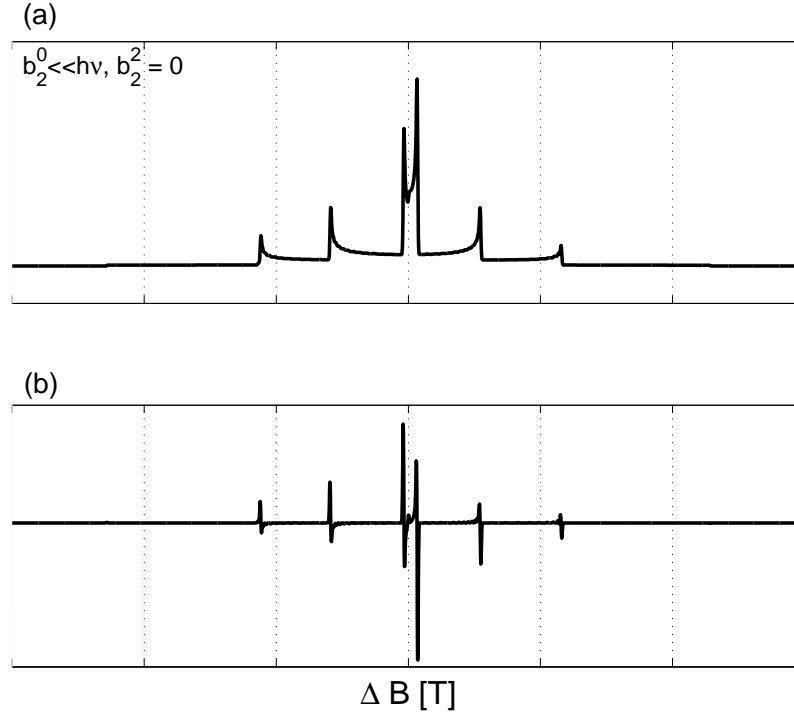


Fig. 4.5: Comparison of (a) the absorption spectrum and (b) the 1<sup>st</sup> derivative spectrum of a  $S = \frac{5}{2}$  paramagnetic centre with axial symmetry in the high field limit ( $\nu = 240$  GHz)

Resonance fields in a powder spectrum are characterised by a rapid enhancements in the absorption. They lead to a large value of its derivative which resembles positive-going and negative-going absorptions. Peaks in the first derivative spectrum reflect discontinuities or turning points in the absorption spectrum. They arise when  $\partial B/\partial\theta = 0$  or  $\partial B/\partial\phi = 0$ . For a single transition, this condition is fulfilled for: (i)  $\theta = 0$ ; (ii)  $\theta = \pi/2, \phi = 0$ ; (iii)  $\theta = \pi/2, \phi = \pi/2$ . Therefore, the most prominent spectral intensities arise from transitions at those angles. Transitions at these angles can be described in some cases by perturbation formulae. They are used for to relate the transition field positions with the spin Hamiltonian parameters.

### 4.4 Numerical simulations of EPR spectra

For general interpretation of powder EPR measurements, computer simulations of EPR spectra have to be used. In order to extract accurate spin Hamiltonian parameters from measurements, the experimental spectra are compared with computationally predicted spectra. The latter are based on the calculation of the eigenvalues of the spin Hamiltonian for a given set of parameters. The calculated eigenvalues are then converted into values of the resonance field. The best fit to the experimental spectrum leads to the most accurate set of parameters. This set of the spin Hamiltonian parameters can be regarded as the experimentally determined set of values.

There are at least two reasons that require a numerical computer simulation for the EPR interpretation. First, integral (4.28) can be evaluated only numerically in the case of powder spectra. Second, the conditions for perturbational calculations are fulfilled only rarely. The spin Hamiltonian parameters of many systems are not always accessible in the high or low field limits. In order to calculate the exact eigenvalues of the general spin Hamiltonian, a numerical solution of the secular equation has to be derived. Both of these tasks can be taken into account by computer packages available. In this work the following programmes have been used: *EasySpin*<sup>1</sup> and *XSophe*<sup>2</sup>

In the *EasySpin* software (reviewed in [104, 103]) the input data for a specific spin system are the effective spin value and parameters of the spin Hamiltonian given in MHz (among others:  $g_i$  and  $B_{ij}$ ). Additionally, line-broadening data have to be specified. Two types of line broadening can be specified: the isotropic line width in the magnetic field domain (full width at half maximum, mT) which is used for the convolution of the field-swept spectrum, and the widths (full width at maximum slope, MHz) of the Gaussian distribution of the scalar parameters  $\sigma(D)$  and  $\sigma(E)$  ( $D$ - and  $E$ -strain, cf. Sec. 4.13). They are related to the 2<sup>nd</sup>-order zero-field interaction distributions as  $\sigma(D) = \sigma(b_2^0)$  and  $\sigma(E) = \sigma(b_2^2)/3$  (cf. Eq. (3.36)). Experimental parameters should be specified as well: microwave frequency and the magnetic field sweep width. The temperature of the EPR experiment may also be included. In this case, Boltzmann populations are computed and included in the line intensities. Additionally, the EPR *detection mode* may be specified. In the perpendicular mode, the excitation and detection microwave magnetic field components are along the laboratory  $x$ -axis. In the parallel mode, they are along the  $z$ -axis, parallel to the external static field. *EasySpin* first computes the resonance field, the line intensity and the line width for a single orientation by means of the function `resfields`. In order to get the powder spectrum, the function `pepper` is invoked. It calls the routine `resfields` to calculate spectra over a triangular orientation grid. The grid is chosen

---

<sup>1</sup> *EasySpin* is a Matlab toolbox freely available from [www.esr.ethz.ch/EasySpin](http://www.esr.ethz.ch/EasySpin). It has been developed by Stefan Stoll in the EPR Group at ETH Zürich.

<sup>2</sup> *XSophe* is a software package developed by Graham Hanson in the Centre of Magnetic Resonance at the University of Queensland ([www.cmr.uq.edu.au/XSopheTitle.htm](http://www.cmr.uq.edu.au/XSopheTitle.htm)). It is commercially available from Bruker Biospin GmbH.

to coincide with the symmetry of the Hamiltonian. Its resolution can be also adjusted. The spectra are calculated for every point of the grid. The computed spectra are then interpolated with cubic polynomials - splines, in order to get data for a much finer grid. This procedure quickly yields many more resonant position, intensity and linewidth data than a calculation for every single orientation. At the end, the absorption powder spectrum is constructed from the computed resonance data. It is calculated as a sum of the partial powder spectra of the single triangles in the grid. The partial spectra are computed with the assumption that within the given triangle the resonance positions vary linearly. Furthermore, one postulates that the intensities and linewidths as being constant. Then the spectrum of each triangle is broadened in a way to consider the specific orientation. Finally, the obtained absorption spectrum is differentiated to get the first derivative spectrum. The resulting computed spectrum eventually can be fitted to the experimental spectrum.

In the *Xsophe* software, the necessary parameters of the spin Hamiltonian are specified as input data. The effective spin of the system also has to be defined. In this work only  $g$ -tensor and  $b_k^q$  parameters have been used. Other - hyperfine, quadrupole etc. - parameters have not been considered. The linewidth model and parameters are specified:  $D$ -strain in MHz and  $E/D$ -strain without dimension. The experimental data have to be given too: the microwave frequency, the magnetic field sweep range and the temperature in the experiment. In *XSophe*, matrix diagonalisation is used to determine resonant field positions and transition probabilities. In order to achieve a reduced computational time, the transition probability is assumed to be constant over a given resonance and the line shape is modelled as symmetric. The numerical integration is performed over all transitions contributing to the spectrum by partitioning the unit sphere with the triangular ('sophe') grid. This software is reviewed in [31].

For the interpretation of EPR measurements in this work the simulations from both software package are compared. On this way, the possible error sources in a particular simulation software have been minimised. The obtained spectra are then fitted to the experiments, as shown later.





## Part II

# EXPERIMENTS AND RESULTS



## 5. OVERVIEW OF EXPERIMENTS

EPR transitions can be detected within a wide frequency range. The sensitivity, however rapidly decreases with lower frequencies. Most common is the microwave frequency at  $\nu = 10$  GHz ( $\lambda = 3$  cm). It is denoted as *X-band* frequency. A resonance in the X-band occurs for a magnetic field of 357 mT for a free electron spin transition with  $g = 2.0023$ . This field is achieved easily by an electromagnet. Together with the so-called Q-band ( $\nu = 34$  GHz,  $\lambda = 0.88$  cm), these are the most commonly used EPR frequencies.

In order to achieve both high sensitivity and high spectral resolution, it is advantageous to perform experiments at higher frequencies. This is particularly important for the investigation of transitions between the atomic ground state levels with large splittings. The obstacle for the high-frequency EPR however is the generation of an homogeneous magnetic field of adequate strength. This problem was solved by the development of commercial superconducting magnets. They work at fields up to 17 T and thus allow EPR measurements in the W-band ( $\nu = 94$  GHz,  $\lambda = 3.19$  mm), G-band ( $\nu = 180$  GHz,  $\lambda = 1.7$  mm) and even higher. These magnets combine high stability and homogeneity. For the investigation of broad spectral features which are typically found in EPR, the main coil current has to be changed, thus preventing use of the persistent mode like in NMR.

EPR measurements performed above 100 GHz are usually denoted as *high-field* EPR. Although high-field EPR spectrometers are still not commercially available, many laboratories have constructed machines working at the frequencies up to 600 GHz ( $\lambda = 0.5$  mm). They require fields more than 20 T, i.e. conditions not accessible by superconducting magnets. For these fields resistive Bitter DC magnets are used. With the help of hybrid magnets combining both Bitter and superconducting technology a field magnitude of 45 T has been achieved [32]. However, these magnets are more complicated for operation and have poorer field resolution than superconducting magnets.

### 5.1 *X-band EPR*

EPR in the X-band requires a magnetic field not higher than 1 T. All X-band EPR spectra in this study have been recorded using two commercial spectrometers: Bruker ESP 300E and Bruker Eleksys 680. They both contain the following main elements: an electromagnetic radiation source, a resonance cavity for the sample, a magnet with a power supply and control, and a detector connected to the signal channel. Both

spectrometers are computer controlled allowing computer for signal processing. For cooling the sample a cryostat is provided. Here only the working principle of ESP 300E will be describe. A detailed description of the X-band operation of Elexsys 680 can be found elsewhere [6].

### 5.1.1 Microwave source

The microwave source used in ESP 300E is a klystron oscillator (cf. Fig. 5.1(1)). The frequency of the signal is determined by the dimensions (bandwidth of  $\Delta\nu = 400$  GHz) of the klystron cavity. The maximum output is 400 mW. The source signal is immediately split into the power arm (2) and the reference arm (3). The power arm is a rectangular microwave waveguide which leads the microwaves to the sample, and back to a detector (4). The intensity of the incident radiation can be modified in a range between 0 dB and 60 dB by a rotary vane attenuator (5). The attenuated signal is further directed to the resonant cavity by a microwave circulator (6).

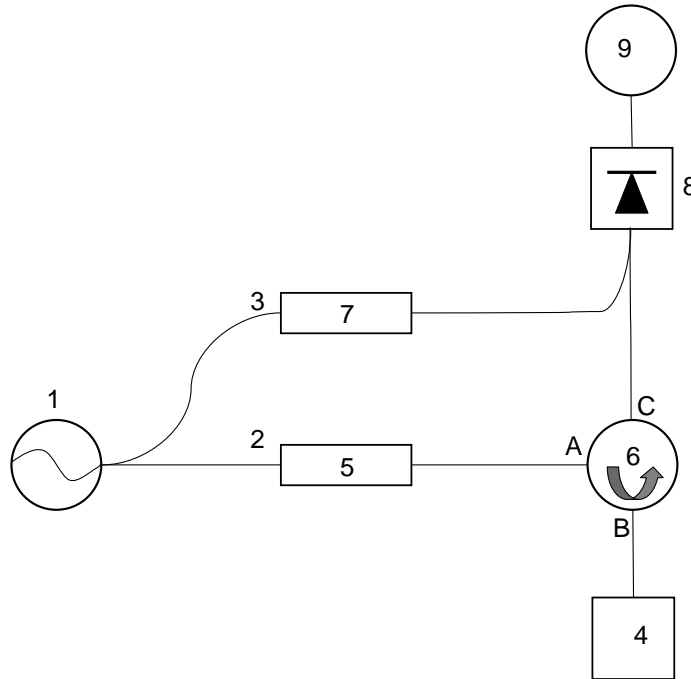


Fig. 5.1: Schematic view of an X-band microwave bridge: (1) microwave source; (2) power arm; (3) reference arm; (4) sample cavity; (5) attenuator; (6) circulator; (7) reference arm attenuator and phase shifter; (8) detector diode; (9) output

The reference arm has two functions. It supplies the detector diode with extra microwave power (biasing), and it discriminates between the absorptive and dispersive component of the signal on the basis of the phase difference. The bias power is provided through the separate reference arm attenuator (7), and its phase is controlled

by the reference arm phase shifter. The stability of the klystron frequency is ensured by locking the source frequency to the resonant frequency of the cavity by an automatic frequency controller (AFC).

### 5.1.2 Resonant cavities

EPR cavities are used to provide a linearly polarised oscillating magnetic field at the sample position. The cavity used with the ESP 300E is a simple rectangular metal box resonating with microwaves. A stack for inserting a sample tube (usually together with the cryostat tube) is also provided. The cavity which resonates with the incident radiation stores the microwave energy. Therefore it is characterised by the so-called  $Q$ -factor which is defined as the fraction of the stored energy times  $2\pi$  and the energy dissipated per microwave period. It can be also expressed as  $Q = \nu_0/\Delta\nu$  where  $\nu_0$  is the resonant frequency and  $\Delta\nu$  is the width at half height of the resonance curve.

The standing waves inside the cavity have their magnetic and electric components in opposite phase. This property is used to distinguish between the resonant absorption due to the magnetic component and the off-resonant absorption due to the electric component. The latter reduces the  $Q$ -factor and is present in many samples. The minimum electric field and the maximum magnetic field is reached in the centre of the cavity, i.e. the proper position for the sample.

Fine resonance coupling of the cavity with the microwave radiation is achieved through an adjustable hole called *iris* which changes the cavity impedance. When the cavity is critically coupled, even a small absorption of microwaves from the sample reduces the  $Q$ -factor. The phenomenon of absorption can be described as a change in the complex impedance  $Z = R + iX$  ( $R$  is the resistivity and  $X$  is the reactance).  $R$  is changed by the absorptive component of the field susceptibility  $X$  by the dispersive component. What is actually measured is the power of the reflected microwave. Therefore the reflection coefficient of the cavity is given as:

$$\Gamma = \frac{Z_c - Z_0}{Z_c + Z_0} \quad (5.1)$$

where  $Z_c$  is the cavity impedance, and  $Z_0$  the wave impedance. When the cavity is critically coupled at resonance, the impedances are equal and  $\Gamma = 0$ . Changes in reflection coefficient through the absorption are given by the vector  $d\Gamma(d\mathbf{R}, d\mathbf{X})$ . The outgoing EPR signal  $S$  is then defined as the scalar product of the original reflection coefficient and its change:

$$S = \Gamma_0 \cdot d\Gamma \quad (5.2)$$

The part of the microwaves which are reflected back is dependent on the phase of  $d\Gamma$  relative to  $\Gamma$ .

The resonant cavity in the experiments of this study was a commercial Bruker ER 4102 ST resonator. In this cavity the standing waves of the type  $TE_{102}$  (transversal-electric) are formed (cf. [58], p.468). Without the cryostat tube it has a nominal

centre frequency of  $\nu_0 = 9.75$  GHz , and  $\nu_0 = 9.30$  GHz with the tube inserted. Its unloaded  $Q$ -factor is 6000, but this value is reduced to 2000 – 3000 after inserting a sample.

For operations at low temperature the commercial helium-flow cryostat *Oxford ESR900* is used. It enables to work in the temperature range of 4–300 K. The cryostat consists of a quartz probe support within a double-walled vacuum-insulated quartz tube. This arrangement is placed into the resonator. The sample is exposed to a flow of helium gas. The liquid helium is pumped through the transfer tube which is shielded by the gas coming back from the cryostat. The quartz probe support has heating wires and a thermosensor in vicinity of the sample. They are connected to a digital temperature control unit which enables fine adjustments and a temperature stability of within a range of few K.

### 5.1.3 Signal detection

The measured EPR signal is defined as change between the intensity of the radiation reflected back from the resonant cavity containing a sample, and the intensity of the incident radiation. The source signal and the refracted signal are mixed at the detector diode which converts the frequency to a DC signal. At low power levels the diode current is proportional to the microwave power. It is biased by the reference arm attenuator in order to ensure that it operates in the linear regime (where  $I$  depends linearly on  $U$ ), which amounts to ca. 200  $\mu$ A.

The *signal channel* is used to separate EPR signals from noise. In the Bruker ESP 300E the field modulated detection is accomplished by the ER 023M signal channel. Operation of the signal channel requires a transfer of the DC signal to an AC signal. Therefore a small time-dependent modulation field  $B_{mod} = B_m \sin \omega_{mod} t$  (in the range 0.01 - 2 mT) at a modulation frequency  $\omega_{mod} \approx 100$  kHz is added to the external magnetic field  $B$ . The modulation magnetic field is generated by small coils mounted outside the cavity. Thus the field actually seen by the sample is:

$$B = B_0 + B_\Delta + B_{mod} \quad (5.3)$$

Here  $B_\Delta$  is a time-dependent field sweep due to slowly field changed from  $(B_0 - B_\Delta)$  to  $(B_0 + B_\Delta)$ . The variation of the signal response is then proportional to the field derivative (slope) of the absorption signal  $dS/dB$ .

After detection, the signal goes to the lock-in amplifier which amplifies only those signals which have the same frequency and the same phase as the original modulation signal. The phase sensitive output is proportional to the amplitude of the input signal times  $\cos \phi$ . An RC circuit with adjustable time constant ( $t_c$ ) is included to average the output.

### 5.1.4 Magnet unit

The requested field values and the length of the field sweep are set and managed by a field controller. The field is regulated with a Hall probe which produces a voltage

proportional to the field strength. A NMR-Gaussmeter (Bruker ER 035M) is used for calibration of the field in combination of a DPPH standard field marker of  $g = 2.0036$ .

## 5.2 W-band EPR

For W-band experiments, a conventional E680 Bruker spectrometer was used. This spectrometer consists of a microwave source at 94 GHz, a hybrid magnet system (combination of a low-temperature superconducting and a room-temperature magnet), a resonant cavity and supplying control electronics.

### 5.2.1 Microwave source

The W-band microwave bridge (ESP 900-1041) couples an input intermediate frequency (IF) signal at 9-10 GHz with the frequency at 84.5 GHz produced by an oscillator. The up-converter generates the operating frequency signal at 94 GHz. An oversized millimetre waveguide leads the microwaves to the probe cavity. A phase-lock loop stabilises the frequency of the W-band oscillator at 84.5 GHz to a low frequency reference. The detected signals are reflected from the probe cavity. They are down-converted to the intermediate frequency and amplified with a low-noise amplifier.

The IF signal is created in the standard X-band microwave bridge (E600 IF). This bridge contains the microwave source, the detection reference arm with the phase and amplitude control, power attenuation and AFC stabilisation units. The W-band microwave source can be also used for pulsed operations.

### 5.2.2 Resonant cavities

The W-band microwave resonator is part of a into commercial Bruker W-band c.w. probehead *TeraFlex*. It is a cylindrical cavity with a diameter of 3 mm. It operates in a  $TE_{011}$  microwave mode. Its size can be changed manually to adjust the resonant frequency (with a range of 10 GHz) after insertion of the sample. Quartz tubes of a 0.9 mm diameter are used to contain the samples. The cryostat used for W-band low-temperature measurements was of the type Oxford CF935P.

### 5.2.3 Magnet unit

The Bruker hybrid magnet system is a combination of a 0-6 T superconducting coil at helium temperature and a  $\pm 60$  mT room-temperature coil which are simultaneously operated. The magnet provides a vertical bore for the probehead. The magnet is placed in a cryostat needed for operations at 4.2 K. The cryostat is filled with liquid helium and liquid nitrogen. The room-temperature magnet has two water-cooled coils inserted into the superconducting magnet's horizontal bore.

A scheme of the additional electric elements for the superconducting magnet field control is shown in Fig. 5.2. The superconducting magnet has the inductance  $L_m$

and is connected to a power supply. The power supply provides the current  $I_0$  by means of normal-conducting leads of resistance  $R_l$ . A switch heater with resistance  $R_h$  is connected in parallel with the magnet. Changes in the current  $I_0$  create first an additional current through  $R_h$ . Consequently also a voltage on the magnet  $L_m$  is created. This induces a change in the magnetic field. The current through the magnet depends on both its actual and previous field values. So a field/current calibration is possible only in the static state, which is achieved only after a long delay. Therefore during a fast magnet sweep there always exists a constant offset in the magnetic field with respect to the supply current. This leads to an unwanted hysteresis behaviour. On the other hand, if the change of the current is too large for a longer time interval, the magnet can be quenched. Magnet quenching means: evaporation of all liquid helium in a very short time which implies a loss of the necessary cryogenic liquid for superconducting operations.

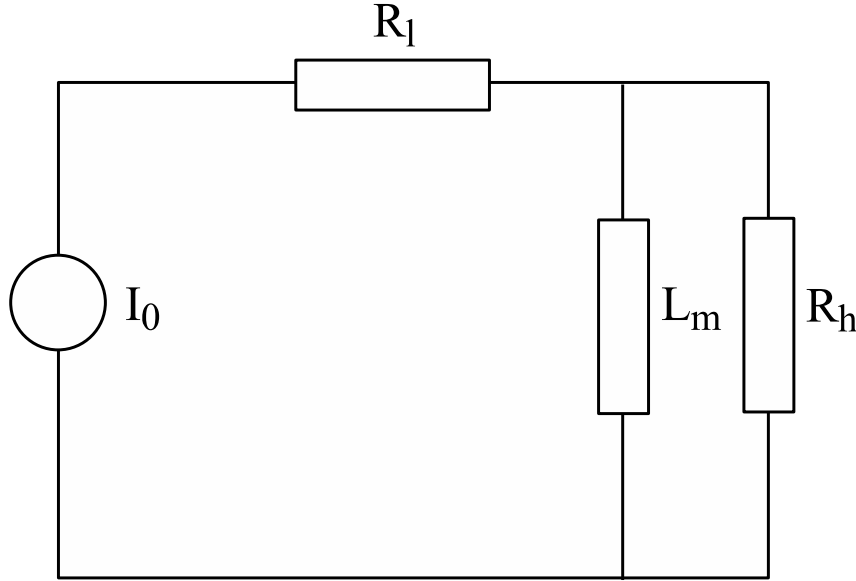


Fig. 5.2: Schematic view of a W-band superconducting magnet

The superconducting magnet uses the so-called *current jump* technique to solve the field determination problem. The jump current exceeds the safe current rate for a short time. This is a necessary condition to push the magnet in desired state without quenching it. The current jump method reduces the uncertainties in the magnetic field to the order of 1 mT and eliminates the field hysteresis.



### 5.3 High-frequency EPR

EPR experiments at frequencies higher than 100 GHz were performed at non-commercial spectrometers at *Center for Interdisciplinary Magnetic Resonance, National High Magnetic Field Laboratory, Florida State University*. The high-field experiments in this work were performed by Andrew Ozarowski, Johan van Tol and Louis Claude Brunel with high-field magnets. These measurements are published in [61, 18, 62]. The measurements at 240 GHz were done with a transient spectrometer with multi-frequency superheterodyne quasi-optical bridge [108].

In comparison to lower frequency bands, high-frequency EPR provides an improvement in the spectral resolution and sensitivity at corresponding higher magnetic fields.

#### 5.3.1 Microwave sources

The development of high-frequency EPR systems has been accompanied by few technical obstacles which have not been solved until recently [32]. Among these was the lack of easy-operating microwave sources in millimetre and sub-millimetre frequency bands.

The NHMFL's spectrometer can operate within a broad range of frequency bands. The microwave frequency range for all measurements in this study, from 92 to 320 GHz, is provided by two solid-state sources (Gunn-diode oscillators) [32]. These oscillators operate at frequencies of 95 and 110 GHz and can be tuned mechanically for  $\pm 3$  GHz. By multiplying these two frequencies, higher frequencies can be achieved. Exchangeable high-pass filters are used to cut off lower harmonics. Frequencies provided by the 110 GHz source can be 220, 330, 440 and 550 GHz. For the 95 GHz source, they can become 190, 285, 380 and 475 GHz.

The use of a standard single-mode rectangular waveguides is inappropriate above 100 GHz. They are becoming very lossy (ca. 12 dB/m at 250 GHz). Therefore, oversized transmission waveguides are used. These cylindrically shaped waveguides have a loss smaller than 1 dB/m for frequencies below 440 GHz. On the other side, they have difficulties to preserve the polarisation and phase. However, these disadvantages are not crucial for c.w. EPR measurements.

#### 5.3.2 Sample holder

EPR is performed without use of a resonator, i.e. in transmission mode. Two setups have been developed: the single-pass and the double-pass transition probes. The single-pass transition probe (Fig. 3 in [32]) has two cylindrical waveguides connected with deflection mirrors made of polished brass. One waveguide contains the sample compartment made of Teflon. The microwave radiation comes through the first waveguide, passes through the sample compartment, is reflected on the mirrors and goes back along the second waveguide. The double-pass transition probe has only one vertical waveguide section which routes microwaves to and from the sample. The

microwaves are reflected back by a flat mirror at the end of the waveguide. Therefore the sample is passed twice by the radiation.

### 5.3.3 *Signal detection*

The microwave detector for 190 and 285 GHz consists of a liquid helium cooled InSb bolometer from QMC Instruments, Model QFI/3BI. A bolometer is a device that measures the radiation power on the basis of the sensor's temperature change. It is the best method for frequency bands in millimetre range. Its sensitivity is very high (noise-equivalent power of  $10^{-13} \text{ W}\cdot\text{Hz}^{-1/2}$ ). Its response at 4.2 K within  $1 \mu\text{s}$  allows to detect field modulations up to 1 MHz. The detector can record spectra with first harmonic of the magnetic field modulation frequency. Additionally, it measures also simultaneously the amplitude and phase of the EPR signals. After detection and pre-amplification, the signal is fed into a phase-sensitive detector.

In the 240-GHz-spectrometer a heterodyne-type detection is used [108]. A superheterodyne detection scheme with high-frequency Schottky diode mixers is used. The detection bandwidth is wider than by bolometer, about 1 GHz. The sensitivity is of the same order of magnitude or even better than that of bolometric detectors.

### 5.3.4 *Magnet system*

The high-field magnet system for the high-frequency spectrometer was built around a prototype commercial magnet Teslatron from Oxford Instruments. The magnet is based on a superconducting technology and can achieve field strengths up to 17 T. It consists of two set of coils. The main set of coils is used for the setting the base field component or for large scans. The sweeping coil allows  $\pm 0.1 \text{ T}$  sweeps around the field set by the main coil.

The main set of coils consists of the many coaxial solenoids made of  $\text{Nb}_3\text{Sn}$  and  $\text{NbTi}$  superconducting filamentary wires. If they operate at 4.2 K, they can achieve 15 T. At 2.2 K, they can reach 17 T. The maximum sweeping rate of the main coil is  $0.5 \text{ T/min}$  at 4.2 K.

## 6. STRUCTURAL CALCULATIONS

### 6.1 Newman superposition model – previous studies

In this study the local structure of paramagnetic ions in the crystal lattice of ferroelectric crystals is investigated. The experimentally determined fine structure parameters are analysed in terms of the semi-empirical *Newman superposition model* (NSM), cf. Sec. 3.4. Additionally, *ab initio* calculations of the equilibrium structure with density-functional theory (DFT) technique is used to confirm conclusions derived from the semi-empirical NSM analysis.

In the NSM, the parameters of the spin Hamiltonian are derived from the atomic positions in the vicinity of the paramagnetic centre. As a necessary condition, the reference NSM parameter  $\bar{b}_k(R_0)$  for a particular ion–ligand pair has to be known (cf. Eq. 3.44). It is specified for a reference distance  $R_0$ . In order to calculate  $\bar{b}_k(R)$  for other distances, the power law (3.45) with exponent  $t_k$  has to be established.

The assumptions of the NSM (cf. Sec. 3.4.2) have been proven repeatedly to hold for the  $\text{Fe}^{3+}$  ions in oxygen coordinations. Therefore, the established literature data for the NSM parameters for those ions has been used in this work.

Tab. 6.1: NSM parameters for  $\text{Fe}^{3+}$  as determined by Siegel and Müller [98].

host	$R_0$ [pm]	$\bar{b}_2$ [GHz]	$t_2$
MgO	210.1	-12.35(75)	8(1)
CaO	239.8	-6.75(60)	5(1)
SrTiO <sub>3</sub>	195.2	-20(3)	8(1)

#### 6.1.1 NSM parameters for $3d^5$ ions

A first attempt to test the NSM for  $3d^5$  ions was done by Newman and Siegel in 1976 [72]. They considered spin Hamiltonian parameters for  $\text{Fe}^{3+}$  and  $\text{Mn}^{2+}$  defects in MgO, CaO,  $\text{CaCO}_3$  and  $\text{CaWO}_4$  crystal hosts. A first detailed study of local distortions (i.e. atomic displacements) around  $\text{Fe}^{3+}$  defect sites in perovskite crystals was performed in 1979 by Siegel and Müller [98]. They correlated the experimental values of reference intrinsic parameters  $\bar{b}_2$  for the  $\text{Fe}^{3+}$  defect with those for the

$\text{Mn}^{2+}$  defect in the following crystals: MgO, CaO and  $\text{SrTiO}_3$ . NSM data were evaluated from EPR experiments under uniaxial strain. The measured uniaxial strain parameter allowed to determine the NSM parameters for MgO and CaO hosts independently. From uniaxial strain experiments on  $\text{SrTiO}_3$ , only the product  $\bar{b}_2 t_2$  could be determined. The data obtained are summarised in Tables 6.1 and 6.2.

Tab. 6.2: NSM parameters for  $\text{Mn}^{2+}$  as determined by Siegel and Müller [98].

host	$R_0$ [pm]	$\bar{b}_2$ [GHz]	$t_2$
MgO	210.1	-4.710(15)	7(1)
CaO	239.8	-1.50(30)	5(1)

For two paramagnetic ions  $\text{Mn}^{2+}$  and  $\text{Fe}^{3+}$ , an important relation is shown to hold. If two ions are found at the same site in a crystal, it can be used for comparative purposes. It is based on the assumption that the intrinsic parameter and the power-law exponent are equal for both ions. Then it can be written:

$$\frac{b_2^0(\text{Mn})}{b_2^0(\text{Fe})} \approx \frac{\bar{b}_2(\text{Mn})}{\bar{b}_2(\text{Fe})} \quad (6.1)$$

where the intrinsic parameters should be defined for the same reference distance  $R_0$ .

### 6.1.2 Application of the NSM for perovskite structures

The NSM has been very successfully applied for the determination of the crystal structure around the paramagnetic ions in the case of high spatial distortions. Possible crystal structures have been parametrised. This enabled a semi-quantitative determination of the local crystal structure. In the studies of Siegel and Müller [98, 97], the NSM was applied to describe the local structure surrounding dopant sites of  $\text{Mn}^{2+}$  and  $\text{Fe}^{3+}$  in perovskites.

In that study, the experimental value of the tetragonal parameter  $b_2^0$  of the spin Hamiltonian was studied for different perovskite compounds. The exceptionally high value of the experimental  $b_2^0$  parameter was rationalised assuming the existence of a distorted oxygen octahedron in which one oxygen is missing, i.e. the presence of a  $\text{Fe}^{3+}\text{-V}_\text{O}$  defect associate. Experimental values of the tetragonal parameter are known for  $\text{Fe}^{3+}$  in  $\text{SrTiO}_3$  ( $b_2^0 = 40.50(45)$  GHz, [112]),  $\text{PbTiO}_3$  ( $b_2^0 = 35.61(6)$  GHz, [52]),  $\text{KTaO}_3$  ( $b_2^0 = 43.2(3)$  GHz, [121]) and for  $\text{Mn}^{2+}$  in  $\text{SrTiO}_3$  ( $b_2^0 = 40.544(15)$  GHz, [94]).

Parameter  $b_2^0$  has been modelled so that  $\text{Fe}^{3+}$  ion is influenced by the five remaining oxygens and the vacancy located at the  $c$ -axis. As relevant parameter, the ratio between the experimental and previously determined intrinsic value  $b_2^0/\bar{b}_2$  was used. It was shown to be  $b_2^0/\bar{b}_2 \approx 2$  for all compounds. The distortion of the cubic unit cell

in the tetragonal phase  $c/a$  was taken as a decisive parameter. Curves representing the dependence of calculated  $b_2^0/\bar{b}_2$  ratios on the displacement of  $\text{Fe}^{3+}$  along the  $c$ -axis are shown in Fig. 6.1. Different curves represent different  $c/a$ -ratios.

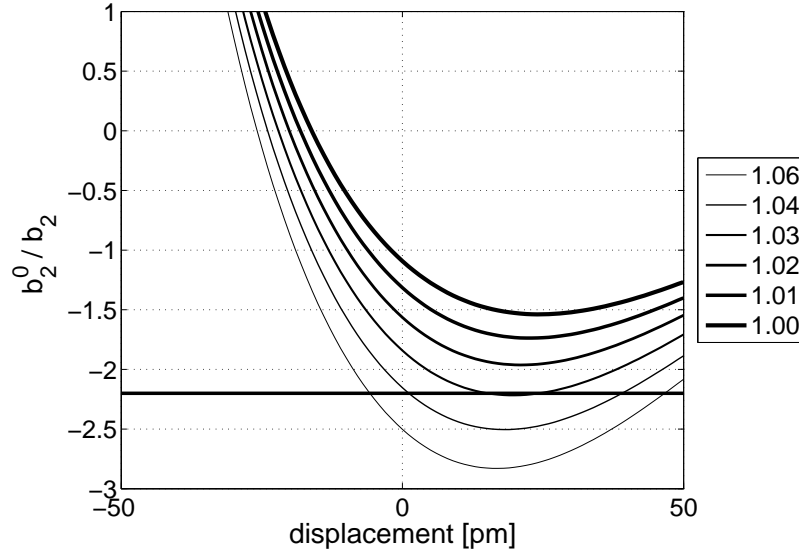


Fig. 6.1: Model for the local distortion of the oxygen octahedra by Siegel and Müller [98]. Different curves represent different  $c/a$ -ratio as quoted in the diagram. Displacement represents a position of the  $\text{Fe}^{3+}$  from the centre of the oxygen octahedron along the crystallographic  $c$ -axis. The positive direction means a displacement towards the oxygen vacancy. A zero value is the plane of 4 planar oxygens.

Each calculated  $b_2^0/\bar{b}_2$  curve has a minimum for a characteristic displacement coordinate. From the NSM calculations it can be concluded that an experimental parameter of  $b_2^0/\bar{b}_2 \approx -2.2$  requires a contraction of the oxygen octahedron which is described by  $c/a \approx 1.03$ . An important result can be related to the position of the paramagnetic ion. From the NSM calculations it follows that it should be shifted by ca. 20 pm towards the vacancy. Such a conclusion was not in agreement with previous considerations about the displacement of the substituted ion into the remaining oxygen pyramid (on the basis of electrostatic forces).

The NSM analysis of the  $\text{Fe}^{3+}$  EPR spectrum has also been successfully applied to describe the phase transition in  $\text{BaTiO}_3$ . Ionic positions and 2<sup>nd</sup> order spin Hamiltonian parameters are known for all phases: cubic, tetragonal, orthorhombic and rhombohedral. Displacement of  $\text{Fe}^{3+}$  relative to the ideal  $\text{Ti}^{4+}$  position was calculated as a function of the parametrised distortion of the oxygen octahedron. It was demonstrated that the  $\text{Fe}^{3+}$  ion does not follow the motion of the  $\text{Ti}^{4+}$  ion relative to the  $\text{O}^{2-}$  octahedron. The latter process actually produces polarisation. This result holds for all three ferroelectric phases of  $\text{BaTiO}_3$ . The  $\text{Fe}^{3+}$  ion is always centred in the oxygen octahedron. This differs from the behaviour of the coordination of

Ti<sup>4+</sup> ion. Therefore, the NSM helped to explain why iron doping diminishes the ferroelectric properties in BaTiO<sub>3</sub>.

## 6.2 Newman superposition model – calculation procedure

### 6.2.1 Computational algorithm

In this work a general approach for calculating spin Hamiltonian parameters via the NSM has been developed. The general approach which is not referred to the lattice symmetry was necessary to calculate the NSM for a general crystal site. At such a site of a paramagnetic ion, the ligands can be distributed arbitrarily around the ion. The number of ligands can also be arbitrary. Additionally, the paramagnetic ion should be able to change its position.

In the NSM calculation procedure, the position of the paramagnetic ion and ligand positions have to be defined at first. They are specified as vectors in the crystal unit cell coordinate frame.  $\mathbf{R}$  is the starting position of the ion and  $\mathbf{r}_i$  is the position of the  $i$ -th ligand. They are specified as a relative atom coordinates within the unit cell. The unit cell is defined with lattice parameters  $(a, b, c)$ . The number of the ligands is specified by  $N$ .

Next, the NSM parameters specific for a particular ion–ligand combination have to be defined. They are: the intrinsic parameter  $\bar{b}_k(R_0)$  specified for a reference distance  $R_0$  and the power-law exponent  $t_k$ .

After specification of the input parameters, a stepwise movement of the paramagnetic ion has to be defined. Its final position is denoted by the vector  $\mathbf{X}$ . The ion is supposed to move in  $M$  small steps along the difference vectors  $\mathbf{X} - \mathbf{R}$  and  $\mathbf{R} - \mathbf{X}$ . Every position  $j$  of the ion is denoted by the vector  $\mathbf{x}_j$ . When all positions are determined, the spin Hamiltonian parameter can be calculated (cf. Eq. 3.44). The vector pointing from the paramagnetic ion to the ligand is symbolised by  $\mathbf{R}_i = \mathbf{r}_i - \mathbf{x}_j$ . The distance between the ion and the ligand is given by the magnitude of  $R_i$ :

$$R_i = |\mathbf{r}_i - \mathbf{x}_j| \quad (6.2)$$

and the polar angle  $\theta_i$  between  $\mathbf{R}_i$  and the  $z$ -axis is given by:

$$\cos \theta_i = \frac{\mathbf{R}_i \cdot \hat{\mathbf{z}}}{|\mathbf{R}_i|} \quad (6.3)$$

The azimuthal angle  $\phi$  can be expressed as

$$\tan \phi_i = \frac{|\mathbf{R}_i \cdot \hat{\mathbf{y}}|}{|\mathbf{R}_i \cdot \hat{\mathbf{x}}|} \quad (6.4)$$

The cases when  $|\mathbf{R}_i \cdot \hat{\mathbf{x}}| = 0$ ,  $|\mathbf{R}_i \cdot \hat{\mathbf{x}}| > 0$  and  $|\mathbf{R}_i \cdot \hat{\mathbf{x}}| < 0$  have to be considered separately.

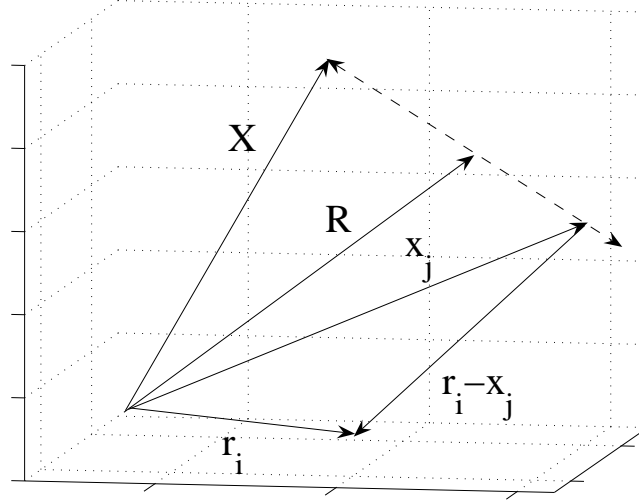


Fig. 6.2: Position vectors for a NSM calculation.

As a result, the contributions  $b_k^q(i)$  of a particular ligand  $i$  to the spin Hamiltonian parameter  $b_k^q$  of the paramagnetic ion at position  $x_j$  can be calculated. Then, according to assumption (a) of the NSM, the contributions are simply summed over all ligands in order to get the final parameter:

$$b_k^q = \sum_i b_k^q(i) \quad (6.5)$$

The orientation of the paramagnetic centre in the crystal coordinate frame generally does not coincide with any of the crystal symmetry axes (if there is any). Therefore, it is necessary to calculate all parameters  $b_k^q$  (i.e. for every  $q$  when a particular order  $k$  is given). For a general position of ligands, there is no *a priori* reason for any parameter  $b_k^q$  to be equal to zero. The parameters  $b_k^q$  are calculated with the help of the coordination factors from Table 3.4 and Eq. (3.44). The analytic forms of the 2<sup>nd</sup>-order spin Hamiltonian parameters ( $b_2^q$ ) are given explicitly:

$$b_2^0(i) = \frac{3}{2} \bar{b}_2(R_0) \left( \frac{R_0}{R_i} \right)^t (\cos^2 \theta_i - 1) \quad (6.6)$$

$$b_2^1(i) = 3 \bar{b}_2(R_0) \left( \frac{R_0}{R_i} \right)^t \sin 2\theta_i \cos \phi_i \quad (6.7)$$

$$b_2^{-1}(i) = 3 \bar{b}_2(R_0) \left( \frac{R_0}{R_i} \right)^t \sin 2\theta_i \sin \phi_i \quad (6.8)$$

$$b_2^2(i) = \frac{3}{2} \bar{b}_2(R_0) \left( \frac{R_0}{R_i} \right)^t \sin^2 \theta \cos 2\phi \quad (6.9)$$

$$b_2^{-2}(i) = \frac{3}{2}\bar{b}_2(R_0) \left(\frac{R_0}{R_i}\right)^t \sin^2 \theta \sin 2\phi \quad (6.10)$$

$$(6.11)$$

This computational scheme gives a single set of the spin Hamiltonian parameters for a specific position  $\mathbf{x}_j$  of the ion. The whole procedure has to be repeated for all supposed  $j = 0 \dots M$  steps. It gives  $b_k^q$  as a function of the displacement of the ion. The displacement is defined as  $d_j = |\mathbf{x}_j - \mathbf{R}|$ , where the direction of each displacement is usually defined separately.

After all spin Hamiltonian parameters necessary have been calculated, they can be transformed in a 'proper' coordinate frame. The 'proper' coordinate frame is defined by the condition that a number of parameters is minimal. The 2<sup>nd</sup>-order parameters can be always transformed into a frame in which only two of them are non-zero:  $b_2^0$  and  $b_2^2$ . This transformation is convenient, because the proper coordinate frame is always used for analysing and fitting experimental spectra. The coordinate transformation requires to write the Hamiltonian parameters as matrix  $\mathbf{D}$  (3.25). The elements  $D_{ij}$  can be calculated in terms of the  $b_k^q$ . The Stevens operators (cf. Table 3.3) are used in this step. By identifying coefficients with matrix  $\mathbf{D}$  (3.21), we finally arrive at [87, 57]:

$$\mathbf{D} = \begin{bmatrix} D_{xx} & D_{xy} & D_{xz} \\ D_{yx} & D_{yy} & D_{yz} \\ D_{zx} & D_{zy} & D_{zz} \end{bmatrix} = \frac{1}{6} \begin{bmatrix} -2(b_2^0 - b_2^2) & 2b_2^{-2} & 2b_2^1 \\ 2b_2^{-2} & -2(b_2^0 + b_2^2) & 2b_2^{-1} \\ 2b_2^1 & 2b_2^{-1} & 4b_2^0 \end{bmatrix} \quad (6.12)$$

The symmetric matrix  $\mathbf{D}$  obtained in this way has to be transformed in its diagonal form by a computational diagonalisation procedure. The result is a matrix with diagonal elements  $D_x$ ,  $D_y$ ,  $D_z$ . The value with the largest absolute magnitude is chosen as  $D_z$ , and the value with the smallest as the  $D_x$ . This matrix is traceless:  $D_x + D_y + D_z = 0$ . The experimental parameters  $b_2^0$  and  $b_2^2$  in the proper coordinate system are obtained by backward transformation:

$$b_2^0 = \frac{3}{2}D_z; \quad b_2^2 = \frac{3}{2}(D_x - D_y) \quad (6.13)$$

The complete procedure has to be repeated over  $M$  steps for every position  $\mathbf{x}_j$  until the final position  $\mathbf{X}$  of the ion is reached. The parameters may be plotted against the distance  $d$ . An example of the  $b_2^0$  parameter of the  $\text{Fe}^{3+}$  ion in cubic octahedral surrounding as a function of shift along the cubic axis is plotted in Fig. 6.3.

Generally, in calculation of the parameters while the ion is re-positioned, the eigenframe of the  $\mathbf{D}$  matrix also changes simultaneously. At every position the matrix should be transformed to its eigenframe by a different transformation. That could lead to discontinuous behaviour of the parameters at the points where two of  $D_i$  values possess the identical absolute magnitude. In this situation the axes have to be re-defined and a coordinate system is transformed with an improper transformation. Angles of the paramagnetic centre relative to the crystal are also functions of the position of the atom. They may also exhibit discontinuous behaviour.



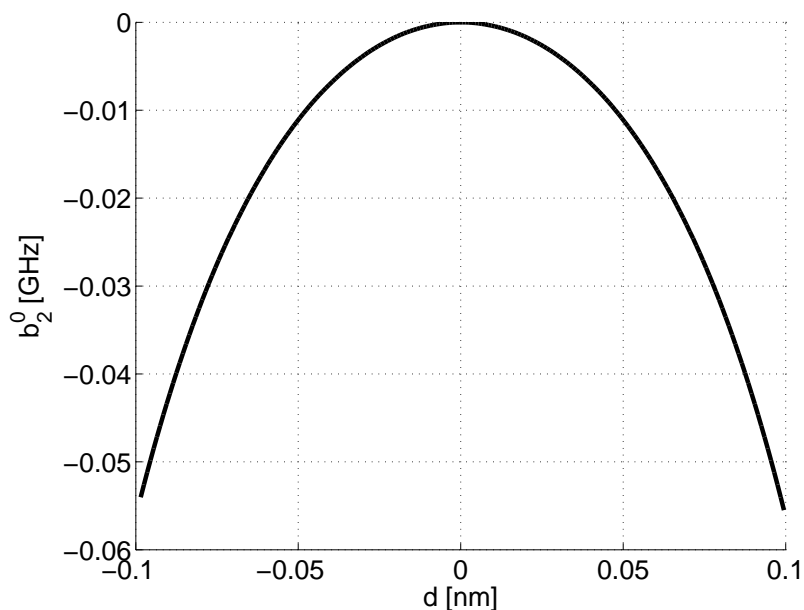


Fig. 6.3: The NSM calculation of parameter  $b_2^0$  for the  $\text{Fe}^{3+}$  ion in the oxygen octahedral coordination in a cubic crystal.  $d$  is shift along the cubic axis.

### 6.2.2 Limitations of the NSM

The main problem in applying the NSM is the determination of the exact positions of the coordinated ligands at the defect site. In principle, crystallographic diffraction analysis yields positions of atoms in a crystal. In practice, the determination of exact positions is hindered by a number of facts:

(a) Structure determination from  $X$ -ray analysis often assumes that isomorphous crystals have ions in identical relative positions in all unit cells. However, this is not a sufficient approximation for the NSM analysis of the spin Hamiltonian.

(b) Experimental EPR measurements are determined on substituted impurities in host crystals. Impurities cause local distortions of the crystal lattice. Diffraction experiments, on the other hand, measure bulk structure. Therefore distortions around impurities are not accessible by diffraction measurements. The real ligands of a paramagnetic defect are therefore in slightly different positions compared to those determined for the host crystal.

(c) EPR measurements are usually performed at very low temperatures. Crystallographic data for host crystals at these temperatures are rarely accessible. However, the crystal structure changes significantly, when going from the room temperature to, e.g., 10 K.

These problems may considerably hinder the possibility to predict reliably the spin Hamiltonian parameters via the NSM. The errors which arise from unfulfilled assumption of NSM (cf. Sec. 3.4.2) could be even smaller than the errors coming

from uncertainties in the ionic positions.

In this work we have tried to avoid these problems caused by uncertainties of atomic positions. First, a low temperature high-resolution diffraction experiments has been used to determine the crystal structures changes at the temperature of EPR experiments. Second, where accessible, refined positions of atoms in the vicinity of the paramagnetic ion provided by *ab initio* calculation have been used.

The present strategy is to calculate the fine splitting parameters by the NSM for different possible structural arrangements. Then the calculated values are compared with experimental data. The experimental values have to be determined with reliable accuracy. The interception points between the calculated curve and the experimental value is used for a prediction of the local structure.

## 7. LEAD TITANATE: EXPERIMENTS

### 7.1 Introduction to $\text{PbTiO}_3$

*Lead titanate* ( $\text{PbTiO}_3$ , PT) is a perovskite-type polar crystal with ferroelectric properties. It is widely used as a functional ceramic material as a result of its excellent ferroelectric and piezoelectric properties [35, 125, 107, 53].  $\text{PbTiO}_3$  belongs to displacive-type ferroelectrics that can be used as dielectric material in capacitors. It is also used as thin-film material with high refractive index in electro-optical components. Its piezoelectric and pyroelectric properties are utilised in sensors, piezoelectric actuators and detectors for infra-red radiation. Lead titanate exhibits a Curie temperature  $T_C$  of 763 K and a dielectric constant of about 200. It is therefore attractive for high-temperature and high-frequency transducer applications.

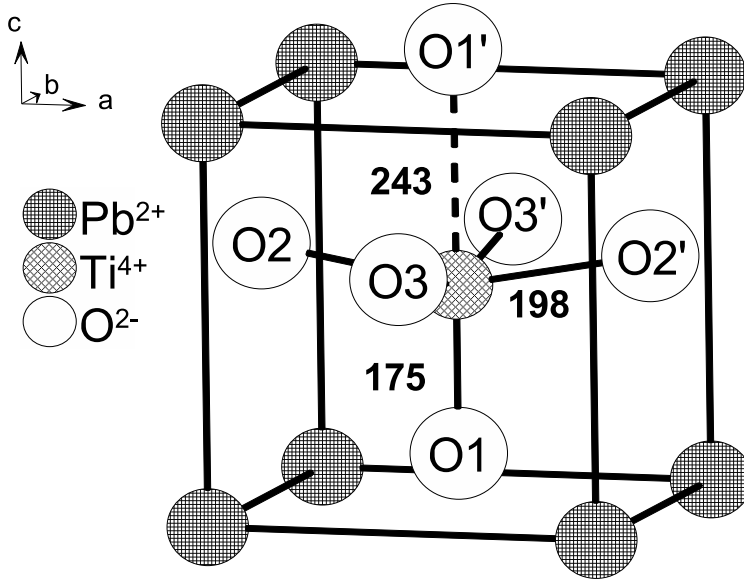


Fig. 7.1: Schematic representation of the tetragonal unit cell of  $\text{PbTiO}_3$  with designation of the different oxygen sites. The experimental atomic distances from the Ti site to the surrounding octahedral oxygen sites are given in pm.

The importance of lead titanate lies in its use as a component in the solid solution system *lead zirconate titanate* ( $\text{Pb}[\text{Zr}_x\text{Ti}_{1-x}]\text{O}_3$ , PZT). A variety of ferroelectric properties can be controlled when replacing the Pb or Ti cations with different ions. In the case of doping with Fe, it is supposed that charge compensation requires the presence of oxygen vacancies ( $V_{\text{O}}^{\bullet\bullet}$ ). If charge compensation occurs within the nearest-neighbour  $\text{O}^{2-}$  ions, a large distortion of the  $\text{O}^{2-}$  octahedron can happen. Because of the short interatomic distances, a large change of the  $\text{Fe}^{3+}$  fine structure terms will be induced. The oxygen vacancies are expected to have a major impact on the properties and the performance of ferroelectric compounds. The coordination sphere required for the charge compensation, however, has not been qualified unambiguously. Because the oxygen vacancies are dominant charge carriers in this class of compounds, this is an issue of both technological and scientific importance [100, 85]. In addition to the charge compensation by  $V_{\text{O}}^{\bullet\bullet}$ , intrinsic double-negatively charged  $V_{\text{Pb}}^{\prime\prime}$  centres have been proposed as additional charge compensating sites [115, 117]. These vacancies, however, are rather immobile and almost without importance for the charge transport.

### 7.1.1 Preparation of $\text{PbTiO}_3$

The samples used in this study was received as  $\text{PbTiO}_3$  doped with 0.5 mol % iron ( $\text{Pb}_{0.95}\text{Fe}_{0.05}\text{TiO}_3$ ). It was produced by Hans Küngl and Michael Hoffmann at the *Institute of Ceramics in Mechanical Engineering, University of Karlsruhe* as a part of the *Research Collaboration Project 595* of the *German Science Foundation*. Here only the short description of its synthesis is given, and for details c.f. [46].  $\text{PbTiO}_3$  was prepared by a mixed-oxide route. In order to determine the proper weights of the oxide components, the stoichiometry was calculated under the assumption that iron  $\text{Fe}^{3+}$  occupies  $\text{Ti}^{4+}$ -sites of the perovskite structure. An oxygen vacancies charge compensation assumption is supported by the observed chemical composition of the material  $\text{Pb}(\text{Ti}_{0.995}\text{Fe}_{0.005})\text{O}_{2.9975}$ . Lead oxide, titanium oxide  $\text{TiO}_2$  and iron oxide  $\text{Fe}_2\text{O}_3$  were mixed by attrition milling in isopropanol. After the separation of the liquid in a rotation distiller, the powder mixture was dried at 100 °C and then passed through a metal sieve. The iron doped lead titanate was then synthesized in a closed alumina crucible by calcination at 850 °C. Fine-grained ceramic powder was produced by milling. The processing was completed by drying and sieving the powder through a 160  $\mu\text{m}$  mesh.

### 7.1.2 Determination of the crystal structure of $\text{PbTiO}_3$

The crystal structure of  $\text{PbTiO}_3$  exhibits a structural ferroelectric phase transition from a high temperature cubic phase to a low temperature tetragonal one. The cubic phase is paraelectric and it has the space group  $Pm\bar{3}m$  ( $O_h$ ). The tetragonal phase is ferroelectric with the space group  $P4mm$  ( $C_{4v}$ ) [95]. The transition occurs at a temperature of 736 K.

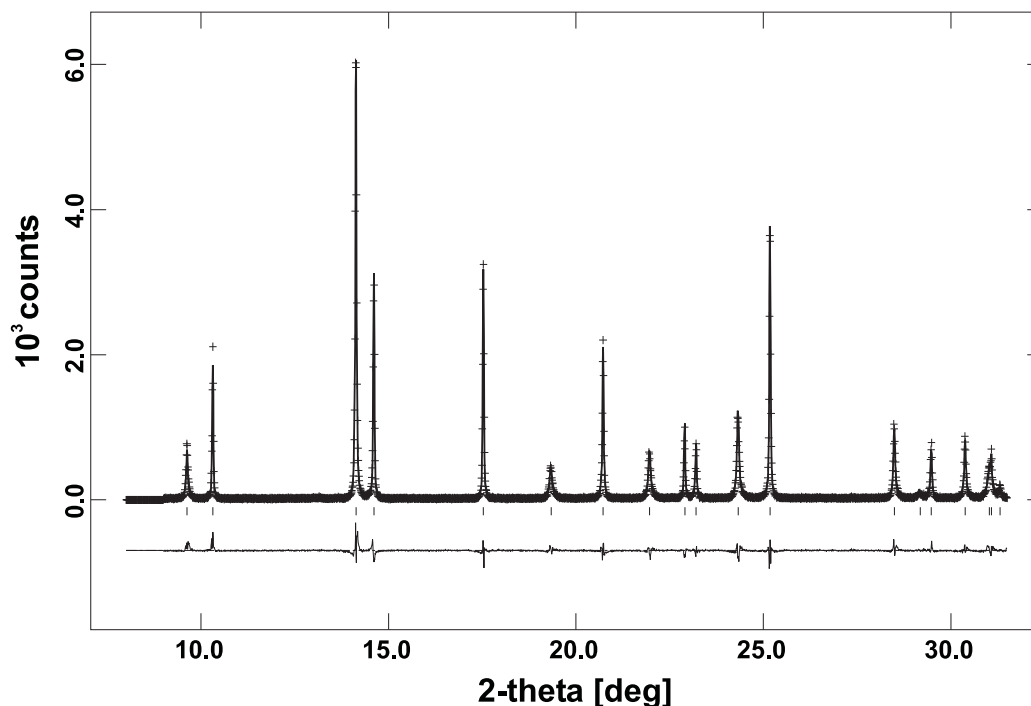


Fig. 7.2: Observed and calculated diffraction profiles for  $\text{PbTiO}_3$ . The experimental data have been obtained from high-resolution synchrotron powder diffraction at 12 K (top). The bottom curve refers to the difference between both curves.  $\lambda = 0.0699988$  nm.

The low temperature crystal structure of  $\text{PbTiO}_3$  has been the subject of some controversial discussion over the past 50 years. Several X-ray, optical and dielectric measurements of  $\text{PbTiO}_3$  indicated small anomalies in the temperature regions around 173 K and 123 K [42]. Changes in lattice parameters in single crystals were detected around 173 K as well. They were interpreted as a possible second order phase transition to a second tetragonal phase. Later this phase has been identified as an antiferroelectric orthorhombic phase [43]. Moreover, the low-temperature tetragonal phase postulated earlier was assumed to transform into another tetragonal phase around 113 K [34]. This was in contradiction with the picture of having an orthorhombic phase in this temperature range. However, neither in neutron powder profiles [28], nor in X-ray and optical measurements using  $\text{PbTiO}_3$  single crystals, additional evidence was seen for a structural transition at low temperatures.

It was necessary to identify the low-temperature structure and to obtain reference values for the NSM interpretation of low-temperature EPR data. Therefore high-resolution synchrotron powder diffraction measurements were carried out at *Hasylab* in Hamburg. They were performed by Kristin Schönauf, Martin Knapp and Helmut Ehrenberg at the *Materials Science Department, Darmstadt University of Technology* as a part of the *Research Collaboration Project 595* of the *German Science Founda-*

Tab. 7.1: Lattice parameters ( $a, b = 389.0673(11)$  pm,  $c = 416.7553(30)$  pm), cell volume ( $0.0630856(5)$  nm<sup>3</sup>) and relative atom coordinates (upper rows) for PbTiO<sub>3</sub> at 12 K, obtained from high-resolution synchrotron powder diffraction.  $U_i$  is the mean square of atomic displacement. The predicted values from *DFT* calculations are listed also with lattice parameters  $a = b = 386.4$  pm,  $c = 404.2$  pm (lower rows). Pb was kept fixed at the origin for both, Rietveld refinement and *DFT* calculations.

atom		$X$	$Y$	$Z$	$U_i \cdot 100$	site symmetry
Pb	exp.	0.000000	0.000000	0.000000	0.820(27)	$4mm$
	DFT	0.000000	0.000000	0.000000		
Ti	exp.	0.500000	0.500000	0.5415(14)	0.66(10)	$4mm$
	DFT	0.500000	0.500000	0.5346		
O1	exp.	0.500000	0.500000	0.1239(19)	0.38(19)	$4mm$
	DFT	0.500000	0.500000	0.0904		
O2 / O3	exp.	0.000000	0.500000	0.6288(13)	0.38(19)	$mm2$
	DFT	0.000000	0.500000	0.6032		

tion. This measurements were published in [63]. The measurements were performed at 12 K using a He closed-cycle cryostat. The powdered sample was measured using an incident beam of wavelength 0.0699988 nm together with an analysing crystal and a scintillation counter.

The measured data was analysed by a Rietveld refinement. The peak profiles were fitted using the generalised model for anisotropic peak broadening (cf. Fig. 7.2). The structural model was refined undo the symmetry of  $P4mm$ . The lead positions were fixed at the origin. No superlattice reflections were detected. The  $c/a$  - ratio at the experimental temperature is 1.0721. It should be noted that it is considerably higher then previously reported  $c/a$  - ratio at higher temperatures. Lattice parameters and atom coordinates obtained are given in Table 7.1.

The reference structure of undistorted cubic PbTiO<sub>3</sub> is the perovskite structure. Ti<sup>4+</sup> ions are octahedrally coordinated by oxygen ions and are positioned at the centre of the unit cell. The Pb<sup>2+</sup> ions are twelve-fold coordinated by oxygens. They are located at the corners of the cube. The O<sup>2-</sup> ions are centred on each face of the unit cell (cf. Fig. 7.1). In the ferroelectric tetragonal phase, the oxygen octahedron is elongated along [001]. It is shifted by 54 pm with respect to the Pb<sup>2+</sup> position. The titanium ion is then displaced along [001] from the centre of the cell by 17 pm. As a result, the titanium ion occupies an *off-centre* position within the shifted oxygen octahedron (cf. Table 7.1).

The detected low-temperature  $P4mm$  symmetry is consistent with the interpretation of the EPR spectra. For this purpose the spin Hamiltonian of axial symmetry (3.38) was used. Therefore no orthorhombic phase around dopant site can be present. Therefore it is concluded that  $\text{PbTiO}_3$  remains tetragonal down to 12 K, as already assumed earlier.

## 7.2 Previous EPR measurements

The first EPR spectrum attributed to  $\text{Fe}^{3+}$  in  $\text{PbTiO}_3$  was measured in 1964 on a single-crystal sample. It led to the discovery of a very large fine structure splitting [27]. This observation was explained by the strong tetragonal distortion of the crystal field experienced by the  $\text{Fe}^{3+}$  ion. The observed EPR parameters from this and other previous EPR studies are summarised in Table 7.2.

Tab. 7.2: fine structure parameters as obtained in this work compared to the values from the previous studies. The sign of the  $b_2^0$  parameter is determined by an analysis of line intensities at low temperatures.

$T$ [K]	$b_2^0$ [GHz]	$b_4^0$ [MHz]	$b_4^4$ [MHz]	$\nu$ [GHz]	Ref.
290	$\geq 30$			9.4	Gainon, 1964 [27]
290	27.0(15)			37.5	Pontin et al., 1969 [79]
	15.9(6)	405(60)			
77	33.0(15)				
	20.1(6)				
85	35.59(6)	130(100)	1500(400)	70	Lewis and Wessel, 1976 [52]
	34.48(9)	130(150)	1650(600)		
290	27.13(1)	-105(1)	4195(15)	9.4	Laguta et al., 1996 [48]
77	32(1)			9.4	
10	35.28(1)			9.3 – 360	this work [61]

In the Q-band (35 GHz) measurements made by Pontin et al. in 1969, two different iron centres were observed [79]. One of them was assigned to a  $\text{Fe}^{3+}\text{-V}_{\text{O}}$  defect associate. It was also observed that the tetragonal fine structure parameter  $b_2^0$  increases by 20% when cooling from room temperature to 77 K. This observation was consistent with a change in the lattice deformation as a function of temperature. The ratio of the unit cell parameters  $c/a$  changes by 19 % in this temperature range. From

these spectra additional higher-order spin Hamiltonian parameters have been determined. The temperature dependence of line intensities at liquid helium temperature proved that the sign of  $b_2^0$  is positive.

In experiments performed at 70 GHz by Lewis and Wessel in 1976, additional transitions have been observed [52]. The high frequency measurements enabled a better determination of the spin Hamiltonian parameters (cf. Table 7.2). In contrast to these findings, only a single  $\text{Fe}^{3+}$  centre was reported as a result of a X-band EPR study in 1996 by Laguta et al. In this work, charge compensation at distant spheres has been assumed [48]. This discrepancy was explained by different techniques for the synthesis of the crystals. A hyperfine structure was also observed at low temperatures. It was assigned to interaction with nearby  $^{207}\text{Pb}$  nuclei.

The spin Hamiltonian parameters reported previously are spread over a wide range. Many attempts to derive structural information about the dopant site made use of the size and sign of the spin Hamiltonian parameters. The existence of  $\text{Fe}^{3+}-\text{V}_{\text{O}}$  defect associates was deduced from the large value of  $b_2^0$ . On the other hand, the large  $b_2^0$  value was explained assigning it to fully coordinated 'free'  $\text{Fe}^{3+}$  centres with off-centre shifts. Therefore a precise determination of the fine structure parameters is of considerable importance. If the reported spin Hamiltonian parameters are taken as input parameters to model the structure of the  $\text{Fe}^{3+}$  centre, different structures result. They range from  $\text{Fe}^{3+}$  centres to  $\text{Fe}^{3+}-\text{V}_{\text{O}}$  defect associates with off-centre shifts towards or away from the oxygen vacancy.

In this study, an unambiguous determination of the tetragonal spin Hamiltonian parameter was performed. In polycrystalline sample, this was possible only by the application of high-frequency EPR. These experiments created the basis for the accurate modelling of the structure (cf. Sec. 8.1) of the  $\text{Fe}^{3+}$  centre.

### 7.3 EPR measurements of $\text{Fe}^{3+}$ centre in $\text{PbTiO}_3$

#### 7.3.1 Low frequency measurements of $\text{Fe}^{3+}:\text{PbTiO}_3$

An X-band (9.315 GHz) EPR spectrum of the  $\text{Fe}^{3+}$  ion in  $\text{PbTiO}_3$  is presented in Fig. 7.3 (ii). It shows one prominent feature at the field of 112.4 mT and a small peak at 334.1 mT. In terms of effective  $g$ -values, the spectrum is described by  $g'_{\parallel} = 2.004(3)$  and  $g'_{\perp} = 5.92(3)$ . Here a typical low-field EPR condition is encountered (cf. Sec. 4.2.2). Only a strong axial spectrum can be detected under these circumstances. As all orientations are statistically realised in a powder, the resonances extend from  $g'_{\parallel}$  to  $g'_{\perp}$ . This is illustrated by simulation in Fig. 7.3 (lower diagram). The probability of  $\mathbf{B}$  in the orientation perpendicular to the  $z$ -axis is the largest. Therefore the resonance peak at  $g'_{\perp}$  is the dominant feature. A linewidth of  $\Delta B_{FWHH} = 4.0(2)$  mT is observed.

At 9 GHz, the axial fine structure parameter of  $\text{Fe}^{3+}$  centres is much larger than the energy of microwave quanta [29, 122]. As a consequence, the Kramers doublets are well separated. Only transitions within each doublet can be observed. It is, however,



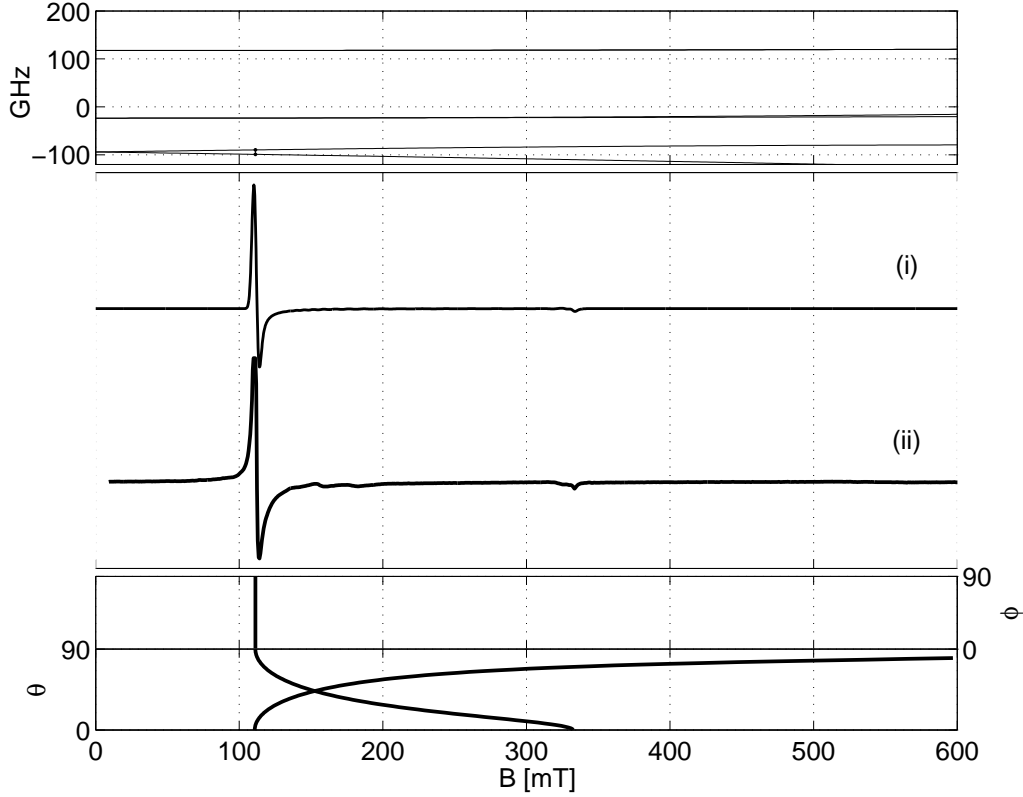


Fig. 7.3: *Centre diagram:* (ii) X-band EPR spectrum of the  $\text{Fe}^{3+}$  impurity center in  $\text{PbTiO}_3$  with the following experimental parameters:  $\nu = 9.315$  GHz,  $T = 10$  K,  $P_{\text{mw}} = 2$  mW,  $B_{\text{mod}} = 0.2$  mT,  $\nu_{\text{mod}} = 100$  kHz,  $t_c = 82$  ms; (i) simulated spectrum with parameters:  $g = 2.0023$ ,  $b_2^0 = 35.3$  GHz,  $\sigma_{\text{lw}} = 7$  mT,  $\sigma_{\text{strain}}(b_2^0) = 1000$  MHz. *Upper diagram:* energy levels of the simulated  $\text{Fe}^{3+}$  ion along the  $x$ -axis with a EPR transition between the two lowest levels. *Lower diagram:* angular dependence of resonances between the two lowest pairs of levels.

necessary that transitions have a high enough transition probability. The spectrum can be described by a separate effective spin Hamiltonian with  $S' = \frac{1}{2}$  for each doublet (4.22). Caused by orientation-dependent states mixing, the corresponding effective  $g'$ -matrices typically exhibit a rather large anisotropy (4.24). If an external field is applied along the axial  $z$ -axis, the quantisation is preserved and  $m_S$  remains a good quantum number. The degeneracy is lifted by proportionally to  $B_0$ . If the magnetic field is perpendicular to the  $z$ -axis, there is no first-order splitting of the  $m_S = \pm \frac{5}{2}$  and  $|\pm \frac{3}{2}\rangle$  states, but the  $|\pm \frac{1}{2}\rangle$  states are split with  $g' \approx 6$ .

Similar EPR conditions are encountered in the Q-band as well. Fig. 7.4 presents a 33.98 GHz spectrum of  $\text{Fe}^{3+}$  ion in  $\text{PbTiO}_3$ . A prominent peak at a field of 429.7(5) mT with small peak at 1212.0(5) mT ( $g \approx 2$ ) can be explained by a strong axial

dependence of the lowest transition. The peaks can be assigned to effective  $g$ -values of  $g'_\perp = 5.646(7)$  and  $g'_\parallel = 2.0020(7)$ . The spectra suggest that the fine structure values are still much larger than the microwave quanta. In contrast to X-band, in the Q-band spectrum also a transition between a second pair of levels is observed (at 1438 mT), although the intensity is much lower. A linewidth at half maximum of  $\Delta B_{\text{FWHH}} = 7.0(5)$  mT is observed.

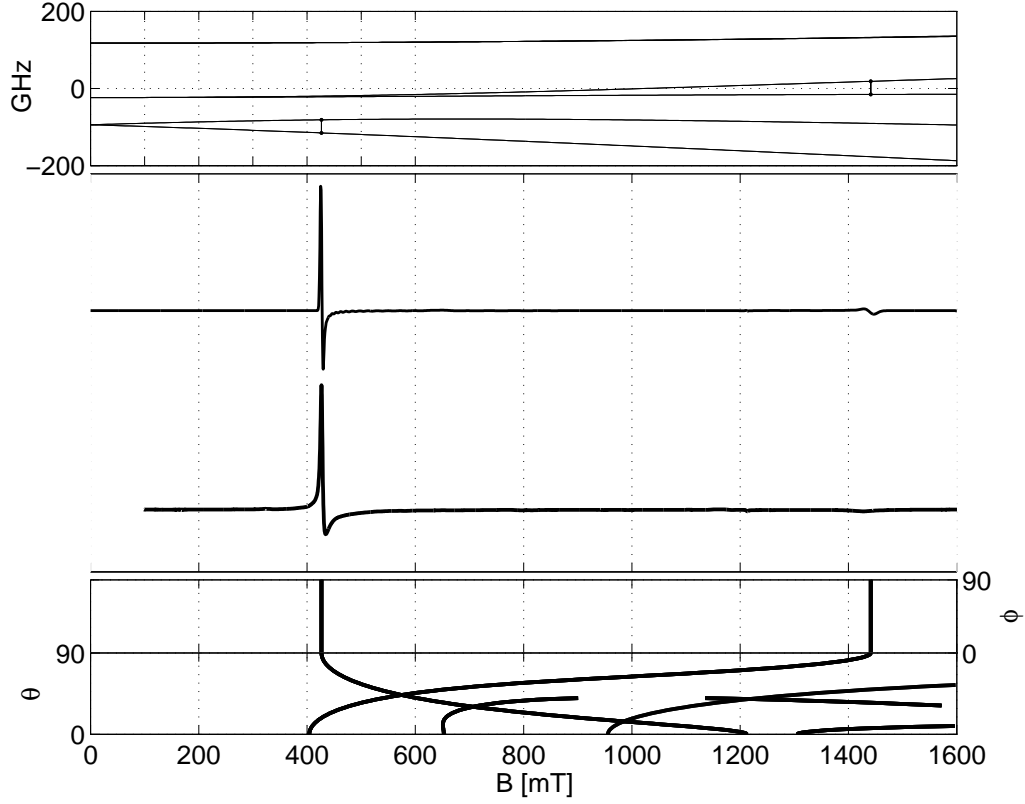


Fig. 7.4: *Centre diagram:* (ii) Q-band EPR spectrum of  $\text{Fe}^{3+}$  impurity centre in  $\text{PbTiO}_3$  with experimental parameters:  $\nu = 33.95$  GHz,  $T = 10$  K,  $P_{\text{mw}} = 1.15$  mW,  $B_{\text{mod}} = 1$  mT,  $\nu_{\text{mod}} = 30$  kHz;  $t_c = 82$  ms; (i) simulated spectrum with parameters:  $g = 2.0023$ ,  $b_2^0 = 35.3$  GHz,  $\sigma_{\text{lw}} = 7$  mT,  $\sigma_{\text{strain}}(b_2^0) = 1000$  MHz.

*Upper diagram:* energy levels of the simulated  $\text{Fe}^{3+}$  ion along the  $x$ -axis with a EPR transition between two lowest levels.

*Lower diagram:* angular dependence of resonances between two lowest pairs of levels

### 7.3.2 W-band measurements of $\text{Fe}^{3+}:\text{PbTiO}_3$

The W-band EPR spectrum (94 GHz), is depicted in Fig. 7.5. The spectrum is taken with the resonator set-up described in Sec. 5.2. It has a well defined polarisation of

the microwave magnetic field component, which is perpendicular to the applied magnetic field. It is a representative example for an intermediate field regime, for which no approximations can be made. The fine structure terms in the spin Hamiltonian are comparable to the electron Zeeman term. Caused by a strong mixing of states,  $m_S$  is not a good quantum number. Resonance may occur between any pair of levels, which have strong orientation dependence. The observed sharp lines, however, can be identified as arising from resonances with minor orientation dependence, see Fig. 7.5 (lower diagram). A linewidth of  $\Delta B_{\text{FWHH}} = 25(5)$  mT is observed.

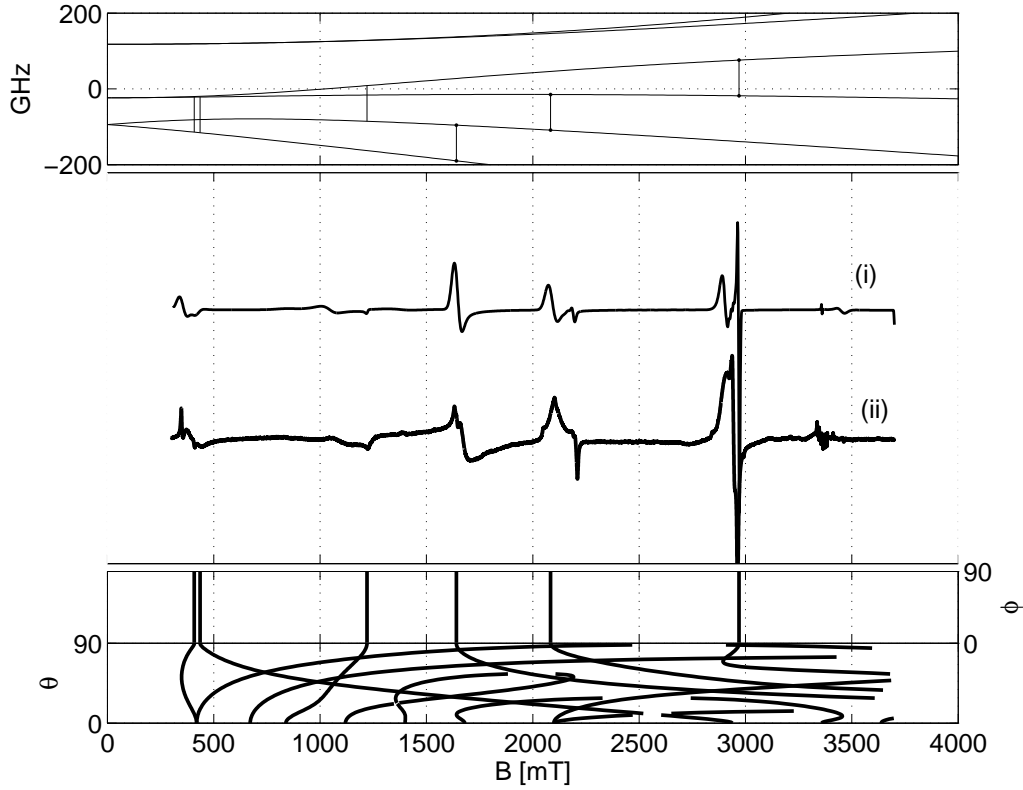


Fig. 7.5: Centre diagram: (ii) W-band EPR spectrum of the  $\text{Fe}^{3+}$  impurity centre in  $\text{PbTiO}_3$  with experimental parameters:  $\nu = 94.11$  GHz,  $T = 10$  K,  $P_{\text{mw}} = 0.005$  mW,  $B_{\text{mod}} = 0.5$  mT,  $\nu_{\text{mod}} = 8$  kHz;  $t_c = 82$  ms; (i) simulated spectrum with parameters:  $g = 2.0023$ ,  $b_2^0 = 35.3$  GHz,  $\sigma_{\text{lw}} = 7$  mT,  $\sigma_{\text{strain}}(b_2^0) = 1000$  MHz (i). Upper diagram: energy levels of the  $\text{Fe}^{3+}$  ion along the  $x$ -axis with allowed EPR transitions.

Lower diagram: angular dependence of all resonances.

Ferroelectric ceramic samples exhibit lossy behaviour in microwave resonator and could not be critically coupled. In this case the quantity of sample should be decreased in order to perform the experiment. Additionally, the experiment could not be carried out with high microwave power because of the baseline problems. Therefore, the W-

band spectrum was also taken with an apparatus without resonator (cf. Sec 5.3), although its sensitivity is generally lower. But in this case there is no limitations for the quantity of sample and more paramagnetic centres can be involved in the resonance. The recorded spectrum, measured at 95.28 GHz, is shown in a Fig. 7.6(ii). When comparing this spectrum to the spectrum in Fig. 7.5(ii), it may be noticed that additional peaks arise. They can be explained by the fact that the direction of the magnetic component of the microwave  $\mathbf{B}_1$  (4.9) is not necessarily perpendicular to the outer magnetic field  $\mathbf{B}$ . This phenomenon is caused by multiple reflections and general imperfections (mode impurity) in the microwave propagation system in a setup without resonator [45]. The transition probability of a resonance is proportional to the scalar product  $\mathbf{B}_1 \cdot \mathbf{S}$  (4.10). Hence it depends directly on the direction of  $\mathbf{B}_1$ . Supposing that all orientations of  $\mathbf{B}_1$  are statistically possible, transitions which are forbidden for the perpendicular mode are induced under these circumstances. In the intermediate EPR condition, the Zeeman and fine structure levels are mixed and  $m_S$  is no good quantum number. In this case the effect of forbidden transitions is substantial.

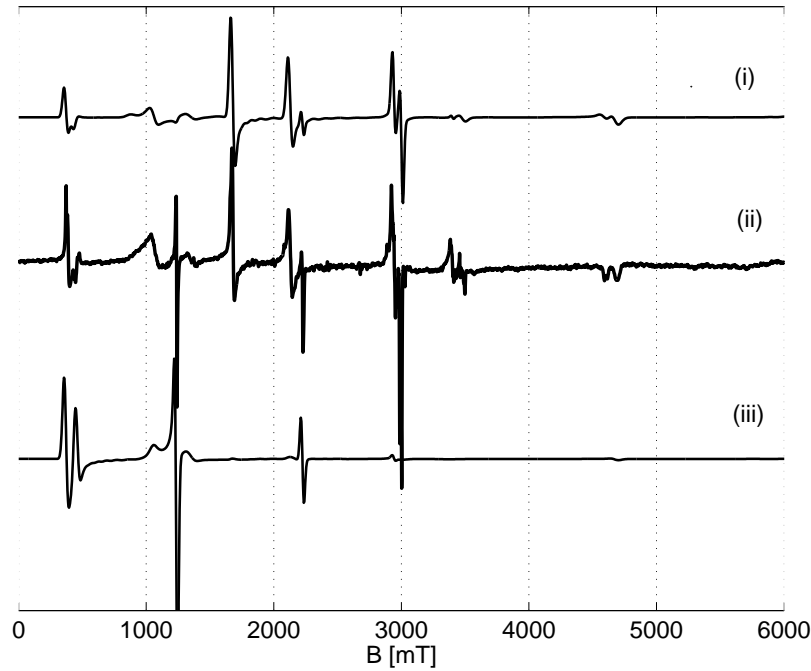


Fig. 7.6: W-band EPR spectrum of the  $\text{Fe}^{3+}$  impurity center in  $\text{PbTiO}_3$ . The experimental parameters are (ii)  $\nu_{\text{mw}} = 95.28$  GHz,  $T = 10$  K,  $P_{\text{mw}} = 0.01$  mW,  $B_{\text{mod}} = 2.0$  mT,  $\nu_{\text{mod}} = 40.33$  kHz. Numerical spectrum simulations involve (i)  $\mathbf{B}_1$  in perpendicular and (iii) parallel mode, with parameters as follows:  $g = 2.002$ ,  $b_2^0 = 35.3$  GHz,  $\sigma_{\text{lw}} = 7$  mT,  $\sigma_{\text{strain}}(b_2^0) = 1000$  MHz

### 7.3.3 High frequency measurements of $\text{Fe}^{3+}:\text{PbTiO}_3$

After considering W-band EPR spectra of the  $\text{Fe}^{3+}$  impurity centre in  $\text{PbTiO}_3$ , it is obvious that the fine structure spin Hamiltonian parameters are still too large to be determined directly from the spectra. Therefore a higher frequency has to be employed to reach high-field conditions. With a high magnetic field (i.e. high frequency) it is assured that the electron Zeeman interactions will be the dominant term in the spin Hamiltonian (cf. Sec. 4.2.1). The quantisation of the lowest atomic levels occurs then nearly parallel to the field direction. As previously mentioned, this condition simplifies the EPR analysis significantly. It also makes possible to determine fine structure parameters of  $\text{Fe}^{3+}$  in polycrystalline  $\text{PbTiO}_3$  by the perturbation theory with some accuracy (cf. 4.19).

The EPR spectrum at 190 GHz is depicted in the Fig. 7.7. It is measured in the vicinity of the high-field regime. Only the left side of the axial symmetric pattern (cf. Fig. 4.1) is observed. The transition between the lowest pair of levels ( $-\frac{5}{2} \leftrightarrow -\frac{3}{2}$ ) is observed at  $B_1 = 4.60$  T, and the transition ( $-\frac{3}{2} \leftrightarrow -\frac{1}{2}$ ) occurs at field  $B_2 = 5.36$  T. The spectrum is centred at  $g = 2.002$  at  $B_0 = 6.78$  T. Because the strong axial dependence of the central, in the present powder spectra it is broadened for  $\Delta B_0 = 1.20$  mT, with peaks at 6.34 mT and 7.54 mT. The next allowed transition is also observed at  $B_3 = 7.73$  T. The linewidth of transitions is  $\Delta B_{\text{FWHH}} = 40(10)$  mT. The field-energy dependence of the signals are quite complicated due to extensive level mixing, resulting in strongly varying resonance fields for most of the transitions. Since the spectrum is recorded without resonator, an additional forbidden transition is observed at  $B_{\text{forb}} = 2.54$  T. That suggests that the high-field regime is not completely achieved.

At low temperatures, the sign of the  $b_2^0$  can be determined from the high field spectrum. This is due to the fact that the transition intensities are a function of the Boltzmann populations of the levels (4.10). At a temperature of 10 K and a microwave frequency of  $\nu = 190$  GHz, the electron Zeeman energies are comparable to the average Boltzmann energy  $k_B T \approx 208$  GHz. Under these conditions, the intensities of particular resonances are strongly temperature dependent. This allows to determine the sign of the splitting parameter  $b_2^0$  (cf. Sec. 7.4.1).

The EPR measurements of  $\text{Fe}^{3+}$  in  $\text{PbTiO}_3$  were taken at an even higher frequency of 319 GHz. The resulting spectra are shown in Fig. 7.8. In these measurements, the field is so high that the Zeeman interaction prevails over the fine structure. Therefore the paramagnetic system is quantised along the  $z$ -axis and  $m_S$  is a good quantum number. Five allowed transitions, according to the selection rules  $\Delta m_S = \pm 1$ , take place between all six levels. A symmetrical pattern centred at pure  $g$ -value is observed:  $B_1 = 9.06$  T,  $B_2 = 10.05$  T are the lower transitions, the upper transition is observed at  $B_3 = 12.44$  T and the highest, fifth line is missing because it is out of the field range. Central transition line is located at  $B_0 = 11.41$  T ( $g \approx 2$ ) and broadened by angular dependence from 11.11 T to 11.86 T by  $\Delta B = 0.75$  T. The spin Hamiltonian parameter may be easily estimated from perturbation theory (cf. 7.4.1).

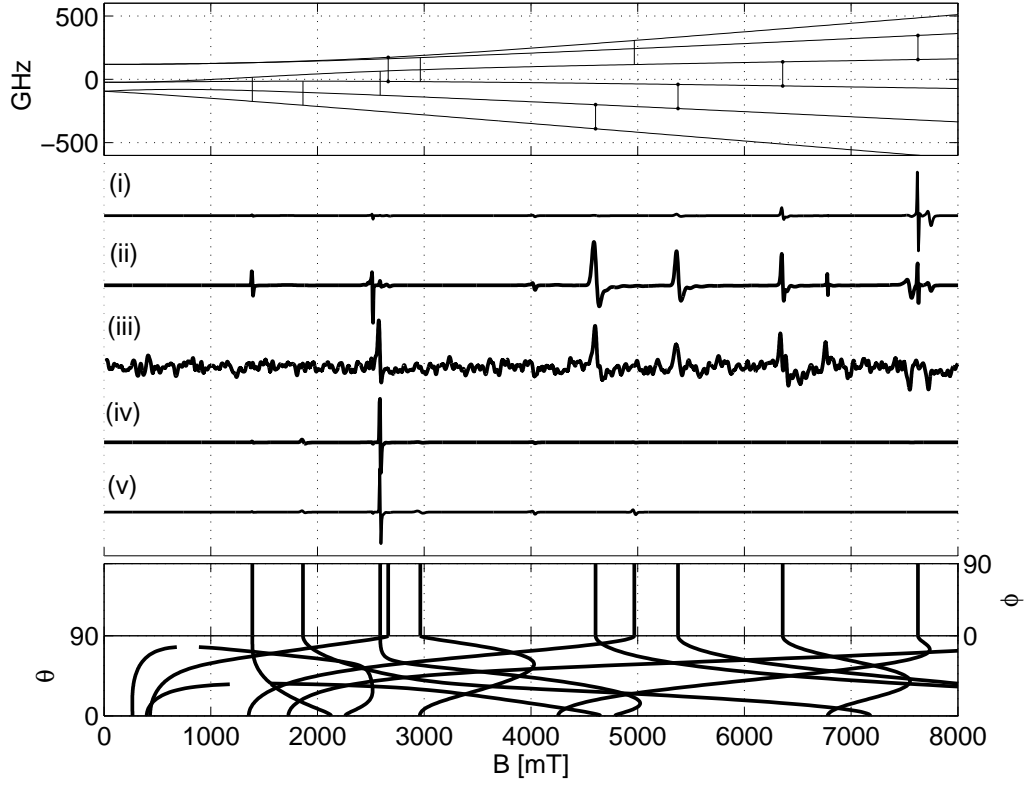


Fig. 7.7: *Centre diagram:* (iii) High field EPR spectrum of the  $\text{Fe}^{3+}$  impurity centre in  $\text{PbTiO}_3$  at  $\nu_{\text{mw}} = 189.96$  GHz and  $T = 10$  K. Other experimental parameters:  $P_{\text{mw}} = 0.01$  mW,  $B_{\text{mod}} = 2.0$  mT,  $\nu_{\text{mod}} = 40.33$  kHz,  $t_c = 300$  ms. Numerical spectrum simulations involve both  $\mathbf{B}_1$  in (i,ii) perpendicular and (iv,v) parallel mode, as well as a positive (ii, v) and negative sign (i,iv) of the axial  $b_2^0$  parameter. Simulation parameters are following:  $g = 2.002(5)$ ,  $b_2^0 = 35.3(2)$  GHz,  $\sigma_{\text{lw}} = 7(2)$  mT,  $\sigma_{\text{strain}}(b_2^0) = 1000(200)$  MHz

*Upper diagram:* Energy levels as function of magnetic field for the canonical parallel orientations relative to the centre principal axes using  $b_2^0 > 0$ .

*Lower diagram:* angular dependence of all resonances.

The linewidth of the transitions amounts to  $\Delta B_{\text{FWHH}} = 70(10)$  mT. A prominent temperature dependence of line intensities is also observed. The Zeeman splitting between the levels (319 GHz) considerably exceeds Boltzmann energy at 5 K (104 GHz). At this temperature, only the transitions between the lowest pair of levels is clearly seen. With increasing temperature, the intensities are increasingly levelled. They approach their theoretical values.

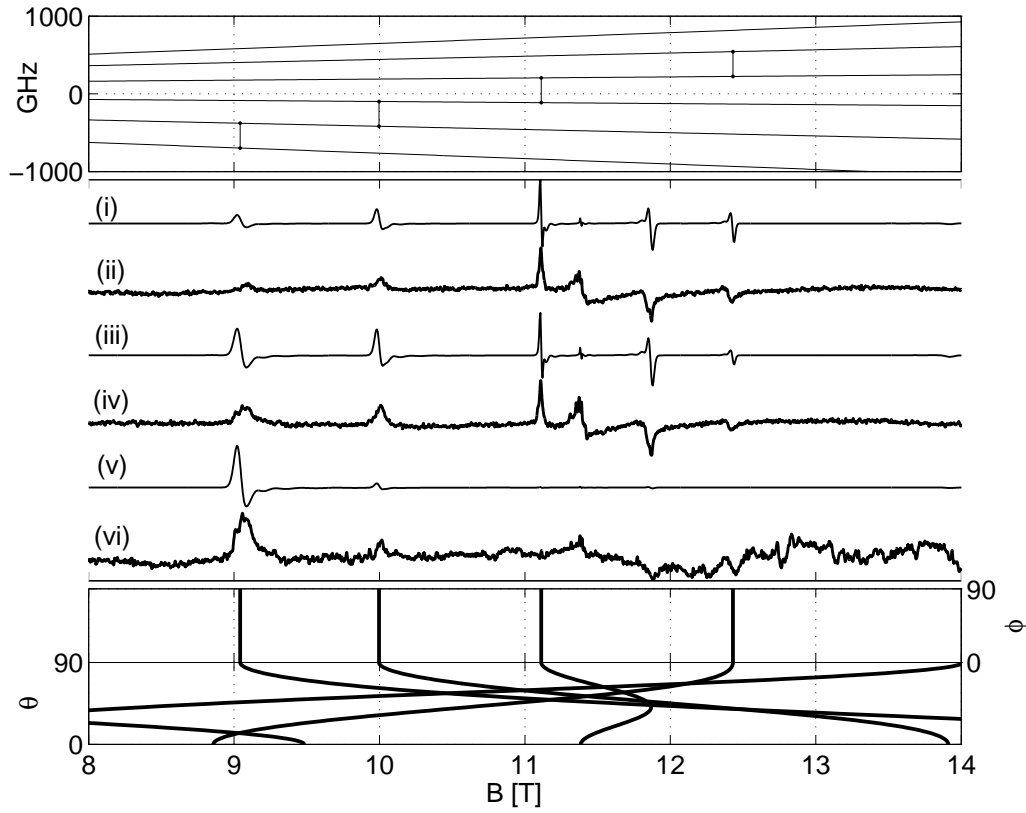


Fig. 7.8: *Centre diagram:* High field EPR spectra of the  $\text{Fe}^{3+}$  impurity centre in  $\text{PbTiO}_3$  at  $\nu_{\text{mw}} = 319.20$  GHz at following temperatures: (ii) 30 K, (iv) 15 K, (vi) 5 K. Other experimental parameters:  $P_{\text{mw}} = 0.01$  mW,  $B_{\text{mod}} = 2.0$  mT,  $\nu_{\text{mod}} = 40.33$  kHz,  $t_c = 300$  ms. The numerical spectrum simulations (i), (iii) and (v) involve a Boltzmann distribution factor and have following parameters:  $g = 2.002$ ,  $b_2^0 = 35.3$  GHz,  $\sigma_{\text{lw}} = 7$  mT,  $\sigma_{\text{strain}}(b_2^0) = 1000$  MHz.

*Upper diagram:* Energy levels as the function of the magnetic field for perpendicular orientations relative to the centre's principal  $z$ -axis ( $\theta = \pi/2$ ,  $\phi = 0$ ).

*Lower diagram:* angular dependence of all resonances.

## 7.4 Determination of the spin Hamiltonian parameters of $\text{Fe}^{3+}:\text{PbTiO}_3$

### 7.4.1 Perturbational analysis of the $\text{Fe}^{3+}:\text{PbTiO}_3$ spectra

The first step in the analysis of the  $\text{Fe}^{3+}:\text{PbTiO}_3$  EPR spectra is to decide whether or not the paramagnetic centre exhibits axial symmetry. That could be determined unambiguously already from the low-field X-band and Q-band measurements. The lowest transition shows typical axial powder pattern (cf. Figs. 7.3 and 7.4). The transition field depends only on the polar angle  $\theta$  in the centre's eigenframe. On the

basis of axial symmetry of the  $\text{Fe}^{3+}$  centre, only the spin Hamiltonian of the form (3.38) has to be considered. From the 2<sup>nd</sup>-order parameters, only  $b_2^0$  is non-zero.

The low-field condition  $b_2^0 \gg h\nu$  (cf. Sec. 4.2.2) is applicable to X- and Q-band frequencies [33]. In this case an estimate of parameter  $b_2^0$  may be obtained from effective  $g'$ -values of the lowest transition at two different frequencies in the framework of a third-order perturbation approach. By inserting the perpendicular  $g'$ -values for the X-band  $B_1 = 112.4(4)$  mT and  $g'_1 = 5.92(3)$  and for the Q-band  $B_2 = 429.7(5)$  mT and  $g'_2 = 5.646(7)$  into formula (4.26), one obtains as estimate for the  $b_2^0$  parameter:

$$|b_2^0| = 37.8(5) \text{ GHz} \quad (7.1)$$

However, one has to keep in mind that this is a rather rough estimate giving only the order of magnitude of the fine splitting parameter.

Another estimate may be given from a measurement at the other extreme frequency of 319 GHz. It is supposed that the high-field approximation holds (4.15). Thus, the axial fine structure parameter can be evaluated via formulae (4.19). The transition fields  $B_{1...5}$  may be taken directly from the spectrum in Fig. 7.8:  $B_1 = 9.05(2)$  T,  $B_2 = 9.98(2)$  T,  $B_3 = 12.43(2)$  T, and the field at  $g = 2.0023$  amounts to  $B_0 = 11.39$  T. These values correspond to the orientation  $(\theta, \phi) = (\pi/2, 0)$ . For this orientation, the formulae (4.19) can be written as

$$\begin{aligned} B_{1,5} &\approx B_0 \mp 2b_2^0 \\ B_{2,4} &\approx B_0 \mp b_2^0 \end{aligned} \quad (7.2)$$

with the 4<sup>th</sup>-order parameters neglected. The  $b_2^0$ -parameter may be estimated from the transition field of  $B_1 = 9.05(2)$  T:

$$b_2^0 \approx 32.8 \text{ GHz}; \quad (7.3)$$

This result confirms the order of magnitude obtained from the low-field approach (7.1). The 190 GHz spectrum (Fig. 7.7) can be analysed with the same method. Although the high-field condition does hold only approximately, the value obtained is:  $b_2^0 \approx 30$  GHz.

The splitting of the 2<sup>nd</sup>-order transitions may also serve as an independent proof of the size of the fine structure parameters. The splitting should amount to  $4\frac{(b_2^0)^2}{B_0}$  in the high-field limit. From the spectra at 190 and 319 GHz, the value the following values  $b_2^0$  may be extracted:

$$\begin{aligned} b_2^0 &\approx 39.9 \text{ GHz} \quad (\nu = 189.89 \text{ GHz}) \\ b_2^0 &\approx 40.6 \text{ GHz} \quad (\nu = 319.20 \text{ GHz}) \end{aligned} \quad (7.4)$$

The discrepancy of the values obtained from the first and second order suggest that the pure high-field limit is still not achieved.



In contrast to the low-field, however, the high-field measurements are necessary for the determination of the sign of the parameter in the powder samples. The ordering of levels in zero field is actually determined by the sign of the fine structure parameter from the perturbation formulae (4.19). In the low field EPR, the populations of the levels are always nearly equal. The average Boltzmann energy ( $\approx kT$ ) is far above the energy of the Zeeman levels. Therefore the ordering of the levels cannot be determined from the symmetrical powder pattern (cf. Fig. 4.1). On the other hand, the levels with energies exceeding the thermal energy become less populated under high field conditions. This strongly influences the transition intensities between those levels. Therefore it is possible to distinguish between transitions occurring between higher levels and between lower levels. Thus one can make unambiguous statement about the ordering of the levels and, hence, about the sign of the fine structure parameters.

The intensities of transitions in the spectra of  $\text{Fe}^{3+}:\text{PbTiO}_3$  exhibit a strongly dependence on temperature. In the 5 K spectrum of Fig. 7.8 (vi) the transition at the lowest field ( $B_1 = 9.05(2)$  T) is the most intensive one. One can conclude that this transition occurs between the lowest pair of levels ( $-\frac{5}{2} \leftrightarrow -\frac{3}{2}$ ). From the perturbational formulae (4.19), this corresponds to a positive sign of  $b_2^0$ .

#### 7.4.2 Numerical simulations of the $\text{Fe}^{3+}:\text{PbTiO}_3$ spectra

The values obtained from the perturbation theory were used as starting point for numerical simulations. The values varied are: the fine structure parameter  $b_2^0$ , real isotropic  $g$ -value, isotropic linewidth  $\sigma_{\text{lw}}$  and distribution (strain) of  $b_2^0$ :  $\sigma_{\text{strain}}$ . The numerical spectrum simulations for all frequencies lead to a unique set of results. Using these best-fit values, numerically simulated spectra are superimposed to the experimental data and show excellent agreement. The simulated spectra are shown in Figs. 7.3 (i); 7.4 (i); 7.5 (i); 7.6 (i) and (iii); 7.7 (ii) and (iv); and 7.8 (i), (iii) and (v). All simulated spectra are obtained with the same set of values, and these are:

$$\begin{aligned} g &= 2.002(5); & b_2^0 &= 35.3(2) \text{ GHz} \\ \sigma_{\text{lw}} &= 7(2) \text{ mT}; & \sigma_{\text{strain}}(b_2^0) &= 1.0(2) \text{ GHz} \end{aligned} \quad (7.5)$$

The spectra can be fully explained without invoking the 4<sup>th</sup>-order spin Hamiltonian terms. It has been proven also that they have no significant influence on the resulting axial spectrum within the following intervals:

$$|b_4^0| < 300 \text{ MHz}; \quad |b_4^4| < 2000 \text{ MHz} \quad (7.6)$$

Under the high-field conditions, the cubic term  $b_4^0$  would produce small shifts of the outer peaks, which were not observed. Term  $b_4^4$  would give rise to an additional splitting of the outer peaks. Because of a linewidth of 40 mT (319 GHz), no such splitting could be observed. Such small values of the 4<sup>th</sup>-order parameters which are

not accessible are in agreement with previous measurements on single crystals (cf. Tab. 7.2, [52]).

A satisfactory reproduction of the spectra recorded at all microwave frequencies was possible only with a statistical Gaussian distribution  $\sigma(b_2^0)$  (strain) of parameters. The variance  $\sigma(b_2^0) = 1.0(2)$  GHz of the fine structure parameter  $b_2^0$  explains a strong variation of the linewidths between low-frequency ( $\Delta B_{FWHH} \approx 10$  mT) and high-frequency ( $\Delta B_{FWHH} \approx 70$  mT) conditions. Thus the final linewidths of spectra are superpositions of the isotropic linewidth of 7(2) mT and the  $b_2^0$ -distribution of 1.0(2) GHz.

In the case of the 95 and 190 GHz spectra taken without resonator (Figs. 7.6 and 7.7), two simulation procedures were performed. This was necessary as a result of the statistically distributed microwave modes in such experiments. It had to be assumed that the sample was separately exposed to an oscillating radiation with its magnetic field component  $\mathbf{B}_1$  is both parallel and perpendicular to  $\mathbf{B}$ . The simulations with the perpendicular mode are shown in Figs. 7.6 (i) and 7.7 (ii). They explain all  $\Delta m_S = \pm 1$  transitions. The transition probabilities for these allowed transitions are the largest when  $\mathbf{B}_1$  is perpendicular to  $\mathbf{B}$  and hence to  $\mathbf{S}$  (cf. Eq. 4.10). Simulations with the parallel mode are shown in Figs. 7.6 (iii) and 7.7 (iv). Here the allowed transition probability drops to zero, but the probability for the forbidden transitions  $\Delta m_S = \pm 2$  are largest. These simulation explains additional peaks observed in the 95 GHz and 190 GHz spectra.

In order to demonstrate the effect of thermal population in high-field measurements, the results for simulations assuming a positive sign of  $b_2^0$  (Figs. 7.7 (ii), (iv)) and a negative sign of  $b_2^0$  (Figs. 7.7 (i),(v)) are shown. The resonance at 4.61 T in the calculated spectrum occurs only for  $b_2^0 > 0$ . This can be considered as a proof that the parameter  $b_2^0$  is positive. The disappearance of the signal for  $b_2 < 0$  can be explained by taking into account the calculated energy level diagrams in Fig. 7.7 (upper diagram), where the particular line corresponds to the transition connecting states of lowest energy. If the sign of  $b_2^0$  would be reversed, this level would be highest in energy and hence this transition has to be activated thermally and should be detectable at elevated temperatures only.

The large fine structure interaction in polycrystalline samples at high fields can be determined accurately via first-order effects rather than by second-order shifts at low fields. Furthermore, the distribution  $\delta(b_2^0)$  of the fine structure parameter is observable as first-order variation of the line positions. In X-band, this effect is of second-order only and thus almost negligible. Hence no information about the  $b_2^0$  distribution can be extracted. In contrast to this behaviour, 4<sup>th</sup>-order fine structure parameters were not accessible by numerical spectrum simulations up to a microwave frequency of 319 GHz. Therefore, to determine 4<sup>th</sup>-order parameters the orientation-dependent single-crystal studies are more appropriate.[79, 52, 48]

## 8. LEAD TITANATE: STRUCTURAL CALCULATIONS

### 8.1 The NSM analysis of $\text{Fe}^{3+}$ in $\text{PbTiO}_3$

The accurately determined fine structure parameter  $b_2^0$  of the  $\text{Fe}^{3+}$  centre in  $\text{PbTiO}_3$  (cf. Chapter 7) is used as a basis for structure analysis via Newman superposition model (cf. Chapter 6). The results obtained from the semi-empirical NSM approach are also compared with results from modelling the same centre via DFT calculations [63]. Therefore a sound basis is provided for the analysis of structural relaxation at the impurity site. As a result, a refined structural model of the iron defect centre in lead titanate is presented.

The fine structure parameter  $b_2^0$  was calculated for different possible structural arrangements. These calculated values are compared with experimental data. The measured  $b_2^0$  value amounts to 33.3(2) GHz (cf. 7.5). The interception points between the calculated  $b_2^0$  parameter and the experimental value is used for a prediction of the realised local structure.

The reference parameters  $t_2$  and  $\bar{b}_2(R_0)$  for the NSM calculation have not yet been determined for iron centres in lead titanate. Therefore, they are taken from crystals having equivalent  $\text{Fe}^{3+}-\text{O}^{2-}$  bonds in octahedral coordination (cf. Table 6.1). The parameters of  $\text{Fe}^{3+}$  in  $\text{MgO}$  at the site with octahedral oxygen coordination are taken:  $\bar{b}_2 = -12.3514$  GHz,  $t_2 = 8$ ,  $R_0 = 210.1$  pm cf. Table 6.1 [98]. The parameters of  $\text{Fe}^{3+}$  in  $\text{CaO}$  were used as an independent proof of calculations and to evaluate errors.

Important input data for the NSM analysis are the crystallographic positions of the  $\text{Fe}^{3+}$  ion and the ligands. These positions were taken: (i) from the diffraction data at 12 K, and (ii) from the *ab initio* DFT calculations (cf. Table 7.1).

It can be concluded from the axial symmetry of the spin Hamiltonian that the orientation of the paramagnetic defect is along the crystallographic  $c$ -axis. That means that: (i) the oxygen octahedron around  $\text{Fe}^{3+}$  is fully preserved retaining crystallographic axial symmetry, or (ii) the oxygen octahedron has one of the apical oxygen atoms O1 or O1' missing. Any other orientation of  $\text{Fe}^{3+}-\text{V}_{\text{O}}$  defect complex either along the  $a$ - or  $b$ -axis would reduce the symmetry of the fine structure tensor to lower symmetry. This case was not observed within spectral resolution. Because the site symmetry defines the direction of the paramagnetic centre axes, the principal spin Hamiltonian  $z$ -axis of the  $\text{Fe}^{3+}$  centre was chosen along the crystal  $c$ -axis. Consequently, degrees of freedom of the  $\text{Fe}^{3+}$  centre are restricted to movements along this axis.

The calculation of  $b_2^0$  was performed as described in Sec. 6.2. The oxygen vacancy

is located either on the O1 position (0.5000 0.5000 0.1239) or on the O1' position (0.5000 0.5000 1.1239) (cf. Table 7.1). The reference position of iron is at the Ti position (0.5000 0.5000 0.5415). For the calculation of  $b_2^0$ , the position of  $\text{Fe}^{3+}$  was varied along the  $c$ -axis. The parameter  $d$  defines the shift of the ion from the starting position. A positive sign of  $d$  defines a shift towards O1'. Therefore  $d$  may be defined with the fractional coordinate  $z$  of the iron position:

$$d = z \times 416.8 \text{ [pm]} \quad (8.1)$$

The following models have been considered:

(a) *Substitution of  $\text{Fe}^{3+}$  at the A-site and B-site.* It was suggested earlier that  $\text{Fe}^{3+}$  substitutes for  $\text{Ti}^{4+}$  at the B-site in the  $\text{ABO}_3$  perovskite structure. However, this assumption is only based on the considerations using atomic radii (cf. Sec. 2.3.2). In order to verify this hypothesis, the possibility of a  $\text{Fe}^{3+}$  substitution at the A-site for  $\text{Pb}^{2+}$  has also been considered. The result of a substitution at the A-site is shown in Fig. 8.1(a) and at the B-site is shown in Fig. 8.1(b,c)).

(b) *Substitution of  $\text{Fe}^{3+}$  at the B-site with and without oxygen vacancy.* It has to be decided, whether the oxygen vacancy is found in the first or more distant coordination sphere. Thus two more structure models were investigated: with and without oxygen vacancy in the nearest neighbour positions. The model with vacancy in the nearest neighbour position is depicted in Fig. 8.1 with dashed-dotted lines. The model without vacancy is depicted with dashed lines.

(c) *Substitution of  $\text{Fe}^{3+}$  at the B-site: crystallographic and theoretical (DFT) atomic positions.* In order to investigate the influence of a change of the local structure around the defect, the *ab initio* calculated atomic positions were taken as the input data (cf. Table 7.1). The results of this model are shown Figs. 8.1(b, c) with full lines.

(d) *Substitution of  $\text{Fe}^{3+}$  at the B-site with vacancies at O1 and O1'.* Since two axial positions for the oxygen vacancy are possible, both cases have to be considered and compared. Fig. 8.1(b) (i.e. 8.1(c)) shows the result with an oxygen vacancy placed at the O1 (i.e. O1').

The results of all NSM calculations are shown in Fig. 8.1. The experimentally obtained value for  $b_2^0$  is represented by a solid horizontal line. The positions of the oxygen ions replaced by the vacancies  $\text{V}_{\text{O1}}$  and  $\text{V}_{\text{O1'}}$  are indicated by arrows. The  $z$ -coordinate of the equatorial plane of O2 and O3 positions is indicated. Additionally, theoretically obtained positions for the  $\text{Fe}^{3+}$  are indicated by arrows above the pictures.

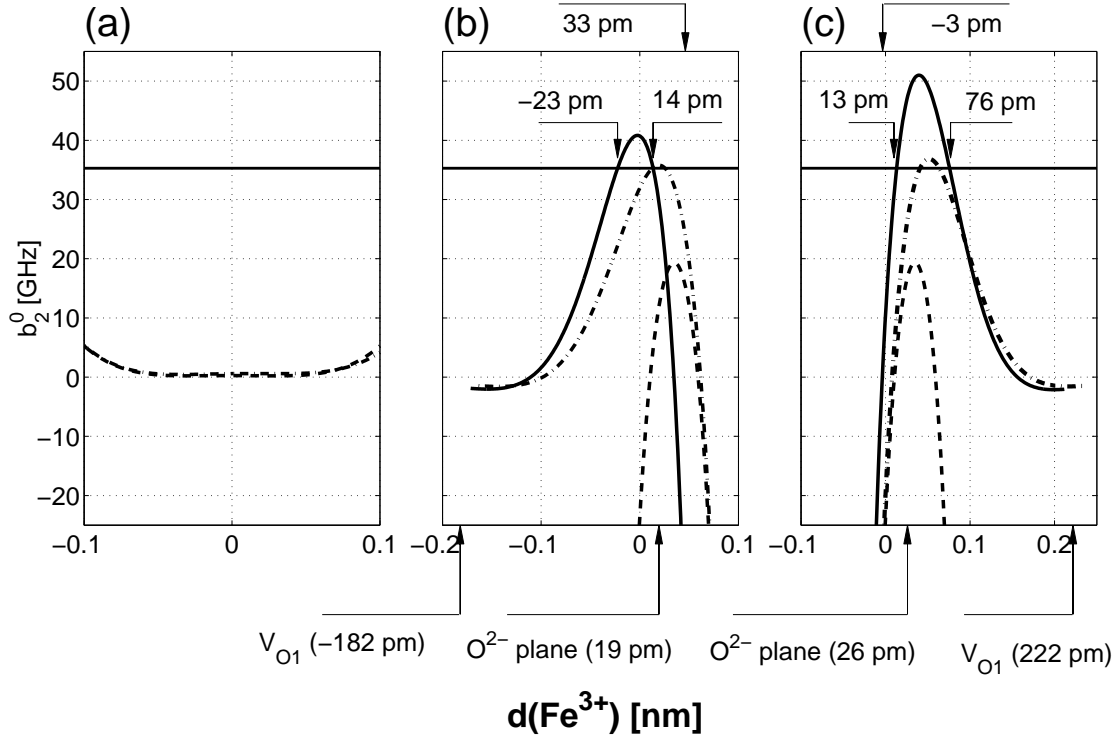


Fig. 8.1: Comparison of the experimentally obtained axial fine structure parameter  $b_2^0 = 35.3(2)$  GHz (solid horizontal line) for the  $\text{Fe}^{3+}$  centre in  $\text{PbTiO}_3$  with the NSM calculated values for  $b_2^0$ , as a function of the displacement  $d$  from the original  $\text{Ti}^{4+}$  position.

- (a) - substitution of the  $\text{Fe}^{3+}$  ion at the A-site
- (b) - substitution of the  $\text{Fe}^{3+}$  ion at the B-site with oxygen vacancy at O1
- (c) - substitution of the  $\text{Fe}^{3+}$  ion at the B-site with oxygen vacancy at O1'

*dashed lines:* models for the 'free iron', i.e. without an oxygen vacancy in the nearest neighbour shell

*dash-dotted lines:* models with an oxygen vacancy in the nearest neighbour position (i.e. iron-oxygen vacancy complex) in the case of crystallographic oxygen position

*solid lines:* models with an oxygen vacancy in the nearest neighbour position (i.e. iron-oxygen vacancy complex) in case of calculated oxygen position

The positions of the oxygen vacancies, of the centre of the oxygen octahedra as well as the DFT-calculated shifts of the  $\text{Fe}^{3+}$  ion are indicated by arrows.

The following conclusions can be derived from the NSM calculations:

(a) The model with substitution of  $\text{Fe}^{3+}$  at the A-site can clearly be discarded. As indicated in Fig. 8.1(a), such a situation would lead to very small values of the  $b_2^0$  parameters. The observed difference between calculated and experimental values thus confirms the assumption from a consideration of atomic radii. *The  $\text{Fe}^{3+}$  impurity always substitutes for  $\text{Ti}^{4+}$  in  $\text{PbTiO}_3$ .*

(b) When comparing models with and without directly attached oxygen vacancy, the calculated results show that only the model with an oxygen vacancy in first coordination is consistent with the experimental value. The model without oxygen vacancy, i.e. with a complete oxygen octahedron around the dopant site, would yield a value  $b_2^0$  of max. 20 GHz. *Therefore, the  $\text{Fe}^{3+}$  defect in  $\text{PbTiO}_3$  always creates an oxygen vacancy in the nearest oxygen octahedron.* Thus, this defect can be considered as a bonded defect associate. It is denoted as  $\text{Fe}^{3+}\text{-V}_\text{O}''$ .

(c) Models with both crystallographic and DFT-derived atomic positions are in agreement with the experimental value. The model with theoretically computed atomic positions, however, yields two well separated intersections with the experimental value. Therefore, it allows two possible positions of  $\text{Fe}^{3+}$  ion. The model with crystallographic structure also yields two intersections. In this case they lie near to each other 8.1(b,c). There is no possibility to decide between those values on the basis of the NSM.

(d) Comparing models with the vacancy at the O1 and O1' oxygen sites give a similar agreement with experimental data. Both models show two different possible positions. Therefore, no distinction can be made based on the NSM.

Tab. 8.1: Predictions of the shifts of the  $\text{Fe}^{3+}$  ion as calculated by the NSM with crystallographic atomic coordinates, by the NSM with calculated coordinates and by exclusively DFT calculations. The shifts  $d_1$  and  $d_2$  are defined relative to the original Ti position.  $z(\text{V}_\text{O})$  is the distance of replaced oxygen, and  $z(\text{O2}, \text{O3})$  is the distance of the 4 planar oxygens.

		$d(\text{V}_\text{O})$	$d(\text{O2}, \text{O3})$	$d_1$	$d_2$
$\text{V}_{\text{O1}}$	NSM, crystal coordinates	-182	+19	+13(5)	+30(5)
	NSM, relaxed coordinates			-23(7)	+14(7)
	DFT			-	+33
$\text{V}_{\text{O1}'}$	NSM, crystal coordinates	+222	+26	+42(5)	+63(5)
	NSM, relaxed coordinates			+13(7)	+76(7)
	DFT			-3	-

The results obtained from the models which lead to the intersection with the experimental value are summarised in Table 8.1. The inclusion of calculated relaxed

positions of the rest of octahedron yields substantially refined  $b_2^0$ -curves. The intersections of the curves with the experimental value yield two distinct positions for the  $\text{Fe}^{3+}$  atom. In the pure, unsubstituted crystal, the  $\text{Ti}^{4+}$  ion is displaced considerably from the centre of the oxygen octahedron. For the  $\text{Fe}^{3+}$  ion which replaces  $\text{Ti}^{4+}$ , there are two predicted positions for the  $\text{Fe}_{\text{Ti}}^{3+}$  ion with an adjacent oxygen vacancy for each of the two models:

(i) With the vacancy at O1 (located at  $d(V_O) = -182$  pm), and with a starting position of substituted  $\text{Ti}^{3+}$  at  $d = 0$ , the  $\text{Fe}^{3+}$  impurity is: either (i.1) displaced by  $d_1 = -23(5)$  pm towards the vacancy, or (i.2) displaced by  $d_2 = +14(5)$  pm away from the vacancy towards the centre of the truncated octahedron. The four planar oxygens are located at  $d(\text{O}2, \text{O}3) = 19$  pm.

(ii) With the vacancy at O1' position (located at  $d(V'_O) = -222$  pm), the  $\text{Fe}^{3+}$  ion is: either (ii.1) shifted towards the vacancy for  $d_1 = +13(5)$  pm; or (ii.2) also shifted towards the vacancy for  $d_2 = +76(5)$  pm. The four planar oxygens are located at  $d(\text{O}2, \text{O}3) = 26$  pm.

A decision between the both coordination schemes cannot be made on the basis of the NSM calculation. Further information provided by the DFT calculation is needed.

## 8.2 DFT analysis of $\text{Fe}^{3+}:\text{PbTiO}_3$

### 8.2.1 DFT analysis of undoped $\text{PbTiO}_3$

First, the iron-free host lattice of  $\text{PbTiO}_3$  was studied. DFT calculations on  $\text{PbTiO}_3$  were performed by Sonja Laubach, Stefan Laubach and Peters C. Schmidt at the *Eduard-Zintl Institute of Inorganic and Physical Chemistry, Darmstadt University of Technology*, as a part of the *Research Collaboration Project 595 of German Science Foundation*. These results are published in [63], and here a short compilation of their results is given. Using the *Vienna Ab Initio Software Package* computer programme, lattice parameters  $a = 386.6$  pm and  $c = 403.9$  pm were obtained, which are in agreement with earlier calculations [64]. The percentage difference between the experimental and calculated numbers are different. Calculated ratio  $c/a = 1.04$  is smaller compared to the experimental value of  $c/a = 1.07$ . The calculated Ti–O bonds are given in Fig. 8.2(a).

Next, one oxygen vacancy was inserted in a  $2 \times 2 \times 2$  supercell without providing charge compensation. In other words, the electronic structure of  $\text{Pb}_8\text{Ti}_8\text{O}_{23}$  was studied to determine the local relaxation of the ions around the vacancy. One finds that both neighbouring Ti ions move away from the vacancy site. If the vacancy is located at the O1 site (cf. Fig. 7.1), Ti moves towards O1'. The Ti ion closest to the vacancy in positive  $c$ -direction is displaced by  $d = +25.4$  pm from its original position. The nearest Ti ion on the opposite side of the vacancy is displaced by  $d = -3.9$  pm. If the vacancy is located at the equatorial O2 site, Ti moves towards the O2' site and the Ti–O2' bond distance decreases from 195.3 pm to 187.6 pm.

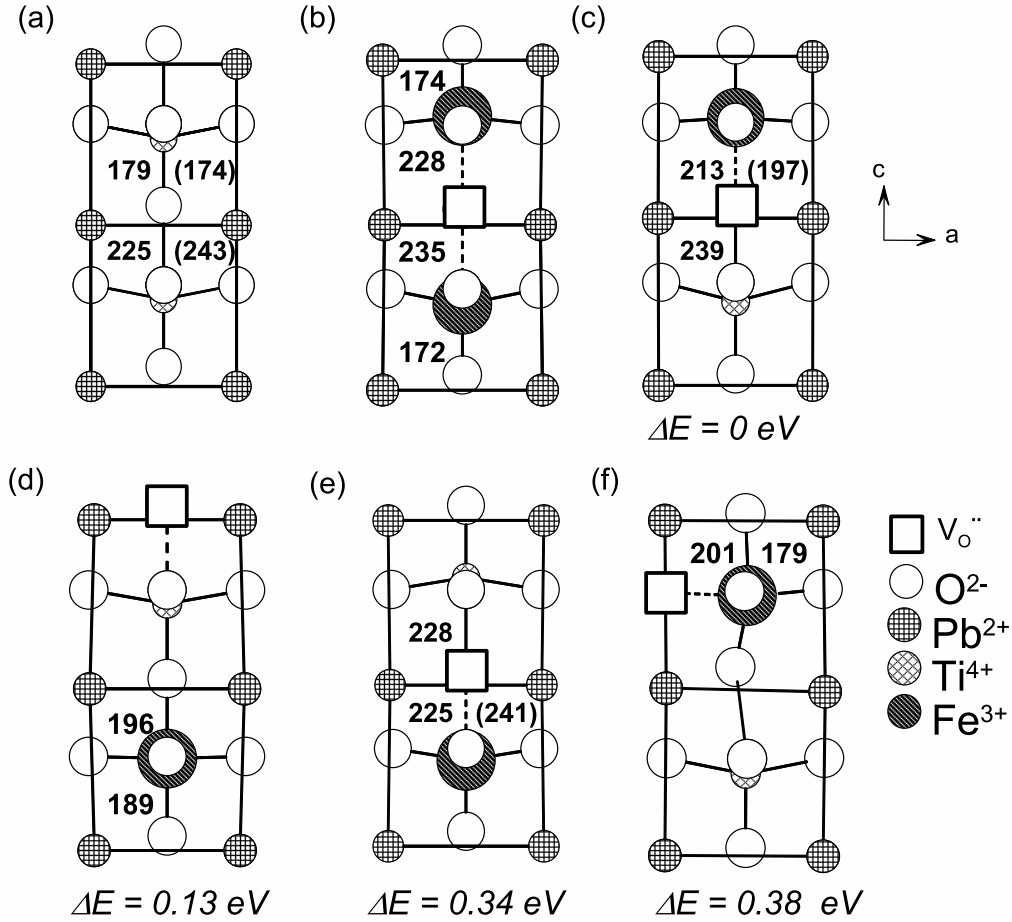


Fig. 8.2: Comparison between different structure models for  $\text{Fe}^{3+}:\text{PbTiO}_3$  deduced from the theoretical and experimental investigations. The given numbers indicate interatomic distances (in pm) calculated by DFT. The values in brackets are experimentally and semi-empirically obtained numbers. The relative energies are shown below the figures.

(a) undoped reference structure obtained from DFT calculations and from synchrotron powder diffraction (cf. Table 7.1);

(b)  $\text{Fe}^{3+}-V_{\text{O}}-\text{Fe}^{3+}$  complex in  $\text{Pb}_8\text{Ti}_6\text{Fe}_2\text{O}_{23}$  oriented along the  $c$ -axis (A.1);

(c)  $\text{Fe}^{3+}-V_{\text{O}}$  defect associate in  $\text{Pb}_8\text{Ti}_7\text{FeO}_{23}^+$  oriented along  $c$ -axis where the O1 oxygen is missing (C.1). The values in brackets are obtained with NSM on the basis of measured fine structure data. This model is the energetically most favourable in the series of the models with one oxygen vacancy.

(d)  $\text{Fe}^{3+}$  and  $V_{\text{O}}$  as isolated defects in  $\text{Pb}_8\text{Ti}_7\text{FeO}_{23}^+$  (C.3);

(e)  $\text{Fe}^{3+}-V_{\text{O}}$  defect associate in  $\text{Pb}_8\text{Ti}_7\text{FeO}_{23}^+$  oriented along  $c$ -axis where the oxygen O1' is missing (C.2);

(f)  $\text{Fe}^{3+}-V_{\text{O}}$  defect associate in  $\text{Pb}_8\text{Ti}_7\text{Fe}_2\text{O}_{23}^+$  oriented along  $a$ -axis where the oxygen O2 is missing (C.4);

Models (B.1-B.4), which consider defects in charged  $\text{Pb}_8\text{Ti}_7\text{Fe}_2\text{O}_{23}$ , show the same energetic sequence.



8.2.2 DFT analysis of  $\text{Fe}^{3+}$ -doped  $\text{PbTiO}_3$ 

The study of the system  $\text{Fe}^{3+}:\text{PbTiO}_3$  has been performed using a  $2 \times 2 \times 2$  super-cell. Now Ti is partly replaced by Fe. Different ion arrangements for the defect structures were studied:

(A) Two  $\text{Ti}^{4+}$  ions were replaced by  $\text{Fe}^{3+}$  ( $\text{Fe}'_{\text{Ti}}$ ). For charge compensation, one oxygen vacancy ( $\text{V}_{\text{O}}^{\bullet\bullet}$ ) was created. The supercell has the composition  $\text{Pb}_8\text{Ti}_6\text{Fe}_2\text{O}_{23}$ . This arrangement is depicted in Fig. 8.2(b)

- (A.1) Two  $\text{Fe}^{3+}$  defects are next-nearest-neighbours and the  $\text{V}_{\text{O}}^{\bullet\bullet}$  is located between these two  $\text{Fe}^{3+}$  atoms. In such a way a clustered defect is formed which is oriented in the  $c$  direction.
- (A.2) Similar as in (A.1), but it is assumed that one of the  $\text{Fe}^{3+}$  is an isolated defect, without near-by vacancy.
- (A.3) Similar as in (A.1), but all three defects are isolated, cf. 8.2(d).
- (A.4),(A.5),(A.6) Similar to models (A.1) to (A.3), but the oxygen vacancy is located in the  $a$  (or  $b$ ) direction (i.e., at O2 or O3).

(B) Analogously to (A), but only one  $\text{Ti}^{4+}$  was replaced by  $\text{Fe}^{3+}$ . The neutral defect  $\text{Pb}_8\text{Ti}_7\text{FeO}_{23}$  was considered.

- (B.1) Vacancy site is at O1 along the  $z$ -axis, cf. Fig. 8.2(c).
- (B.2) Vacancy site is at O1' along the  $z$ -axis, cf. Fig. 8.2(e).
- (B.3) Vacancy and  $\text{Fe}^{3+}$  are isolated point defects, cf. Fig. 8.2(d).
- (B.4) Vacancy site is at O2 (or O3), along the the  $a$ -axis (or  $b$ -axis), cf. Fig. 8.2(f).

(C) Analogously to (B), only one  $\text{Ti}^{4+}$  was replaced by  $\text{Fe}^{3+}$ . The charged defect  $\text{Pb}_8\text{Ti}_7\text{FeO}_{23}^+$  was considered. Charge compensation was established by assuming a homogeneously charged background.

- (C.1) Vacancy site is at O1 along the  $z$ -axis, cf. Fig. 8.2(c).
- (C.2) Vacancy site is at O1' along the  $z$ -axis, cf. Fig. 8.2(e).
- (C.3) Vacancy and  $\text{Fe}^{3+}$  are isolated point defects, cf. Fig. 8.2(d).
- (C.4) Vacancy site is at O2 (or O3), along the the  $a$ -axis (or  $b$ -axis), cf. Fig. 8.2(f).

For all these models an optimisation of the structure was carried out. The atomic positions were varied, but the lattice constants  $a$  and  $c$  were kept fixed to the values of the pure host lattice (cf. Table 7.1). The total energy of the optimised structures is used to estimate structural preferences.

An oxygen vacancy in the  $c$ -direction is energetically favoured in comparison to an orientation along  $a$ . This preference is valid for all three model series (A) to (C). For models of series A, the defect associate  $\text{Fe}^{3+} - \text{V}_{\text{O}}^{\bullet\bullet} - \text{Fe}^{3+}$  along the  $c$  orientation of (A.1) gives the lowest energy  $E_{\text{A1}}$  followed by model (A.2) with energy  $E_{\text{A2}}$  where  $\text{Fe}^{3+} - \text{V}_{\text{O}}^{\bullet\bullet}$  is placed along the  $c$  direction. The energy difference  $E_{\text{A2}} - E_{\text{A1}}$  amounted to 0.59 eV per supercell.

For models (B.1) and (C.1), with one  $\text{Fe}^{3+}$  defect, the orientation of the  $\text{Fe}^{3+} - \text{V}_{\text{O}}^{\bullet\bullet}$  associate along the  $c$ -axis is preferred over the orientation along the  $a$ -axis. More precisely, the most stable arrangement is the arrangement in which O1 and not O1' is missing. The models (B.1) and (C.1) are lower in energy than (B.2) and (C.2):  $E_{\text{B2}} - E_{\text{B1}} = 0.35$  eV and  $E_{\text{C2}} - E_{\text{C1}} = 0.34$  eV. The arrangements (A.4) and (C.4) with an orientation of the  $\text{Fe}_{\text{Ti}}' - \text{V}_{\text{O}}^{\bullet\bullet}$  dipole along the  $a$ -axis are less stable by  $E_{\text{B4}} - E_{\text{B1}} = 0.45$  eV and  $E_{\text{C4}} - E_{\text{C1}} = 0.38$  eV than the optimum arrangement within this model series. The defect associate  $\text{Fe}^{3+} - \text{V}_{\text{O}}^{\bullet\bullet}$  is favoured compared to the isolated defects by  $E_{\text{B1}} - E_{\text{B2}} = 0.27$  eV and  $E_{\text{C3}} - E_{\text{C1}} = 0.13$  eV.

Next, the shifts of the ions around the vacancy are described. Qualitatively, the cation nearest to the vacancy moves away from the vacancy site. This results in a shortening of the defect-oxygen bond opposite to the vacancy.

The undoped structure (Fig. 8.2 (a)) and the defect structures (Figs. 8.2 (b)-(f)) are compared next.

The displacement of the  $\text{Fe}^{3+}$  ion from the original  $\text{Ti}^{4+}$  position in the undoped host lattice is represented by the distance parameter  $d$ . It amounts to  $d_{\text{A1}}^1 = +46.6$  pm and  $d_{\text{A1}}^2 = -11.6$  pm for the two  $\text{Fe}^{3+}$  atoms in model A.1. For the structures with only one  $\text{Fe}^{3+}$  defect, the following values were calculated:  $d_{\text{A2}} = +32.9$  pm,  $d_{\text{B1}} = +31.2$  pm,  $d_{\text{B2}} = -3.0$  pm,  $d_{\text{C1}} = +33.5$  and  $d_{\text{C2}} = -6.8$  pm.

All calculations were repeated with the fixed lattice ratio,  $c/a = (c/a)_{\text{exp}} = 1.0721$ . From these additional calculations the same conclusions as described above emerge. The associate  $\text{Fe}^{3+} - \text{V}_{\text{O}}^{\bullet\bullet}$  in the  $c$  direction has the lowest energy. Compared to the original Ti and O positions, the  $\text{Fe}^{3+}$  is moving away from the vacancy  $\text{V}_{\text{O}}^{\bullet\bullet}$ .

### 8.3 Discussion of the structure of $\text{Fe}^{3+}:\text{PbTiO}_3$

First important conclusion of the NSM calculations is as follows. The  $\text{Fe}^{3+}$  paramagnetic centre in lead titanate forms a charged  $\text{Fe}^{3+} - \text{V}_{\text{O}}^{\bullet\bullet}$  defect associate with an oxygen vacancy in the surrounding oxygen octahedron. The  $\text{Fe}^{3+}$  ion is found at the B-site of the perovskite  $\text{ABO}_3$  lattice. The similar ionic radii of  $\text{Ti}^{4+}$  (68 pm) and  $\text{Fe}^{3+}$  (64 pm) in comparison to 124 pm of  $\text{Pb}^{2+}$  supports this assignment. DFT simulations also show that the association of the defects is preferred over the arrangement as

isolated point defects. Therefore, these conclusions obtained from experiment and DFT coincide.

Second conclusion of the EPR analysis is that the  $\text{Fe}^{3+}-\text{V}_{\text{O}}$  defect associate has to be oriented along the crystallographic  $c$ -axis. That is, the vacancy position is either at O1 or O1', and not at the O2 or O3. The DFT calculations in all three models considered obviously favour  $c$ -axis orientation.

The other results can be interpreted as follows. An  $\text{Fe}^{3+}$  ion with the oxygen vacancy has a position near the centre of the truncated oxygen octahedron, i.e. at the (0.5000 0.5000 0.6288) position. This position corresponds to one of the intersections of the NSM-predicted value with experimental value. These values are (cf. Table 8.1):  $d_2 = +14$  pm in the case with vacancy O1 (centre at  $d(\text{O1}, \text{O2}) = +19$  pm), cf. Fig 8.2(b));  $d_1 = +13$  pm in the case with vacancy at O1' (centre at  $d(\text{O1}, \text{O2}) = +26$  pm).

The second intersections of experimental value with the NSM prediction can be discarded on the basis of the DFT results. The DFT calculation predicted  $d = +33$  pm in the case with vacancy at O1,  $d = -3$  pm in the case with vacancy at O1'. They are in better agreement with above mentioned values then with the second intersections ( $d_1 = -23$  pm with vacancy at O1 and  $d_2 = +76$  with vacancy at O1', cf. Table 8.1).

Hence, the DFT calculations of the atomic structures around the defects helped us to decide between two options which have emerged from the NSM structures. Moreover, only on the basis of EPR and the NSM calculations it is not possible to decide which structure is preferred: one with the vacancy at O1 or one with the vacancy at O1'. However the DFT calculations clearly show preference towards the structure with the vacancy at O1.

The finally preferred structure of the  $\text{Fe}^{3+}-\text{V}_{\text{O}}$  defect associate from the NSM calculations is presented in Fig. 8.2(c).

For all DFT calculations a  $2 \times 2 \times 2$  unit cell was used. This size of this unit cell seems to be too small to avoid interactions between the defects. Probably the relaxation of ligands at the defect site would be smaller if larger unit cells are used. For computation time reasons, however, the unit cell could not be extended. Nevertheless, it is encouraging that the local structures predicted by DFT calculation and by the semi-empirical model based on experiment are quite similar.

Finally, the observed EPR spectra can almost exclusively be interpreted in terms of  $\text{Fe}^{+3}-\text{V}_{\text{O}}$  associates. It can be concluded that no 'free'  $\text{Fe}^{3+}$  signals, i.e., iron ions without associated  $\text{V}_{\text{O}}$  are present. This structure would lead to considerably smaller fine structure values.

The condition of an overall charge compensation is not satisfied in this defect complex. There is a charge mismatch, because the  $\text{Fe}^{3+}$  can accept one electron less than the  $\text{Ti}^{4+}$  ion. With respect to the neutral lattice, the associated oxygen vacancy has a positive charge of two ( $\text{V}_{\text{O}}$ ). Hence, additional mechanisms for charge compensation have to be discussed. Candidates for the charge compensation are: free electrons ( $e'$ ) trapped in the lattice, lead vacancies ( $\text{V}_{\text{Pb}}''$ ), and the formation

of positively charged cations (e.g.  $\text{Pb}^{2+} \rightarrow \text{Pb}^+$ ,  $\text{Ti}^{4+} \rightarrow \text{Ti}^{3+}$ , or  $\text{Fe}^{3+} \rightarrow \text{Fe}^{2+}$ ). However, there is neither an evidence for colour centres nor for variable valency ions such as  $\text{Pb}^+$ ,  $\text{Ti}^{3+}$  in the EPR spectra. These species are paramagnetic with  $g$ -values of about  $g \approx 2.0 - 1.9$ . They were not observed in the EPR spectra and thus can be excluded. Intrinsic double negatively charged lead vacancies  $V_{\text{Pb}}''$  have been suggested as additional charge compensation in lead zirconate titanate ceramics [115, 117]. Thus it is proposed that the overall electro-neutrality condition for iron modified  $\text{PbTiO}_3$  is guaranteed by:

$$[V_{\text{O}}^{\cdot\cdot}] = [\text{Fe}_{\text{Ti}}'] + \frac{1}{2}[V_{\text{Pb}}''] \quad (8.2)$$

This model is supported by the observation of an inherent loss of  $\text{PbO}$  during processing. For this reason a natural intrinsic  $V_{\text{O}}^{\cdot\cdot} - V_{\text{Pb}}''$  di-vacancy pair was proposed [38]. Its existence, however, is discussed controversially on the basis of DFT calculations [81].

In principle, a charge-compensation could also be obtained by the creation of  $\text{Fe}^{3+} - V_{\text{O}}^{\cdot\cdot} - \text{Fe}^{3+}$  defect associates without the need for lead vacancies at all. The existence of such a defect structure is also supported by the DFT results, predicting that this arrangement is of lowest energy. For this structure, the DFT calculations predicts two different iron sites. Thus two  $\text{Fe}^{3+}$  EPR spectra with different fine structure parameters are expected. Using the calculated  $d$  displacements of  $+46.6$  pm and  $-11.6$  pm, the NSM estimates of  $b_2^0 = 9.6$  GHz and  $b_2^0 = -34.7$  GHz would be observed. These values differ considerably from the experimentally obtained one. For this reason this model can be discarded. Furthermore, for samples with low iron doping, the assumption of an  $\text{Fe}^{3+} - V_{\text{O}}^{\cdot\cdot} - \text{Fe}^{3+}$  defect associate cannot be supported. Finally, from the present EPR experiment there is no further evidence for this hypothesis. In the EPR spectra there is no indication for strongly dipolar coupled iron centres.

In earlier studies of the  $\text{Fe}^{3+}$  centre in  $\text{PbTiO}_3$  (cf. Sec. 6.1.2), only the crystallographic oxygen positions were used. Additionally, it was not distinguished between structures with vacancy at O1 and O1' positions. The result was a predicted 20 pm shift towards the vacancy. The shift was referred to the centre of the octahedron (i.e. the plane of the 4 equatorial oxygens). This behaviour is qualitatively also reproduced here. Difference between the displacement from the Ti position  $d$  and the centre of the octahedron may be compared to the earlier result (cf. Table 8.1). In the case of the vacancy at O1, this difference amounts to 5 pm towards the vacancy. This vacancy position is also preferred by the DFT calculations, as stated above. In the case of the vacancy at O1', the shift amounts to 13 pm away from the vacancy. These difference is a result of considering the relaxed oxygen positions. However, this is still closer to the centre of octahedron than the original Ti position.

In lead titanate, vacancies are charge balanced by other defects forming an overall neutral system. It can be assumed that partial charge compensation takes place at a nearest-neighbour oxygen site in the octahedron as the resulting Coulomb attraction is the driving force for association. Experimental findings, however, indicate that for

other acceptor centres in similar compounds, like chromium-doped  $\text{PbTiO}_3$  [21] and copper-modified  $\text{Pb}[\text{Zr}_{0.54}\text{Ti}_{0.46}]\text{O}_3$  [17, 16], no such association is present. Alternatively an equilibrium between 'free'  $\text{Fe}^{3+}$  centres and  $\text{Fe}^{3+}-\text{V}_{\text{O}}^{\bullet}$  defect associates can be present [59]. An example for this behaviour is iron-doped  $\text{SrTiO}_3$ .

In comparison to the ionic mobility of free oxygen vacancies, the iron–oxygen vacancy defect associates probably have lower mobilities in ceramic materials. Because oxygen vacancies represent main charge carriers in this material, conductivity will be hindered considerably. It is supposed that these charged defects influence the poling properties. They provide pinning centres for domain walls [55] via agglomerations which stabilise movements of the walls. In the case of iron doping, the immobilised oxygen vacancy probably do not agglomerate. This behaviour probably accounts for the observation that the iron-doped  $\text{PbTiO}_3$  material shows an improved resistance to fatigue behaviour [56].



## 9. LEAD ZIRCONATE: EXPERIMENTS

### 9.1 *Introduction to lead zirconate*

Lead zirconate ( $\text{PbZrO}_3$ , PZ) is a perovskite crystal with antiferroelectric properties. It is the best known and most frequently studied example of antiferroelectricity in perovskites. Antiferroelectricity means polarisation occurs on the level of crystal cells while the overall polarisation of material remains zero. An antiferroelectric crystal also exhibits a structural phase transition (cf. 2.2.5). The phase transition in  $\text{PbZrO}_3$  occurs at a Curie temperature of 504 K, a value which is considerably lower than  $\text{PbTiO}_3$ . Above this temperature, lead zirconate exhibits a cubic structure. Below the Curie point,  $\text{PbZrO}_3$  has a complex orthorhombic structure with 8 formula units in the unit cell.

It has been also reported that a phase transition from an antiferroelectric to a ferroelectric state occurs under the application of a strong electric field. This process leads to a significant energy storage for a DC field. This property of  $\text{PbZrO}_3$  may lead to applications in energy storage. [99].

$\text{PbZrO}_3$  is most important as an 'end-member' of the lead zirconate titanate solid solutions ( $\text{Pb}[\text{Zr}_x\text{Ti}_{1-x}]\text{O}_3$ , PZT). When doped with aliovalent acceptor-type ions, the dominant charge compensation process in  $\text{PbZrO}_3$  is the creation of oxygen vacancies ( $\text{V}_{\text{O}}^{\cdot\cdot}$ ). The vacancies may form an oriented and charged  $\text{Fe}^{3+}-\text{V}_{\text{O}}^{\cdot\cdot}$  defect associate similarly as in lead titanate (cf. Chapter 8). For  $\text{PbZrO}_3$  it is still an open question whether 'free'  $\text{Fe}^{3+}$  and  $\text{V}_{\text{O}}^{\cdot\cdot}$  defects or  $\text{Fe}^{3+}-\text{V}_{\text{O}}^{\cdot\cdot}$  defect associates prevail.

To answer this question it is necessary to determine the fine structure spin Hamiltonian parameters of  $\text{Fe}^{3+}$  in  $\text{PbZrO}_3$ . In this work high-frequency EPR studies of  $\text{Fe}^{3+}$  defect centres in lead zirconate were carried out. The fine structure interaction is induced by the crystal field originating from the  $\text{O}^{2-}$  ligands around the  $\text{Fe}^{3+}$  defect. This allows a sensitive test of the local symmetry at the dopant site.

Considering the ionic radii, one can assume that the site of incorporation is – similar to lead titanate – the ( $\text{Zr}^{4+}$ ) B-site. An accurate determination of the fine structure parameters provides a profound basis for local structure modelling by the semi-empirical Newman superposition model (NSM).

#### 9.1.1 *Preparation of $\text{PbZrO}_3$*

The lead zirconate used in this work was doped with 0.5 mol % iron. It was prepared by Hans Küngl and Michael Hoffmann at the *Institute of Ceramics in Mechanical*

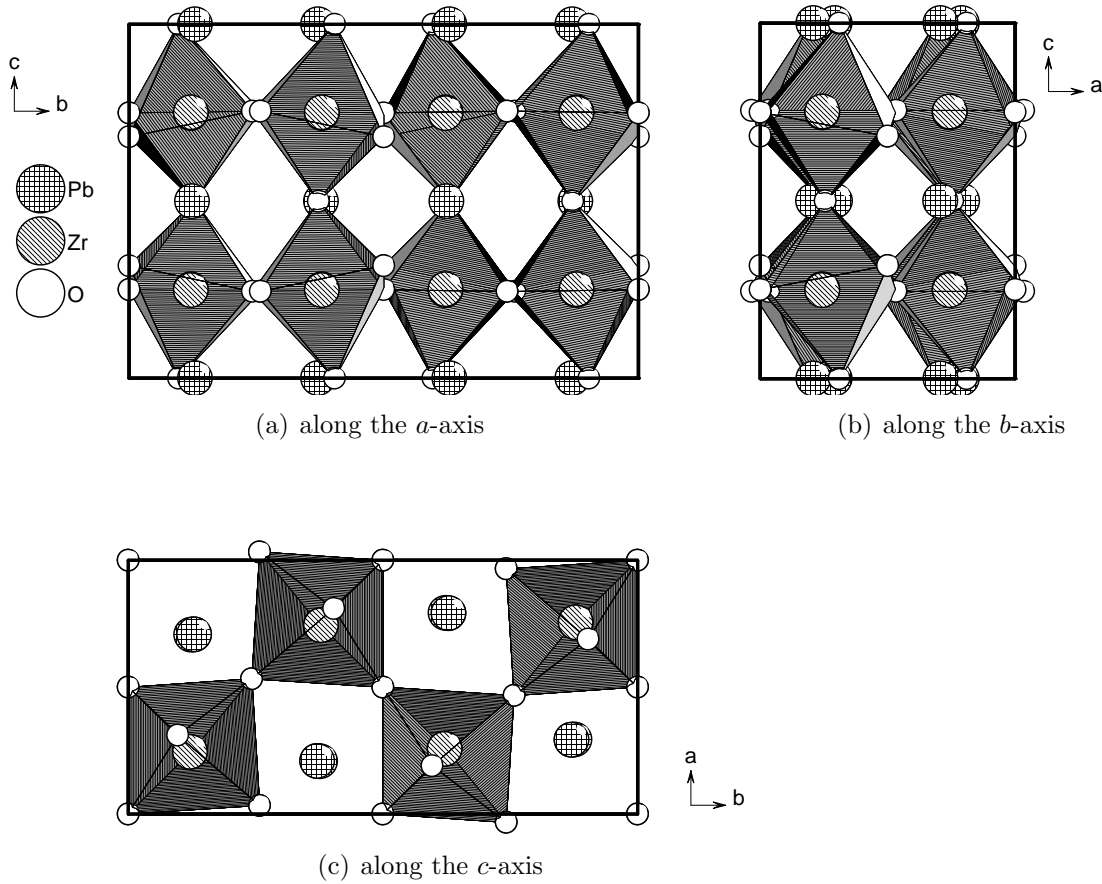


Fig. 9.1: Crystallographic unit cell of  $\text{PbZrO}_3$ . Legend of the atoms and the coordinate frame is showed.

Engineering, University of Karlsruhe as a part of the *Research Collaboration Project 595* of the *German Science Foundation*. In analogy to  $\text{PbTiO}_3$ ,  $\text{PbZrO}_3$  was prepared by a mixed oxide route (cf. Sec. 7.1.1). It was assumed that iron  $\text{Fe}^{3+}$  occupies the  $\text{Zr}^{4+}$ -sites of the perovskite structure. The observed chemical composition of the material was:  $\text{Pb}(\text{Zr}_{0.995}\text{Fe}_{0.005})\text{O}_{2.9975}$ . It has been assumed that the charge compensation was due to oxygen vacancies. Lead oxide, zirconia and iron oxide  $\text{Fe}_2\text{O}_3$  were mixed in isopropanol. The liquid was separated in a rotation distiller. The powder mixture was dried at  $100^\circ\text{C}$  for 48 hours and then sieved. The iron doped lead zirconate was then synthesized by calcination at  $850^\circ\text{C}$  for 2 hours in a closed alumina crucible. Fine grained ceramic powder was produced by milling for 6 hours. The material was dried and then sieved again.

### 9.1.2 Determination of the crystal structure of $\text{PbZrO}_3$

At the temperature of  $508\text{ K}$ ,  $\text{PbZrO}_3$  undergoes a displacive-type phase transition. The paraelectric cubic high-temperature phase changes into an antiferroelectric or-



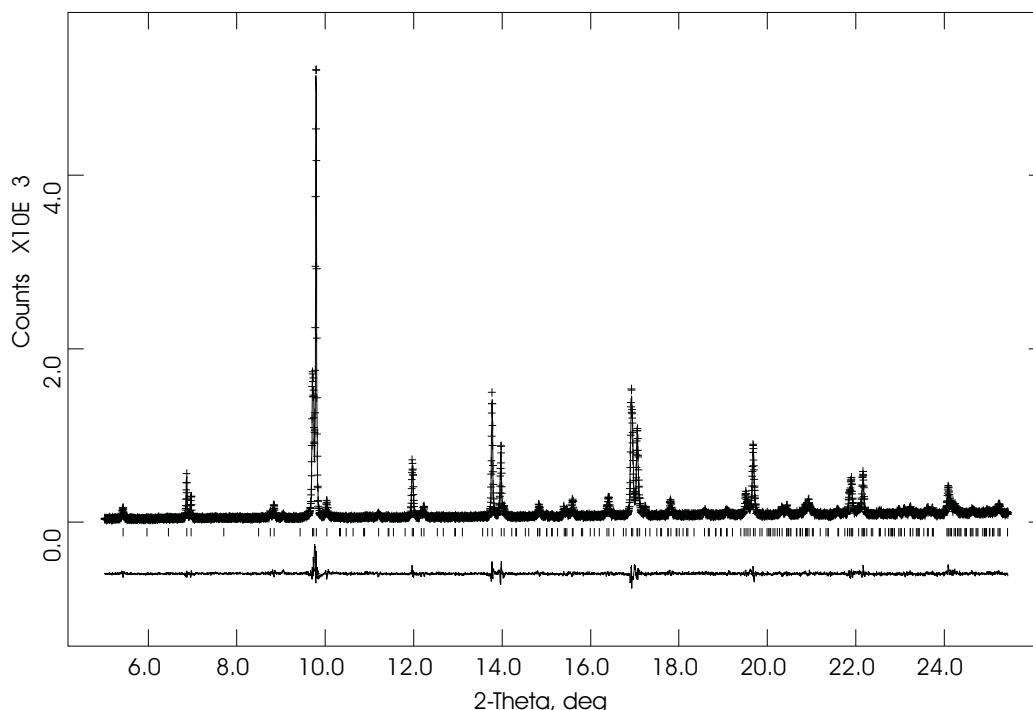


Fig. 9.2: Observed and calculated diffraction patterns of  $\text{PbZrO}_3$  obtained from high-resolution synchrotron powder diffraction at 20 K (top) together with the difference curve (bottom). Differences between the observed and calculated diffraction pattern are due to real-structure effects caused by the domain structure of the compound. Wavelength  $\lambda = 0.0499256$  nm.

thorhombic phase at low temperature via an intermediate phase. This intermediate phase exhibits an additional structure which differs from the low-temperature one. In course of heating this phase is formed between 506 K – 508 K. On cooling it is formed between 508 K – 501 K.[24].

For many years there is a discussion on the antiferroelectric or ferroelectric character of the low temperature phase. First, a non-centrosymmetric  $Pba2$  structure has been assumed [37]. It exhibited a polarisation along the  $[001]$  direction which is caused by unbalanced shifts of oxygen atoms. This structure is ‘antiferroelectric’ only in its  $ab$  plane as all atomic shifts are antiparallel. However, it should show ferroelectric effects along the  $c$ -direction.

Later, ferroelectric hysteresis effects have been detected only in the intermediate phase. No piezoelectricity in the room-temperature structure has been observed [93]. Furthermore, convergent beam electron diffraction suggested that the point group is  $mmm$  instead of  $mm2$  [105]. This has lead to the space group  $Pbam$ . Its antiferroelectric character was supported by neutron diffraction [26].

A weak ferroelectricity in  $\text{PbZrO}_3$  at room-temperature has been reported too [12]. Various subsequent temperature dependent X-ray and neutron single-crystal

Tab. 9.1: Lattice parameters ( $a = 587.149(10)$  pm,  $b = 1177.186(18)$  pm,  $c = 8.19614(12)$  pm, cell volume  $0.566504(16)$  nm<sup>3</sup>) and relative atom coordinates for PbZrO<sub>3</sub> at 20 K, obtained from high-resolution synchrotron powder diffraction.  $U_i$  is the mean square of the atomic displacement. The fluctuations due to shifts in the oxygen positions can be explained partly by the influence of real structure effects on peak profiles.

atom	$x$	$y$	$z$	$U_i \cdot 100$	site sym.	Wyckoff pos.
Pb1	0.7083(9)	0.1293(4)	0.000000	1.42(15)	$m$	4g
Pb2	0.7032(10)	0.1236(4)	0.500000	2.94(18)	$m$	4h
Zr	0.2438(4)	0.1215(8)	0.2489(11)	1.50(7)	1	8i
O1	0.2556(72)	0.1287(73)	0.500000	2.24(31)	$m$	4h
O1'	0.3099(86)	0.0973(39)	0.000000	2.24(31)	$m$	4g
O2	0.0346(27)	0.2578(16)	0.245(11)	2.24(31)	1	8i
O3	0.000000	0.500000	0.318(5)	2.24(31)	2	4f
O4	0.000000	0.000000	0.250(19)	2.24(31)	2	4e

and powder diffraction studies were performed. This low-temperature were compatible with the centrosymmetric  $Pbam$  structure. Additionally, an antiferroelectric structure was stable down to 8 K [10, 106, 25]. By combining neutron experiments with a pair distribution function modelling it could be demonstrated that the Pb atoms are – in addition to the antiparallel shifts within the  $ab$  plane – also displaced in the  $c$ -direction. This shift increases with increasing temperature and is most probably the origin of the small  $c$ -axis polarisation detected.

In this work high-resolution synchrotron powder diffraction experiments were used. They were performed by Kristin Schönauf, Martin Knapp and Helmut Ehrenberg at the *Materials Science Department, Darmstadt University of Technology* as a part of the *Research Collaboration Project 595* of the *German Science Foundation*. This was necessary in order to obtain precise structural data for the interpretation of the EPR fine structure parameters at low temperature. The measurements were carried out in reflection geometry at B2, *Hasylab* in Hamburg. The measurement was performed at 20 K. The powdered sample was measured using an incident beam of wavelength  $\lambda = 0.0499256$  nm.

A Rietveld refinement using the general structure analysis system (GSAS) [49] has been performed. Then the unit-cell parameters, atomic positions and thermal displacement parameters of each atom were refined individually. The best fit is shown in Fig. 9.2 confirming recent results [10, 106, 25]. It was achieved with the structural model of the centrosymmetric space group  $Pbam$ . The unit-cell parameters and

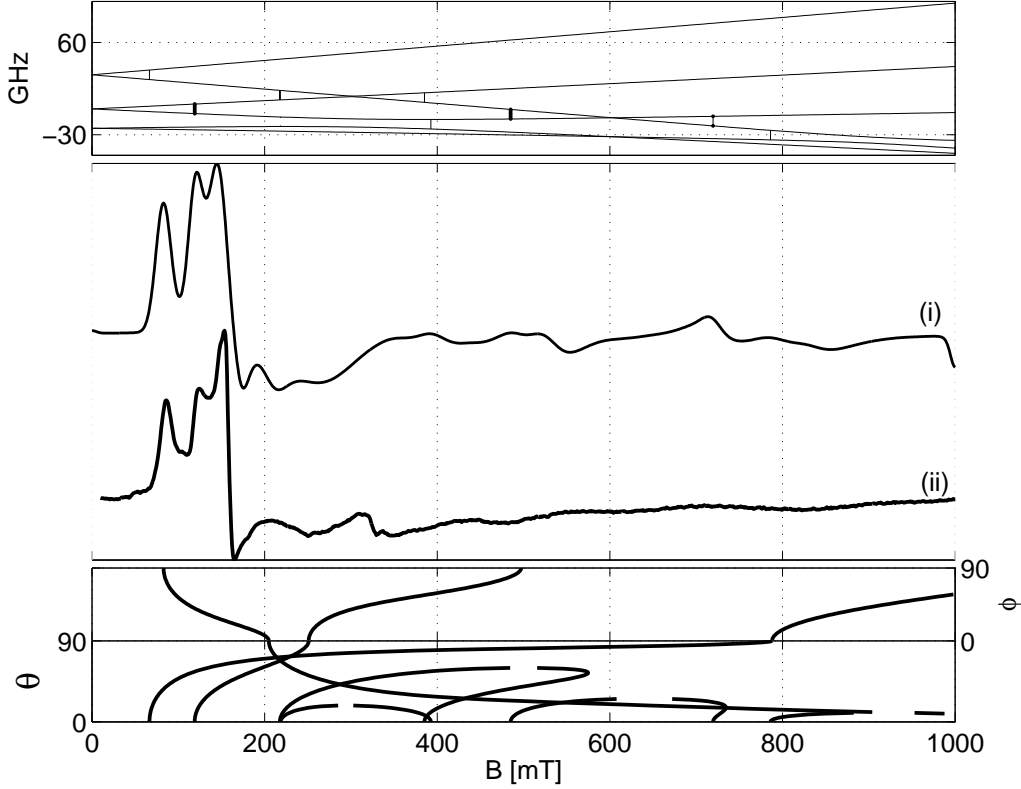


Fig. 9.3: *Centre diagram*: X-band EPR spectra of  $\text{Fe}^{3+}:\text{PbZrO}_3$  (ii) The experimental parameters are  $\nu = 9.312$  GHz,  $T = 10$  K,  $P_{\text{mw}} = 2$  mW,  $B_{\text{mod}} = 1$  mT,  $\nu_{\text{mod}} = 100$  kHz,  $t_c = 82$  ms. (i) Simulated spectrum with parameters:  $g = 2.0023$ ,  $b_2^0 = 8.5$  GHz,  $b_2^2 = 2.8$  GHz,  $\sigma_{\text{lw}} = 13$  mT,  $\sigma_{\text{strain}}(b_2^0) = 300$  MHz,  $\sigma_{\text{strain}}(b_2^2) = 2400$  MHz. *Upper diagram*: energy levels of the  $\text{Fe}^{3+}$  ion along  $x$ -axis with all possible EPR transitions. Allowed transitions are denoted by thicker lines. *Lower diagram*: angular dependence of resonances between two lowest pairs of levels.

atom coordinates obtained agree within standard deviations with the parameters determined earlier. They are summarised in Table 9.1. These result were also published in [62].

## 9.2 EPR measurements of the $\text{Fe}^{3+}$ centre in $\text{PbZrO}_3$

### 9.2.1 Low frequency measurements $\text{Fe}^{3+}:\text{PbZrO}_3$

For commonly employed X-band frequencies a low field EPR condition (cf. Sec. 4.2.2) is expected for  $\text{Fe}^{3+}:\text{PbZrO}_3$ , similar as in  $\text{PbTiO}_3$ . The fine structure interaction of  $\text{Fe}^{3+}$  in a distorted or incomplete oxygen octahedron should be larger than the energy of microwave quanta. However, an important difference to  $\text{PbTiO}_3$  arises

from the symmetry of the dopant site. In  $\text{PbTiO}_3$ , the symmetry of the  $\text{Ti}^{4+}$  site is tetragonal ( $mm$ ), hence allowing axial symmetry for  $\text{Fe}^{3+}$ . In  $\text{PbZrO}_3$  the  $\text{Zr}^{4+}$  site has no symmetry (point group 1). Therefore a paramagnetic centre of completely broken symmetry is expected for the latter compound. This behaviour is in principle possible both for an intact oxygen octahedron and for an incomplete octahedron with oxygen vacancy.

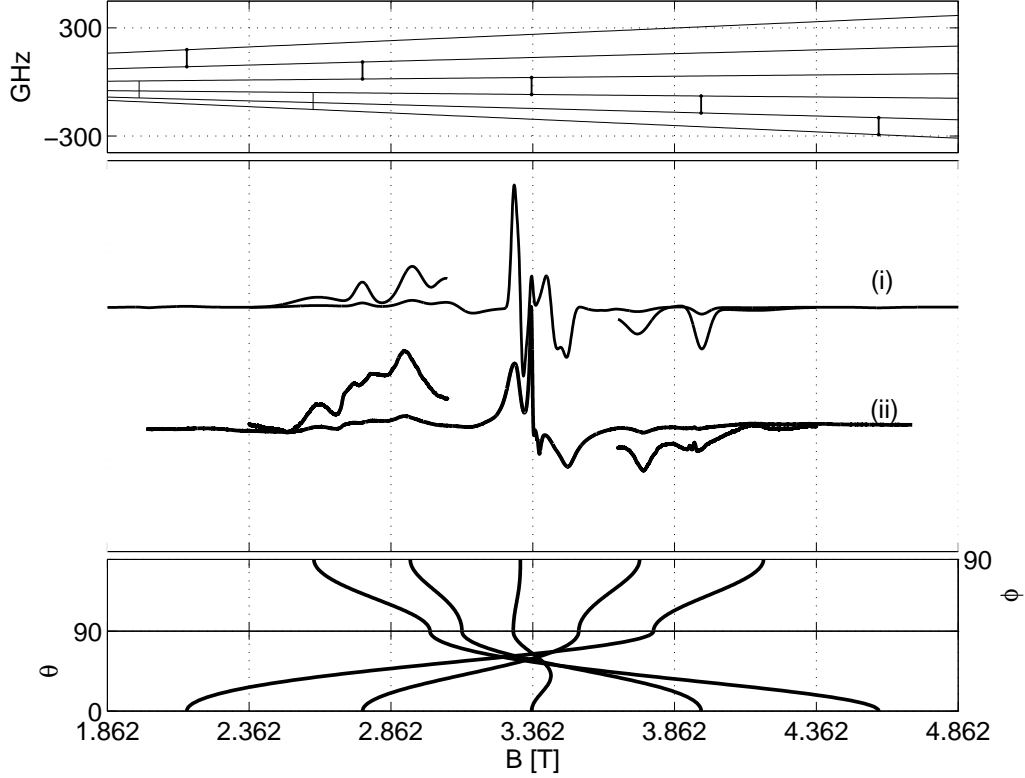


Fig. 9.4: *Centre diagram*: (ii) W-band EPR spectrum of  $\text{Fe}^{3+}:\text{PbZrO}_3$  with experimental parameters are  $\nu = 94.16$  GHz,  $T = 10$  K,  $P_{\text{mw}} = 0.0125$  mW,  $B_{\text{mod}} = 0.1$  mT,  $\nu_{\text{mod}} = 100$  kHz,  $t_c = 82$  ms. (i) Simulated spectrum with parameters:  $g = 2.0023$ ,  $b_2^0 = 8.5$  GHz,  $b_2^2 = 2.8$  GHz,  $\sigma_{\text{lw}} = 13$  mT,  $\sigma_{\text{strain}}(b_2^0) = 800$  MHz,  $\sigma_{\text{strain}}(b_2^2) = 2400$  MHz.

*Upper diagram*: energy levels of the  $\text{Fe}^{3+}$  ion along the  $x$ -axis with all possible EPR transitions.

*Lower diagram*: angular dependence for resonances between the two lowest pairs of levels.

The EPR measurement at 10 K with a frequency of 9.312 GHz is presented in Fig. 9.3 (ii). It exhibits three remarkable resonances at fields of  $B_1 = 88(3)$  mT,  $B_2 = 123(3)$  mT,  $B_3 = 159(3)$  mT and a broad features in the  $g \approx 2$  area. This pattern corresponds neither to axial ( $b_2^0 \neq 0$  and  $b_2^2 = 0$ ) nor to fully rhombic symmetry

( $b_2^0 \neq 0$  and  $b_2^0 = b_2^2$ ). Similar to  $\text{PbTiO}_3$ , axial symmetry in low-field conditions would show a peak at  $g' \approx 2$ . Fully rhombic symmetry in low-field conditions usually exhibits a resonance at  $g' \approx 4.2$  (cf. Eq. 4.27). Therefore, it may be concluded that the spin Hamiltonian parameters of 2<sup>nd</sup>-order for this centre fulfil intermediate relation  $0 < b_2^2/b_2^0 < 1$ . This ratio could be evaluated, in principle, from the X-band spectra of single crystals [47]. However, for the determination of absolute values of the parameters of the spin Hamiltonian, measurements at higher frequencies are an absolute prerequisite.

Relative magnitudes in the fine structure and Zeeman term are of the same order of magnitude.  $m_S$  is no good quantum number and transitions may occur between all levels. However, they differ in the transition probabilities. Thus, a manifold of resonances is spanned over a wide field range. Their dependence on the orientation of the magnetic field is also prominent. In particular, so-called 'looping transitions' occur that do not continue over all possible orientations. Additionally, so-called 'crossing transitions' are expected that have equal eigenvalues at some particular orientations [65]. The resulting spectrum is complicated and consequently the determination of fine structure parameters is not unambiguous.

### 9.2.2 W-band measurements $\text{Fe}^{3+}:\text{PbZrO}_3$

To precisely determine the fine structure parameters for polycrystalline compounds, the use of microwave frequencies exceeding the fine structure interaction are required. If the high-frequency regime (cf. Sec. 4.2.1) is established, the fine structure interaction may be treated as a perturbation of the Zeeman levels. The corresponding energy levels are well-separated and  $m_S$  becomes a good quantum number. Consequently, the 2<sup>nd</sup>-order parameters  $b_2^q$  may be determined directly on the basis of perturbation expressions, via first-order shifts of the resonance-line positions (cf. Eq. 4.20). The 4<sup>th</sup>-order parameters  $b_4^q$  are typically orders of magnitude smaller than the 2<sup>nd</sup>-order ones. Therefore, their impact on the high-field spectra is only a shifting in the positions of resonance lines. However, in order to use perturbation formulae, additional conditions have to be fulfilled, e.g.  $b_2^2 \ll b_2^0$ . This constraints are not necessary fulfilled for this paramagnetic centre.

The EPR spectrum recorded in the W-band is presented in Fig. 9.4(ii). Since it shows a nearly symmetric  $S = 5/2$  spectral pattern, we conclude that the high-field condition is already achieved. The spectrum is centred at  $B_0 = 3.359$  T and side peaks appear at field offsets of  $\Delta B_1 = -0.762$  T,  $\Delta B_2 = -0.454$  T,  $\Delta B_3 = 0.401$  T and  $\Delta B_4 = 0.608$  T. The central line is split by  $\Delta B_0 = 0.197$  T. However, it can be noticed that the side peaks are extremely broadened. The central line, on the other hand, has a linewidth  $\Delta B$  of only 12(2) mT. This behaviour suggests that the fine structure parameters have no sharp values. Instead they are distributed over wide range, leading to the broad side transitions in the spectrum.

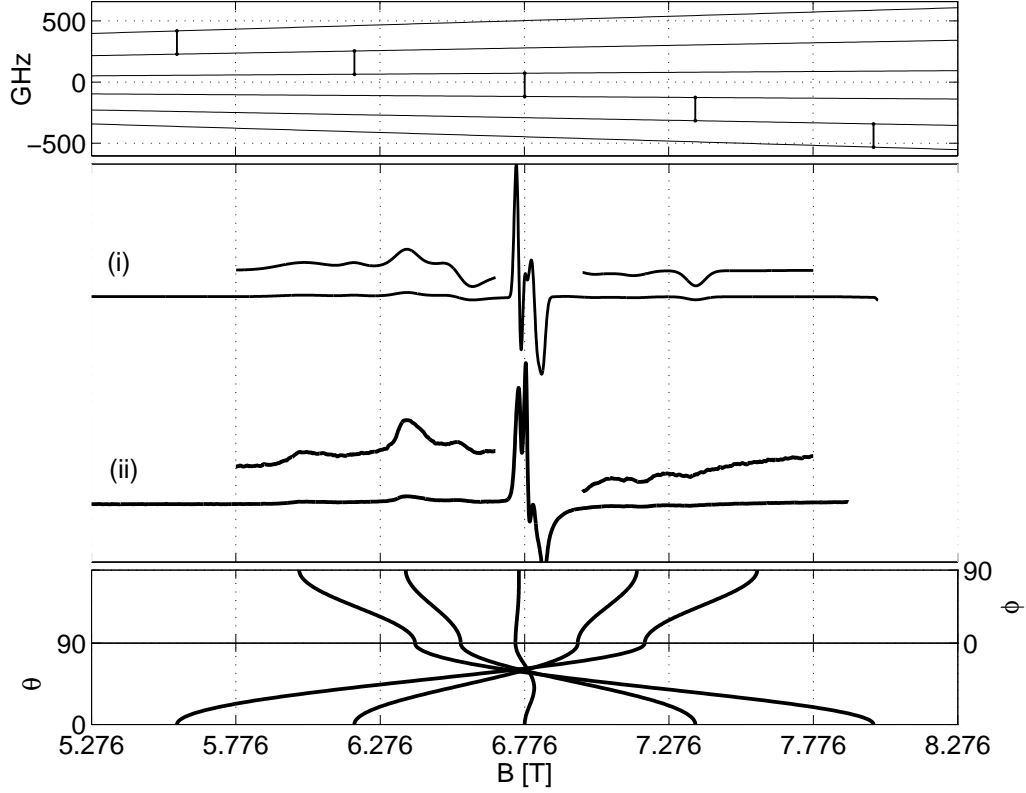


Fig. 9.5: *Centre diagram*: 189.912 GHz spectrum of  $\text{Fe}^{3+}:\text{PbZrO}_3$ . (ii) Experimental spectrum with parameters  $T = 10$  K,  $P_{\text{mw}} = 0.0125$  mW,  $B_{\text{mod}} = 0.6$  mT,  $\nu_{\text{mod}} = 37.7$  kHz,  $t_c = 300$  ms. (i) Simulated spectrum with parameters:  $g = 2.0023$ ,  $b_2^0 = 8.5$  GHz,  $b_2^2 = 2.8$  GHz,  $\sigma_{\text{lw}} = 13$  mT,  $\sigma_{\text{strain}}(b_2^0) = 1000$  MHz,  $\sigma_{\text{strain}}(b_2^2) = 2400$  MHz.

*Upper diagram*: energy levels of the  $\text{Fe}^{3+}$  ion along the  $z$ -axis with all possible EPR transitions.

*Lower diagram*: angular dependence of resonances between two lowest pairs of levels.

### 9.2.3 High frequency measurements $\text{Fe}^{3+}:\text{PbZrO}_3$

The high-frequency EPR spectrum at 190 GHz is presented in Fig. 9.5(ii). It is quite similar to the W-band spectrum in Fig. 9.4(ii). It is centred at  $B_0 = 6.766$  T ( $g \approx 2$ ) where the central transition  $|-\frac{1}{2}\rangle \leftrightarrow |+\frac{1}{2}\rangle$  is observed. The side peaks originate from other transitions. The offsets from the central line are as follows:  $\Delta B_1 = -0.75$  T,  $\Delta B_2 = -0.40$  T,  $\Delta B_3 = 0.40$  T,  $\Delta B_4 = 0.59$  T. The central line is split by  $\Delta B_0 = 0.096$  T. Other small lines near to centre arise from the orientations of the field along the  $y$ -axis.

A frequency of 240 GHz was also employed to measure  $\text{Fe}^{3+}:\text{PbZrO}_3$  at two different temperatures (Fig. 9.6). The spectra at this frequency are dominated by the

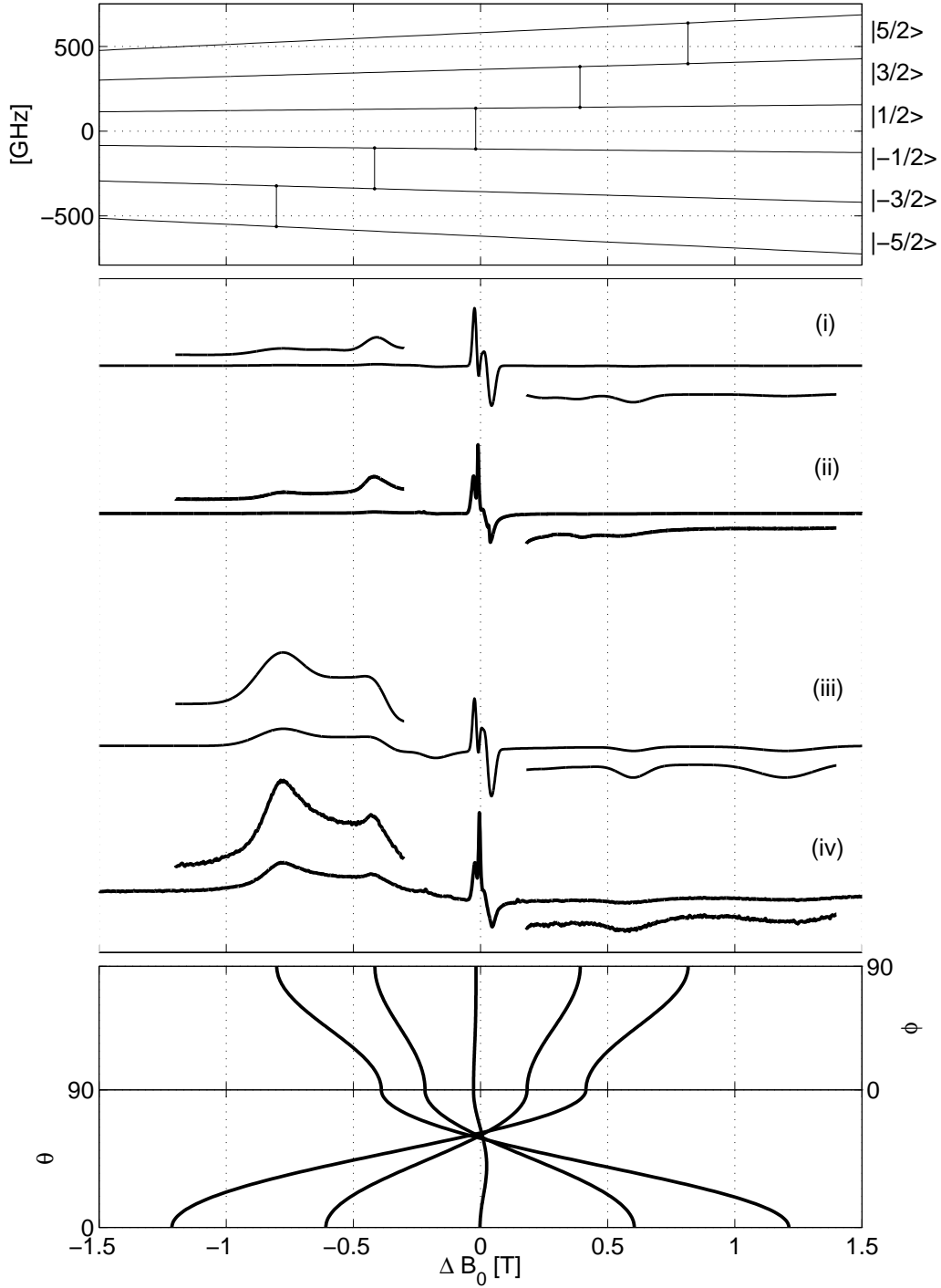


Fig. 9.6: *Centre diagram:* (ii, iv) The experimental 240 GHz spectra of  $\text{Fe}^{3+}:\text{PbZrO}_3$  with parameters:  $P_{\text{mw}} = 0.0125$  mW,  $B_{\text{mod}} = 0.6$  mT,  $\nu_{\text{mod}} = 40.34$  kHz,  $t_c = 300$  ms. (i, iii) Simulated spectra with parameters:  $g = 2.0023$ ,  $b_2^0 = 8.5$  GHz,  $b_2^2 = 2.8$  GHz,  $\sigma_{\text{lw}} = 13$  mT,  $\sigma_{\text{strain}}(b_2^0) = 1800$  MHz,  $\sigma_{\text{strain}}(b_2^2) = 2400$  MHz. (i, ii) spectra at 15 K, (iii, iv) spectra at 4.8 K.

*Upper diagram:* energy levels of the simulated  $\text{Fe}^{3+}$  ion along the  $x$ -axis with all possible EPR transitions.

*Lower diagram:* angular dependence of resonances between two lowest pairs of levels.

central  $|\frac{1}{2}\rangle \leftrightarrow |+\frac{1}{2}\rangle$  transition. The outer spectral features originate from the higher transitions  $|\frac{5}{2}\rangle \leftrightarrow |-\frac{3}{2}\rangle$ ,  $|\frac{3}{2}\rangle \leftrightarrow |-\frac{1}{2}\rangle$ ,  $|+\frac{1}{2}\rangle \leftrightarrow |+\frac{3}{2}\rangle$  and  $|+\frac{3}{2}\rangle \leftrightarrow |+\frac{5}{2}\rangle$ , which – in first order – are orientation-dependent. The most prominent transition among these is the  $|\frac{5}{2}\rangle \leftrightarrow |-\frac{3}{2}\rangle$  transition with resonance lines at field offsets  $\Delta B_1 = -0.801$  T and  $\Delta B_4 = 1.26$  T from the central line. The central line is at  $B_0 = 8.567$  T ( $g = 2.002$ ). It is split by second order effects for  $\Delta B_2 = -0.07$  T. Further EPR signals at fields  $\Delta B_2 = -0.43$  T and  $\Delta B_3 = 0.53$  T arise from the  $|\frac{3}{2}\rangle \leftrightarrow |-\frac{1}{2}\rangle$  transition. The  $|+\frac{1}{2}\rangle \leftrightarrow |+\frac{3}{2}\rangle$  transition has a rather small intensity at 4.8 K, but it can be seen at 15 K ( $\Delta B_5 = 0.385$  T). The remaining  $|+\frac{3}{2}\rangle \leftrightarrow |+\frac{5}{2}\rangle$  transition is not observed at this temperature.

The absence of certain resonance lines may be explained by the spin-level populations in thermal equilibrium. At room temperature line intensities are expected that exhibit an inversion symmetry with respect to the central line. At 4.8 K, ( $k_B T \approx 100$  GHz) a significant absolute difference in the level populations is only obtained for the two states of lowest energy. The change of the line intensities when at a higher temperature (15 K) can be observed without difficulties.

### 9.3 Determination of the spin Hamiltonian parameters of $Fe^{3+}:PbZrO_3$

#### 9.3.1 Perturbational analysis of the $Fe^{3+}:PbZrO_3$ spectra

The positions of the EPR lines in the high-frequency regime of 240 GHz facilitate a direct estimate of 2<sup>nd</sup>-order fine structure parameters. From the positions of the EPR lines with the field along the  $z$ -axis it is possible to estimate both 2<sup>nd</sup>-order spin Hamiltonian parameters with the formulae from Eq. (4.20). 4<sup>th</sup>-order parameters are supposed to be zero. The assumption which enables the analytical diagonalisation of the spin Hamiltonian reads  $b_2^2/b_2^0 \ll 1$ . Thus term  $b_2^2(S_x^2 - S_y^2)$  is taken as perturbation to the rest of the Hamiltonian (cf. Sec. 4.2.1).

By means of perturbation formulae from the 240 GHz spectrum the following values can be calculated:

$$\begin{aligned} |b_2^0| &\approx 9.2 \text{ GHz} \\ |b_2^2| &\approx 2.0 \text{ GHz} \end{aligned} \tag{9.1}$$

The lines with stronger angular dependence are more broadened as result of the statistical distribution of the fine structure parameters.

The splitting of the central transition comes from 2<sup>nd</sup>-order of the perturbation. It is equal to  $4\frac{(b_k^q)^2}{B_0}$ . In contrast to the outer transitions which are dominated by 1<sup>st</sup>-order effects, the central transition is frequency dependent. This can be seen in the W-band measurements as well as in other high frequency bands. The splitting of the central transition arises at the angles  $\theta = 0, 0.2322 \pi$  and  $\frac{\pi}{2}$ .



From the 2<sup>nd</sup>-order splitting of central transition the following values may be extracted:

$$\begin{aligned} b_2^0 &\approx 11.4 \text{ GHz} \quad (\nu = 94.16 \text{ GHz}) \\ b_2^0 &\approx 11.3 \text{ GHz} \quad (\nu = 189.89 \text{ GHz}) \\ b_2^0 &\approx 10.8 \text{ GHz} \quad (\nu = 240 \text{ GHz}) \end{aligned} \quad (9.2)$$

However, these values are obtained under the assumption that  $b_2^0 \gg b_2^2$ , which is not *a priori* valid.

The set of the parameters derived by perturbation theory was used as a starting point for numerical calculations. Further refinement of the parameters was carried out in order to obtain the best fit the experimental spectra.

The high frequency spectrum of 240 GHz is easier to interpret then the low frequency X-band EPR spectra. The latter contains transitions that exhibit a complicated orientation dependence. The turning points of these transitions do not correspond necessarily to canonical orientations. The complete set of fine structure parameters thus can be only obtained by a simultaneous multi-frequency numerical spectrum simulation.

### 9.3.2 Numerical simulations of $\text{Fe}^{3+}:\text{PbZrO}_3$ spectra

In the X-band, it is observed that the spectral full-widths at half-heights of lines amount to  $\Delta B_{\text{FWHH}} = 12.7 \text{ mT}$  are considerably broader than those for  $\text{Fe}^{3+}$  in lead titanate which amount to  $\Delta B_{\text{FWHH}} = 4 \text{ mT}$ . A conventional description of this situation would be assuming a single set of parameters which are statistical distributed. This behaviour is illustrated schematically in Fig. 9.7(a,b).

A numerical refinement for a set of parameters by means of simulation programs was performed simultaneously for all frequencies. All frequency spectra could be reproduced numerically by the following set of spin Hamiltonian parameters:

$$\begin{aligned} b_2^0 &= 8.5 \text{ GHz}; \\ |b_2^2| &= 2.7 \text{ GHz}; \\ b_4^0 &= 0.1 \text{ GHz}; \quad b_4^4 = 0.5 \text{ GHz}; \\ b_2^2/b_2^0 &= 0.32 \end{aligned} \quad (9.3)$$

However, as a result of the intensive line broadening, a single set of line widths could not be achieved.

When performing simulations, different strain values had to be used to obtain good agreement with the experimental spectra, assuming an isotropic linewidth of 13 mT. These are, as indicated in figures:  $\delta b_2^0 = 0.30 \text{ GHz}$  and  $\delta b_2^2 = 2.4 \text{ GHz}$  for the X-band spectrum;  $\delta b_2^0 = 0.80 \text{ GHz}$  and  $\delta b_2^2 = 2.4 \text{ GHz}$  for W-band spectrum;

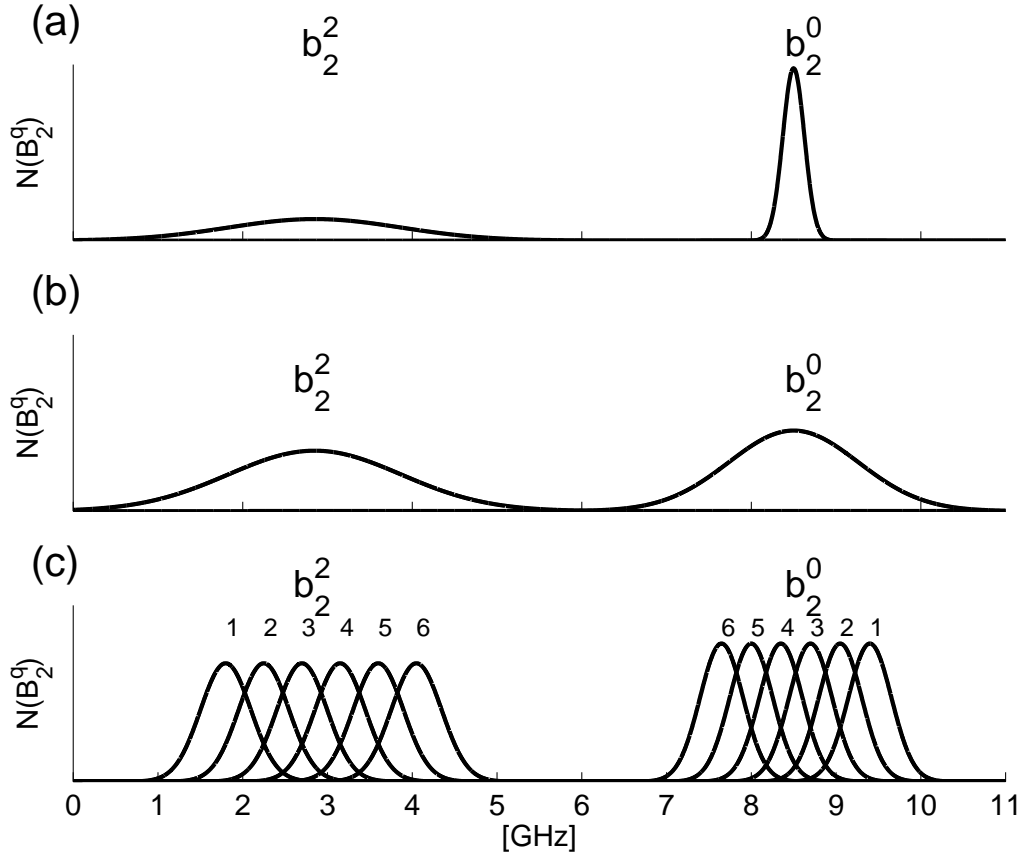


Fig. 9.7: Schematic representation of the distribution of fine structure parameters used for simulations of  $\text{Fe}^{3+}:\text{PbZrO}_3$ .

(a) distribution of parameters for X-band simulation assuming a single average set of parameters with  $\delta(b_2^0) = 0.3$  GHz and  $\delta(b_2^2) = 2.4$  GHz.

(b) distribution of parameters for 240 GHz simulation assuming a single average set of parameters with  $\delta(b_2^0) = 1.8$  GHz and  $\delta(b_2^2) = 2.4$  GHz.

(c) distinct energy levels for a basis set of six different sites, where  $\delta(b_2^0) = 0.6$  GHz and  $\delta(b_2^2) = 0.7$  GHz.

$\delta b_2^0 = 1.0$  GHz and  $\delta b_2^2 = 2.4$  GHz for the 190 GHz spectrum and  $\delta b_2^0 = 1.8$  GHz and  $\delta b_2^2 = 2.4$  GHz for the 240 GHz spectrum. These values correlate with the respective full-width half-height of a Gaussian distribution of parameters. Calculated spectra are shown together with experimental spectra and show good agreement.

It should be possible to simulate the spectra measured at different microwave frequencies with a single set of parameters as well as their distribution values. The fine structure interaction does not depend on the external field. Consequently, an alternative approach was undertaken.

If it is assumed that in  $\text{PbZrO}_3$  the  $\text{Fe}^{3+} - V_{\text{O}}^{\bullet\bullet}$  defect associate is encountered

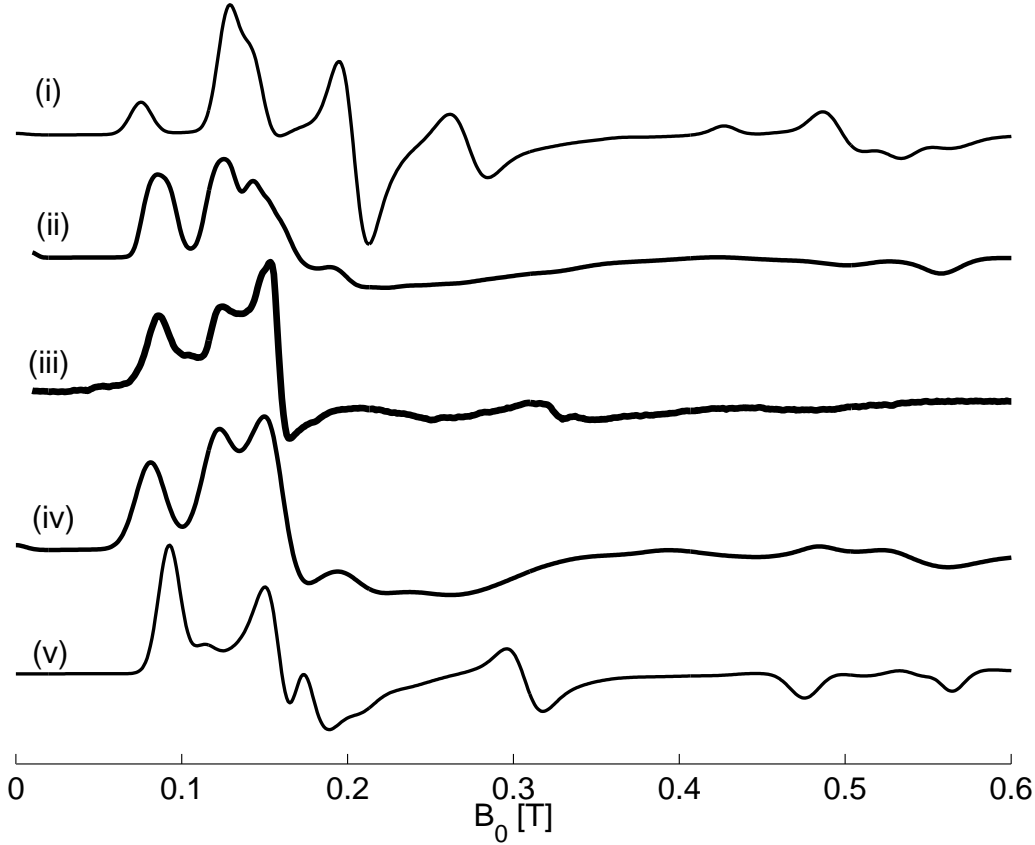


Fig. 9.8: (i) - numerical spectrum simulations invoking extreme values of the fine structure parameters (cf. Table 9.2, centre 1)  
(ii) - numerical spectrum simulation with the sum over the six basic EPR spectra taken with equal weight  
(iii) X-band EPR spectra of  $\text{Fe}^{3+}:\text{PbZrO}_3$  compared to numerical spectrum simulations  
(iv) - numerical spectrum simulation invoking FS-strain  
(v) - numerical spectrum simulations invoking extreme values of the fine structure parameter (cf. Table 9.2, centre 6)

as well, a physically realistic description should be developed. According to the crystal structure of  $\text{PbZrO}_3$ , an irregular octahedron of oxygen ligands surrounds the dopant site ( $\text{Zr}^{4+}$ ). Therefore, six oxygen atoms are positioned at six different distances from the substituting  $\text{Fe}^{3+}$  (cf. Table 9.2). Hence, six possible positions for an oxygen vacancy exist. For this reason six different  $\text{Fe}^{3+}-\text{V}_{\text{O}}$  defect dipoles may be formed. In contrast to this situation, it has been shown for  $\text{Fe}^{3+}:\text{PbTiO}_3$  that oxygen vacancies are found only in direction of the crystallographic  $c$ -axis. From the  $\text{Fe}^{3+}$  position, this yields  $\text{Fe}^{3+}-\text{V}_{\text{O}}$  defect dipoles strictly oriented along the  $c$ -axis. For  $\text{PbZrO}_3$  such an well defined orientation of defect associate is *a priori* not expected.

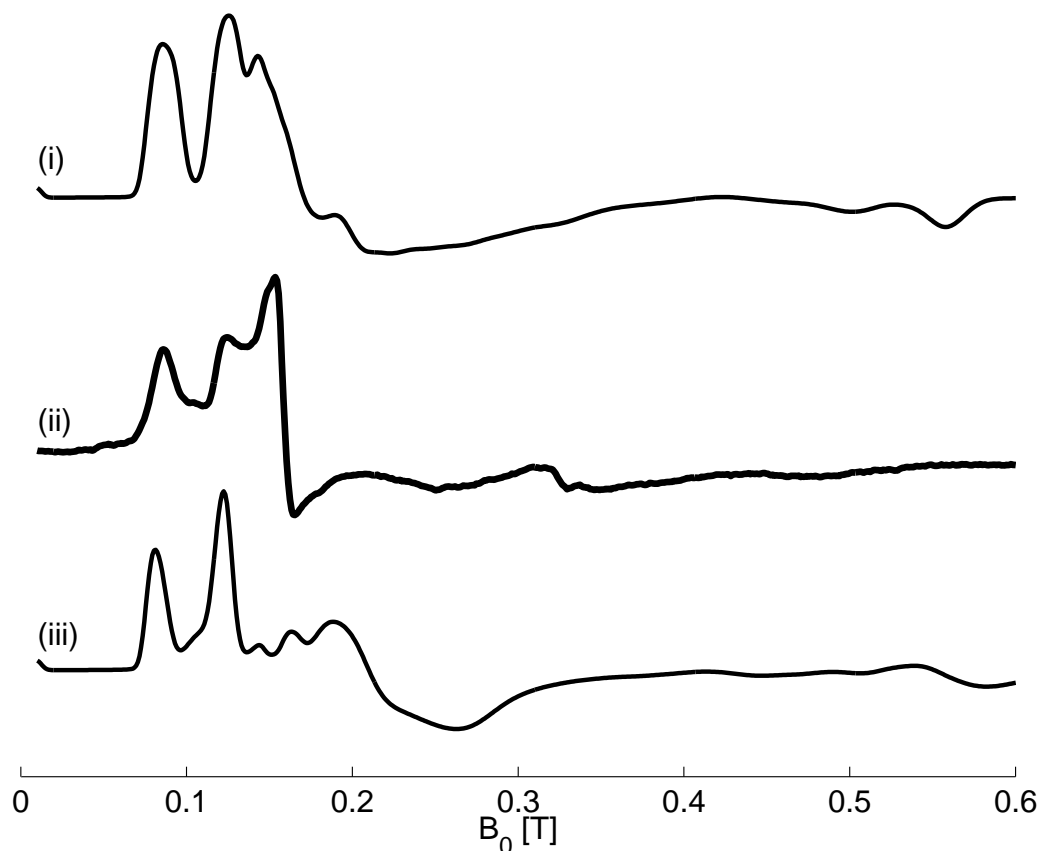


Fig. 9.9: (ii) X-band EPR spectra of  $\text{Fe}^{3+}:\text{PbZrO}_3$  as compared to: (iii) a inverse proportionality and (i) direct proportionality of  $b_2^0$  and  $b_2^2$ .

Both crystal structure and low symmetry of measured EPR spectra suggest that. Therefore, there is no reason to find paramagnetic centres with a distinct set of spin Hamiltonian parameters.

In order to account for this difference, a set of six EPR spectra was assumed with variable fine structure parameters has been assumed. The range of values chosen corresponds to the widths of the continuous distributions that has been used for simulation of the 240 GHz spectrum. A set of parameters separated by equal amounts around the respective mean values was used. Two spectra of this set are depicted in Fig. 9.8(i,v) together with the sum of all six EPR spectra (Fig. 9.8(ii)).

Good agreement with the experimental spectra could only be obtained, if the  $b_2^0$  and  $b_2^2$  parameters exhibit an inverse proportionality (cf. Table 9.2). In other words, for a centre with the highest  $b_2^0$  value, the  $b_2^2$  value is the lowest one, and *vice versa*. This inverse proportionality is essential for the correct reproduction of the multi-frequency EPR spectra. This is illustrated by simulations invoking a direct proportionality of the  $b_2^0$  and  $b_2^2$  parameters in Figs. 9.8(iv) and 9.10(iv,v). A com-

Tab. 9.2: fine structure parameters for the basis set of six paramagnetic centres. They are employed in the numerical simulation of the  $\text{Fe}^{3+}:\text{PbZrO}_3$  spectra.

center	$b_2^0$ [GHz]	$b_2^2$ [GHz]	$b_2^2/b_2^0$
1	9.40	1.80	0.19
2	9.05	2.25	0.25
3	8.70	2.70	0.31
4	8.35	3.15	0.38
5	8.00	3.60	0.45
6	7.65	4.05	0.53

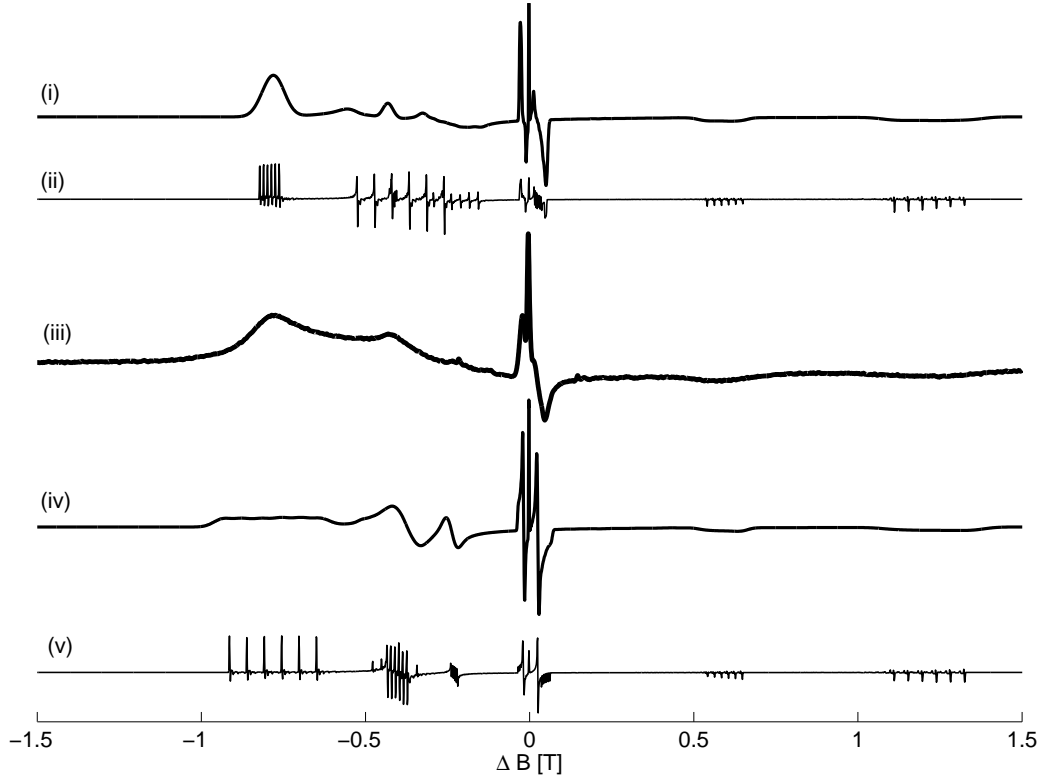


Fig. 9.10: 240 GHz EPR spectra of  $\text{Fe}^{3+}:\text{PbZrO}_3$  (iii) as compared to a proportionality (iv,v) and inverse proportionality (i,ii) of  $b_2^0$  and  $b_2^2$ . The 'stick-spectra' (ii,v) show the superposition of all six constituent EPR spectra.

parison with the broad side resonances of the high-frequency spectra clearly suggests that the inverse proportionality of the parameters is favoured.

As a matter of fact, the  $\text{Fe}^{3+}$  centre in  $\text{PbZrO}_3$  is better described by a distinct set of different centres than by a broad distribution of values. Experimentally it could not be proved that only six distinct centres are involved. By considering the crystal structure, however, the presumed six centres seems to be an obvious assumption. In comparison to the spin Hamiltonian values for  $\text{Fe}^{3+}$  centres in different crystals, the mean values including their distributions may be considered as representative.

$$\begin{aligned} b_2^0 &= 8.5(9) \text{ GHz}; \\ |b_2^2| &= 2.7(12) \text{ GHz}; \\ b_4^0 &= 0.1(1) \text{ GHz}; \quad b_4^4 = 0.5(3); \text{ GHz} \\ b_2^2/b_2^0 &= 0.3(2); \end{aligned} \tag{9.4}$$

These results may be compared to previous studies of  $\text{Fe}^{3+}$  in  $\text{PbTiO}_3$  (cf. Chapter 7). In this crystal fine structure interaction was found to be  $b_2^0 = 35.3(2)$  GHz was found. It may be noticed that the amount of the fine structure in  $\text{PbZrO}_3$  is considerably smaller. This result may be traced back to the considerably reduced distortion of the oxygen octahedron in the  $\text{PbZrO}_3$  structure.

These results may be further compared with previous X-band results for a  $\text{Fe}^{3+}$  impurity centre in a  $\text{PbZrO}_3$  single crystal [47]. In this study only the ratio of the 2<sup>nd</sup>-order spin Hamiltonian parameters could be determined. Four nearly axial  $\text{Fe}^{3+}$  centres with identical ratios  $b_2^2/b_0^2 = -0.138$  were identified. They are of different orientations in the single crystal. For two of the centres the orientations are close to the pseudocubic  $[100]_c$  direction. The other are were in the pseudocubic  $[010]_c$  direction. The reported  $b_2^2/b_0^2$ -ratio of this measurements differs considerably from our result.

## 10. LEAD ZIRCONATE: STRUCTURAL CALCULATIONS

### 10.1 The NSM Analysis of $\text{Fe}^{3+}$ in $\text{PbZrO}_3$

The determined set of fine structure parameters in  $\text{Fe}^{3+}:\text{PbZrO}_3$  (cf. Chapter 9) is used for the analysis of the local structure of the  $\text{Fe}^{3+}$  paramagnetic centre. It will be studied with the help of the Newman superposition model (cf. Chapter 6). By means of these semi-empirical calculations the different possible structural arrangements around the impurity site were considered. In contrast to  $\text{Fe}^{3+}:\text{PbTiO}_3$  (cf. Chapter 8), *ab initio* calculations for the  $\text{Fe}^{3+}:\text{PbZrO}_3$  are not yet available. Therefore the predicted defect structures are based solely on the experimental EPR and the NSM semi-empirical analysis.

The parameters  $b_2^0$  and  $b_2^2$  of the  $\text{Fe}^{3+}$  defect are estimated for various arrangements of oxygen ligands via the NSM. These parameters are then compared with those determined experimentally. Mean values  $b_2^0 = 8.5(9)$  GHz and  $b_2^2 = 2.7(12)$  have been found. A large distribution width of  $\pm 10\%$  and  $\pm 40\%$  respectively, has to be assumed, much larger than the values found for  $\text{Fe}^{3+}:\text{PbTiO}_3$ . Apparently, in this crystal a set of different paramagnetic centres is found, leading to an apparent large ‘strain’ of  $b_2^0$  and  $b_2^2$ . As first guess we assume that all six oxygen positions can contribute to defect formation.

The reference NSM parameters  $t_2$  and  $\bar{b}_2(R_0)$  (cf. Sec. 6.2) are adopted from similar single crystal studies having  $\text{Fe}^{3+}-\text{O}^{2-}$  bonds in an octahedral coordination. For  $\text{Fe}^{3+}$  in  $\text{MgO}$ , the set of NSM parameters determined is  $\bar{b}_2(R_0) = -12.3514$  GHz,  $t_2 = 8$ , and  $R_0 = 210.1$  pm. The same parameters as in  $\text{PbTiO}_3$  are used. The set of NSM parameters determined from  $\text{CaO}$  is used to estimate expected errors.

For our calculations, the nearest-neighbour oxygen positions were taken from the X-ray data at 20 K (cf. Table 9.1). The coordinate system for the NSM calculation was chosen to coincide with the crystal coordinate system. In Fig. 10.1 one pseudocubic perovskite cell is depicted. It is assumed that the  $\text{Fe}^{3+}$  ion substitutes for  $\text{Zr}^{4+}$  at the centre of the pseudocubic cell.

The unit cell of  $\text{PbZrO}_3$  contains  $4 \times 2 \times 2 = 16$  distorted pseudocubic perovskite subunits. The pseudocubic subunit is of orthorhombic symmetry with lattice parameters  $(a_c, b_c, c_c)$ . In the low-temperature (antiferroelectric) phase, the Pb atoms are shifted antiparallel from the ideal perovskite positions into the direction  $[1\bar{1}0]_c$ . The  $\text{O}^{2-}$  octahedra are rotated around the  $[1\bar{1}0]_c$  axis. The Zr atoms are slightly displaced along  $[001]_c$  of the pseudocubic coordinate frame. All  $\text{Zr}^{4+}$  sites can be described by the same Wyckoff position (8i). Therefore the arrangement of the oxygen ligands is

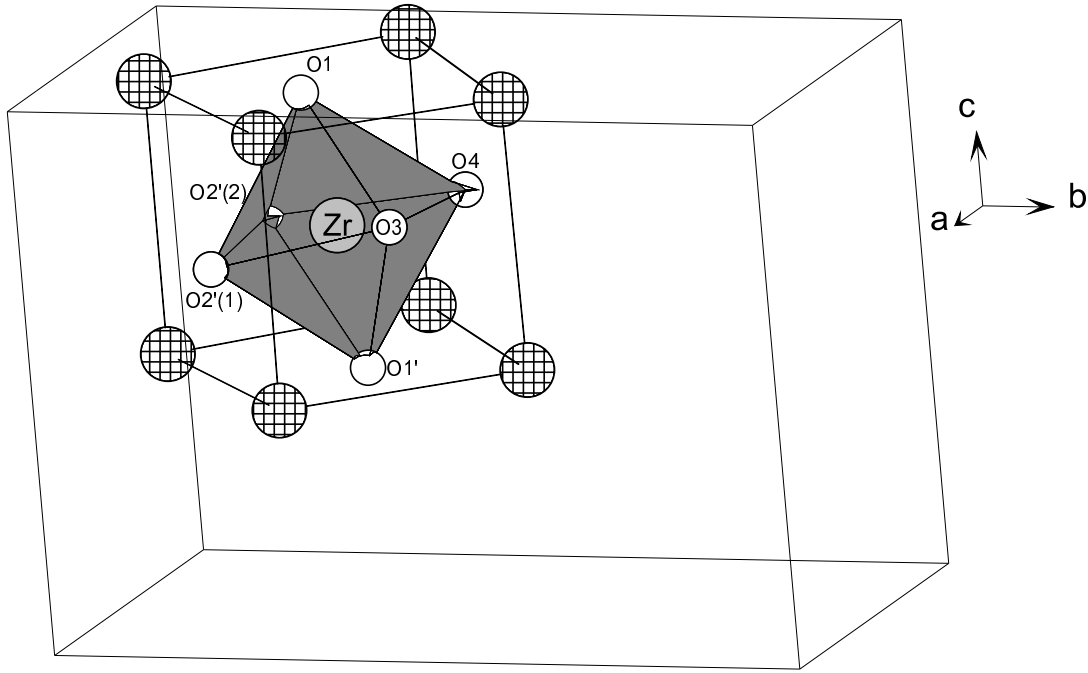


Fig. 10.1: An oxygen octahedron of  $\text{PbZrO}_3$  selected from the unit cell for the NSM calculations.

identical for all  $\text{Zr}^{4+}$  positions in the unit cell. Thus only a single oxygen octahedron has been taken into consideration. The influence of the Pb ions is neglected in the NSM analysis.

The crystal coordinate frame does not necessarily coincide with the proper crystal frame of the paramagnetic centre. Therefore, as indicated already in Sec. 6.2, all possible 2<sup>nd</sup>-order parameters  $b_k^q$  have to be evaluated. Finally, the fine structure tensor is transformed into its eigenframe. Then the resulting  $b_2^0$  and  $b_2^2$  parameters can be compared with the experimental data. Namely, all others  $b_k^2$  vanish in the proper coordinate frame.

Two different possibilities for structural arrangements are considered: (i) the  $\text{Fe}^{3+}$  ion has an oxygen vacancy in its first coordination sphere; or (ii) the  $\text{Fe}^{3+}$  ion has no oxygen vacancy in the first coordination sphere. The  $\text{Fe}^{3+}$  defect may occur as an  $\text{Fe}^{3+}-\text{V}_\text{O}$  defect associate or as a free defect surrounded by an intact oxygen octahedron. In Figs. 10.3 and 10.4 the models with a vacancy are symbolised by full lines, while the models without vacancy are marked by dashed lines.

In pure  $\text{PbZrO}_3$  all Zr-O distances differ (cf. Fig. 10.2). The symmetry determined for the spin Hamiltonian imposes no constraints on the orientation of a



$\text{Fe}^{3+}-\text{V}_{\text{O}}^{\bullet}$  defect dipole. The model of a directly coordinated oxygen vacancy can be realised in six different arrangements.  $\text{V}_{\text{O}}^{\bullet}$  can substitute for each of the oxygen ligands. Their positions in the local octahedron are defined by the crystal coordinate system given in Table 9.1.

The parameters  $b_2^0$  and  $b_2^2$  were calculated by varying the position of  $\text{Fe}^{3+}$  along the line connecting its initial position with the position of oxygen (vacancy). We tentatively have chosen displacements along this line. This assumption does not have a profound physical meaning even in the case of the intact octahedron. The distance  $d$  is defined as the shift of the  $\text{Fe}^{3+}$  ion along this line. A positive sign of  $d$  indicates a shift towards the respective oxygen (vacancy) position.

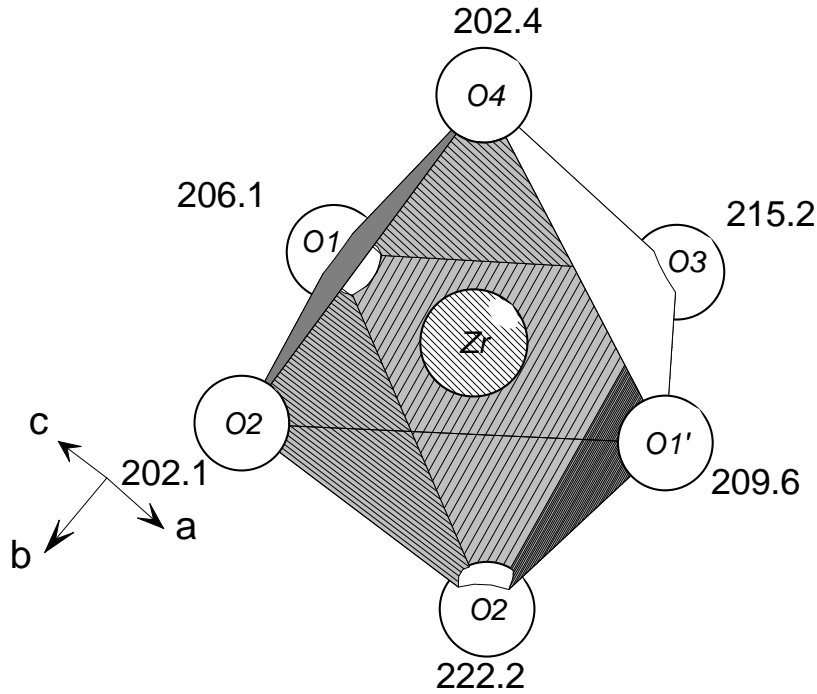
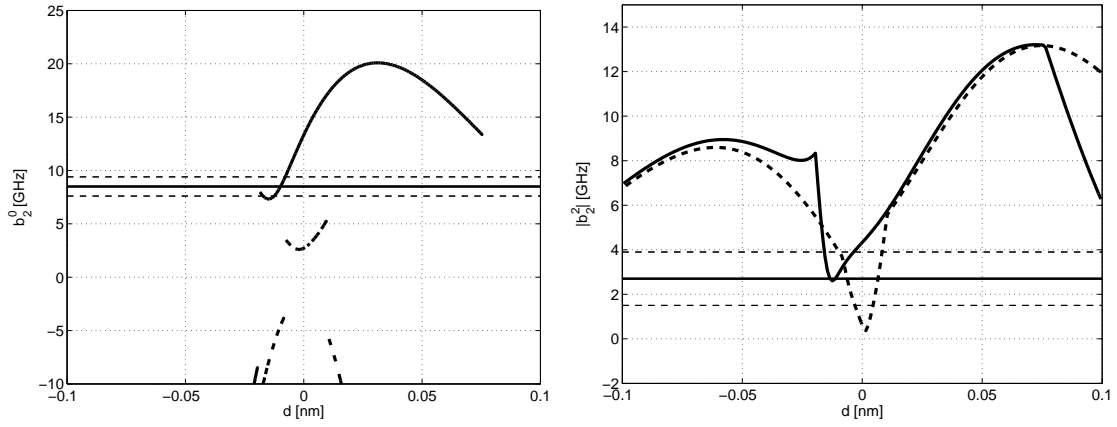
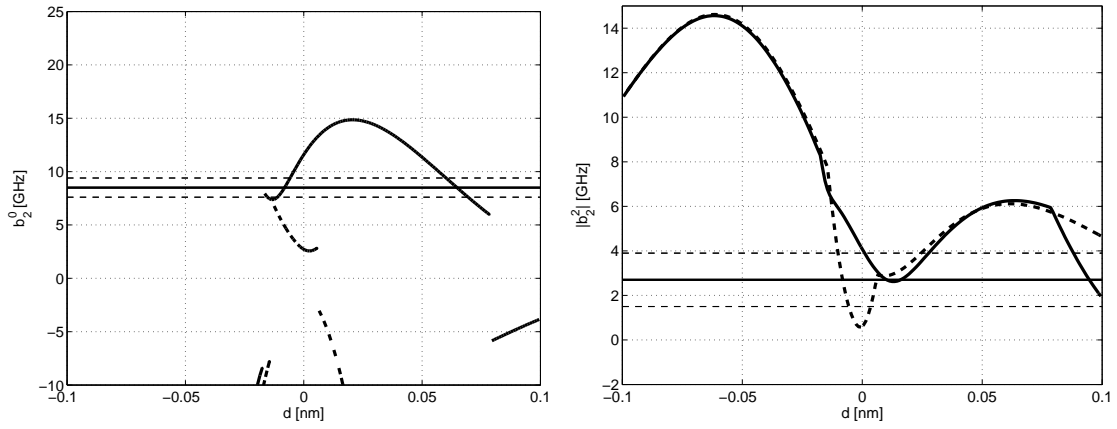


Fig. 10.2: An oxygen octahedron of  $\text{PbZrO}_3$  for the NSM calculations. Crystallographic symbols of the  $\text{O}^{2-}$  atoms are quoted. The numbers besides the  $\text{O}^{2-}$  atoms are distances from the  $\text{Zr}^{4+}$  ion in pm.

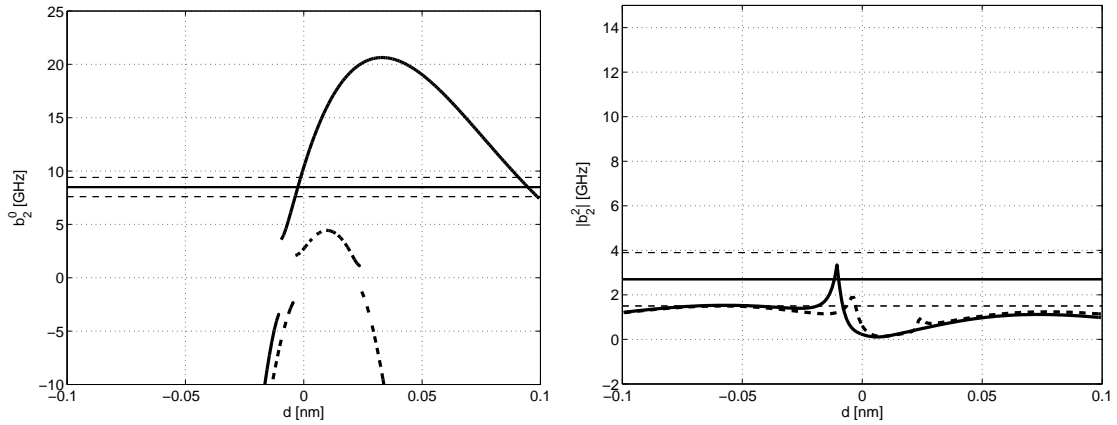
In Figs. 10.3 and 10.4, the calculated parameters  $b_2^0$  and  $b_2^2$  are displayed. They are shown as a function of the distance  $d$  for six structural models. For comparison, the experimentally observed values  $b_2^0$  and  $b_2^2$  are represented by solid horizontal lines. There is no way to relate one of the six possible EPR spectra to a certain structural model. Therefore the distribution of  $b_2^0$  and  $b_2^2$  values as determined by experiment is indicated by dashed horizontal lines. This interval is spanned by the six sets of spin Hamiltonian parameters which have been used to explain the width of structures in the EPR spectra (cf. Table 9.2).



(a) NSM calculations of  $b_2^0$  (left) and  $b_2^2$  (right) regarding oxygen position O1 at 206.1 pm



(b) NSM calculations of  $b_2^0$  (left) and  $b_2^2$  (right) regarding oxygen position O1' at 209.6 pm



(c) NSM calculations of  $b_2^0$  (left) and  $b_2^2$  (right) regarding oxygen position O2 at 222.2 pm

Fig. 10.3: The axis is defined along  $O^{2-}-Zr^{4+}$  bond with the positive direction towards the  $O^{2-}$  position; *solid horizontal lines* – experimental mean values; *dashed horizontal lines* – the range of values of the six constituent EPR spectra; *full lines* – NSM calculations assuming an oxygen vacancy; *dashed lines* – NSM calculations assuming a complete octahedron.

From the calculated diagrams the following conclusions can be drawn.

(a) When considering the axial  $b_2^0$  parameter, only the model with a nearby vacancy coincides with the range of experimental values for all six arrangements. In this context, the reliable determination of the sign of  $b_2^0$  should be mentioned. The model with a complete octahedron does not reproduce the experimental value. This is true for all six possible models. An oxygen vacancy substituting at any of the six nearest neighbour oxygen sites reproduces the experimental value of  $b_2^0$ . For each arrangement, however, two different displacements of  $\text{Fe}^{3+}$  are possible.

(b) When only considering the rhombic  $b_2^2$  parameter, an unambiguous decision concerning the neighbouring vacancy cannot be made, because its sign could not be determined from the powder EPR spectra. Therefore only absolute values of  $b_2^2$  are compared. Both models, i.e. with and without vacancy, are in agreement with experimental values because each model has at least one intersection with the experimental value. Experimental  $b_2^2$  values also cover a wider range than  $b_2^0$ . Hence, the above predictions are not as reliable as those coming from  $b_2^0$ . However, they may be used to support the predictions based on the  $b_2^0$  value.

(c) Discontinuities in the calculated dependence of parameters are observed. At certain points a discontinuous sign change can be noticed. This behaviour is explained by the fact that the displacement of  $\text{Fe}^{3+}$  is not necessarily along any proper axis of the fine structure tensor. In this low symmetry system, the proper coordinate frame can change when the ion is displaced to an other position. In the calculation procedure, however, the parameters are always expressed in the proper frame for every displacement. The  $z$ -axis is chosen so as to coincide with the largest absolute value in diagonalised  $\mathbf{D}$  matrix (cf. Sec. 6.2). Therefore these jumps may be considered as indicative for eigenframe reorientation, which happens when two parameters from fine structure matrix have same values. If all data would be expressed in the same coordinate system, smooth functions would appear. But in this case it would not be possible to compare the calculated numbers with experimental data.

In connection with the displacements of the  $\text{Fe}^{3+}$  centre from the original  $\text{Zr}^{4+}$  position, the  $b_2^0$ -calculations predict two possible displacements ( $d_1(b_2^0)$  and  $d_2(b_2^0)$ ) for each position of the vacancy. They are summarised in Table 10.1. The different displacements of  $\text{Fe}^{3+}$  can be compared qualitatively for different positions of vacancy. The displacement  $d_1(b_2^0) \approx 10$  pm corresponds to a small shift of  $\text{Fe}^{3+}$  in negative direction (away from vacancy). The second possible displacement  $d_2(b_2^0) \approx 70 - 90$  pm corresponds to a shift in positive direction (towards the vacancy). There is a remarkable coincidence for the predictions for all 6 different positions of oxygen vacancy.

Additional information provided by the calculation of  $b_2^2$  can be taken into account as well. The uncertainties in predicted displacement positions obtained in this way are much higher. They range from 5 – 30 pm. However, the predicted displacements could be used to discriminate between the two shifts  $d_1(b_2^2)$  and  $d_2(b_2^2)$ . For vacancy positions at O1, O2(1), O2(2) and O3, only one position  $d_1(b_2^2)$  near zero is predicted. In all four cases it is near to  $d_1(b_2^0)$ . For the vacancy positions at O1' and O4, a larger

$d_2(b_2^2)$  in addition to a smaller shift  $d_1(b_2^2)$  is found. Therefore the latter two cases do not offer a way to decide between the two positions.

However, on the basis of  $b_2^2$  calculation, we may conclude that a small shift  $d_1$  away from the oxygen vacancy is favoured. This is a displacement into a pyramid of remaining oxygen ions. Situation in which the  $\text{Fe}^{3+}$  centre is further displaced by  $d_2$  towards the oxygen vacancy does not seem to be probable.

Tab. 10.1: Possible displacement (in pm) of  $\text{Fe}^{3+}$  ion resulting from the NSM calculations of the  $b_2^0$  and  $b_2^2$  parameters for  $\text{Fe}^{3+}-\text{V}_{\text{O}}$  centre. The calculations were performed for  $\text{V}_{\text{O}}$  replacing an oxygen in the octahedron.

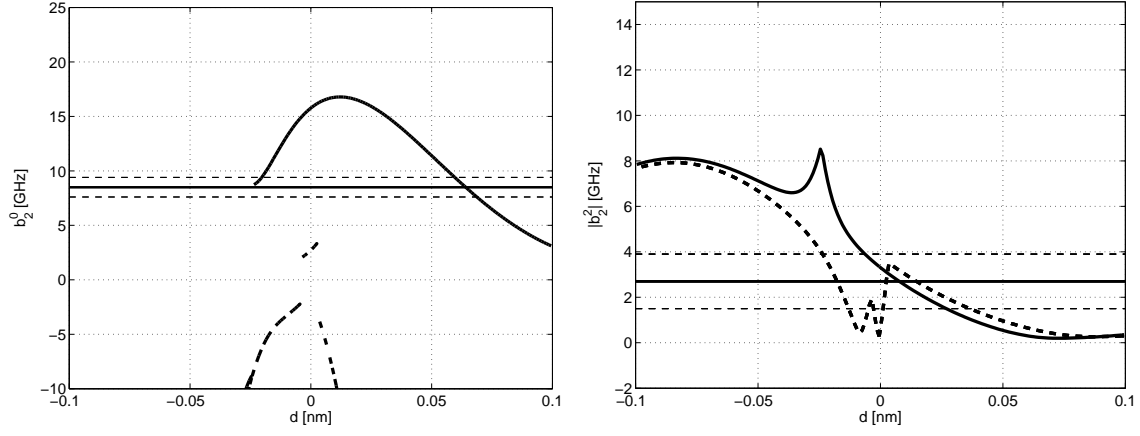
$\text{V}_{\text{O}}$ position	Zr-O length	from $b_2^0$		from $b_2^2$	
		$d_1(b_2^0)$	$d_2(b_2^0)$	$d_1(b_2^2)$	$d_2(b_2^2)$
O1	206.1	-10(6)	+75(5)	-12(5)	-
O1'	209.6	-10(6)	+64(5)	+13(10)	+95(7)
O2(1)	222.2	-2(6)	+94(5)	-14(4)	-
O2(2)	202.1	-23(5)	+64(5)	+7(15)	-
O3	214.0	-2(6)	+82(5)	-2(6)	-
O4	202.4	-10(6)	+70(5)	-28(10)	+50(30)

## 10.2 Discussion of the structure of $\text{Fe}^{3+}:\text{PbZrO}_3$

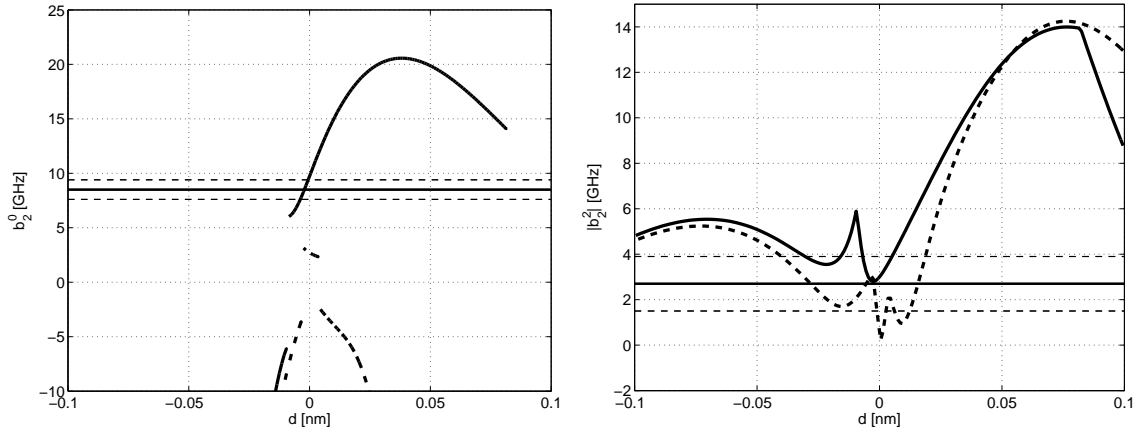
The most important information derived from the NSM calculations is that the  $\text{Fe}^{3+}$  paramagnetic ion in  $\text{PbZrO}_3$  always forms a charged  $\text{Fe}^{3+}-\text{V}_{\text{O}}$  defect associate. The oxygen vacancy  $\text{V}_{\text{O}}$  is part of the local oxygen octahedron. The same situation occurs in  $\text{Fe}^{3+}$ -modified  $\text{PbTiO}_3$ .

Next, in contrast to the  $\text{Fe}^{3+}-\text{V}_{\text{O}}$  defect associate in  $\text{PbTiO}_3$ , in which the defect associate occurs in a single orientation, the orientation of  $\text{Fe}^{3+}-\text{V}_{\text{O}}$  in  $\text{Fe}^{3+}:\text{PbZrO}_3$  is not determined by the crystal symmetry. The obtained result suggests the existence of a *multi site* situation in  $\text{Fe}^{3+}:\text{PbZrO}_3$ . This situation is generated by different possible orientations of the  $\text{Fe}^{3+}-\text{V}_{\text{O}}$  associate. The oxygen vacancy may occupy any of the six different ligand oxygen sites in  $\text{PbZrO}_3$  with equal probability.

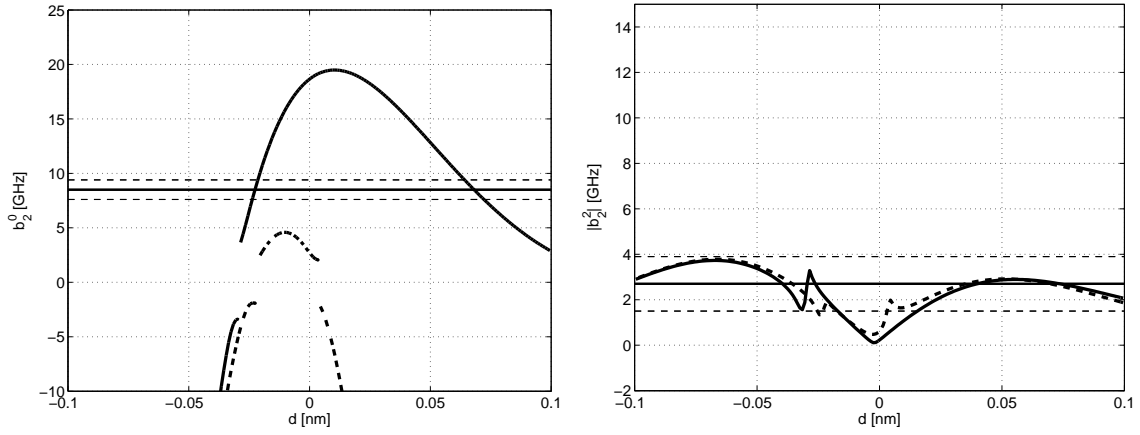
Further discussion about the details of six different centres would require a linear least-square fit of six individual spectra. The latter should be constructed with all possible combinations of the individual fine structure parameters. However, the exact individual parameters are not accessible by EPR. We only supposed a combination of six equally displaced spectra with anti-correlated  $b_2^0$  and  $b_2^2$  parameters. This set of spectra demonstrated better agreement with experiments than the correlated set.



(a) NSM calculation of  $b_2^0$  (left) and  $b_2^2$  (right) regarding oxygen position O2 at 202.1 pm



(b) NSM calculations of  $b_2^0$  (left) and  $b_2^2$  (right) regarding oxygen position O3 at 215.2 pm.



(c) NSM calculations of  $b_2^0$  (left) and  $b_2^2$  (right) regarding oxygen position O4 at 202.4 pm

Fig. 10.4: The axis is defined along  $\text{O}^{2-}\text{-Zr}^{4+}$  bond with the positive direction towards the  $\text{O}^{2-}$  position; *solid horizontal lines* – experimental mean values; *dashed horizontal lines* – the range of values of the six constituent EPR spectra; *full lines* – NSM calculations assuming an oxygen vacancy; *dashed lines* – NSM calculations assuming a complete octahedron.

However, this should be interpreted mere as a tendency, and not as the exact solution of the multi-site situation in  $\text{Fe}^{3+}$ -doped  $\text{PbZrO}_3$ .

Relative displacement of the  $\text{Fe}^{3+}$  ion in the truncated oxygen octahedron  $\text{PbZrO}_3$  are obtained via the NSM calculation of both second-order fine structure parameters. For this calculation only the average values of six sets of parameters are used. Qualitatively,  $\text{Fe}^{3+}$  tends to move towards the rest of the oxygen octahedron, away from vacancy. The shift amounts to between 2 and 20 pm, depending on the vacancy position. In these calculation the crystal distortions near the substituted ion are neglected.

This result can be compared to the situation in  $\text{PbTiO}_3$ . A displacement of the  $\text{Fe}^{3+}$  centre with respect to the original Ti position have been also observed in  $\text{PbTiO}_3$  (cf. 8.3). The displacement amounted either to  $d \approx -10$  pm in direction away from vacancy or to  $d > 20$  pm in direction towards vacancy, the former possibility being supported by DFT results.

In the case of  $\text{Fe}^{3+}:\text{PbZrO}_3$ , density functional calculations are not yet available. To select the preferred  $\text{Fe}^{3+}$  displacement, calculated and experimentally determined  $b_2^2$  parameters were compared instead. Because of the missing DFT data, the relaxation of the oxygen ions towards the oxygen vacancy, however, could not be considered in the NSM calculation. This may lead to further refinements of the functional dependence of the curves. In analogy to  $\text{PbTiO}_3$ , we expect that use of relaxed crystal coordinates will not have a strong influence on the qualitative conclusions.

From EPR measurements and NSM calculations alone it could not be predicted which (if any) of the six different arrangements of  $\text{Fe}^{3+}-\text{V}_{\text{O}}$  centre is most probable. Enhanced line broadening suggests, however – in contrast to  $\text{PbTiO}_3$  – that more than one arrangement occurs. The DFT calculation would be useful here in order to predict relative energy of various predicted arrangements.

This assignment is supported by results obtained for the  $\text{Cu}^{2+}$  centre in  $\text{PbZrO}_3$  that is not associated to an oxygen vacancy [16]. Here, the EPR lines for  $\text{Cu}^{2+}$ -modified  $\text{PbZrO}_3$  are not broadened as compared to  $\text{Cu}^{2+}:\text{PbTiO}_3$ . Consequently, the  $\text{Fe}^{3+}-\text{V}_{\text{O}}$  centre is expected being easier to reorient in lead zirconate as compared to lead titanate.

The mechanism of charge compensation in this compound can be discussed in analogy to  $\text{Fe}^{3+}:\text{PbTiO}_3$  (cf. Sec. 8.3). Partial charge compensation takes place at a nearest-neighbour oxygen site of the oxygen octahedron. The exclusive observation of defect associates excludes the existence of 'free'  $\text{Fe}^{3+}$  ions. It is suggested that overall charge compensation is rendered possible by double negatively charged lead vacancies  $V_{\text{Pb}}''$

$$[\text{V}_{\text{O}}] = [\text{Fe}'_{\text{Zr}}] + \frac{1}{2}[\text{V}_{\text{Pb}}''] \quad (10.1)$$

The charge-compensation could also be more complicated. Another unit of defect associates  $\text{Fe}^{3+}-\text{V}_{\text{O}}-\text{Fe}^{3+}$  might be formed. Lead vacancies would be not required to form these defect associates. The present EPR experiments do not support this hypothesis. In this case the strongly dipolar coupled iron centres would be detected.

Thus this model can be discarded.

In summary, the NSM provides reliable results from the 2<sup>nd</sup>-order fine structure parameters of  $\text{Fe}^{3+}$ -doped lead zirconate. It predicts necessary association of defects into the  $\text{Fe}^{3+}\text{-V}_{\text{O}}^{\bullet\bullet}$  complex and excludes possibility of ‘free’  $\text{Fe}^{3+}$ . This behaviour corresponds to the results obtained for lead titanate. However, while in lead titanate the defect complex was strictly oriented along  $c$ -axis, in lead zirconate it may take any orientation replacing any of the nearest oxygen ions. This result suggests much easier reorientation of the  $\text{Fe}^{3+}\text{-V}_{\text{O}}^{\bullet\bullet}$  complex in lead zirconate.





## 11. CONCLUSIONS AND OUTLOOK

Polycrystalline iron-modified lead titanate ( $\text{PbTiO}_3$ ) and lead zirconate ( $\text{PbZrO}_3$ ) have been investigated by electron paramagnetic resonance (EPR) techniques. A multi-frequency approach has been employed to determine the fine structure interaction of the  $\text{Fe}^{3+}$  centre in both compounds. Experiments have been performed at 9 GHz, 94 GHz, 190 GHz, 240 GHz and 319 GHz.

The EPR spectra of the  $\text{Fe}^{3+}$  ion in  $\text{PbTiO}_3$  exhibits axial symmetry. The fine structure parameter  $b_2^0$  of the spin Hamiltonian has been determined from high-frequency measurements. It amounts to  $b_2^0 = 32.3(2)$  GHz. Fourth-order tetragonal and cubic splitting parameters were not necessary because the spectra could be explained sufficiently at all frequencies by invoking second-order parameters only.

The  $\text{Fe}^{3+}$  centre in  $\text{PbZrO}_3$  has no symmetry (point group 1). The EPR spectra have been explained by a set of six different centres with low symmetry. Their spin Hamiltonian parameters have been averaged leading to the following mean values:  $b_2^0 = 8.5(9)$  GHz and  $b_2^2 = 2.8(12)$  GHz. In comparison to the iron centre in lead titanate, this reflects a considerably reduction of the fine structure interaction. Additionally, the  $\text{Fe}^{3+}$  spectra in  $\text{PbZrO}_3$  exhibit considerably broadened transitions. This observation has been explained by a multi-centre situation in  $\text{PbZrO}_3$ .

The local structure of the paramagnetic centres in both materials has been analysed via the Newman superposition model. The intrinsic parameters for the  $\text{Fe}^{3+}\text{--O}^{2+}$  pair have been taken from the measurements of Siegel and Müller [98]. The NSM analysis on the basis of the size and sign of  $b_2^0$  shows that the  $\text{Fe}^{3+}$  ion in both compounds is substituted at the B-site ( $\text{Ti}^{4+}/\text{Zr}^{4+}$ ) of the perovskite cell. Furthermore, only the structures assuming a directly coordinated oxygen vacancy agree with the experimental data. Hence, the incorporation of the  $\text{Fe}^{3+}$  ion in both  $\text{PbTiO}_3$  and  $\text{PbZrO}_3$  necessarily induces an oxygen vacancy in the surrounding oxygen octahedron.

The proposed orientation of the  $\text{Fe}^{3+}\text{--V}_\text{O}$  defect associate in  $\text{PbTiO}_3$  is along the crystallographic [001] axis. Any other orientation of the defect dipole would result in a fine structure tensor of lower than axial symmetry. In  $\text{PbZrO}_3$ , the  $\text{Fe}^{3+}\text{--V}_\text{O}$  defect associate can be oriented along any direction defined by the six oxygen atoms of the octahedron. This behaviour in  $\text{PbZrO}_3$  accounts for the six different paramagnetic centres observed by EPR.

*Ab initio* DFT calculations for  $\text{PbTiO}_3$  furthermore confirm the proposed model. They show that the total energy for the arrangement along the crystallographic [001]-axis is below the energy predicted for the orientations along the [100] and [010]-axes.

From two possible orientations along the [001]-axis, the structure with the vacancy at the nearest apical oxygen (O1) is energetically favoured.

The NSM analysis offers also some information on the position of the  $\text{Fe}^{3+}$  ion relative to the oxygen octahedron. The  $b_2^0$  calculation in both compounds is compatible with two possible distinct positions for the  $\text{Fe}^{3+}$  ion. Their preference can be discriminated on the basis of: (i) a DFT calculation for  $\text{PbTiO}_3$ , and (ii) a NSM calculation of  $b_2^0$  for  $\text{PbZrO}_3$ . Both calculations show that  $\text{Fe}^{3+}$  in both compounds is shifted by roughly 10 pm away from the vacancy. The origin chosen refers to the original  $\text{Ti}^{4+}/\text{Zr}^{4+}$  site. In every case the shift is towards the centre of the truncated oxygen octahedron.

According to the NSM results, the  $\text{Fe}^{3+}$  ion doped in  $\text{PbTiO}_3$  is almost centred in the perovskite pseudocubic subunit, a behaviour which differs from the site preference of the substituted  $\text{Ti}^{4+}$  ion. This suggests that the unit cells with the  $\text{Fe}^{3+}$  ion cannot participate in the same way in microscopic polarisation effects as encountered for  $\text{Ti}^{4+}$ . The present results confirm and extend the earlier investigations of Siegel and Müller [98] on  $\text{PbTiO}_3$ .

In  $\text{PbZrO}_3$ , the  $\text{Fe}^{3+}$  ion is moved also away from the oxygen vacancy. This result is valid for any of the six possible vacancy positions. The present analysis has been done for the first time. It can be compared with the  $\text{PbTiO}_3$  results. The same behaviour is found:  $\text{Fe}^{3+}$  is shifted towards the remaining oxygen pyramid.

The identification of a multi-site iron centre with different orientations of the  $\text{Fe}^{3+}-\text{V}_{\text{O}}$  defect dipole suggests that the reorientation of this dipole in lead zirconate occurs easier than in lead titanate. There the  $\text{Fe}^{3+}-\text{V}_{\text{O}}$  dipole is oriented strictly along the crystallographic [001] axis.

To support the low-temperature EPR results of this study, high-temperature experiments would be desirable. They would be helpful to answer the following question: Is the  $\text{Fe}^{3+}-\text{V}_{\text{O}}$  defect associate preserved at the high-temperature transition, or does the oxygen vacancy leaves the next-neighbour position? The latter behaviour would lead to a considerable decrease of the 2<sup>nd</sup>-order fine structure parameters, and in the cubic phase even to their disappearance. Some preliminary X-band experiments with  $\text{Fe}^{3+}$ -doped  $\text{PbZrO}_3$  were already carried out. The disappearance of the rhombic structure as well as a rise of the broad  $g \approx 2$  line at temperature near the tetragonal-to-cubic transition was observed. This might indicate a dissociation of the  $\text{Fe}^{3+}-\text{V}_{\text{O}}$  complex. Thereby  $\text{Fe}^{3+}$  is surrounded by the complete cubic oxygen octahedron. These experiments should be performed also for  $\text{PbTiO}_3$ , preferentially, under high field conditions. They would allow to monitor the change of the fine structure parameters as a function of temperature. In short, the observed changes in the spectra above the transition temperature might support our low-temperature spectra assignment of the  $\text{Fe}^{3+}-\text{V}_{\text{O}}$  defect.

In addition to the powder EPR experiments performed in this study, single-crystal experiments should confirm the presence of different centres in  $\text{PbZrO}_3$ . This has been indicated already in the previous X-band experiments by Laguta et al. [48]. In X-band, however, it was not possible to determine the values of the spin Hamiltonian

parameters. This clearly indicates the utility of the high-field EPR single crystal measurements. These experiments might also provide the exact spin Hamiltonian parameters for every individual centre.

In contrast to  $\text{PbTiO}_3$ , the  $\text{Fe}^{3+}$ -position in the  $\text{PbZrO}_3$  cell could be determined exclusively by NSM with its inherent large error margin. In  $\text{PbTiO}_3$ , *ab initio* results were available to select the preferred structural model. Such an approach would be also helpful to predict the relative energy of each possible structure of  $\text{Fe}^{3+}$ -doped  $\text{PbZrO}_3$ . The number of possible structural models which should be taken into account might be reduced in this way. It can be expected that the number of paramagnetic centres involved in the simulation might be reduced, allowing – at the same time – a better fit of the experimental spectra.

The next step in the systematic investigation of the defects in ferroelectrics would be analysis of donor-doped materials. From the EPR point of view, the  $\text{Gd}^{3+}$  ion should be a suitable choice. Multi-frequency experiments on  $\text{Gd}^{3+}$ -doped  $\text{PbTiO}_3$  have been performed already in the course of this work. The tetragonal fine structure parameter has been determined precisely [19]. At room temperature it amounts to  $b_2^0 = 2.330(5)$  GHz. A considerable variation with temperature has been observed. The 5 K value of  $b_2^0$  amounts to 2.580(5) GHz. The  $\text{Gd}^{3+}$  ions were assigned to substitute for  $\text{Pb}^{2+}$  at the A-site of the perovskite  $\text{ABO}_3$  lattice. The proposed charge-compensation mechanism is based on the creation of lead vacancies. The structure modelling in the  $\text{Gd}^{3+}$ -doped perovskite materials via the NSM is however limited by the fact that the nearest neighbour ions are  $\text{Pb}^{2+}$ . The intrinsic NSM parameters for this ions pair have not been determined yet.

The present investigation of  $\text{Fe}^{3+}$ -doped ferroelectrics should be considered also in the context of the mixed lead-zirconate-titanate system (PZT).  $\text{PbTiO}_3$  and  $\text{PbZrO}_3$  represent the end-members of this solid solution system. The  $\text{Fe}^{3+}$  ion may serve as a sensitive local probe to monitor phase changes [117]. Therefore EPR may help to determine the phase diagram of the PZT compound. Detailed EPR measurements of the various compositions of  $\text{Fe}^{3+}$ -doped PZT also have been carried out in the course of this work. The X-band spectra lead to the following conclusions: (i) the fine structure spin Hamiltonian parameters considerably exceed the microwave frequency of 10 GHz (low-field limit); (ii) a huge broadening of the  $\text{Fe}^{3+}$  transitions is observed when leaving the end-members of this solid-solution system; (iii) a change of the symmetry from tetragonal to extreme rhombic ( $b_2^2/b_2^0 \approx 1$ ) happens when changing the Zr/Ti ratio; and (iv) a co-existence of the  $\text{Fe}^{3+}$  centres of both tetragonal and rhombic symmetry in Ti-rich and morphotropic compositions has been observed. The conclusion that an  $\text{Fe}^{3+}$  defect always attracts an oxygen vacancy in the nearest octahedron can be extended to the mixed PZT system.

Under the assumption that the  $V_{\text{O}}$  defects are associated to  $\text{Fe}^{3+}$  centres also in PZT, any agglomeration of oxygen vacancies seems to be rather unlikely. The iron–oxygen vacancy defect complex is probably immobile in comparison to the ionic mobility of free oxygen vacancies. Thus, the charge transport in ceramic, which is mainly due to oxygen vacancies, will be hindered considerably. The agglomeration

of vacancies has been proposed in order to account for the observed ferroelectric fatigue mechanisms [76, 81, 55]. This consideration may serve as an explanation why iron-doped materials show better resistance to fatigue [56].

Acceptor–oxygen vacancy associates are probably less stable than donor–oxygen vacancy associates. They can be reorientated thermally in the presence of local or applied fields. These defect associates, once oriented in a common direction, produce an additional local field which stabilises the domain structure. From the inhibition of domain wall movements, a reduction in permittivity and an increase in the coercive field can be expected.

In order to derive quantitative results, the phase diagram of PZT should be measured with high-field EPR. During this work the low temperature W-band EPR spectra of the  $\text{Fe}^{3+}$ -doped PZT have already been measured. The analysis of these experiments shows that the fine structure parameters of  $\text{Fe}^{3+}$  are substantially changed. This behaviour has been observed already for the addition of 5% Ti to the  $\text{PbZrO}_3$ . The large line broadening in the mixed systems may, however, prevent a clear distinction and characterisation of the anticipated variety of paramagnetic centres.

A detailed analysis of these spectra may lead to important conclusions on the changes of the macroscopic properties of these technologically important ferroelectric materials under the influence of oxygen vacancies and iron doping.

## 12. ZUSAMMENFASSUNG

In dieser Arbeit wurden die mit Eisen modifizierten polykristallinen Bleititanat- ( $\text{PbTiO}_3$ ) und Bleizirkonat-Keramiken ( $\text{PbZrO}_3$ ) mit der Methode der Elektronen Paramagnetischen Resonanz untersucht. Für die Bestimmung der Feinstrukturparameter des  $\text{Fe}^{3+}$  Zentrum in beiden Verbindungen war ein Multifrequenz Vorgehen notwendig. Die EPR Experimente wurden bei 9 GHz, 94 GHz, 190 GHz, 240 GHz und 319 GHz durchgeführt.

Das EPR Spektrum des  $\text{Fe}^{3+}$  Ions in  $\text{PbTiO}_3$  weist eine axiale Symmetrie auf. Der axiale Feinstrukturparameter  $b_2^0$  wurde mit der Hochfeld EPR bestimmt. Er beträgt  $b_2^0 = 32.3(2)$  GHz. Parameter in vierter Ordnung werden nicht ausgewertet, da die Spektren für alle Frequenzen hinreichend mit einem Parameter der zweiten Ordnung erklärt werden konnten.

Das  $\text{Fe}^{3+}$  Zentrum in  $\text{PbZrO}_3$  weist keine Symmetrie auf (Punktgruppe 1). Die EPR Spektren wurden mit einem Satz von sechs unterschiedlichen Zentren niedriger Symmetrie simuliert. Die Parameter des Spin Hamilton Operators wurden danach gemittelt. Für den axialen und rhombischen Parameter wurden folgende Werte beobachtet:  $b_2^0 = 8.5(9)$  GHz und  $b_2^2 = 2.8(12)$  GHz. Diese Werte weisen auf eine bemerkenswerte Reduzierung der Feinstruktur Wechselwirkung im Vergleich zu den Eisenzentren im Bleititanat hin. Eine erhebliche Verbreiterung der Linien in Bleizirkonat wurde mit mehreren paramagnetischen Zentren erklärt.

Die lokale Struktur der paramagnetischen Zentren in beiden Materialien wurde anschließend mit dem Newman Superpositionsmodell analysiert. Der Wert für den intrinsischen Parameter des  $\text{Fe}^{3+}\text{-O}^{2-}$  Paares wurde aus den Messungen von Siegel und Müller [98] entnommen. Die NSM Analyse unter Verwendung der Grösse und des Vorzeichens des Parameters zeigt eindeutig, dass das  $\text{Fe}^{3+}$  Ion in beiden Verbindungen auf dem  $\text{Ti}^{4+}/\text{Zr}^{4+}$  Platz der Perowskit-Zelle eingelagert wurde. Nur die Strukturen, die eine zu  $\text{Fe}^{3+}$  direkt koordinierte Sauerstoff Leerstelle haben, stimmen mit den experimentellen Parametern überein. Deshalb führt eine Dotierung von Bleititanat und Bleizirkonat mit Eisen immer zu einer Leerstelle in dem umgebenden Sauerstoffoktaeder.

Das vorgeschlagene  $\text{Fe}^{3+}\text{-V}_{\text{O}}$  Defektassoziat in  $\text{PbTiO}_3$  ist entlang der kristallographischen  $[001]$  Achse orientiert. Entweder wird die Leerstelle des näheren (O1) oder weiter entfernten Sauerstoffs (O1') substituiert. Jede andere Orientierung würde zu einem Feinstruktur Tensor einer niedrigeren Symmetrie führen. Das  $\text{Fe}^{3+}\text{-V}_{\text{O}}$  Defektassoziat in  $\text{PbZrO}_3$  kann entlang jeder der von sechs Sauerstoffatomen definierten Richtungen orientiert werden. Diese verschiedenen Möglichkeiten für die Position

der Sauerstoffleerstelle sind für die Beobachtung von sechs unterschiedlichen paramagnetischen Zentren verantwortlich.

Die *ab initio* DFT Rechnungen für  $\text{PbTiO}_3$  haben zusätzlich das vorgeschlagene Modell bestätigt. Die Rechnungen haben gezeigt, dass die Anordnung mit dem Defektassoziat entlang der  $[001]$  Achse eine günstigere Energie aufweist als die Modelle mit dem Defektassoziat entlang der  $[100]$  oder  $[010]$  Achsen. Von den beiden Möglichkeiten die mit der  $[001]$ -Achse vereinbar sind, bevorzugt die DFT Rechnung eine Leerstelle an der näheren Sauerstoffposition (O1).

Die NSM Analyse hat auch Informationen über die Position des  $\text{Fe}^{3+}$  Ions bezüglich des Sauerstoffoktaeders geliefert. Mit Rechnungen auf der Basis eines axialen Feinstrukturparameters sind zwei möglichen Strukturen mit unterschiedlichen Positionen des  $\text{Fe}^{3+}$  Ions vereinbar. Zwischen beiden Positionen konnte folgendermassen unterschieden werden: (i) die DFT Berechnungen für  $\text{PbTiO}_3$ , und (ii) die NSM Analyse basiert auf dem rhombischen Feinstrukturparameter. (i) und (ii) haben gezeigt, dass das  $\text{Fe}^{3+}$  Ion um ungefähr 10 pm von der ursprünglichen  $\text{Ti}^{4+}/\text{Zr}^{4+}$  Position verschoben ist. Die Richtung der Verschiebung ist entgegengesetzt zur Leerstelle.

Nach den NSM Berechnungen ist das  $\text{Fe}^{3+}$  Ion in der Nähe des Zentrums der pseudokubischen Einheit der Perowskit-Zelle positioniert. Dieses Verhalten unterscheidet sich von dem des substituierten  $\text{Ti}^{4+}$  Ions. Eine Struktureinheit mit einem  $\text{Fe}^{3+}$  Defekt partizipiert nicht in der gleichen Weise an der mikroskopischen Polarisierung wie in  $\text{Ti}^{4+}$ . Diese Resultate bestätigen und erweitern eine frühere Untersuchung an Bleititanat von Siegel und Müller[98].

Im  $\text{PbZrO}_3$  ist das  $\text{Fe}^{3+}$  Ion auch entgegengesetzt zur Sauerstoffleerstelle um ungefähr 2 pm bis 20 pm verschoben. Dieses Ergebnis gilt für jede der sechs Sauerstoffpositionen. In dieser Arbeit wurde diese Analyse erstmals für  $\text{PbZrO}_3$  unternommen. Die Identifikation mehrerer Eisenzentren mit unterschiedlichen Orientierungen des  $\text{Fe}^{3+}-\text{V}_{\text{O}}$  Assoziats zeigt, dass seine Reorientierung im Bleizirkonat leichter als im Bleititanat möglich ist.

## BIBLIOGRAPHY

- [1] A. Abragam and B. Bleaney. *Electron paramagnetic resonance of transition ions*. Clarendon Press, Oxford, 1970.
- [2] A. Abragam and M. Pryce. Theory of the nuclear hyperfine structure of paramagnetic resonance spectra in crystals. *Proc. Roy. Soc. A*, 205:135, 1951.
- [3] R. Baer, G. Wessel, and R. Rubins. Paramagnetic resonance study at millimeter wavelents of an axial  $\text{Fe}^{3+}$  spectrum in strontium titanate. *J. Appl. Phys.*, 39:23–28, 1968.
- [4] H. Bethe and G. Gentile. Termaufspaltung in kristallen. *Ann. Physik.*, 3:133, 1929.
- [5] B. Bleaney and R. Trenam. The paramagnetic resonance spectra of gadolinium and neodymium ethyl sulphates. *Proc. Roy. Soc. A*, 223:15–29, 1954.
- [6] Bruker Biospin GmbH. *Bruker Elexsys 680*, 2000.
- [7] H. Buckmaster and Y. Shing. A survey of the EPR spectra of  $\text{Gd}^{3+}$  in single crystals. *Phys. Stat. Sol. A*, 12:325, 1972.
- [8] T. Castner, G. Newell, W. Holton, and C. Stichter. Note on the paramagnetic resonance of iron in glass. *J. Chem. Phys.*, 32:668, 1960.
- [9] B. Chowdari and P. Venkateswarlu. Electron paramagnetic resonance of  $\text{Mn}^{2+}$  in  $\text{K}_2\text{SO}_4$  single crystal. *J. Chem. Phys.*, 48:318–322, 1968.
- [10] D. Corker, A. Glazer, J. Dec, K. Roleder, and R. Whatmore. A re-investigation of the crystal structure of the perovskite  $\text{PbZrO}_3$  by X-ray and neutron diffraction. *Acta Cryst.*, B53:135–142, 1997.
- [11] L. Cross. *Ferroelectric ceramics*, chapter *Ferroelectric cermaics: tailoring properties for specific applications*. Birkhäuser Verlag Basel, 1993.
- [12] X. Dai, J.-F. Li, and D. Viehland. Effects of quenched disorder on La-modified lead zirconate titanate: Long- and short-range ordered structurally incommensurate phases, and glassy polar clusters. *Phys. Rev. B*, 51:2651–2655, 1995.

- [13] D. Damjanovic. Ferroelectric, dielectric and piezoelectric properties of ferroelectric thin films and ceramics. *Rep. Prog. Phys.*, 61:1267–1324, 1998.
- [14] R. de L. Kronig and C. Bouwkamp. Spin-levels and paramagnetic dispersion in iron-ammoniumalum. *Physica*, 6:290, 1939.
- [15] P. Debye. *Ann. Phys.*, 32:85, 1938.
- [16] R.-A. Eichel, K.-P. Dinse, H. Kungl, M. H. , A. Ozarowski, J. van Tol, and L.-C. Brunel. Exploring the morphotropic phase boundary in copper(II)-modified  $\text{Pb}[\text{Zr}_{0.54}\text{Ti}_{0.46}]\text{O}_3$  ferroelectrics. *Appl. Phys. A*, 80:51–54, Jan. 2005.
- [17] R.-A. Eichel, H. Kungl, and M. J. Hoffmann. Determination of functional center local environment in copper-modified  $\text{PbZr}_{0.54}\text{Ti}_{0.46}\text{O}_3$  ceramics. *J. Appl. Phys.*, 95(12):8092–8096, 2004.
- [18] R.-A. Eichel, H. Meštrić, K.-P. Dinse, A. Ozarowski, L. B. J. van Tol, H. Kungl, and M. Hoffmann. High-field EPR of paramagnetic functional centers in  $\text{Cu}^{2+}$ - and  $\text{Fe}^{3+}$ -modified PZT ferroelectrics. *Magn. Res. Chem.*, 43:S166 – S173, 2005.
- [19] R.-A. Eichel, H. Meštrić, H. Kungl, and M. J. Hoffmann. Multi-frequency electron paramagnetic resonance analysis of polycrystalline gadolinium-doped  $\text{PbTiO}_3$  - charge compensation and site of incorporation. *Appl. Phys. Lett.*, in print, 2006.
- [20] R. Elliott and K. Stevens. The theory of the magnetic properties of rare earth salts - cerium ethyl sulphate. *Proc. R. Soc.*, A215:437, 1952.
- [21] E. Erdem, R. Böttcher, H.-C. Semmelhack, and H. Gläsel. Multi-frequency EPR study of  $\text{Cr}^{3+}$  doped lead titanate ( $\text{PbTiO}_3$ ) nanopowders. *Phys. Stat. Sol. b*, 239:R7–R9, 2003.
- [22] E. R. Feher. Effect of uniaxial stresses on the paramagnetic spectra of  $\text{Mn}^{3+}$  and  $\text{Fe}^{3+}$  in  $\text{MnO}$ . *Phys. Rev.*, 136:A145–A157, 1964.
- [23] J. Fousek and V. Janovec. The orientation of domain walls in twinned ferroelectric crystals. *J. App. Phys*, 40(1):135–142, 1969.
- [24] H. Fujishita and S. Hoshino. A study of structural phase-transitions in anti-ferroelectric  $\text{PbZrO}_3$  by neutron-diffraction. *J. Phys. Soc. Japan*, 53:226–234, 1984.
- [25] H. Fujishita, Y. Ishikawa, S. Tanaka, A. Ogawaguchi, and S. Katano. Crystal structure and order parameters in the phase transition of antiferroelectric  $\text{PbZrO}_3$ . *J. Phys. Soc. Japan*, 72:1426–1435, 2003.



- 
- [26] H. Fujishita, Y. Shiozaki, N. Achiwa, and E. Sawaguchi. Crystal-structure determination of antiferroelectric  $\text{PbZrO}_3$  - application of profile analysis method to powder method of X-ray and neutron-diffraction. *J. Phys. Soc. Japan*, 51, 1982.
- [27] D. Gainon. Electron paramagnetic resonance of  $\text{Fe}^{3+}$  in the strong axial field of  $\text{PbTiO}_3$  host. *Phys. Rev*, 134:A1300–A1301, 1964.
- [28] A. Glazer and S. Mabud. Powder profile refinement of lead zirconate titanate at several temperature. 2. Pure  $\text{PbTiO}_3$ . *Acta Cryst.*, B34:1065–1070, 1978.
- [29] J. S. Griffith. Theory of the isotropic  $g$  value of 4.27 found for some high-spin ferric ions. *Mol Phys*, 8:213–216, 1964.
- [30] G. H. Haertling. Ferroelectric ceramics: History and technology. *J. Am. Ceram. Soc.*, 82(4):797 – 818, 1999.
- [31] G. Hanson, K. Gates, C. Noble, M. Griffin, A. Mitchell, and S. Benson. XSophe-Sophe-XeprView (R). A computer simulation software suite (v. 1.1.3) for the analysis of continuous wave EPR spectra. *J. Inorg. Biochem.*, 98:903–916, 2004.
- [32] A. K. Hassan, J. Pardi, L. A. and Krzystek, A. Sienkiewicz, P. Goy, M. Rohrer, and L.-C. Brunel. Ultrawide band multifrequency high-field EMR technique: A methodology for increasing spectroscopic information. *J. Magn. Res.*, 142:300–312, 2000.
- [33] G. T. D. Hutton. Paramagnetic resonance of  $\text{Fe}^{3+}$  in kyanite. *Brit. J. Appl. Phys.*, 15:1493–1499, 1964.
- [34] S. Ikegami, I. Ueda, and T. Miyazawa. Phase transitions of  $\text{PbTiO}_3$  at low temperatures. *J. Phys. Soc. Japan*, 26:1324, 1969.
- [35] B. Jaffe, W. Cook, and H. Jaffe. *Piezoelectric ceramics*. Academic Press, London, 1971.
- [36] Q. Jiang, E. Subbarao, and L. Cross. Effect of composition and temperature on electric fatigue of La-doped lead zirconate titanate ceramics. *J. Appl. Phys.*, 75:7433–7443, 1994.
- [37] F. Jona, G. Shirane, F. Mazzi, and R. Pepinsky. X-ray and neutron diffraction study of antiferroelectric lead zirconate,  $\text{PbZrO}_3$ . *Phys. Rev.*, 105:849–856, 1957.
- [38] D. Keeble, B. Nielsen, A. Krishnan, K. Lynn, S. Madhukar, R. Ramesh, and C. Young. Vacancy defects in  $(\text{Pb}, \text{La})(\text{Zr}, \text{Ti})\text{O}_3$  capacitors observed by positron annihilation. *Appl. Phys. Lett.*, 73:318, 1998.

- [39] A. Kip, C. Kittel, R. Levy, and A. Portis. Electronic structure of F centers: hyperfine interactions in electron spin resonance. *Phys. Rev.*, 91:1066–1971, 1953.
- [40] E. Kirkpatrick, K. Müller, and R. Rubins. Strong axial electron paramagnetic resonance spectrum of  $\text{Fe}^{3+}$  in  $\text{SrTiO}_3$  due to nearest-neighbor charge compensation. *Phys. Rev.*, 135:A86–A90, 1964.
- [41] C. Kittel. Theory of antiferroelectric crystals. *Phys. Rev.*, 82:729–732, 1951.
- [42] J. Kobayashi and R. Ueda. X-ray study of phase transition of ferroelectric  $\text{PbTiO}_3$  at low temperature. *Phys. Rev.*, 99:1900, 1955.
- [43] J. Kobayashi, Y. Uesu, and Y. Sakemi. X-ray and optical studies on phase-transition of  $\text{PbTiO}_3$  at low-temperatures. *Phys. Rev. B*, 28:3866, 1983.
- [44] E. König and R. Schnakig. Zero-field splitting of  $\text{S}(\text{d}^5)\text{-S-6}$  ions in tetragonal and rhombic symmetry. 1. Complete d-electron calculation of crystal-field dependence of D and E. *Phys. Status Solidi B*, 77:657, 1976.
- [45] J. Krzystek, S. Zvyagin, A. Ozarowski, A. Fiedler, T. Brunold, and J. Telser. Definitive spectroscopic determination of zero-field splitting in high-spin cobalt(II) . *J. Am. Chem. Soc.*, 126:2148–2155, 2004.
- [46] H. Kungl. PhD thesis, University of Karlsruhe, 2005.
- [47] V. Laguta, T. Antimirova, M. Glinchuk, I. Bykov, J. Rosa, M. Zaritskii, L. Jastrabík, L. Soukupnstitute, Y. Wanzong, Z. Jianrong, and L. Gaomin. Distortion of oxygen octahedron in antiferroelectric  $\text{PbZrO}_3$ : ESR evidence. *J.Kor. Phys. Soc.*, 32:S700–S702, 1998.
- [48] V. Laguta, M. Glinchuk, I. Bykov, Y. Maksimenko, J. Rosa, and L. Jastrabík. Impurity centers in  $\text{PbTiO}_3$  single crystals: An electron-spin-resonance analysis. *Phys. Rev. B*, 54:12353–12360, 1996.
- [49] A. Larson and R. V. Dreele. General Structure Analysis System (GSAS). *Los Alamos National Laboratory Report LAUR*, pages 86–748, 2004.
- [50] L. Levin and K. Eriksonas. Characteristic parameters of the  $\text{Eu}^{2+}$  S-state splitting in low-symmetric centres with  $\text{F}^-$  and  $\text{Cl}^-$  ligands . *J. Phys. C*, 20:2081–2088, May 1987.
- [51] G. Lewis and C. Catlow. Computer modeling of barium-titanate. *Rad. Eff*, 73:307–314, 1983.
- [52] O. Lewis and G. Wessel. Electron-spin-resonance investigation of ferroelectric lead titanate. *Phys. Rev. B*, 13:2742–2746, 1976.

- 
- [53] M. Lines and A. Glass. *Principles and applications of ferroelectrics and related materials*. Oxford University Press, Oxford, 2001.
- [54] W. Low. *Paramagnetic resonance in solids*. Academic Press, New York, 1960.
- [55] D. Lupascu. *Fatigue in Ferroelectric Ceramics and Related Issues*. Springer, Heidelberg, 2004.
- [56] S. B. Majumder, B. Roy, R. S. Katiyar, and S. B. Krupanidhi. Improvement of the degradation characteristics of sol-gel derived PZT(53/47) thin films: Effect of conventional and graded iron doping. *Integrated Ferroelectrics*, 39:127–136, 2001.
- [57] H. Matsuoka, K. Furukawa, K. Sato, D. Shiomi, Y. Kojima, K. Hirotsu, N. Furuno, T. Kato, and T. Takui. Importance of fourth-order zero-field splitting terms in random-orientation EPR spectra of Eu(II)-doped strontium aluminate. *J. Phys. Chem. A*, 107(51):11539–11546, 2003.
- [58] H. Meinke and F. Gundlach. *Taschenbuch der Hochfrequenztechnik*. Springer-Verlag, Berlin, 1968.
- [59] R. Merkle. Defect association in acceptor-doped  $\text{SrTiO}_3$ : case study for  $\text{Fe}'_{\text{Ti}}\text{V}_\text{O}$  and  $\text{Mn}''_{\text{Ti}}\text{V}_\text{O}$ . *Phys. Chem. Chem. Phys.*, 5:2297–2303, 2003.
- [60] A. Messiah. *Quantum Mechanics*. Dover Publications, New York, 2000.
- [61] H. Meštrić, R.-A. Eichel, K.-P. Dinse, A. Ozarowski, J. van Tol, and L. Brunel. High-frequency EPR investigation of the  $\text{Fe}^{3+}$  impurity center in polycrystalline  $\text{PbTiO}_3$  in its ferroelectric phase. *J. Appl. Phys.*, 96:7440–7444, 2004.
- [62] H. Meštrić, R.-A. Eichel, K.-P. Dinse, A. Ozarowski, J. van Tol, L. Brunel, H. Kungl, M. Hoffmann, K. Schönau, M. Knapp, and H. Fuess. Iron-oxygen vacancy defect association in polycrystalline iron-modified  $\text{PbZrO}_3$  antiferroelectrics – multi-frequency electron paramagnetic resonance and Newman superposition model analysis. *Phys. Rev. B*, in print, 2006.
- [63] H. Meštrić, R.-A. Eichel, T. Kloss, K.-P. Dinse, S. Laubach, S. Laubach, P. Schmidt, K. Schönau, M. Knapp, and H. Ehrenberg. The nature of iron-oxygen vacancy defect centers in  $\text{PbTiO}_3$ . *Phys. Rev. B*, 71:134109, 2005.
- [64] B. Meyer and D. Vanderbilt. Ab initio study of ferroelectric domain walls in  $\text{PbTiO}_3$ . *Phys. Rev. B*, 65:104111, 2002.
- [65] S. Misra. A rigorous evaluation of spin-Hamiltonian parameters and linewidth from a polycrystalline EPR spectrum. *J. Magn. Res.*, 140:179–188, 1999.
- [66] A. Moulson and J. Herbert. *Electroceramics: materials, properties, applications*. Chapman and Hall, London, 1993.

- 
- [67] K. Müller. Paramagnetische Resonanz von  $\text{Fe}^{3+}$  in  $\text{SrTiO}_3$  Einkristallen. *Helv. Phys. Acta*, 31:173–204, 1958.
- [68] F. Neese. *Calculation of NMR and EPR Parameters*, chapter Zero-Field Splitting, pages 541–564. Wiley-VCH Verlag, Weinheim, 2004.
- [69] D. Newman. Theory of lanthanide crystal fields. *Adv. Phys.*, 20:197–256, 1971.
- [70] D. Newman. On the g-shift of S-state ions. *J. Phys. C*, 10:L315–L318, 1977.
- [71] D. Newman and B. Ng. The superposition model of crystal fields. *Rep. Prog. Phys.*, 52:699–763, 1989.
- [72] D. Newman and E. Siegel. Superposition model analysis of  $\text{Fe}^{3+}$  and  $\text{Mn}^{2+}$  spin-hamiltonian parameters. *J. Phys. C*, 9:4285–4292, 1976.
- [73] D. Newman and W. Urban. Interpretation of S-state ion EPR spectra. *Adv. Phys.*, 24:783–844, 1975.
- [74] J. F. Nye. *Physical Properties of Crystals*. Clarendon Press, Oxford, 1985.
- [75] J. Orton. *Electron paramagnetic resonance: An introduction to transition group ions in crystals*. London Iliffe Books, London, 1968.
- [76] G. Pike, W. Warren, D. Dimos, B. Tuttle, R. Ramesh, J. Lee, V. Keramidas, and J. Evans. Voltage offsets in  $(\text{Pb},\text{La})(\text{Zr},\text{Ti})\text{O}_3$  thin films. *Appl. Phys. Lett.*, 66:484, 1995.
- [77] J. Pilbrow. Effective  $g$  values for  $S = \frac{3}{2}$  and  $S = \frac{5}{2}$ . *J. Magn. Reson.*, 31:479–490, 1978.
- [78] J. Pilbrow. *Transition ion electron paramagnetic resonance*. Clarendon Press, Oxford, 1990.
- [79] R. Pontin, E. Slade, and D. Ingram. Millimeter wave e.s.r. studies of ferric iron in perovskite-type oxides. *J. Phys. C*, 2(7):1146–1150, 1969.
- [80] A. Portis. Electronic saturation of F centers: saturation of the electron spin resonance. *Phys. Rev.*, 91:1071–1078, 1953.
- [81] S. Pöykkö and D. Chadi. First principles study of Pb vacancies in  $\text{PbTiO}_3$ . *Appl. Phys. Lett.*, 76:499–501, 2000.
- [82] M. Pryce. A modified perturbation procedure for a problem in paramagnetism. *Proc. Phys. Soc. A*, 63:25–29, 1950.
- [83] M. Pryce. Spin-spin interaction within paramagnetic ions. *Phys. Rev.*, 80:1107, 1950.

- 
- [84] E. Purcell. *Electricity and magnetism*. McGraw-Hill, New York, 2nd edition, 1984.
- [85] M. Raymond and D. Smyth. Defects and charge transport in perovskite ferroelectrics. *J. Phys. Chem. Solids*, 57:1507, 1996.
- [86] U. Robels and G. Arlt. Domain wall clamping in ferroelectrics by orientation of defects. *J. Appl. Phys.*, 73(7):3454–3460, 1993.
- [87] C. Rudowicz. Relations between arbitrary symmetry spin-Hamiltonian parameters  $B_k^q$  and  $b_k^q$  various axis systems. *J. Magn. Res.*, 63(1):95–106, 1985.
- [88] C. Rudowicz. Concept of spin Hamiltonian, form of zero field splitting and electronic Zeeman Hamiltonians and relations between parameters used in EPR. A critical review. *Magn. Reson. Rev.*, 13:1–89, 1987.
- [89] C. Rudowicz. Comment on ‘Analytical expressions for zero-field splittings of  $3d^5$  ions in low-symmetry fields and their applications’. *Phys. Rev. B*, 63:106401, 2001.
- [90] C. Rudowicz and S. K. Misra. Spin-Hamiltonian formalisms in electron magnetic resonance and related spectroscopies. *Appl. Spectr. Rev.*, 36(1):11–26, 2001.
- [91] C. Rudowicz and H. Sung. Can the electron magnetic resonance (EMR) techniques measure the crystal (ligand) field parameters? *Physica B*, 300:1–26, 2001.
- [92] G. Sághi-Szabó, R. Cohen, and H. Krakauer. First-principles study of piezoelectricity in  $\text{PbTiO}_3$ . *Phys. Rev. Lett.*, 80:4321–4324, 1998.
- [93] B. Scott and G. Burns. Crystal-growth and observation of ferroelectric phase of  $\text{PbZrO}_3$ . *J. Am. Ceram. Soc.*, 55:331, 1972.
- [94] R. Serway, W. Berlinger, K. Müller, and R. Collins. Electron-paramagnetic resonance of 3 manganese centers in reduced  $\text{SrTiO}_3$ . *Phys. Rev. B*, 16:4761, 1977.
- [95] G. Shirane, R. Pepinsky, and B. C. Frazer. X-ray and neutron diffraction study of ferroelectric  $\text{PbTiO}_3$ . *Acta Cryst.*, 9:131–140, 1956.
- [96] V. Shur. *Ferroelectric Thin Films: Synthesis and Basic Properties*, chapter *Fast polarisation reversal process*. Gordon and Breach Publishers, Amsterdam, 1996.
- [97] E. Siegel and K. Müller. Local position of  $\text{Fe}^{3+}$  in ferroelectric  $\text{BaTiO}_3$ . *Phys. Rev. B*, 20:3587–596, 1979.

- 
- [98] E. Siegel and K. Müller. Structure of transition-metal oxygen-vacancy pair centers. *Phys. Rev. B*, 19:109–120, 1979.
- [99] K. Singh. Antiferroelectric lead zirconate, a material for energy storage. *Ferroelectrics*, 94:433, 1989.
- [100] D. Smyth. Defects and order in perovskite-related oxides. *Annu. Rev. Mater. Sci.*, 15:329, 1985.
- [101] A. Sonin and B. Strukow. *Einführung in die Ferroelektrizität*. Akademie-Verlag-Berlin, 1974.
- [102] L. Sorin and M.V.Vlasova. *Electron spin resonance of paramagnetic crystals*. Plenum Press, New York London.
- [103] S. Stoll. *Spectral Simulations in Solid-State Electron Paramagnetic Resonance*. PhD thesis, ETH Zürich, 2004.
- [104] S. Stoll and A. Schweiger. EasySpin, a comprehensive software package for spectral simulation and analysis in EPR. *J. Magn. Reson.*, 178(1):42–55, 2006.
- [105] M. Tanaka, R. Saito, and K. Tsuzuki. Electron-microscopic studies on domain-structure of  $\text{PbZrO}_3$ . *Jap. J. Appl. Phys.*, 21:291–298, 1982.
- [106] S. Teslic and T. Egami. Atomic structure of  $\text{PbZrO}_3$  by pulsed neutron diffraction. *Acta Cryst.*, B54:750–765, 1998.
- [107] K. Uchino. *Ferroelectric devices*. Dekker, New York, 2000.
- [108] J. van Tol, L.-C. Brunel, and R. Wylde. A quasioptical transient electron spin resonance spectrometer operating at 120 and 240 GHz. *Rev. Sci. Inst.*, 76:074101, 2005.
- [109] C. Verdier. *Fatigue effects in bulk lead-zirconate-titanate*. PhD thesis, Technische Universität Darmstadt, 2003.
- [110] J. V. Vleck. Theory of the variations in paramagnetic anisotropy among different salts of the iron group. *Phys. Rev.*, 41:208, 1932.
- [111] J. V. Vleck and W. Penney. *Phil. Mag.*, 17:961, 1934.
- [112] T. von Waldkirch, K. Müller, and W. Berlinger. Analysis of the  $\text{Fe}^3\text{-V}_\text{O}$  center in the tetragonal phase of  $\text{SrTiO}_3$ . *Phys. Rev. B*, 5:4324–4334, 1972.
- [113] Y. Wan-Lun and Z. Ming-Guang. Spin-Hamiltonian parameters for S-state ions. *Phys. Rev. B*, 37:9254–9267, 1988.
- [114] D. Wang and G. Hanson. Extreme rhombic distortion in electron paramagnetic resonance and a superposition model account. *J. Magn. Res. A*, 118:1–6, 1996.

- 
- [115] W. Warren, G. Pike, K. Vanheusden, D. Dimos, B. Tuttle, and J. Robertson. Defect-dipole alignment and tetragonal strain in ferroelectrics. *J. Appl. Phys.*, 79:9250–9257, 1996.
- [116] W. Warren, B. Tuttle, and D. Dimos. Ferroelectric fatigue in perovskite oxides. *Applied Physics Letters*, 67(10):1426–1428, 1995.
- [117] W. Warren, B. Tuttle, F. Rong, G. Gerardi, and E. Poindexter. Electron paramagnetic resonance investigation of acceptor centers in  $\text{Pb}(\text{Zr,Ti})\text{O}_3$  ceramics. *J. Am. Ceram. Soc.*, 80:680–684, 1997.
- [118] R. Waser and D. Smyth. *Ferroelectric Thin Films: Synthesis and Basic Properties*, chapter *Defect chemistry, conductuon, and breakdown mechanism of perovskite-structure titanates*, pages 47–92. Gordon and Breach, Amsterdam, 1996.
- [119] M. Weissbluth. *Atoms and molecules*. Academic Press, New York, 1978.
- [120] R. Wenzel and Y. Kim. Linewidth of the electron paramagnetic resonance of  $(\text{Al}_2\text{O}_3)_{1-x}(\text{Cr}_2\text{O}_3)_x$ . *Phys. Rev.*, 140:A1592–A1598, 1965.
- [121] G. Wessel and H. Goldick. Electron spin resonance of iron-doped  $\text{KTaO}_3$ . *J. Appl. Phys.*, 39:4855, 1968.
- [122] H. Wickmann, M. Klein, and D. Shirley. Paramagnetic resonance of  $\text{Fe}^{3+}$  in polycrystalline ferrichrome A. *J. Chem. Phys.*, 42:2113, 1965.
- [123] B. Wybourne. *Spectroscopic properties of rare earths*. Interscience Publishers, New York, 1965.
- [124] B. Wybourne. Energy levels of trivalent gadolinium and ionic contributions to ground-state splitting. *Phys. Rev.*, 148:317, 1966.
- [125] Y. Xu. *Ferroelectric materials and their applications*. Elsevier, Amsterdam, 1991.
- [126] M. G. Zhao and M. Chiu. Analytical expressions for zero-field splittings of  $3d^5$  ions in low-symmetry fields and their applications. *Phys. Rev. B*, 52:10043–10052, 1995.

# Curriculum vitae

HRVOJE MEŠTRIĆ

born: 10 August 1973, Varaždin, Croatia

permanent address: Mihavićeva ul. 5. HR-42220 Novi Marof, Croatia

e-mail: mestric@chemie.tu-darmstadt.de

## EDUCATION

1980 – 1988

Elementary school in Novi Marof

1988 – 1992

High school (*Gymnasium*) in Varaždin

1992 – 2000

Graduate degree in physics (Dipl. ing. phys.); University of Zagreb, Faculty of Science;

*thesis title:* Determination of hyperfine coupling tensor in ENDOR spectroscopy;

*supervisor:* Prof. Dr. J. N. Herak

2002 – 2006

Doctorate degree in chemistry, TU Darmstadt, Chemistry Department;

*thesis title:* Local structure and symmetry of paramagnetic ions in ferroelectric ceramics;

*supervisor:* Prof. Dr. K.-P. Dinse

## WORK

02/2001 - 07/2002

Associate for software and publishing, Matrix Croatica, Zagreb

09/2002 - 01/2006

Research assistant, Darmstadt University of Technology, Eduard Zintl Institute for Inorganic and Physical Chemistry



## PUBLICATIONS

- H. Meštrić, R.-A. Eichel, K.-P. Dinse, A. Ozarowski, J. van Tol, L.C. Brunel: *High-frequency EPR investigation of the  $Fe^{3+}$  impurity center in polycrystalline  $PbTiO_3$  in its ferroelectric phase*, J. Appl. Phys. **96**, (2004), 7440-7444
- H. Meštrić, R.-A. Eichel, T. Kloss, K.-P. Dinse, So. Laubach, St. Laubach, P.C. Schmidt, K.A. Schönau, M. Knapp, and H. Ehrenberg: *The nature of iron-oxygen vacancy defect centers in  $PbTiO_3$* , Phys. Rev. B, **71**, (2005), 134109
- R.-A. Eichel, H. Meštrić, and K.-P. Dinse, A. Ozarowski, J. van Tol, L.C. Brunel, H. Kungl and M.J. Hoffmann: *High-field EPR of paramagnetic functional centers in  $Cu^{2+}$ - and  $Fe^{3+}$ -modified PZT ferroelectrics*, Magn. Res. Chem. **43** (2005), S166 - S173
- H. Meštrić, R.-A. Eichel, K.-P. Dinse, A. Ozarowski, J. van Tol, L.C. Brunel, H. Kungl, M.J. Hoffmann, K.A. Schönau, M. Knapp, and H. Fuess: *Iron-oxygen vacancy defect association in polycrystalline iron-modified  $PbZrO_3$  antiferroelectrics – multi-frequency electron paramagnetic resonance and Newman superposition model analysis*, Phys. Rev. B **73** (2006), 184105
- R.-A. Eichel, H. Meštrić, H. Kungl, M. J. Hoffmann: *Multi-frequency electron paramagnetic resonance analysis of polycrystalline gadolinium-doped  $PbTiO_3$  - charge compensation and site of incorporation*, Appl. Phys. Lett. **88** (2006), 122506

## CONFERENCES

- 08/2003, poster, *Gordon Research Conference ‘From Point Defect to Macroscopic Properties in Functional Ceramics’*, New London MA
- 09/2003, participant, *WE Heraeus Summerschool ‘Ferroelectrics’*, Halle
- 12/2003, talk *The Sixth Students’ Meeting ‘School of Ceramics’*, Novi Sad
- 11/2004, talk, *Annual Meeting of Joint Research Project 595*, Schmitten
- 03/2005, poster, *Colloquium ‘High-field EPR in Biology, Chemistry and Physics’*, Hühnfeld
- 04/2005, poster, *Status Colloquium of Joint Research Project 595*, Darmstadt
- 07/2005, poster, *EPR Summerschool*, Wiesbaden



Hrvoje Meštrić  
Nieder-Ramstädter-Straße 191/12  
64285 Darmstadt

Darmstadt, 19. 01. 2006

## Eidesstattliche Erklärung

Hiermit erkläre ich an Eides Statt, daß ich meine Dissertation selbständig und nur mit den angegebenen Hilfsmitteln angefertigt habe.

Hrvoje Meštrić



Hrvoje Meštrić  
Nieder-Ramstädter-Straße 191/12  
64285 Darmstadt

Darmstadt, 19. 01. 2006

## Erklärung

Ich erkläre hiermit, noch keinen Promotionsversuch unternommen zu haben.

Hrvoje Meštrić